1-30-2017

In-situ TEM Lithiation of Alternative Battery Electrode Materials

Matthew T. Janish
University of Connecticut - Storrs, matthew.janish@uconn.edu

In-situ TEM Lithiation of Alternative Battery Electrode Materials

Matthew Thomas Janish, PhD

University of Connecticut, 2017

The world-wide effort to produce and use cleaner energy also necessitates more advanced energy storage capabilities. For example, clean sources of electricity, such as wind or solar, are intermittent and require load leveling. Electric vehicles require more energy- and power-dense batteries in order to truly compete with fossil-fuel-based combustion engines. Lithium-ion batteries (LIBs) currently dominate the secondary battery market. However, in order to build a better LIB, there is a clear need for a better understanding of the fundamentals of lithiation processes. Transmission electron microscopy (TEM) is unique in its ability to correlate structural data with chemical information; as such, in-situ TEM techniques can provide vital, fundamental data on alternative electrode materials that will support the development of advanced batteries.

In general, lithium storage in a host material may be accomplished by one of two mechanisms. The first is intercalation of layered materials, which is minimally disruptive to the host structure at the cost of Li storage capacity. The second is alloying, which in many cases allows the uptake of several Li atoms per host atom, but rapid structural evolution and expansion occur during the reaction. MoS_2 and Sn were the materials chosen for this work, to represent both Li storage mechanisms and to demonstrate the power of in-situ TEM experimentation for identifying atomic-scale processes that contribute to the lithiation of an electrode material. MoS_2 is a layered material with a high specific capacity and excellent rate capability, while elemental Sn forms several intermetallics with Li, storing up to 4.25 Li atoms per Sn atom in its fully-lithiated phase.

Solid-state half-cells were constructed inside the TEM using a holder designed to perform simultaneous scanning-tunneling microscopy (STM) and TEM. Li metal was used as the counter/reference electrode, with either MoS_2 or Sn as the working electrode and solid Li_2O on the surface of the Li metal acting as an

electrolyte. Real-time observations of the structural evolution of the working electrode materials, as well as *post mortem* analysis, are presented and discussed.

In-situ TEM Lithiation of Alternative Battery Electrode Materials

Matthew Thomas Janish

B.S., University of Texas at Dallas, **2009**

A Dissertation

Submitted in Partial Fulfillment of the

Requirements for the Degree of

Doctor of Philosophy

at the

University of Connecticut

2017

APPROVAL PAGE

Doctor of Philosophy Dissertation

In-situ TEM Lithiation of Alternative Battery Electrode Materials

Presented by

Matthew Thomas Janish, B.S.

Major Advisor _____
C. Barry Carter

Associate Advisor _____
George A. Rossetti, Jr.

Associate Advisor _____
S. Pamir Alpay

University of Connecticut
2017

Acknowledgements

The work described in this dissertation only represents a fraction of my PhD work, and none of it would have been possible without collaborations with Katie Jungjohann, Bill Mook, Andrew Leenheer, Paul Kotula, Brad Boyce, Stan Chou, Bryan Kaehr, Joe Michael, Yang Liu, N. Ravishankar, Terry Holesinger, Avinash Dongare, Helena Silva, Julia Valla, Radenka Maric, Chris Cornelius, David Mitlin, David Bell, Grant Norton, Ned Thomas, Justin Roller, David Mackay, and Craig Owen.

The support of Pamir Alpay, George Rossetti, Mark Aindow, Bryan Huey, Puxian Gao, Adam Wentworth, Lorri Lafontaine, Cathy McCrackan, Susan Soucy, Leah Winterberger, Kerrie Alberts, Sean Hearne, Claire Chisholm, Heather Brown, Jessica Vanderburg, Sriram Vijayan, Arun Mannodi-Kanakkithodi, Drew Clearfield, Manny Rivas, Vahid Rastegar, and Weyshla Rodríguez was indispensable.

This work is dedicated to my family: my parents, Tony and Cheryl; my sister Elyse; my grandmothers, Edna and Sharon; and to the memory of my grandfathers, Julian and Ted.

And finally, special thanks are due to my advisor, Professor Barry Carter, whose super-human patience and understanding have made my career possible in more ways than one.

Table of Contents

Approval page..... iii

Acknowledgements..... iv

Chapter 1 - Introduction..... 1

Chapter 2 - Materials and Methods..... 53

Chapter 3 - Characterization of MoS_2..... 83

Chapter 4 - Lithiation of MoS_2..... 126

Chapter 5 - Characterization of Sn..... 151

Chapter 6 - Lithiation of Sn..... 172

Chapter 7 - Future Work..... 203

References..... 210

1 Background

This dissertation proposes the thesis: new materials are essential for future energy-storage needs and TEM is an essential technique for assessing such materials.

The goal of this project was threefold: (i) to develop skills in a variety of *in situ* transmission electron microscopy techniques, (ii) to develop skills in traditional electron microscopy techniques, and (iii) to apply these skills to extend the scientific community's understanding of some alternative lithium ion battery electrode materials.

The specific areas of study will include in-situ electrochemical lithiation experiments using Sn and MoS_2. The lithiation of Sn and MoS_2 relates directly to goals (i) and (iii), and the study of defects in Sn is important since dislocations and grain boundaries in the host material will affect the transport mechanisms of Li as it is inserted and removed; this aspect of the project addresses goals (ii) and (iii).

The research was carried out primarily at the Center for Integrated Nanotechnologies (CINT), a national user facility which is shared between Sandia National Laboratories in Albuquerque, NM and Los Alamos National Laboratory in Los Alamos, NM.

1.1 Batteries

1.1.1 Terminology

The Merriam-Webster dictionary defines electrochemistry as "a science that deals with the relation of electricity to chemical changes and with the interconversion of chemical and electrical energy." This definition is particularly apt to the discussion of secondary (rechargeable) batteries, the purpose of which is to convert electrical energy into chemical energy for storage and then to re-convert the stored chemical energy to electrical energy when it is needed.

It is interesting to note that originally, the term “battery” was applied in the general sense to mean a collection of galvanic cells, in much the same way that a collection of heavy (e.g., anti-aircraft) guns is known as a battery [1]. It is indicative of how important energy storage has become to modern society that in the vernacular, *battery* is nearly synonymous with *galvanic cell*, and indeed in modern dictionaries the traditional meanings of the word are now listed second and third. There are three main components of a galvanic cell: two electrodes (usually called the anode and the cathode) and an electrolyte.

The electrode that accepts electrons from the external circuit is called the cathode; in secondary Li-ion batteries the positive electrode is generally taken as the cathode even though technically the anode and cathode switch on each half-cycle.

The electrode that provides electrons to the external circuit; in secondary Li-ion batteries the negative electrode is generally taken as the anode. The convention of using the discharge half-cycle as a reference for naming electrodes is common in the literature, and will be adopted in this work.

The electrolyte is a material that is electrically insulating but conducts ions. In lithium-ion batteries (LIBs), the most common electrolytes are organic liquid solvents, especially ethylene carbonate (EC, $(CH_2O)_2CO$) and dimethyl carbonate (DMC, $OC(OCH_3)_2$) or a mixture thereof, containing the salt lithium hexafluorphosphate ($LiPF_6$), which dissolves readily in non-polar solvents. This ensures that the ions and electrons must take different paths between the electrodes, so that as the ions are driven from one electrode to the other through the electrolyte, the electrons are driven through the device the battery is powering.

A lithium-ion battery is a galvanic cell (or collection- *battery*- of them) wherein the species that transports charge through the electrolyte is ionized lithium, Li^+. Commercial LIBs typically have

a positive electrode consisting of lithium cobalt oxide ($LiCoO_2$), with graphite as the negative electrode. The two most common LIB geometries are cylindrical cells, in which the electrode sheets are rolled up into a cylinder-shape (common in laptop computer batteries), and planar cells, in which electrode sheets are stacked on top of one another (as in cell-phone batteries). To ensure that the cell does not short circuit due to electrical contact between the cathode and anode, a polymer membrane is employed as a physical separator.

The driving force responsible for the discharge of a battery is the reduction in Gibbs free energy that occurs when ions leave the negative electrode, travel through the electrolyte, and react with the positive electrode. In other words, as the chemical energy of the battery is reduced during discharge, the energy is being provided as electricity to the device that the battery is powering. Obviously, the driving force for the reverse reaction is an externally applied voltage of the opposite polarity; during charging the battery converts electrical energy, usually supplied by a wall socket, back into chemical energy.

The voltage that the battery can provide to the external circuit is then defined by the magnitude of the reduction of the Gibbs free energy associated with the chemical reaction. In the LIB literature, this is often expressed as the voltage vs. Li/Li^+, where lithium metal is used as a reference in the Nernst equation [1]:

$$V = -\frac{RT}{z_i F} ln\left(\frac{a_i(+)}{a_i(-)}\right)$$

where V is the potential difference across the cell, R is the gas constant (in $Jmol^{-1}K^{-1}$), T is the absolute temperature, z_i is the number of elementary charges carried by species i (+1 in the case of Li), F is the Faraday constant, and a_i is the activity of species i in the positive (+) and negative (-) electrodes. If one of the activities is always a standard reference value (i.e., if one of the

electrodes is always Li metal) then if the activity of Li in an electrode material is known, the Nernst equation gives the voltage of that material vs. Li.

The cell voltage is reduced by the ionic impedance within the electrodes, at the electrode-electrolyte interface, and within the electrolyte itself; additionally, any electrical conduction within the electrolyte will result in a reduction of the cell voltage (as well as self-discharge).

Capacity describes how much charge an electrode can hold. The units of capacity are simply Coulombs, but this is an extensive property. Charge capacity may be normalized by electrode weight (specific capacity, often given in mAh/g for LIBs), by mole of material (molar capacity, mAh/mol), or by volume of the electrode (capacity density, given in mAh/cm^3). In some cases, some of the lithium atoms (and their associated electrons) will not come back out of an electrode material. The charge that is "stored" this way, that cannot be retrieved, is known as the irreversible capacity of a cell. The charge associated with Li atoms that will freely move back and forth between the electrodes is the reversible capacity. In Li-ion cells, the reversible capacity tends to decrease with each cycle as the very active Li ions participate in irreversible, "parasitic" side reactions, often with the electrolyte or in conjunction with reactions between the electrolyte and the electrode(s). The rate of these side reactions increases with temperature, which also increases as a battery operates and some of the electrical energy is dissipated as heat. Therefore, the more a battery is used, the faster its capacity will fade.

The solid-electrolyte interphase (sometimes interface instead of interphase; SEI) layer is the main result of these undesirable, irreversible side reactions. It is a solid layer of the side-reaction products and has been known to adversely affect the performance of a cell, not only by leeching the Li atoms that are used to store charge but also by decreasing the rate at which Li can flow

into and out of the electrode. SEI layer formation and evolution is an important area of study in the field of battery research.

The cycling rate of a battery can have a significant impact on its performance (see, e.g., Fig. 1a in [2]. This figure is often expressed as "C-rate," e.g., 0.1C, which refers to what fraction of the battery's capacity is charged or discharged in one hour. Thus, at a rate of 1C, discharging the battery takes one hour. At a rate of 0.5C, discharge takes two hours, and at 2C the battery discharges in half an hour. In general, the higher the rate at which a LIB is cycled, the faster its performance (especially its charge capacity) will degrade.

Energy density describes how much energy an electrode can store in a fixed volume. It has units of Wh/l and is one of the key figures of merit for small portable devices that run on low power; the higher the energy density of the battery, the longer a device of a fixed size can run or the smaller a device can be made that will run for a fixed amount of time.

The energy storage ability of an electrode may also be normalized by weight. This is called the specific energy, which has units of Wh/kg. The specific energy of a cell is one of the main figures of merit for hybrid- or fully-electric vehicles; in fact, there is an approximate relation between a battery's specific energy and the effective range, in miles, of an electric vehicle powered by that battery (a ratio of approximately 1:2).

Power density describes how much of the energy stored in the battery can be drawn at a time, normalized by volume. Likewise, specific power represents the rate at which energy can be drawn from (or stored in; this raises the point that a cell contains two electrodes which may have different properties, and therefore the overall performance of the cell is limited by the weakest figures of merit between the two electrodes) an electrode normalized by its weight.

Power density and specific power are also important for high-power applications such as electric vehicles, since a large amount of energy is required at any given instant to simultaneously run climate control, lights, speakers, and, of course, move the vehicle.

1.1.2 Evaluating batteries: useful plots and figures of merit

One of the main figures of merit for a particular battery configuration is its Coulombic efficiency. This is the percent of the capacity on the nth cycle that is still available on the $(n+1)$th cycle. Even a slight deviation from 100% is indicative of rapid capacity fading. For example, Figure 1.1 shows the remaining charge capacity vs. number of cycles for Coulombic efficiencies of 100%, 99.5%, and 98%. It can be observed that even with a Coulombic efficiency of 99.5%, only 61% of the original capacity remains after 100 cycles, while a battery with a Coulombic efficiency of 98% will lose half of its original capacity after only 35 cycles and only 13.5% remains after 100 cycles.

Discharge curves are a common method of visualizing the characteristics of the electrochemical reaction that takes place as a cell is cycled. They plot the cell voltage against the cell capacity; in some cases the capacity is normalized as a percentage, which is useful in comparing cells with very different capacities, while in other cases the specific capacity of the cell is used. In LIB literature, when a single electrode is being tested, the mole fraction of Li in the electrode material of interest is sometimes used as the abscissa. Several examples of discharge curves are shown in Figure 1.2. The different shapes of the curves are discussed in greater detail in §1.2.

Another common plot that is used to evaluate battery or electrode performance is the current-voltage (I-V) curve, wherein the electric current provided by (or to) the cell is plotted against the cell voltage. When an I-V curve is applied to the cycling behavior of an electrochemical half-cell, it is known as a cyclic voltammogram; cyclic voltammetry is often referred to by the

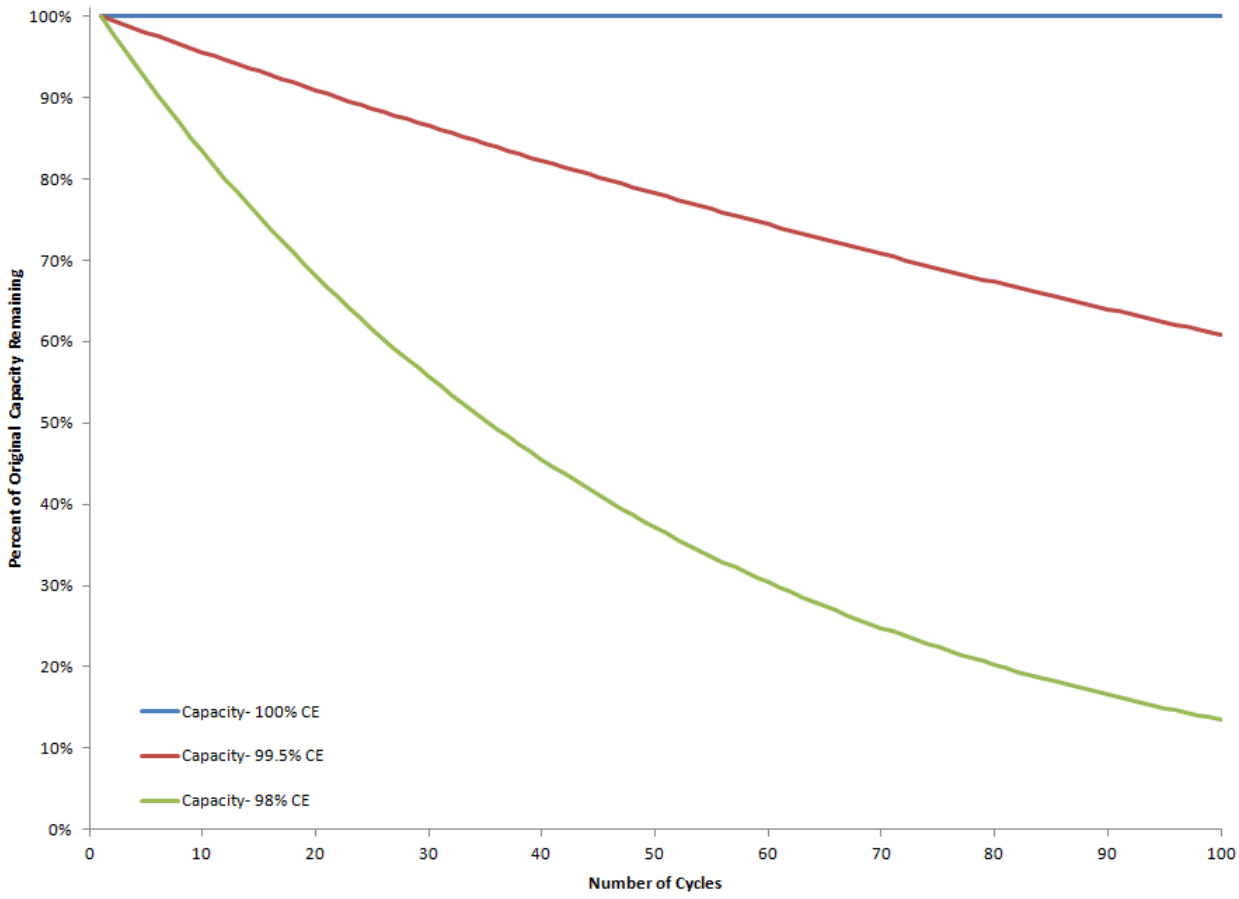

Figure 1.1. Capacity fading as a function of the number of cycles for coulombic efficiencies of 100%, 99.5%, and 98%.

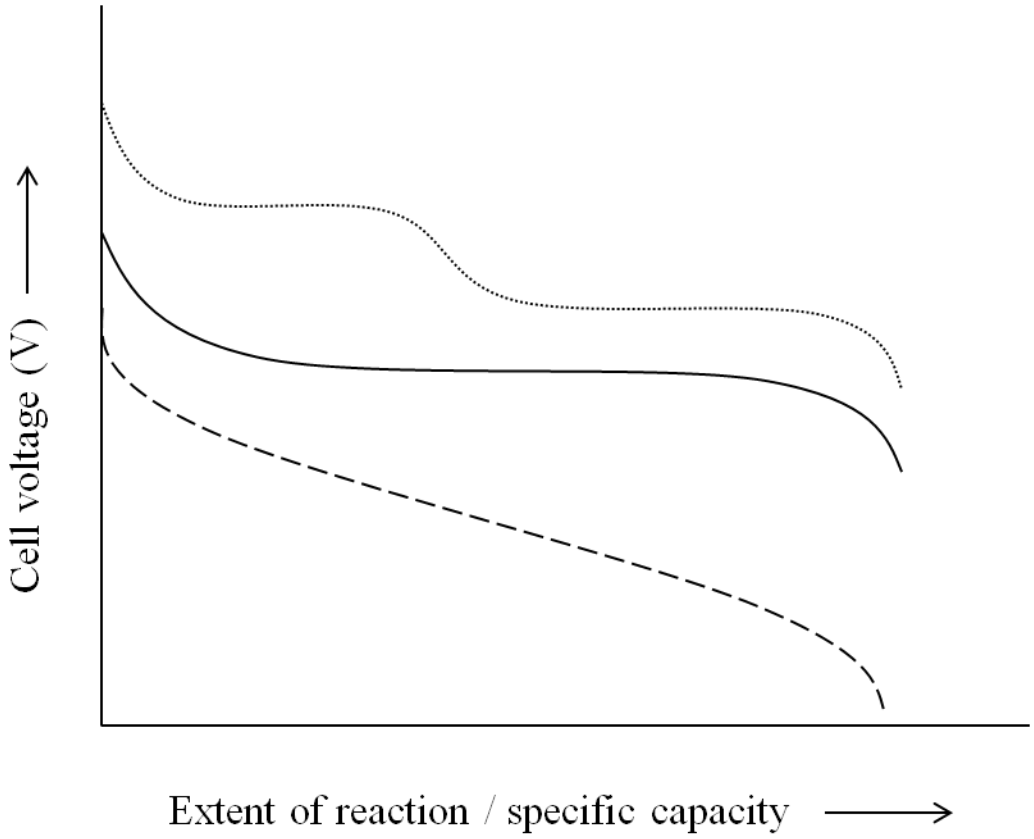

Figure 1.2. Schematic example of discharge curves for different kinds of battery electrodes. The dotted curve represents a multi-stage reconstitution reaction while the solid line is characteristic of a single-stage reconstitution reaction; the dashed curve represents an insertion reaction in which the product of the reaction is constantly changing.

abbreviation CV, and is not to be confused with capacitance-voltage profiling. An example is shown in Figure 1.3. When the current is positive, it is called anodic; peaks in the anodic current are associated with oxidation reactions in the electrode. Likewise, when the current is negative it is called cathodic, and peaks in the cathodic current indicate reduction reactions occurring in the electrode. These reactions correspond to plateaus in the discharge curve for the cell, such that the plateaus occur at the same voltage that the cathodic or anodic peaks are centered at in the cyclic voltammogram (see, e.g. [1, 3, 4]).

1.1.3 Common secondary battery chemistries

The first rechargeable galvanic cell was invented in 1859 by Gaston Planté and is known today as the lead-acid battery. In a fully-charged cell, the negative electrode is elemental Pb while the positive electrode is PbO_2; the electrolyte is concentrated sulfuric acid (H_2SO_4). During discharge, both electrodes are converted to lead sulfate ($PbSO_4$) while the electrolyte is converted to water. The total reaction of the cell is

$$Pb + PbO_2 + 2H_2SO_4 \leftrightarrow 2PbSO_4 + 2H_2O$$

Lead-acid batteries still represent the dominant battery market in the world today because, although their energy density and specific energy are quite low due to the high atomic weight of Pb, they have a very high specific power (180 W/kg) and are much cheaper than any other battery chemistry on the market. They are used in vehicles to power starter motors because of their high specific power, and even in large-format applications such as backup power supplies because of their low cost. In 2014 the global lead-acid battery market was valued at US$47.9 billion; this number is only predicted to grow for the foreseeable future due to the continued

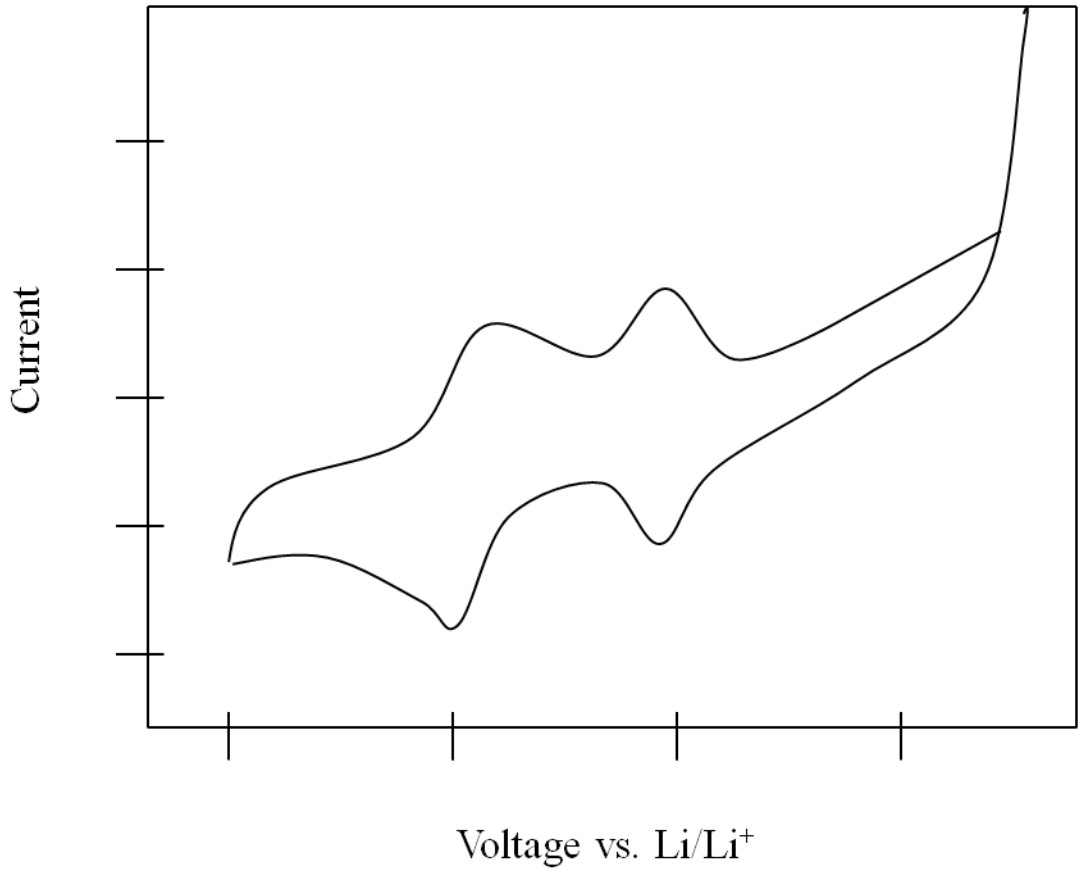

Figure 1.3. Schematic example of a cyclic voltammogram (sometimes known as a CV curve).

growth of the automotive industry (which accounted for nearly 58% of the lead-acid battery market in 2014) as well as increased demand for uninterruptible power supplies (UPS) [5].

The second major secondary galvanic cell chemistry was based on the nickel-cadmium system. The NiCd battery was invented in 1899 by Waldemar Jungner, and apparently independently in 1902 by Thomas Edison. The total reaction in a NiCd cell is

$$2NiO(OH) + Cd + 2H_2O \leftrightarrow 2Ni(OH)_2 + Cd(OH)_2$$

The ion responsible for charge transfer through the electrolyte is OH^-, which moves in the opposite direction as the electrons (i.e., from the NiO(OH) positive electrode to the Cd negative electrode during discharge). The electrolyte that facilitates this reaction is typically KOH, although unlike in the lead-acid case, ions associated with the electrolyte are not actively consumed at the electrodes in a NiCd cell; rather, water is consumed at the Cd plate. Until recently, NiCd batteries dominated the secondary battery market, but between growing environmental concerns surrounding the disposal of highly-toxic cadmium and the development of the superior nickel-metal hydride cell, the use of NiCd batteries is diminishing rapidly. Indeed, in the European Union, NiCd batteries have been outlawed and may only be supplied as replacement parts for existing equipment that requires them.

The nickel-metal hydride chemistry (abbreviated NiMH) uses the same positive electrode as a NiCd cell does; however, both the negative electrode and the mechanism of charge transport through the electrolyte differ from the NiCd case. Commercial metal hydride electrodes were developed in the late 1980s following the discovery of the reaction of $LaNi_5$ with hydrogen gas to form $LaNi_5H_6$ at the Philips laboratory, although the technology was first proposed in 1967. The structure of $LaNi_5$ is hexagonal, where a third of the Ni atoms on alternating layers are replaced by La (as in $CaCu_5$). Hydrogen atoms are stored in the tetrahedral interstices. Variations

on $LaNi_5$ replace most of the La with other elements, especially with other lanthanides such as Ce, Nd, and Pr, in order to reduce the cost and increase the cycle life.

Since the discovery of $LaNi_5$, other alloys that can reversibly store hydrogen have been employed as negative electrodes in NiMH batteries; these have the general composition AB_2 where A is usually Ti or Zr and B can be any of the other first-row transition metals (V through Zn), or Mo. In these structures the B atoms are close-packed in either a hexagonal ($MgZn_2$ structure) or cubic ($MgCu_2$ structure) arrangement, although the hexagonal structure tends to demonstrate superior hydrogen storage performance (e.g., when B is V, Ni, or Cr). Some of the AB_2-type electrodes provide charge storage densities that are 5-10% higher than $LaNi_5$.

Because NiMH cells have higher capacities than NiCd (the energy density of a typical NiCd cell is 100 mWh/cm^3, compared to 200 mWh/cm^3 for a NiMH cell) and carry the additional advantage of not containing the environmentally-hazardous Cd, they have largely taken over the share of the secondary battery market once held by NiCd cells.

1.2 Li-ion battery materials

Improving energy-storage (i.e., battery) technology is one of the most important scientific problems facing the world today [6]. As countries push to reduce their dependence on non-renewable fossil fuels for energy generation and transportation, performance demands related to the energy and power density of batteries are skyrocketing as new applications such as grid load-leveling (necessary because of the increased reliance of intermittent energy sources like wind and solar) and fully-electric vehicles emerge. Because LIBs dominate the various secondary battery chemistries on the market today, significant effort is being put into searching for electrode materials with higher capacity and greater rate capability than those commercially available at present.

There are three main classes of lithium storage materials.

• The first is the intercalation compound. These materials are characterized by loosely-bound layered structures (e.g., graphite), or by wide, open channels along specific directions (e.g., iron phosphate, $LiFePO_4$). Lithium atoms are stored between these layers or within these channels, causing minimal disruption of the host structure. The relatively high structural stability of this class of materials has led to their commercial success, but it comes at the cost of specific capacity since the host structure accommodates few Li atoms per host atom.

• The second type of Li storage material is the lithium alloy. In these materials Li is stored by the formation of intermetallics with other elements [7]. In some cases, especially for the group 14 elements Si, Ge, and Sn, these intermetallics are quite Li-rich; fully lithiated Si, for example, contains 4.4 Li atoms for every Si atom, and Sn is not far behind at 4.25 Li atoms per Sn. This results in extremely high specific capacities for Li-alloy electrodes in comparison to intercalation electrodes (e.g., 3579 mAh/g for Si compared to 372 mAh/g for a commercial graphite anode [8]; see Table 1.1), however, the uptake and release of such large quantities of lithium involves extreme changes in volume during cycling of the battery that lead to the rapid mechanical failure of such electrodes. Additionally, the rate at which Li is driven into this class of materials can have a significant effect on the performance of a cell. Although the theoretical capacity of Si is impressively high, if it is lithiated at a rate faster than 0.1C [9] almost all of this capacity is lost.

• The third type of Li storage material is a variation of the lithium alloy known as a convertible oxide [10]. In such an electrode, a metal that alloys with Li (e.g., Sn) begins in oxide form (e.g., SnO_2). During the first cycle, lithium reduces the electrode so that it transforms into metal particles dispersed in a Li_2O matrix. Once the electrode is completely

Table 1.1. Specific capacities of selected lithium-ion battery anode materials.

Material	Capacity (mAh/g)
Graphite	372
Silicon	4200
Germanium	1100
Tin	994
Molybdenite	1250

reduced by the Li, subsequent Li atoms are stored in the metal particles. Because the reduction of the electrode is often irreversible, many of the convertible oxides have the obvious disadvantage of requiring some of the Li in the battery to be "wasted" in the formation of the Li_2O. Additionally, the extra inactive material reduces the specific capacity of convertible oxides compared to their pure metal counterparts.

Each class of Li storage material operates on the basis of a different kind of chemical reaction. For example, intercalation is an insertion reaction, whereas alloying and oxide conversion are different kinds of reconstitution reactions (formation and displacement, respectively). Because the driving force for the discharge of a cell is related to the reduction in Gibbs free energy associated with these chemical reactions, the specific mechanism of Li storage can influence the voltage provided by a cell as it is discharged. In other words, if the character of the chemical reaction that is occurring changes, the voltage of the cell will also change to reflect this. The discharge curves in Figure 1.2 illustrate this: the dashed curve is characteristic of an insertion reaction, during which the reactants and products are constantly changing; the solid curve is typical of a single-stage reconstitution reaction (e.g., the formation of $LaNi_5H_6$); while the dotted curve represents a multi-stage reconstitution reaction, as might be expected in a Li-X system where Li and X form several, increasingly Li-rich intermetallic compounds as the reaction proceeds.

With the rise of nano-structured materials, the fields of battery research and transmission electron microscopy (TEM) have begun to see significant overlap. After the successful implementation of spherical aberration correction in the TEM in the late 1990s, for many purposes the quest for better resolving power was at an end and more emphasis began to be

placed on increasing the capabilities of specimen holders. Because of this, great strides have been made in the fields of *in situ* and *operando* electron microscopy in the last two decades.

Recently this has led to specimen holders in which electrochemical experiments can be carried out during imaging, and these holders have been brought to bear in studying the structural changes that take place during lithium insertion and removal in electrode materials for LIBs.

1.3 In-situ and *operando* TEM

Before delving into how experiments are performed within the microscope, a discussion on what is generally meant by the terms *ex situ*, *in situ*, and *operando* as applied to TEM will be useful.

The term *ex situ* refers to an experiment that is performed outside of the microscope, wherein the microscopy serves as a "post-mortem" and processes that occurred in the specimen during the experiment are deduced by comparing images from before and after. For example, in the 1970s layered materials such as MoS_2 were chemically sodiated in the laboratory, and the intercalated material examined afterwards in the TEM [11]. The implication is that the specimen is done changing by the time the microscopy is performed, and in fact this is not generally the case. One must always consider that the incredibly reducing atmosphere of the microscope column as well as the high-energy electron beam shooting through it are likely to have some effect(s) on the specimen, and these effects must be taken into account when interpreting the images. It is telling that most of the high-voltage (>1 MeV) TEMs were constructed to study radiation damage to materials, and this damage was inflicted by simply putting the specimen in the microscope and looking at it.

The term *in situ* is perhaps the most honest of the three, as it is broadly applied to any experiment that is performed inside the microscope so that images and data can be recorded as the processes of interest are occurring within the specimen. There are some microscopists who argue that

technically, all microscopy is actually in-situ microscopy since specimens are always changing, even when that change is not deliberate or desired. Many types of in-situ TEM experiments have been devised over the years. The earliest examples include heating, cooling, and both tensile and compressive deformation. As holders have become more sophisticated, electrical capabilities and liquid cells have been added to the list, and many custom setups combine several of the above features. Modification of the microscopes themselves has also been used to enable in-situ experiments. For example, differential pumping of the microscope column allows a small region of higher pressure near the specimen so that it can be exposed to gases during observation. This is known as environmental TEM (ETEM); because the gaseous environment can be tailored precisely, ETEM has been applied very successfully to the study of catalysis. Some labs have introduced ion beam lines to the TEM column so that the effects of ion irradiation can be studied in-situ.

Although in-situ experiments undoubtedly represent the future of TEM, ex-situ experiments still have their place in modern microscopy. They represent an important control for the effects of the beam during an in-situ experiment, which can be significant. This is illustrated dramatically in Figure 1.4, where the beam had an obvious impact on the crystal nucleation kinetics of a thin $Ge_2Sb_2Te_5$ (GST) film during a heating experiment. The average grain size in the region affected by the beam is ~30 nm, while in the region that was not exposed to electron irradiation the average grain size is ~80 nm; many more crystallites were nucleated in the area illuminated by the beam. It is not always this straightforward to tell when the beam is influencing the experimental results, however, and in these cases it is critical to complement the in-situ experiment with ex-situ work.

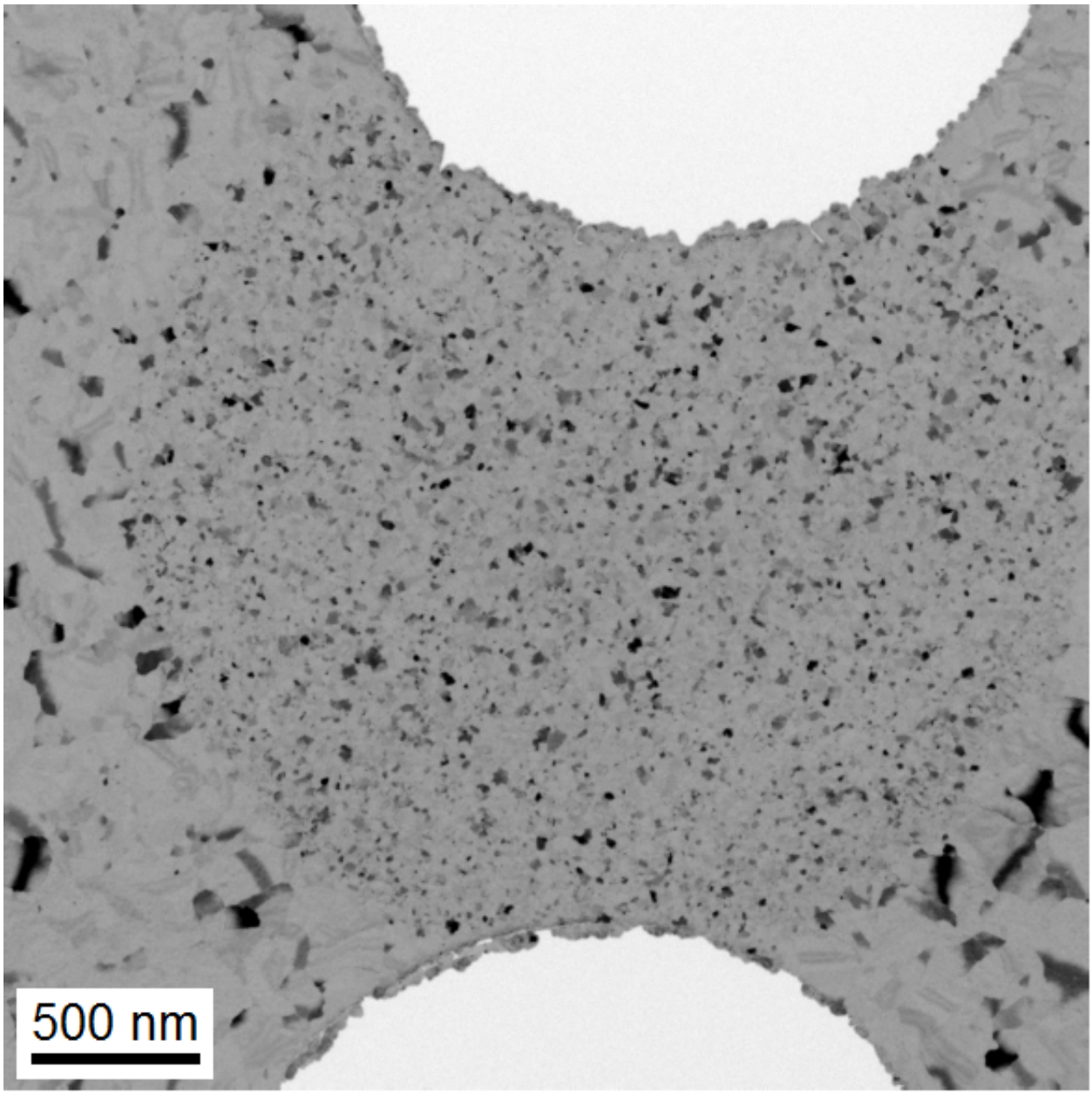

Figure 1.4. A thin film of $Ge_2Sb_2Te_5$ (GST) after a heating experiment in the Protochips Aduro 300 heating holder. The region of the specimen irradiated by the electron beam during the heat treatment is clearly identifiable by the much smaller grain size, demonstrating that the beam had a significant effect on the crystallization process and hence the final microstructure of the film.

The term *operando* is taken to mean that the process of interest is occurring in a specimen that is in an environment that exactly replicates a real device. However, by the nature of TEM, what it actually means is that the specimen is in an environment that is as close as possible to a real device while maintaining electron transparency; the enormity of this caveat is drastically understated when it is not ignored completely for the sake of placing a buzzword in a paper title.

To illustrate the line between *in situ* and *operando* TEM, consider the lithiation of a Sn nanowire (which will be discussed in detail in the following chapters). In the case where the Sn nanowire is lithiated by making direct contact with Li metal, with a surface oxide layer on the Li acting as an improvised electrolyte, the experiment is described as an in-situ one. When the same nanowire is lithiated in a liquid cell filled with a commercial ethylene carbonate-dimethyl carbonate electrolyte, the experiment is described as *operando.*

A key consideration for any in-situ or *operando* TEM experiment is the camera that will be used to record it. Cameras capable of very high frame rates are preferable (although these come with their own set of problems, discussed below) so that processes that occur faster than the human eye can follow may be recorded. Currently, the Gatan K2 direct electron detector is one of the fastest on the market. It is capable of recording 2048x2048 images at a rate of 1600 per second, which allows processes that take place on the order of 10^{-4} s to be captured. Impressive though this is, it also means that processes that occur at a shorter timescale, e.g., micro- or nanoseconds, remain beyond the reach of conventional TEM for now.

One way to work around this limitation and gain insight into nanosecond timescale processes is by using dynamic TEM (DTEM). DTEM sends pulses of several electrons down the column at once rather than a steady current that works out to one electron at any given time (as in conventional TEM). By clever use of the beam shift coils, the CCD camera is divided up into

nine segments so that, in one exposure of the camera, a nine-frame "movie" is recorded with mere nanoseconds separating the frames. Naturally, this method is limited by the restriction of only recording a few nanoseconds at a time, making it very difficult to capture the process of interest. Moreover, dividing up the CCD area has the obvious disadvantage of significantly decreasing the number of pixels available for each frame.

Of course, the ability to record large frames continuously at a high rate comes at high cost in terms of data storage. As an example, recording only pixel intensity data (i.e., no image metadata such as magnification or time and date recorded), and if each pixel can have values between 0-255 so that only one byte is required per pixel, then recording 2048x2048 pixels at 1600 frames per second will generate 6.71 GB of data per second. In comparison, the serial ATA (SATA) 3 interface by which most data storage drives "talk to" the rest of a computer saturates at 6 Gb (remember that *b* is for bit and *B* is for byte; data transfer rates are frequently reported in bits per second as a marketing tool since the number is eight times larger than the bytes per second figure) per second. This is less than one eighth of the rate the TEM camera can generate data, and furthermore there are very few drives- even consumer solid-state drives (SSDs)- on the market right now that have a write speed fast enough to saturate the SATA3 interface. It would take more than eight SATA3 SSDs capable of saturating the SATA3 interface to keep pace with the K2 camera. SSDs using the PCI express (PCIe) interface are just beginning to hit the consumer market; the fastest of these drives is currently able to write over 2 GB/s and so three or four of these working in parallel would be required to keep up with the data output of a high-speed TEM camera. Additionally, the cost per gigabyte of high-performance SSDs compared to mechanical hard disk drives (HDDs) is extremely high. For example, it costs $2.147/GB for a 2 TB PCIe SSD capable of writing data at 2 GB/s as opposed to only $0.032/GB for a 4 TB HDD

that writes data at an average of 0.015 GB/s at the time of this writing (keep in mind that when a company labels a drive as having a capacity of 4 TB they mean 4×10^{12} bytes, which is actually 3.64 TB when divided by 1024^4); however, note that in terms of cost per write speed the $4000 PCIe SSD is nearly four times as cost efficient as the $120 HDD. Therefore, common practice is to use the SSDs for data-recording purposes only, and to offload the data to file servers composed of banks of HDDs for long-term storage. Because the chance of a HDD failing increases rapidly with time, it is also important to take safety measures for the file server (i.e., setting up the drives in an appropriate RAID configuration). Clearly, significant planning needs to go even towards the computer(s) that will support in-situ and *operando* TEM experiments.

1.4 A brief history of in-situ TEM

Holders capable of cooling the specimen were proposed by Marton in 1934 [12], only two years after Knoll and Ruska's paper [13] describing the electron microscope; the following year, he also proposed the idea of environmental TEM via differential pumping of the specimen chamber [14]. Heating and straining holders had similarly early beginnings. However, due to the poor resolution of electron microscopes at the time (e.g., 3.5-10 nm in 1937 [15]), along with the massive drift introduced by these early "multifunctional stages" (at the time, even stages that could translate the specimen in two dimensions were not taken for granted; cf. Table 1 in the review on TEM stage design by Valdrè [16]), they were aimed at observing specimens in equilibrium but at conditions other than room temperature at low pressure. In other words, these were not holders designed to enable in-situ experimentation, but rather to record *post situ* (as it was sometimes called) the results of changes that were imposed while the specimen was in the microscope, or, in the case of environmental and cryo TEM, just to be able to observe biological specimens at all. True in-situ experimentation in the TEM appears to have begun in the late

1950s and early 1960s. This section briefly describes the early in-situ TEM experiments, and how modern holders and cameras have changed the information that it is possible to obtain in the TEM.

The first in-situ TEM heating experiments were conducted in 1958 by Whelan, who sandwiched his specimen between two pieces of metal that together acted as a resistive heater [17], and by Pashley and Presland who built their own crucible-style heating stage and used it to report on anti-phase boundary formation during the heating of CuAu [18].

Also in 1958, Wilsdorf described the design and application of a side-entry straining holder using a mechanical motor [19], which was based on a 1955 design by Weichan (although the latter was only used on polymer specimens, at the time). Wilsdorf also explained the preparation of metal specimens for tensile testing, and suggested how this holder could be modified for compression, bending, or torsion experiments. A top-entry holder designed to strain the specimen via differential thermal expansion of metallic bilayers during heating was described by Forsyth and Wilson in 1960 [20], and a similar design that strained the specimen upon cooling was published by Price the following year [21].

In 1963, Piercy, Gilbert and Howe cooled specimens to <29 K using liquid He. They estimated the temperature by condensing gases on a Cu foil [22]. The same year, Venables published a paper detailing a similar stage design, with the added capability of ±10° tilt on a single axis [23]. The minimum temperature that can be obtained in a cold stage is limited primarily by the transfer of energy from the electron beam to the specimen, although the overall increase in temperature induced by the electron beam depends on the thermal conductivity and heat capacity of the specimen (i.e., the temperature rise can be mitigated if the specimen conducts heat well and has a relatively thick area near the region of interest to act as a heat sink) [23]. Later, Heide and Urban

described a more advanced cold stage with high-resolution microscopy specifically in mind, and demonstrated this stage in an experiment studying radiation damage in Ni in a 650 kV electron beam [24]. It should be noted that all three of these holders were top-entry designs, as opposed to the modern side-entry holders.

Environmental TEM got a big push from the introduction of high-voltage TEMs in the late 1960s and early 70s [25, 26] because of the increased tolerance for thick specimens, but the first ETEM observations in a differentially-pumped column were detailed by Hashimoto et al. in 1959 [27]. When column modification was not feasible, gaseous or liquid atmospheres could be introduced by containing the atmosphere between two thin membranes (e.g., [28, 29]).

Today, the field of in-situ TEM is in the midst of another revolution due in part to the incorporation of devices based on micro-electromechanical systems (MEMS). Heating, electrical, and mechanical-deformation holders have been the main beneficiaries of these developments. A detailed description of the Protochips Aduro heating holder and how it compares to traditional crucible-style heating holders is provided in Chapter 2, along with Sandia's electrochemical Discovery platform and Nanofactory's (now FEI's) combined scanning-tunneling-microscopy/TEM stage.

The Hysitron PI-95 picoindenter is an excellent example of how MEMS integration is changing in-situ TEM capabilities. Not only do piezoelectric actuators allow nanometer-precision positioning of an indenter tip, quantitative force-displacement data is also generated by the holder while the deformation processes in the specimen are being imaged and recorded in real-time. By combining this quantitative approach to indentation with so-called "push-to-pull" devices, quantitative tensile tests can also be performed in the TEM.

1.5 Battery research in the electron microscope

As a general note, the reader is encouraged to pay particular attention to the actual dimensions of the materials being classified as a "nano-X" (X = wire, particle, etc.). Although for many years the usual definition of a nanomaterial required at least one dimension to be less than 100 nm [30], there is a distinct pattern in this body of literature of adding the nano- prefix to any material with sub-micron dimensions. This trend is a reflection of materials research papers in general, and is not surprising considering the effectiveness of "nano-things" at attracting funding. Although it is simple (and potentially gratifying) to dismiss this trend as the shameless stretching of a definition for the sake of visibility, citations, and the money that attends them, language is a constantly-evolving thing and scientific language is not immune to this phenomenon. Perhaps, at this point, it is in fact the definition of a nanomaterial that has changed, if a rigid definition can be applied at all [30].

This section represents a partial review of the modern literature on the lithiation and delithiation of battery electrode materials. Most of the literature covered involves in-situ TEM experimentation, and it should be noted that a significant body of ex-situ work preceded it. Also notable (though not discussed here) is the in-situ *SEM* lithiation of V_2O_5 by Strelcov et al. [4].

The lithiation of Cu_6Sn_5 was studied using ex-situ techniques by Choi et al. [31]; this is particularly relevant to the work described in Chapter 5, which is concerned with Sn films on Cu substrates. The material in [31] was also prepared by electroplating Sn onto Cu, but in this case it was heat-treated at 110 °C in an Ar atmosphere to encourage the formation of the intermetallic. Coin cells were partially lithiated (to 0.5 V) and fully lithiated (to 0.01 V), and cross-sectional TEM specimens were prepared by microtomy after the cells were cycled. The plateau at 0.4 V in the discharge curve was interpreted as the formation of Li_2CuSn, or possibly $Li_{13}Cu_6Sn_5$.

However, below 0.4 V, all traces of Li-Cu-Sn and Cu-Sn alloys vanished from the XRD spectra. The authors hypothesized that beyond this point, Li-Sn intermetallics were forming instead and the Cu was precipitating out, which they supported with a high-resolution TEM image and corresponding diffraction pattern indexed as Li_7Sn_2.

It was the work of Jian Yu Huang's group at Sandia National Laboratories (in particular Xiao Hua Liu, Yang Liu, and Jiang Wei Wang) that started the era of in-situ electrochemical experiments in the TEM for battery research. The first such paper was published in Science in 2010 [32] and was concerned with the lithiation of a SnO_2 nanowire. The experiment used a $LiCoO_2$ cathode and an ionic liquid electrolyte. Their results showed explicitly the conversion reaction from crystalline SnO_2 to Sn nanoparticles dispersed in an amorphous matrix.

The following literature is organized loosely by the type of material studied.

1.5.1 Pure materials

Liu et al. [8] demonstrated the same anisotropic lithiation rate in crystalline Si nanoparticles (NPs). They also noted a sharp cutoff in particle size at ~150 nm, above which the particles would crack and fracture during lithiation and below which they would remain intact. Interestingly, the possible effect of the lithiation rate on this behavior was investigated and determined to be a non-factor; small particles that were lithiated quickly did not fracture, while large particles that were lithiated slowly did. The results of this work also demonstrated that fracture of the NPs initiated at the surface rather than the center. The authors attributed this to the curved, sharp interface between the lithiated outer shell and the pure Si core, which reverses the expected stress at the surface of the particle from compressive to tensile. Although not explicitly discussed in the paper, this hypothesis is further supported by the images the authors present; in each case cracking began at the top and bottom of the Si NP, where the support structure was on

the left and the Li source was on the right. This geometry would provide a compressive stress, alleviating the tensile stress at the points of contact (especially as the NP expanded during lithiation) and exacerbating it elsewhere on the surface.

A related study by McDowell et al. [33] was published the same year that dealt with the lithiation of amorphous Si (a-Si) NPs. The NPs were supported on Si nanowires, and it was the nanowires that were in direct contact with the Li source. Data was collected from 26 different NPs; the wide variation in volume expansion reported (minimum 101%, maximum 332%, average 204%) was likely due to unreliable contact of the NPs with the Li and e^- sources. A maximum "allowed" particle size that would not result in mechanical failure upon lithiation was also demonstrated for a-Si, though the limit of ~800 nm is significantly higher than for crystalline Si NPs. This is (at least partially) related to the fact that a-Si lithiates isotropically whereas crystalline Si does not. The authors hypothesized that the lithiation of a-Si is a two-phase process rather than single-phase, and that the lithiation reaction is controlled by the slow Si-Si bond-breaking process at the Li_xSi-Si interface.

Liu et al. published a study on the lithiation of Ge nanowires [34]. The as-grown wires were crystalline, produced by chemical vapor deposition (a relatively slow and expensive process). The first two cycles were of particular interest, because while the starting material was crystalline and the fully-lithiated $Li_{15}Ge_4$ phase was also crystalline, after the first delithiation the nanowire became amorphous and porous. Upon the second lithiation of the wire, the lithiated phase was again crystalline. In fact, the phenomenon of amorphous material crystallizing as a result of lithiation has also been observed in Si (e.g., [35]), although as demonstrated in [33] this is not always the case. This amorphous Ge ↔ crystalline $Li_{15}Ge_4$ transformation was characteristic of all cycles after the first. Regarding the pores, the authors observed a so-called

"pore memory effect" whereby pores formed in the nanowire in nearly the same positions during every delithiation cycle. They hypothesized the following mechanism for this effect: first, pores form during the contraction involved in the initial delithiation cycle. Then, in subsequent cycles, regions around the pore get lithiated and delithiated first since surface diffusion is faster than bulk, and the pores are unlikely to close all the way during lithiation, which maintains their position in the nanowire. The authors furthermore proposed that pore formation might be controllable by doping the Ge to control atomic mobilities.

The lithiation behavior of Ge nanoparticles, as reported by Liang et al. [36], is in many ways similar to the NW case. It was noted that the amorphous to crystalline transition of the lithiated phase occurred at the same time throughout the particles as opposed to the crystalline phase nucleating at a specific location and growing. The crystallization process required holding the NPs at -1V vs. Li for an extended period of time. The Ge NPs did not fracture upon lithiation for the same reason that a-Si was not observed to fracture: the lithiation of Ge occurs isotropically.

Wang et al. [37] studied the lithium and sodium cycling behavior of Sn nanoparticles in a solid-state half-cell. The size of the pristine NPs ranged from 86 to 423 nm, and the volume expansion upon full lithiation was in the rage of 239 – 271%, where 258% is the theoretical expansion. They observed that the Sn NPs did not crack upon lithiation or sodiation as crystalline Si does. However, they reported that large Sn particles tended to be pulverized into smaller ones during cycling, and that small particles tended to aggregate during Li or Na uptake, and then be pulverized as the ions were removed. This agglomeration/pulverization behavior often took several cycles to complete. The lithiation mechanism was determined to be a two-step process, first involving a transformation from pristine Sn to amorphous Li_xSn with x close to 1, then from

Li_xSn to crystalline $Li_{22}Sn_5$. The reporting of this particular stoichiometry of the fully-lithiated phase is typical but questionable; this is discussed in detail in Chapter 6.

A closely-related ex-situ study on the lithiation behavior of monodisperse Sn nanoparticles was reported by Xu et al. [38]. The Sn NPs in this study were produced in solution in a glove box with a nitrogen atmosphere, and had diameters ranging from 4 – 17 nm (10 nm average with a sample size of 300 particles; it is noted that this is very thorough for a TEM study). The particles were cycled in half-cells against Li metal with a typical EC/DMC/$LiPF_6$ electrolyte, and were incorporated into these cells as both composite electrodes using carbon and PVDF binder, and drop-cast onto Cu TEM grids to enable post-mortem analysis in the microscope. No aggregation of the Sn NPs was reported in this study, although pulverization was observed during both lithiation and delithiation in spite of the particles' small size and the relatively slow charge/discharge rate of 0.1C. Interestingly, the formation of the diamond-cubic alpha phase of Sn was observed in these particles upon delithiation, which the authors attributed to the small particle size. A similar result was reported in [39], in which SnO_2 particles 4 nm in diameter were observed to delithiate to the α-Sn phase. Considering that the fully-lithiated phase belongs to the $F\bar{4}3m$ space group [40] in addition to the small particle size significantly changing the thermodynamic stability of particular crystal faces, it is not entirely surprising that the Sn particles in this study reverted to the closely-related $Fd\bar{3}m$ space group upon delithiation. Although the image showing the α-Sn particle displays signs of faceting (slightly difficult to spot due to delocalization effects) and twinning, no discussion was presented on the relative surface energies of common α- and β-Sn surfaces or twinning in Sn.

Recently, Leenheer et al. published groundbreaking results of the lithiation of Al, Au, and amorphous Si thin films that were fully immersed in a commercial electrolyte in the TEM [41];

in other words, as close to *operando* as possible in the TEM. Details on the holder that was used to accomplish this are presented in detail in Chapter 2, §2.7. In contrast to the results presented in [33], no phase boundary was observed during the first lithiation of the a-Si film. It was hypothesized that the very low contrast between the film and the surrounding liquid could have rendered such a phase boundary invisible, or that it simply was not present at all due to differences in processing methods (i.e., evaporation in [41] vs. [33], which used the CVD process described in [42]) causing different defect densities and hence a different lithiation mechanism. The authors also noted that the electron beam had a significant impact on the experiment. A high electron dose increased the overpotentials necessary to lithiate and delithiate the film.

In the polycrystalline Al film, the transformation to the lithiated LiAl phase was demonstrated to occur by a nucleation and growth mechanism, limited by the nucleation process. Because the growth of the lithiated phase occurred quickly relative to the nucleation of new lithiated regions, the phase boundaries were observed to move horizontally throughout the films; interestingly not all regions of the phase boundary moved at identical rates. If the lithiation process were growth-limited rather than nucleation-limited, there would have been many nucleation points covering the surface and the lithiation front would have moved vertically down the film instead. Because of the many well-known papers showing nanoparticles with pristine cores and lithiated shells (as discussed above) there has certainly developed a "prevailing wisdom" that lithiation proceeds from the outside in; one of the key conclusions drawn in this work is that this is not always the case. The authors hypothesized that in this case, nucleation of the lithiated phase was preferred at the corners of the film (for both Al and Au) because this resulted in the smallest increase in energy due to strain. Additionally, the Al films in this study were demonstrated to be quite robust

during cycling compared to other studies on Al (e.g., [43]) and even the Au films discussed in the same work.

The Au films themselves were included primarily as a model material because although the Al film has the advantage of providing some diffraction contrast as compared to the a-Si, its density is still rather close to that of its liquid environment which presents some of the same challenges to image interpretation as discussed for the a-Si case. The high atomic weight of Au, however, ensures that even thin films provide high contrast in the images. (As a philosophical aside, it should be noted how rare such attention to detail is in this particular subset of the literature. Recognizing the limits of the technique when it comes to working on materials that are "hot," and then designing the experiment and discussing the results within those limits, is not currently the *modus operandi* in this field.)

A unique study was published by Liang et al. [44] (another CINT-Sandia paper) on the lithiation of Ga droplets. This material conveniently avoids the pulverization issues that plague many other Li-alloy materials by the simple fact that it is a liquid in its delithiated state. Thus, although the electrode solidifies and expands as Li is inserted, and voids were observed to form during delithiation, the liquid-solid phase transformation also reverses upon full delithiation and the mechanical damage is "healed." Li and Ga form three different intermetallics with compositions of LiGa (cubic system), Li_3Ga_2 (rhombohedral), and Li_2Ga (orthorhombic), although it has been shown by Wen and Huggins that the stoichiometry of these phases can vary significantly [45]. It is interesting, then, that the final product in [44] was identified as a composite consisting of the LiGa and Li_2Ga phases; this identification was made by way of an electron diffraction pattern which is always exceedingly complicated when dealing with a polycrystalline material that forms several intermetallics. For example, the (012) plane of Li_3Ga_2, which gives the most intense peak

in the powder XRD pattern [45], has a theoretical spacing of 3.322 Å while the (021) plane in Li_2Ga (I/I_0 = 43%) has a spacing of 3.220 Å. Especially considering that each phase can be non-stoichiometric, it would not be possible to confidently ascribe a spot or ring corresponding to a ~3.25 Å plane spacing to either of these phases. It is also interesting to note that none of the three most intense peaks in the XRD pattern for Li_2Ga, namely those corresponding to (131), (110), and (021) (100%, 89%, and 43% relative intensity, respectively) is identified in the diffraction pattern; furthermore no mention of the rhombohedral Li_3Ga_2 phase is made at all.

Xia et al. recently published a study wherein the material of interest was black phosphorus [46]. Black phosphorus (BP) is the most stable P allotrope, and owing to its unique "puckered" layer structure (illustrated in Figure 1.5) it is natural to assume that it achieves Li storage by an intercalation mechanism. However, although such a mechanism is discussed in other literature, for example in [47], the high lithium content of the fully-lithiated Li_3P phase and the very large volume change that BP undergoes during cycling are both characteristic of an alloying reaction. Based on the data presented in [46] the volume expansion of BP is highly anisotropic; for example, figure 2 in the paper shows an electrode expanding in excess of 50% along its length and only 2% along its width. However, because the diffraction pattern presented does not appear to have been aligned with the images it is associated with, no information about which crystallographic direction is preferred for this volume expansion is conveyed.

1.5.2 Oxides

Kushima et al. described the lithiation of ZnO nanowires in the TEM [48]. The as-grown wires were single-crystal with the longitudinal axis aligned with the [0001] direction, but the material was amorphized during the lithiation process. The authors reported the observation of crack formation in the radial direction in the nanowires ahead of the lithiation front, dividing the wires

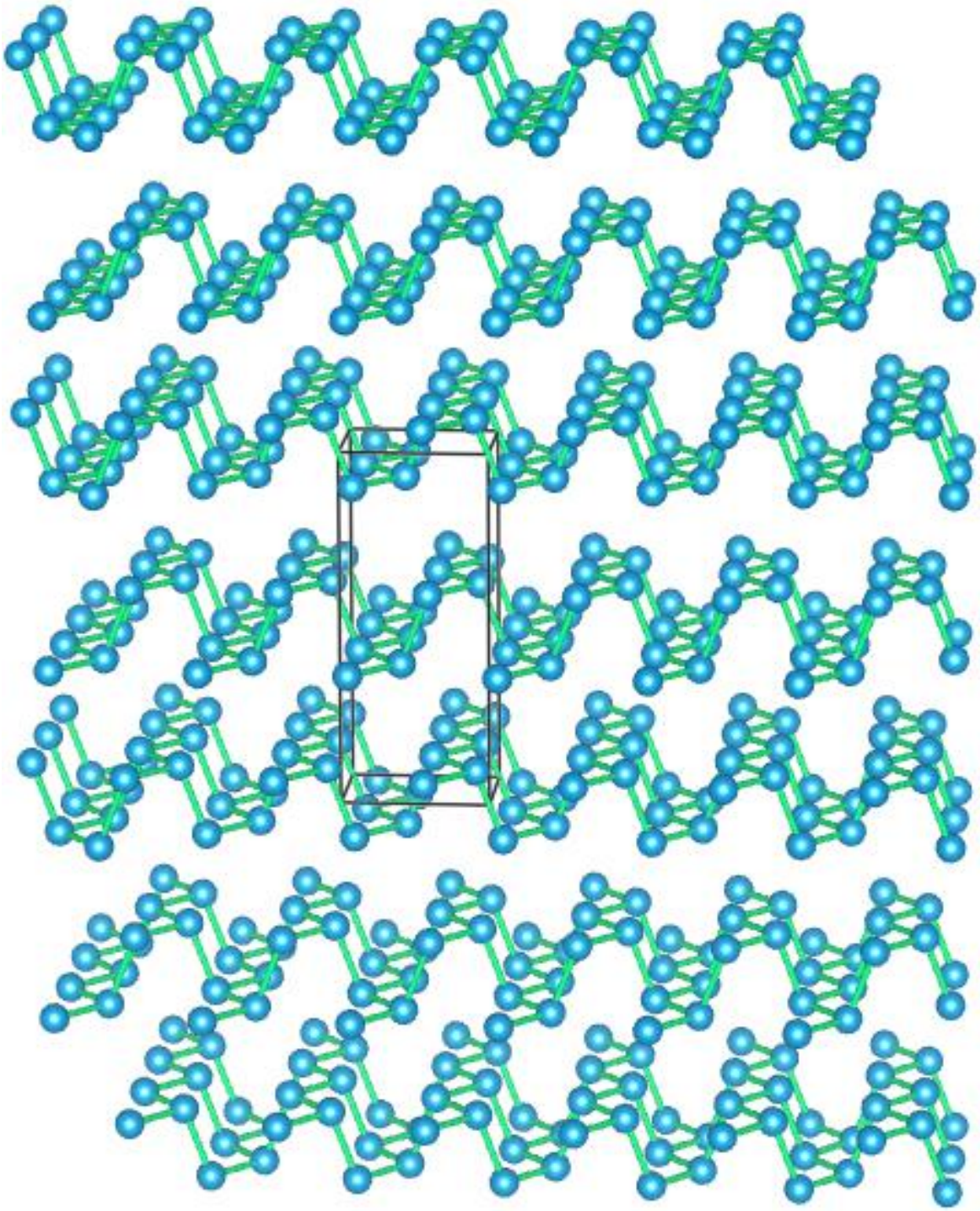

Figure 1.5. Model of the structure of black phosphorus, with a unit cell outlined.

into segments that then lithiated quickly because of the extra surface area provided by the fracture surfaces. This is in line with the experimental results on several other materials, where Li diffusion is much faster on the surface of a nanomaterial than it is in the bulk.

However, in contrast to the case of SnO_2, which described a "dislocation cloud" at the reaction front [32], nothing that was identified as a dislocation was observed during the lithiation of the ZnO nanowires. This was attributed to the Li-induced embrittlement of ZnO, which does not occur in SnO_2; this, in turn, was attributed to the ability of Sn to accommodate either a +2 or +4 charge state while Zn tends not to stray from +2.

This work describes two kinds of glass-glass interfaces that are produced by this mechanism. The first type is formed by the expansion of segment *n* back into the crack as it lithiates, while the near end of the (*n*+1) segment also begins to lithiate, amorphize and expand into the crack. The second type is formed by the lithiation fronts from the two ends of each segment eventually meeting in the middle. This implies a much faster diffusion rate along [0001] than other directions, which is not discussed in the paper.

Two other curious observations were reported in this work. First, the authors reported evidence of pristine ZnO in the cracks even after lithiation and suggested the possible presence of pores. Second, they described a "glass-glass interface memory effect," wherein glass-glass interfaces of the first type were observed to remain in roughly the same locations even after multiple cycles.

Iron phosphate (with the orthorhombic olivine structure) is one of the best-known alternatives to $LiCoO_2$ as a choice of cathode material in LIBs, and it has even begun to see some incorporation into commercial products. As such there is a large quantity of literature related to its battery applications. One fundamental concern in this subset of the literature is the presence of a sharp

phase boundary between the lithiated and de- (or un-) lithiated regions of the material, and in this regard in-situ TEM appears to have actually muddied the waters.

From a theoretical standpoint, the olivine structure contains large, open channels that lie parallel to the *b*-axis and so Li diffuses fastest along this direction. It might therefore be expected that such a phase boundary (PB) would lie parallel to the (010) planes and move in the [010] direction. Instead, calculations have predicted that a coherent PB parallel to (101) is actually the most stable, while a loss in coherence in the [001] direction can stabilize the PB parallel to (100) [49].

On the other hand, in their in-situ TEM study Zhu et al. observed a lithiation process that matched the intuitive mechanism originally described, i.e., the PB parallel to (010) [50]. They also reported the presence of misfit dislocations with Burgers vector ½<011>, which they interpreted as a loss of coherence in both the [010] and [001] directions, and, partially applying the logic of [49], hypothesized that loss of coherence in these two directions could stabilize the (010)-oriented PB.

However, this hypothesis does not make sense: a switch from coherence to semi-coherence in the [001] direction changes the relative stabilities of the (101)- and (100)-oriented PBs by virtue of their shared, non-zero *h* index. However, a loss in coherence in [010] cannot make a difference to the strain energy of a PB parallel to (010) because the two are perpendicular, and the coherence of a PB only makes sense in terms of directions parallel to it.

Furthermore, upon close examination the evidence for the ½<011>-type dislocations is tenuous, although it seems clear on first inspection and the discussion is presented quite confidently. First, based on the raw images, the apparent dislocations in the Fourier-filtered images cannot actually be distinguished from artifacts [51]. Second, the authors argue that because a fringe spacing

corresponding to the average of the $LiFePO_4$ and $FePO_4$ (002) spacings was not observed, the strain at the PB was not coherent and so misfit dislocations were responsible for the relaxation. However, the theoretical difference between $FePO_4$ (002) and $LiFePO_4$ (002) is only ~3 pm, and the difference between either of these spacings and their average, then, is ~1.5 pm. This is not a level of precision one expects an uncorrected, workhorse TEM to be able to achieve for any specimen, let alone one that is in excess of 160 nm thick and undergoing a dynamic electrochemical reaction. See §1.6 for further discussion of precision in the TEM and image processing artifacts.

Nanoscale TiO_2 is currently a popular subject of research in materials science; Kim et al. reported on the lithiation of rutile TiO_2 nanowires grown by a hydrothermal method [52]. The sizes of the wires varied significantly and their surfaces were rough, but were apparently single-crystal and aligned with the longitudinal direction parallel to [001] (no evidence is presented to support this, however).

Much like the [010] direction in iron phosphate, rutile TiO_2 has channels of vacant tetrahedral sites along the [001] direction, and Li diffusion is expected to be preferred along these channels. During lithiation, the authors observed that the rutile structure distorts from tetragonal to monoclinic as an intermediate phase when x in Li_xTiO_2 is 0.5. They reported that full lithiation involves a transformation to a rock-salt-like phase where the O atoms form a fcc lattice and the Li and Ti atoms sit in octahedral sites on alternating (002) planes. The mechanism for the transformation from the monoclinic phase, which strongly resembles the rutile structure with Li atoms situated near the (100) and (010) face centers, to the proposed cubic phase is unclear.

During lithiation, the authors also observed an expansion of the nanowires of ~140% in the radial direction(s) along with a contraction in the longitudinal direction to 97% of their original lengths.

Certainly, a contraction along *c* is not consistent with the monoclinic-to-cubic transformation shown in Fig. 4 of [52].

Qi et al. reported the lithiation of WO_3 nanowires in a solid-state half-cell. Unlike the behavior of many other oxides upon lithiation, this study reported no reduction of the W by the Li atoms; in other words, the lithiation process is ostensibly a pure insertion reaction. The authors present data on the position of the lithiation front with time, and demonstrate that the velocity of the front is approximately constant over short time intervals, with the velocity decreasing as the front gets further away from the Li source. No observations of the delithiation process were reported.

As is common with convertible oxide electrodes, upon lithiation the Li was observed to reduce the Mo, resulting in Mo particles dispersed in a Li_2O matrix. However, unlike with other convertible oxide electrode materials, the alloying of Li with these Mo clusters was not identified as the mechanism of reversible Li storage, with the Li_2O representing an irreversible capacity loss. Rather, during the first delithiation the Mo clusters were converted to crystalline $Li_5Mo_2O_6$ and then amorphous Li_2MoO_3, while the Li_2O disappeared. This way, only two Li atoms per MoO_3 formula unit are lost to an irreversible chemical reaction rather than six if Li_2O were the irreversible product.

Su et al. published results on the lithiation of Co_3O_4 nanoplates, which was accomplished using the solid-state half-cell experimental geometry with the active material supported on graphene [53]. The paper claims to put forward a new mechanism for the cycling behavior of Co_3O_4, which they observed to involve a conversion reaction to Co and Li_2O during the first lithiation and subsequently a reversible transformation between the latter composition and CoO + Li_2O. However, this is based on a statement that the previous understanding of the cycling behavior of Co_3O_4 involved a completely reversible transition between Co_3O_4 and Co + Li_2O, which is

attributed to a 2000 paper by Poizot et al. that concerned the lithiation behavior of several transition metal oxides [54]. In fact, the particular oxide of cobalt that was studied in the latter work was CoO, not Co_3O_4, and the reversible cycling reaction was reported as

$$CoO + 2Li \leftrightarrow Li_2O + Co \qquad [54]$$

and so the only difference in the mechanism proposed by Su et al. is an extra Li_2O on each side of the equation for every three Co atoms.

He et al. reported on the details of the transition of the lithiation reaction of NiO nanosheets from the surface to the interior of the sheets [2]. Initially, the reaction of NiO takes place at the edges of the sheet in what the authors refer to as a shrinking-core mechanism. That is, the NiO core gradually shrinks as the lithiation front proceeds inward. However, in some cases a "finger" of lithiated material was observed to penetrate into the core, eventually reaching all the way across the sheet, providing a drastically increased surface area for the reduction of Ni and greatly accelerating the lithiation of the sheet. However, the increase in the reaction rate was not proportional to the increase in surface area; on average, the reaction front moved an order of magnitude faster at the interior of the sheet compared to the initial surface-only reaction. However, these "fingers" that enabled the interior reaction only appeared after an average time of 156.1 s (see Fig. 2f in [2]).

The lithiation of the NiO nanosheets was studied for two different discharge rates: 0.1C and 10C. The authors reported significantly less SEI formation in the 10C case because of the drastically reduced time of the reaction. Notably, in the 10C case about half of the NiO was reduced after only 1.5 minutes; the material then took the remaining 4.5 minutes to fully saturate with Li.

This work also describes an interesting specimen preparation method, referred to by the authors as the grid-in-a-coin-cell method, which was used as an ex-situ complement to the in-situ TEM lithiation experiment. This involves submerging a TEM grid in the NiO electrode, although this implies a liquid (suspension) electrode material, which the report provides no details on. However, this approach allowed the post-mortem characterization of large areas (on the order of 100μm x 100μm) of lithiated material, at various states of discharge, which enables a more statistical analysis than is possible from a few in-situ experiments.

1.5.3 Chalcogenides and InAs

Su et al. described the lithiation of CoS_2 nanoparticles, both supported on graphene and in direct contact with the current collector [55]. In the Li-Co-S system, the Co atoms are reduced upon discharge to form Co nanoparticles, which were reported in this work to have a diameter of 1-2 nm, in a Li_2S matrix. The authors discuss a very surprising phenomenon whereby the CoS_2 particles are lithiated by different physical mechanisms and undergo different volumetric expansions depending on whether they were supported on graphene layers or in direct contact with the current collector. In the former case, the particles were observed to lithiate from the outside in, in a uniform fashion with few cracks and only a 26% increase in volume. On the other hand, when the particles were in direct contact with the W wire, they expanded anisotropically with a total increase in volume of 47%, leading to the formation of many large cracks. This rapid mechanical failure resulted in the retention of only 5.4% of the initial capacity after 30 cycles, with 43.4% of the initial capacity lost on the first cycle. Meanwhile, the particles supported on graphene sheets retained 55.8% of their initial capacity after 30 cycles, with 32.6% of the initial capacity lost on the first cycle. In general, the idea of supporting particles that are prone to fracture on graphene is a good one since the fracture piece will remain electrochemically active,

although in this case the graphene support tended to reduce the probability of the CoS_2 particles fracturing.

There has been some in-situ TEM lithiation work published on MoS_2 in the plan-view orientation (cf. §2.2), but this particular subject is covered extensively in Chapters 3 and 4.

Li et al. published a report on the lithiation of InAs nanowires [56]. The main points of interest of this material appear to be its very fast lithiation rate (reported as 275 nm/s along the length of the wire; compare this with the 1.2 nm/s rate in SnO_2 nanowires as reported in [57]) and the phase separation of the Li-As and Li-In compounds as lithiation proceeds. In this case, the reaction of the Li with As is irreversible, so the entire reversible capacity of an InAs electrode is provided by the In; three Li atoms per As are immediately lost in the formation of the Li_3As phase. The presence of a large number of stacking faults in the as-grown wires is hypothesized by the authors to play a significant role in their lithiation behavior, but there is insufficient characterization of the pristine material presented (i.e., none) to support these claims.

1.5.4 Comments

Aside from the broadening of the definition of a nanomaterial, the research discussed above is also marked by a rather more concerning trend that is growing in TEM literature in general, involving the explicit disregard for the limitations of transmission electron microscopy, which results in an implicit overstatement of its abilities. While the former is simply a tacit change in the usage of a word, the latter represents a serious decline in the scientific merit of the literature it affects, which includes not only the papers written by researchers participating in such behavior but potentially every study that cites them. With the sheer quantity of information being published on a given topic, it is difficult at best for a researcher to be aware of every publication

that is relevant to his or her work and so it is more important than ever for each individual publication to be accurate.

Specifically, there is a general unwillingness to admit that indexing diffraction patterns recorded from binary systems that form several intermetallic compounds is extraordinarily difficult, and the greater the number of intermetallics, the greater the difficulty. Of all the papers that have attempted it, none have done so convincingly. This is also true of the work presented in Chapter 6, the main difference being that in this case the author makes no pretense of having convincingly indexed the patterns presented!

Additionally, it is generally not acknowledged that most signals available for data generation in the TEM are not well-suited to detecting lithium, or that the electron beam itself may have a significant effect on where the lithium goes and how. The electron energy-loss signal is perhaps best-suited to sensing an electron's interaction with a lithium atom, but EELS spectra and energy-filtered images are not commonly presented in the literature. Of course, if another of the elements involved has a low-loss edge near 55 eV (the energy of the Li K edge) it may be difficult to detect the Li this way on a microscope without a monochromator, and regardless, fitting the background signal at low energy is more difficult.

1.6 Critical analysis of the field of in-situ TEM and its future

For the field of in-situ TEM, an analogy to Intel's CPU development process is apt. Until this year, Intel developed their processors on what was famously known as the "tick-tock" cycle. On a "tock," the aim is to push the raw power of a chip as far as it will go with the introduction of a new microarchitecture. On a "tick," the goal is to maintain the same performance while reducing the power requirements by using a smaller feature size, i.e., to push efficiency by upgrading the manufacturing process (see, e.g., [58]).

The current state of in-situ TEM is directly analogous to Intel's "tock" half of the cycle. With nanomaterials and MEMS-based devices enabling the most advanced holders the TEM community has ever seen, the emphasis has been on pushing what is possible within the column. However, there is also a degree of tunnel-vision when it comes to pushing the experimental capabilities within the TEM, exacerbated by the increasing competition for less total funding, and this single-mindedness has had a negative impact on the reliability of data from in-situ TEM experiments. The field is badly in need of a "tick," where researchers should be encouraged to focus on things like reliable calibration of temperature in heating holders, or the precise relationship of the electron beam to the results of electrochemical experiments. It is essential not to overlook that experiments must be reproducible to be science, and thus from a purely scientific standpoint it doesn't matter how incredible *what* is done in an experiment is, if it is impossible to tell *why* and *how* and then do it again.

Furthermore, the field of modern in-situ TEM tends not to pay proper respect to the research it derives from, or even complementary research that focuses on different characterization techniques. For example, few of the papers on the in-situ lithiation of battery materials are actually proposing new electrode materials. Lithium alloys, convertible oxides, and layered materials like TMDCs have all been written about extensively in the context of batteries by the likes of Goodenough, Huggins, Whittingham, Yoffe, and many others for nearly 50 years. While in-situ TEM certainly adds a new level of understanding to the field, it is inherently derivative. And yet, it is not uncommon to see an in-situ TEM paper ignore the groundwork that was laid so long ago: take as an example the lithiation of gallium. The in-situ TEM paper from 2013, [44], which was published in Nano Letters, does not cite the paper titled "Electrochemical Investigation of the Lithium-Gallium System" by John Wen and Robert Huggins [45] that was

published 32 years before. This inherent disconnect between modern researchers and the original research in their fields has resulted in, for example, the mis-reporting of the expected percent expansion of MoS_2 in the *c*-direction (e.g., [59]) because the authors of that work did not spend enough time with the old literature to realize that the *c* lattice parameter of layered materials was reported differently in the 1970s and 80s than it is today (the specifics of this are discussed in Chapter 4). Regarding research that is complementary, from the late 1980s until the early 2000s there was a serious debate in the literature regarding the exact structure and composition of the fully-lithiated phase of Si, Ge, Sn and Pb [40, 60, 61]. Ultimately, in 2003 a combined X-ray and neutron diffraction study came out in collaboration with Argonne National Laboratory that convincingly demonstrated that rather than $Li_{22}Sn_5$, which was the commonly accepted composition partly due to the fact that silicon can take up 4.4 Li atoms per Si, the fully-lithiated phase of tin is actually $Li_{17}Sn_4$ (4.25 Li per Sn) [40]. In spite of this, in-situ TEM studies on the lithiation of Sn continue to report the ultimate phase as $Li_{22}Sn_5$ (e.g., [37]) and do not endeavor to discuss the work of Lupu et al. or the other papers concerned with the structure of lithiated Sn that preceded it.

In fact, neutron diffraction should be seriously considered as an important complementary technique to any modern lithiation study. Electrons and X-rays are not particularly sensitive to Li. X-rays interact with the electron cloud of an atom rather than the nucleus and so the interaction scales with atomic number (Z); electrons interact with both but electron-nucleus interactions are electrostatic and thus also scale with Z. And yet, in the case of Li-Sn the difference between the $Li_{4.4}Sn$ and $Li_{4.25}Sn$, both structurally and chemically, is in the location and occupancy, respectively, of the Li sites. The arrangement of the Sn atoms is the same in both structures [40]. Therefore, a characterization technique that is sensitive to the position of lithium

atoms is imperative for any serious discussion of the structure of a lithiated material, especially in binary systems in which the other element is heavy. Neutron diffraction is uniquely suited to this since neutrons interact with atomic nuclei and the interaction does not depend on Z, which makes the technique sensitive even to the positions of light elements like Li. The very large penetration depth of neutrons represents the main challenge to applying the technique in this way, but this has been circumvented in the past by using large quantities of powder, and in a certain sense powder can be considered the "bulk" form of most nanomaterials anyway (i.e., a vial full of nanoparticles is just a vial full of powder with a very small particle size).

There is also an unfortunate tolerance for the publishing of images that are clearly microns out of focus. While many reports related to in-situ TEM focus on low-magnification images and videos that give a good overview of the process being described, so that the only ill effects are the unsightly regions of bright contrast out in the middle of nowhere that result from the images of the diffracted beams and the direct beam not lining up properly, there are some papers that venture into HRTEM. The following discussion draws heavily from Chapter 28 of Williams and Carter [62].

Before delving into this issue further, it must be emphasized that there is generally a very good reason that the specimen is out of focus during an in-situ TEM experiment. Because these experiments often involve significant deformation of the specimen, and there is not usually a method for controlling how the specimen responds to the deformation, in many cases the region of interest will move a significant distance in the z-direction (this is also true for heating or cooling experiments, since the thermal expansion or contraction of the constrained support grid/film will cause it to bow up or down). Consider, for example, the lithiation of a nanowire in a solid-state half-cell. The wire expands as it takes up lithium, but both of its ends are fixed, so it

must bend. Unless it bends perfectly in the x-y plane, the specimen will go out of focus. Moving the stage with the specimen in contact with the Li source risks breaking the specimen or otherwise ruining the experiment, and is therefore out of the question. The only other option is the focus knob, but in most cases the change in the z-position of the specimen is so large that this represents a significant change in the objective lens current in order to properly focus the specimen. A conscientious microscopist will always avoid recording images immediately after making a large adjustment to the objective lens current (in fact, a good microscopist will never make such large adjustments at all if it can be avoided, but one rarely has an instrument to oneself) because this disrupts the stability of the microscope and by itself introduces additional focus spread, which is the ultimate consequence of any lens aberration; cf. §2.2 of Haider et al. (2010) [63] (the various lens aberrations describe all the different ways in which one electron might be focused differently than another).

Returning to the problem of high-resolution micrographs appearing in papers alongside wildly out-of-focus low-magnification images, there are very serious implications for the HRTEM images in these works. Either the images were acquired while the objective lens was in a state not suitable for performing reliable work (because if the experimenter had waited for the lens to stabilize, the experiment would be over), or they were acquired with unknown defocus values on the order of thousands of nanometers.

In HRTEM one of the most important quantities to understand and to know how to manipulate is the contrast transfer function H(**u**), where **u** is a general reciprocal lattice vector, because this function dictates how information in reciprocal space (i.e., the position of the diffracted beams relative to the optic axis) is transferred into image contrast. H(**u**) can be described as the product of three other functions:

$$H(\mathbf{u}) = A(\mathbf{u})E(\mathbf{u})B(\mathbf{u})$$

where A(**u**) is the aperture function, which is a step function that describes how the objective diaphragm blocks all diffracted beams that are outside the aperture; E(**u**) is the envelope function, which describes how chromatic aberration, electrical instabilities associated with the objective lens and gun, source coherence, specimen drift and vibration, and detector properties affect the attenuation of the wave and impose a virtual aperture on the back-focal plane of the objective lens; and B(**u**) is the aberration function, which accounts for spherical aberration, and, critically, defocus:

$$B(\mathbf{u}) = \exp[i(\pi \Delta f \lambda u^2 + \tfrac{1}{2}\pi C_s \lambda^3 u^4)]$$

or

$$B(\mathbf{u}) = \exp(i\chi(\mathbf{u}))$$

where Δf is the defocus, λ is the (relativistic) de Broglie wavelength of the electron, u is the magnitude of **u**, and C_s is the spherical aberration coefficient (this is a simplified form of B(**u**); for additional terms and their derivations cf. § 3.3 of [64]). This is the crux of negative spherical aberration imaging (NCSI) [65]: in a C_s-corrected machine both Δf and C_s are freely tunable, which means that B(**u**) can be tailored to produce a very specific form of H(**u**), which allows the acquisition of images that are so quantitatively interpretable that they have been used to deduce, for example, the percent occupancy of barium and oxygen columns in a twin boundary in $BaTiO_3$ [66].

An unknown defocus value in excess of 1 μm in a microscope that is being operated under far-from-ideal conditions represents the opposite case. In general, in order for the contrast in an image to be directly interpretable it is desirable for H(**u**) to be as constant as possible over as

wide a range of spatial frequencies as possible. This ensures that diffracted beams at different distances from the optic axis contribute to image contrast in the same way: when H(**u**) is negative, atoms will appear dark on a bright background, and vice versa. However, as Δf increases, the form of B(**u**), and by extension H(**u**), becomes increasingly oscillatory. This is illustrated in the series of plots of $sin\chi$[1] calculated at different values of Δf, shown in Figure 1.6. This means that a high-resolution image of a specimen that is microns out of focus is totally uninterpretable without comparison to image simulations because it is impossible to intuitively know whether any given diffracted beam contributes positive or negative contrast to the image. Furthermore, the theory behind the contrast transfer function for HRTEM is built on approximations (combined, these are known as the weak-phase-object approximation or WPOA) that are nowhere near valid for the specimens used in many in-situ TEM experiments, especially considering the tendency toward a more lenient usage of the "nano-" prefix. In fact, in the field of HRTEM it is well-understood that for crystalline materials of any appreciable (i.e., practical) thickness information transfer in the TEM is nonlinear due to strong diffraction of the beam, which means that there is not a uniquely defined relationship between the exit-plane wave function and the intensity in the image even if H(**u**) is rigorously determined. These aspects of microscopy are not acknowledged or discussed in the papers presenting in-situ TEM experiments that include high-resolution micrographs.

[1] $sin\chi$ comes from the imaginary part of the trigonometric representation of B(**u**); physically, this term represents how the aberration function influences the phase of the electron wave, which is what is ultimately responsible for the contrast in high-resolution micrographs. Indeed, by following the discussion in Section 28.4 of Williams and Carter [61] and filling in the mathematical steps that were skipped there for brevity, it is easy to demonstrate that within the WPOA all of the terms in the equation describing the intensity in the image (i.e., $\psi^*\psi$) that contain $cos\chi$ either cancel or may be neglected.

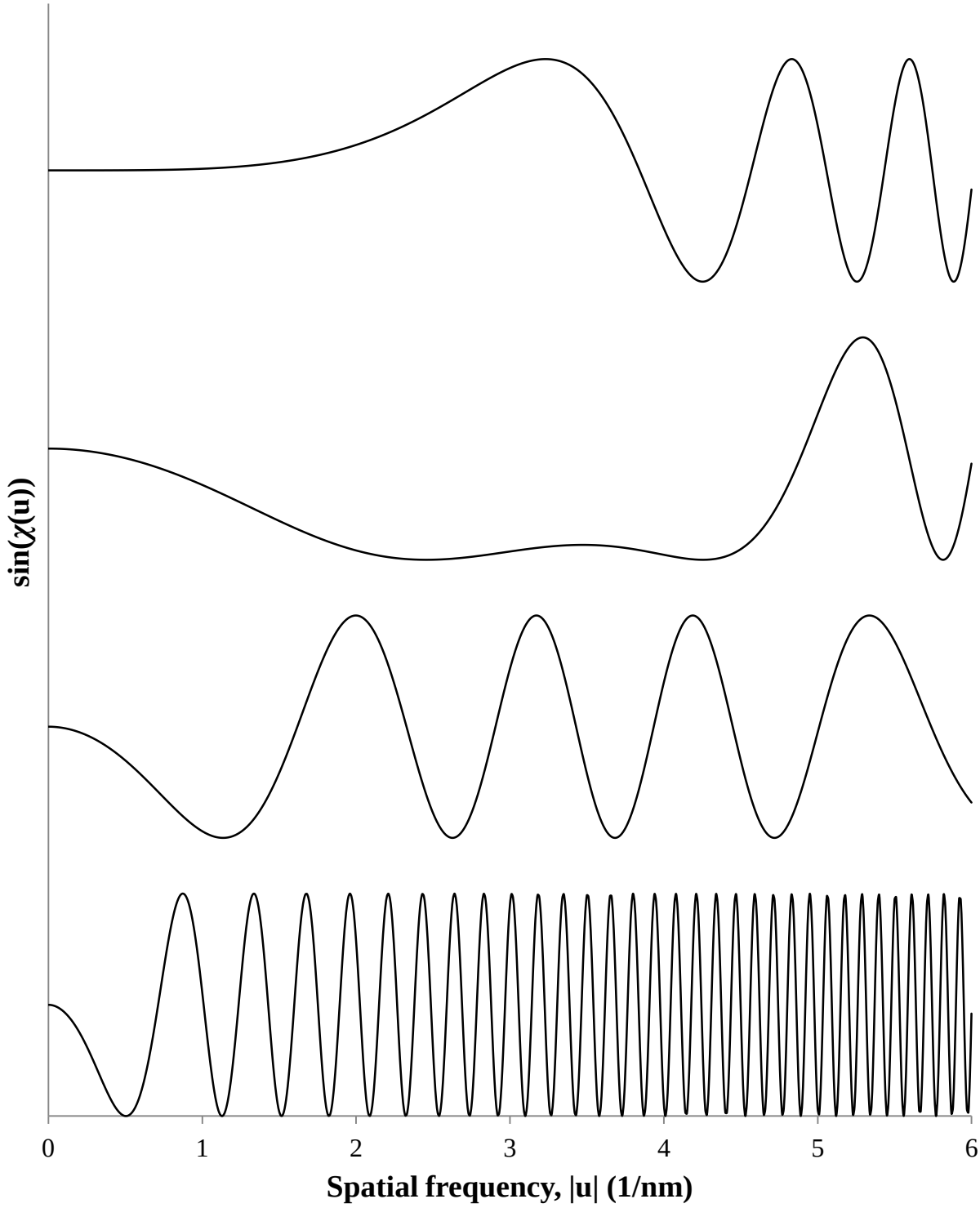

Figure 1.6. Plot of *sinχ* as a function of spatial frequency for different defocus values: from top to bottom, 0 nm, -56.1 nm (Scherzer defocus for the Tecnai F30), -200 nm, and -1000 nm. The curves are plotted on the same axes for clarity; *sin*(χ(0)) is always 0, and each curve has its maxima at 1 and minima at -1.

A related aspect of analyzing high-resolution images is the idea of precision. Rather than being concerned with which values of **u** can contribute contrast to an image and how, precision is mainly a question of how sensitive an image is to small changes in a particular **u**, as might be expected when the spacing of certain planes in a material increases (or decreases) as lithium is added. The precision of a measurement is given by twice the standard deviation of a collection of such measurements, and while the resolution and information limits of microscopes are often-cited figures of merit, precision tends to slip through the cracks. Because of this, there are many cases in the TEM literature in general where the precision of the instrument is overstated, since authors and reviewers alike tend to be unaware of what a realistic precision for TEM measurements is. In 2009 the electron microscopy group at Jülich published a report detailing the advantages of using a slightly negative value of C_s for quantitative analysis of HRTEM images, and this included a discussion of precision [67]. Their results showed that the precision of atomic spacing measurements in HRTEM images is better for heavier elements and worse for thicker amorphous layers on the specimen; this is because amorphous material contributes to noise while high-Z elements produce stronger signals. Furthermore, the precision is much more sensitive to these variables when C_s is positive (see Fig. 7 in [67]). In the positive (but still corrected) C_s case, for a 3.3 nm-thick specimen of $SrTiO_3$, the measured precision ranged from ~3 pm for SrO columns with low noise to ~32 pm for O columns with high noise [67]. Meanwhile, in the in-situ TEM literature, precision better than 1.5 pm has been implied for a specimen two orders of magnitude thicker in an uncorrected Tecnai F30 (e.g., [50]) and measurements that rely on such unrealistic precision are furthermore used to support hypotheses for atomic-scale mechanisms of dynamic processes.

Another general abuse of high-resolution microscopy in the field of in-situ TEM regards the cavalier use of image processing techniques. For example, because many in-situ TEM experiments deal with the direct observation of phase transformations, and because it is possible to obtain high-resolution images of the associated phase boundaries, the subject of dislocations frequently makes a cameo appearance. That is, the discussion of dislocations is (often, but not always) limited, makes no contribution to the overall content of the work, and is primarily designed to cheaply inject "star power." One of the easiest ways to visualize (and "prove" the existence of) a dislocation in a complex HRTEM micrograph is by producing a Fourier-filtered image. This is achieved by applying a mask to the FFT of an image so that only the planes relevant to the dislocation(s) in question contribute to the filtered image, and then inverting the Fourier transform. An image processed in this way tends to contain a single set of very high-contrast fringes and extra half-planes of atoms corresponding to edge dislocations become intuitively obvious to even a casual observer.

However, it was demonstrated in a 1988 *Ultramicroscopy* paper that lattice fringe images showing clear evidence of edge dislocations can be generated by applying a circular mask to the noise in an FFT, and that the location, orientation, and quantity of these "dislocation" artifacts could be changed by varying the diameter (in pixels) of the mask: see Figure 5 in [51]. Pradère et al. concluded that the only way to verify whether an apparent dislocation in a Fourier-filtered image is real is through comparison with the raw image; if the dislocation is not visible in the latter, then its presence in the former must be considered an artifact [51]. Considering the issues surrounding high-resolution imaging during in-situ experiments as discussed above, verification of anything from the raw images in such an experiment is difficult at best.

The main contributor to this problem is the fact that it is incredibly straightforward now to generate a FFT of an image, apply a mask (whose default shape is circular; there are other issues associated with the shape of the mask that are discussed in, e.g., [68]), and then to invert the masked FFT to produce a filtered image. This entire process can be accomplished in approximately ten seconds using Digital Micrograph, for example. The filtered images then have the unfortunate property of *seeming* to be directly interpretable, when in fact there are many complicating factors that are glossed over by the sheer accessibility of this image processing technique. At the same time as complex imaging and processing techniques are becoming easier to use, the increasing intersection of microscopy with other fields (which is itself partially a consequence of the rise of in-situ TEM) means that an increasing number of scientists who are performing the microscopy and analyzing its results are not microscopists *per se*. That is, because their expertise lies in other fields (and indeed this expertise is often critical to designing and setting up in-situ TEM experiments to begin with), the mechanisms involved in both image formation and image processing are a "black box" whose limitations they do not fully understand or know how to work around.

Regarding the future of in-situ TEM experimentation, for the next decade or two progress is likely to be driven by advances in the capabilities of the specimen holders rather than the microscopes. This is not to say that the two are not coupled, in a way: as the resolving power of TEMs is increased by various aberration correction technologies, the polepiece gap may be increased so that the resolution of such a microscope might stay the same as what is currently available, but more equipment can be put inside of it for making measurements during experiments. The ultimate extension of this idea is to be able to put a fully-functional "lab in the gap."

1.7 Objectives and novelty of this research

Although nanomaterials have both enabled and inspired in-situ TEM experiments, working solely on nanomaterials requires only a few of the skills traditionally required of electron microscopists (i.e., the basics of running a microscope and controlling the electron dose). In particular, such a narrow focus would exclude conventional TEM specimen preparation techniques as well as many advanced microscopy techniques. For example, when imaging crystalline nanoparticles, there is no need to know how to tilt any given particle to a particular crystallographic orientation because there will always be another particle that is already at that orientation.

To develop expertise in using the TEM as more than simply a tool for recording high-magnification images of small particles, studies on dislocations are ideal. Intimate knowledge of the direct and reciprocal lattices of a material, how they relate to the electron beam, and how a dislocation changes this relationship is required in order to provide a full analysis.

The research described in this dissertation had three principal objectives:

1. Develop skills in a variety of *in situ* transmission electron microscopy techniques

2. Develop skills in traditional electron microscopy techniques

3. Apply these skills to extend the scientific community's understanding of some alternative lithium ion battery electrode materials, namely MoS_2 and Sn. In particular, this work endeavors to explain phenomena associated with the lithiation of MoS_2, such as the formation of dark bands in the plan-view orientation and steps between planar defects in the edge-on orientation; and to characterize the apparent total reversibility of Li insertion and removal in Sn nanoneedles, in the Sn-rich regime.

Each of these will be addressed in this dissertation, and, as should go without saying after the previous section, particular care will be taken to do so with attention to and respect for relevant original papers, complementary characterization techniques (or at least papers that are based on them, since learning microscopy is a singularly absorbing task), and the limitations of the transmission electron microscope.

The novel aspects of this work are:

1. Although in-situ work has been published on the lithiation of Sn, the material in this case is commercially viable, which is novel, and its morphology is quite different from the nanoparticles and long wires that have been studied previously.

2. Nearly perfect reversibility of the lithiation process in the Sn-rich regime has not been previously reported.

3. Observation of the lithiation of any layer material with the layers edge-on has never been reported before. Furthermore, an explanation for the dark bands hypothesized to be the precipitation of Mo during the lithiation of MoS_2 has yet to be reported in the literature.

2 Materials and Methods

There are three primary components of a battery: the anode, the cathode, and the electrolyte. As for many devices, there are also two levels of research operating concurrently on battery materials: one focused on the basic science of each component, and the other focused on applications, i.e., combining the components into real devices. The work presented here belongs to the basic science level of research, and is primarily concerned with materials that are candidates to replace carbonaceous negative electrodes (anodes). Electrolytes are discussed only as they relate to the relevance of the results to the anode's actual performance in a real cell, and cathode materials are not discussed outside of a brief overview of what is currently on the market. This work focuses on two anode materials, tin and molybdenum disulfide, and the different mechanisms by which they take up and release lithium during electrochemical cycling.

The main techniques that were used in this research were various forms of in-situ and *operando* TEM. The preparation of the materials for TEM ranged from the standard implementation of modern techniques (FIB), to modifications of traditional techniques (mechanical exfoliation of layered materials using tape), to the adaptation of new techniques to suit the desired experiment (growing Sn nanostructures directly on specific grids).

The instruments used were, for the most part, not state-of-the-art, although the special holders required for in-situ TEM were, and both image- and probe-corrected microscopes were used for some of the high-resolution imaging in this work. The in-situ experiments were all carried out in a “workhorse” microscope. This is because few people are willing to risk the well-being of an expensive, aberration-corrected microscope by conducting “messy” experiments inside of it, and also because in many cases such experiments are not carried out at magnifications that take full advantage of the high-performance capabilities of such machines. Especially in the case of the

observation of lithiation processes, wherein the Li atoms are so mobile, the effect of condensing the beam on the specimen enough to achieve any sort of signal in a high-magnification image can be detrimental to the results of the experiment. This also highlights the value of maintaining and knowing how to use older microscopes.

The following sections deal with each of these topics in greater detail.

2.1 Materials

This section describes some figures of interest about the materials used in this work: where and how they are produced, and in what quantities; which industries they are used in; their costs, etc. It also explains why each material was chosen for this work.

2.1.1 Tin

The mineral form of tin is cassiterite, which is just tin dioxide (SnO_2) and has the rutile structure. Mines in what are now the United Kingdom and Germany were the first sources of Sn in Europe between 4000 and 5000 years ago, and indeed the Sn mining operation in Cornwall, England remained one of the most significant suppliers of Sn worldwide until the mid-1800s.

Tin is not currently mined or smelted in the United States, nor has it been for the last 23 years. The largest remaining Sn deposits in the U.S. are located in Alaska, and are not considered significant in comparison to other sources in the rest of the world. However, about 14,000 metric tons of Sn are recovered from scrap metal in the U.S. every year, in comparison to an average imported quantity of ~35,700 t. China and Indonesia together account for about 70% of the nearly 300,000 t of Sn mined annually; other significant sources include Peru, Bolivia, Brazil, and Burma [69]. Sn is currently worth just over $20,100 (U.S.) per metric ton on the London Metal Exchange, although the average price in September 2016 was about $19,500/t.

The most common uses of Sn metal in the U.S. are in cans and containers, in construction materials, in the transportation industry, and in electronics (especially in solder) [69].

Sn was chosen for objectives 1 and 2 because of its high theoretical specific capacity (~992 mAh/g). Additionally, a commercially viable method for producing large arrays of Sn nanostructures has been developed by Professor Grant Norton's group at Washington State University [70]; details of this process are discussed briefly in §5.1. Sn specimens for the in-situ lithiation experiments were prepared by Prof. Norton's group at WSU and shipped to CINT. Sn was chosen for objective 5 directly because of objectives 1 and 2. Crystallographic analysis of defects in single-crystal Sn whiskers was carried out on specimens prepared in various orientations by Joe Michael's group at Sandia National Laboratories.

2.1.2 Molybdenum disulfide

The MoS_2 mineral is known as molybdenite, with the most important natural deposits in the United States currently located in Colorado and Idaho. It is also obtained as a byproduct from copper mining operations in Arizona, New Mexico, Nevada, Utah, and Montana [69]. Molybdenite is the most common and economically viable source of pure Mo metal, and, surprisingly, of Re metal as well. Rhenium atoms substitute for up to 1-2% of Mo atoms in natural samples, which has interesting implications for the structure of the material as discussed in detail in Chapter 3. The most common use of the Mo metal extracted from molybdenite is the formation of ferromolybdenite, which is used in high-strength and corrosion-resistant steel. According to the London Metal Exchange, the current price of Mo metal is ~$15,000 per metric ton [71]. Current data on the price of molybdenite is not readily available; 100 years ago it sold for $528-2772/t depending on the purity (30-90% MoS_2) [72]. However, this is $11,667-61,252 in 2016 dollars [73], which does not make economic sense given the price of Mo.

MoS_2 was chosen for objective 3 because it is a layered ceramic material, which introduces variety in terms of the class of material being studied as well as the lithiation mechanism compared to Sn. Specimens were prepared in the plan-view geometry from natural, bulk molybdenite by mechanical exfoliation (commonly known as the "scotch tape method"). Natural MoS_2 may be expected to contain a greater quantity and variety of impurity species, as well as a larger number of crystal defects in comparison to a synthetic sample. A focused ion beam (FIB) instrument was used to prepare lamellae of MoS_2 so that the basal planes were parallel to the electron beam, with foil planes of $\{11\bar{2}0\}$ and $\{1\bar{1}00\}$. All MoS_2 specimen preparation took place at CINT.

2.1.3 Electrolytes

The type of electrolyte that can be used for an in-situ or *operando* TEM experiment depends primarily on two factors: the capabilities of the holder and the geometry of the material to be lithiated. Clearly, commercial liquid electrolytes, which usually consist of lithium hexafluorophosphate ($LiPF_6$) dissolved in an organic solvent (generally a mixture of ethylene carbonate (EC), dimethyl carbonate (DMC), ethyl methyl carbonate (EMC) and/or diethyl carbonate (DEC)), can only be used in closed cells designed to hold liquids with high vapor pressure. However, this does not exclude the use of liquid electrolytes in open-cell configurations. An ionic liquid electrolyte (ILE), commonly known as simply ionic liquid or room-temperature ionic liquid, is a liquid salt with a low melting temperature [74]. Many ionic liquids have very low vapor pressures, which is why they are safe to use in the vacuum of the TEM column. They are also generally poor conductors of electricity, and so by choosing an ionic liquid that is conductive for a particular ion (e.g., Li) it is possible to use such a liquid as an electrolyte in a battery.

However, not all specimen geometries are compatible with the use of an ILE. For example, the Sn nanoneedles discussed in this work are electrodeposited onto Cu TEM grids, and do not protrude more than a few hundred nanometers from the film surface. When contact is made between this kind of specimen and a drop of ionic liquid, all of the liquid wicks onto the TEM grid, which not only breaks contact between the two electrodes but also renders the Sn side opaque to the electron beam. In these cases where ILEs cannot be used, a solid electrolyte must be used instead. Although polymer-based materials such as LiPON have been studied for application as solid electrolytes in LIBs (e.g., [75]), a simpler approach is to use Li metal as the counter-electrode and to briefly expose the Li to air. This forms a thin oxide layer on the surface that can act as a solid electrolyte, although Li_2O is not generally recognized as a good conductor of Li ions. This method is convenient for in-situ TEM experiments, since some exposure to air is unavoidable when loading the holder in the microscope (unless special modifications are made to the goniometer).

However, this method also has several drawbacks. First, the formation of the electrolyte layer is not controlled and so its thickness varies in an indeterminate way from experiment to experiment. This is to say nothing of the chemistry of the film; the assumption in the literature is that it is strictly Li_2O, but lithium can also readily form a peroxide (Li_2O_2) as well as a hydroxide (LiOH) and a nitride (Li_3N). Furthermore, the poor ionic conductivity of this makeshift electrolyte requires driving voltages that are higher than those required for real batteries. This leads to unrealistic cyclic voltammetry data, and this issue is only exacerbated by the randomness of the thickness and chemical composition of the electrolyte film. In cases where the electrolyte layer is thin, it may be pierced by the electrode material being tested as the latter

expands during lithiation. This puts the working and counter/reference electrodes in electrical contact, thus shorting the half-cell and effectively ending the experiment.

Because the Li metal is usually scraped onto a wire (either blunt or electropolished to a sharp probe) in a glove box, the shape and quantity of Li is also inconsistent. The glove box at CINT is dry, with a He atmosphere, but the bulk Li metal strips still begin to corrode after weeks of storage. This corrosion is associated with nitride formation, as well as the uptake of other, unknown contaminants depending on what other users or CINT scientists may be working on in the glove box at any given time. This also causes variation in the chemistry of the half-cell between experiments that cannot be accurately accounted for.

2.2 TEM specimen preparation

This section describes the steps that were taken to prepare specimens of Sn and MoS_2 for both in-situ TEM experiments and conventional TEM characterization.

2.2.1 Sn

Preparing the needles for in-situ TEM experiments presented a challenge, because the process for creating battery electrodes composed of Sn nanoneedles was developed with large-scale production in mind. The preliminary microscopy on the needles was performed by using a flattened wire to scrape them off of one of the small Cu coupons they had been deposited on; however, this approach posed several concerns. First, it was possible that the needles were being damaged by the scraping process. Second, the yield was low, which also meant that containment of the scraped-off nanomaterials was a potential health and safety issue. Finally, because of the exceedingly small dimensions of the needles, the scraping method was unlikely to result in any needles that were simultaneously in good electrical contact with the support structure and also in

a suitable position and orientation to make contact with the Li source for the lithiation experiment.

To get around these obstacles, it was noted that since the deposition of the needles was already carried out on Cu current collectors, it should be possible to deposit them directly onto Cu TEM grids. By using half-grids designed to hold FIB lift-out specimens, it was guaranteed that some of the needles would be sticking straight out from the edges in positions where they could be readily accessed by the Li source for lithiation. The specimen preparation process was further refined by switching from FIB grids to low-mesh, parallel-bar Cu grids. After the deposition, the grids were cut in half under a visible-light microscope using a razor blade, as illustrated schematically in Figure 2.1a. Any number of needles on the outermost bar could be lithiated in a single session, and afterwards the bar could be carefully removed with tweezers, allowing the next bar to be used in the next session (Figure 2.1b). This drastically increased the efficiency of the experiments, increasing the number of runs that could be performed on a single grid from one to, in theory, ten or more.

2.2.2 MoS_2

MoS_2 specimens in the plan-view orientation were prepared by mechanical exfoliation. 400 mesh Cu grids with no support film were cut in half with a razor blade and set aside. Higher-mesh grids are desirable for the lithiation experiments since the regions of interest are suspended over the cut edge; closely-spaced grid bars provide a more stable support and a higher probability of establishing good electrical contact between the MoS_2 and the holder. Wafer dicing tape was used for the exfoliation, and the top layer of the MoS_2 sample was removed first to expose a clean surface. Then, the end of a long piece of tape (~20cm x 2.5cm) was used to cleave a small

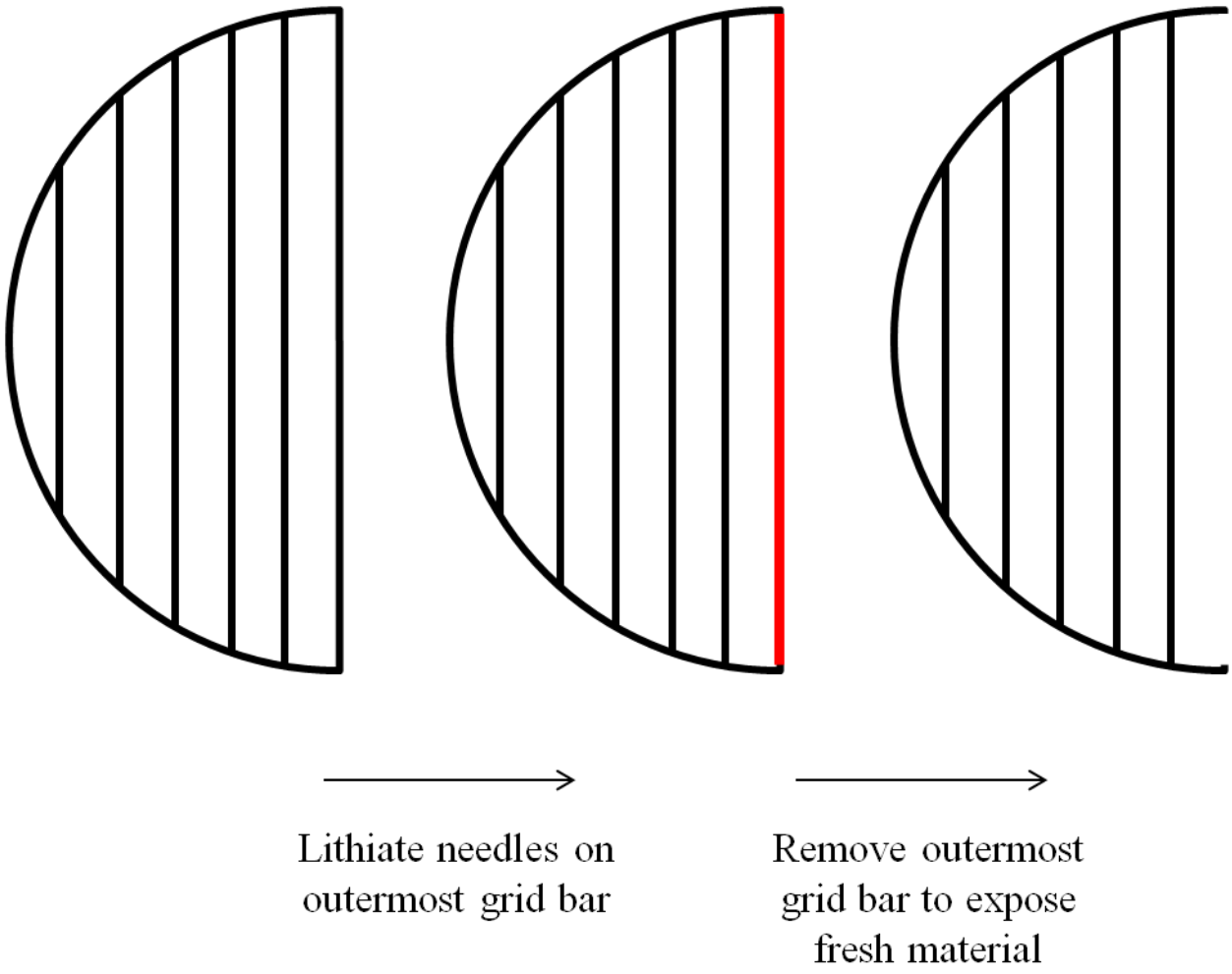

Figure 2.1. Schematic illustration showing how parallel-bar Cu TEM grids can be used for many in-situ lithiation experiments. Sn needles are deposited evenly on the entire grid, and pristine grid bars can be accessed by carefully removing the outermost bar (that supports the lithiated material) with tweezers.

amount of clean MoS_2 from the sample. The tape was then repeatedly folded over on itself and peeled back, thinning the MoS_2 each time. A clean section of tape was used for every fold.

Although it is possible to thin MoS_2 to electron transparency by this method, and the thickness of the sheets can be monitored by the color of the flakes in transmission in a visible light microscope (they turn a progressively lighter green as they get thinner), flakes that are thinned to such an extent are difficult to position reliably on a grid and are also extremely delicate. For in-situ lithiation experiments, rather large, thick flakes are preferable. The average dimensions of a MoS_2 flake used for the experiments described below are hundreds of microns laterally and microns or even tens of microns thick: easily visible to the unaided eye. Traditionally, such a specimen would be dismissed out of hand as useless for TEM; however, there is always a significant amount of very thin area at the edges of these large flakes. Even at rather low magnifications (25-50 kX), this thin area can easily fill the camera's field of view. Thus, using such large MoS_2 flakes provides ease of handling, reduced bending of the specimen resulting in flatter thin areas, and more reliable electrical contact with the holder while detracting nothing from the experiment.

To produce flakes of this size, the sample was cleaved 7 times, always using the most recently cleaved cluster of flakes to make the next one. This left 8 clusters of flakes along the length of the tape, and the section of tape holding the last three clusters was cut off and placed in acetone in a petri dish. Two pairs of tweezers were used to manipulate the tape in the acetone, as it tended to wrinkle, expand, and roll up as the glue dissolved. The rolling of the tape was one of the primary mechanisms for removing the MoS_2 flakes because it curled with the glue side out, pulling away from the flakes. The tape was then carefully unrolled with tweezers and sprayed gently with acetone to remove more of the flakes. At this point the tape was removed from the

acetone and disposed of to limit the amount of glue dissolved in the acetone. Additionally, using only the most loosely-attached flakes reduced contamination from the glue.

This left many large MoS_2 flakes in the petri dish, suspended in acetone. The previously-prepared Cu half-grids were retrieved and placed on three sheets of filter paper. The MoS_2 suspension was drawn into a plastic Pasteur pipette, and the pipette was gently pressed down so that it was centered on the straight edge of one of the half-grids. As the filter paper drew the acetone out of the pipette, MoS_2 flakes floated down onto the edge of the grid. When at least one flake was properly positioned so that it was protruding slightly from the edge of the grid, the pipette was removed and the grid allowed to dry. In cases where the grid got too cluttered with flakes but none were properly positioned, the grid could be washed of the flakes by gently squeezing the pipette to make the acetone flow out more vigorously.

One such "batch" of flakes can be used to make 10 or more specimens at a time, if desired. The same process was used to deposit MoS_2 flakes on whole grids for conventional TEM characterization. In this case, 300-mesh grids are preferable to balance mechanical stability with viewable area.

For the lithiation experiments, while the half-grids were drying, Al wires 0.03175 cm (0.0125 in) in diameter were cut to ~1.5 cm lengths, and one end of each wire was flattened in a mechanical press. This flattened end was then trimmed with a razor blade so that its edge was straight. A small bead of conductive Ag epoxy was then placed on the flat end of each wire, held in self-closing tweezers, and the Cu grids affixed to the wires such that the epoxy was in contact with the MoS_2 flake(s) where possible to ensure good electrical contact. The epoxy was cured in an oven at 60 °C for one hour in air.

To prepare MoS_2 specimens in such a way that the basal planes were parallel to the electron beam, a focused ion beam (FIB) instrument was used. Lamellae were lifted out from the same bulk sample that was used to generate the plan-view flakes. By aligning the lamellae both parallel and perpendicular to clearly-visible surface steps (see Figure 2.2), foil planes of the types $\{10\bar{1}0\}$ and $\{1\bar{2}10\}$, respectively, were selected. The latter orientation was more commonly used, as it allows direct visualization of stacking faults at high magnification [76]; see §3.7.

2.3 Equipment: the microscopes

This section describes briefly the specifications and capabilities of the microscopes that were used to perform this work. For the TEMs, the parameters required for image simulation are given.

2.3.1 FEI Tecnai F30

The FEI Tecnai F30 TEM at CINT-Sandia, which operates at 300 kV, was used for the in-situ experiments. The F30 is capable of 2 Å resolution in TEM mode and 1.9 Å resolution in HAADF STEM. The F30 is equipped with an EDAX Si-Li X-ray detector with a Be window for XEDS collection, as well as a Gatan Imaging Filter (GIF) Tridiem spectrometer for EELS and energy-filtered imaging. The objective lens is a "super-twin," with a maximum current instability of 2 ppm/min and a spherical aberration coefficient (C_s) of ~1.2 mm. It is interesting to note that FEI does not routinely measure C_s during the installation of new microscopes, even though the tools to do so have become much more widely available since the advent of spherical aberration correction (i.e., one cannot correct a quantity without measuring it first). The diffraction lens has an average current stability of 0.5 ppm/min (the actual rating is 5 ppm/10 min).

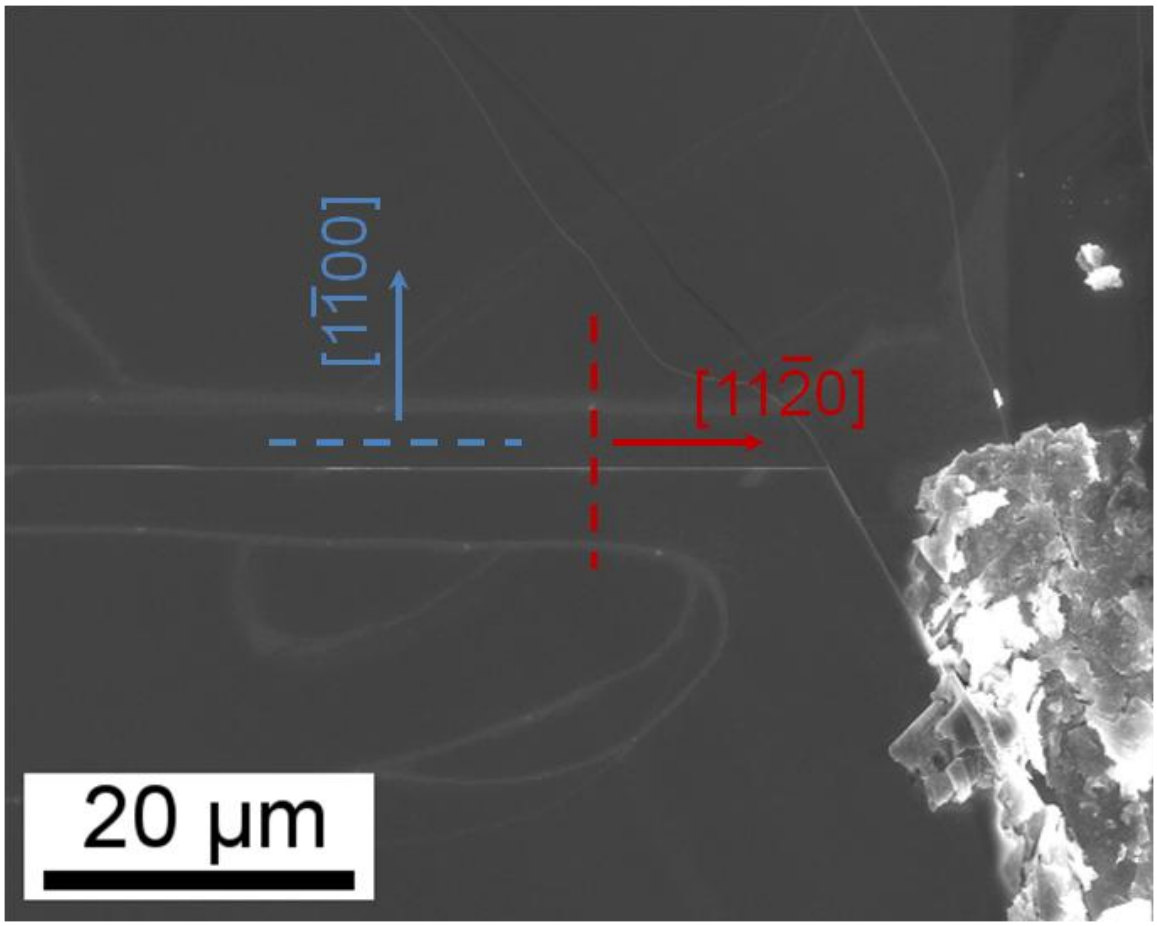

Figure 2.2. Secondary-electron image recorded in the FIB showing surface steps on a flat MoS_2 surface. The indicated directions can be selected as the foil normal by cutting lamellae either parallel to or perpendicular to the surface steps.

2.3.2 FEI Titan

The electron microscopy laboratory (EML) at Los Alamos National Laboratory (LANL) houses two microscopes that CINT has half-time access to. The first is an image-corrected FEI Titan 80-300 that operates at 300 kV, with a resolution of 0.8 Å in TEM mode and 1.4 Å in HAADF-STEM. This Titan is also equipped with a monochromator, allowing it to achieve an energy resolution of 0.17 eV in EELS. The GIF spectrometer is equipped with a 2048x2048 CCD camera for energy-filtered imaging and energy-loss spectrum imaging. It has a single Si-Li X-ray detector for collecting X-ray spectra.

CINT also has limited access to a probe-corrected FEI Titan 80-200 at Sandia, which is operated at 200 kV and specially equipped for analytical microscopy. This Titan has four silicon-drift X-ray detectors (Chemi-STEM) that, combined with multivariate statistical analysis, can detect fractional compositions as low as 0.5 at%. It is also equipped with a Gatan spectrometer for EELS acquisition; atomic-resolution chemical mapping is possible with this machine. It regularly operates with a resolution of 1.2 Å, although with extra effort put into the aberration correction routine this can easily be pushed to 0.8 Å.

2.3.3 Focused Ion Beam instruments

The cleanroom at CINT-Sandia is equipped with an FEI Nova 600 Nanolab dual-beam FIB with in-situ liftout that is also equipped for electron beam lithography. Secondary-electron images recorded with this instrument operating at 15 kV contain information down to 1.1 nm.

The second microscope at the EML at LANL that is available to CINT users is an FEI Helios Nanolab 600 FIB with in-situ liftout; this instrument can deposit carbon as well as platinum films

to protect specimens from the ion beam. The Helios at the EML is also equipped for electron backscatter diffraction (EBSD).

2.3.4 Scanning electron microscopes

The cleanroom at CINT-Sandia houses an FEI Nova NanoSEM 450 scanning electron microscope. This machine is also equipped with the Nabity electron beam lithography patterning hardware.

2.4 Equipment: specimen holders for in-situ TEM experiments

A detailed description of the specimen holders used to carry out the in-situ TEM experiments is provided in this section. How the holders interact with the device(s) that control them is discussed where this information is relevant to the capabilities of the holder. In addition to the holders listed here, standard single-tilt, low-background single-tilt, and standard double-tilt holders were used for conventional S/TEM characterization of specimens.

2.4.1 Nanofactory STM holder

The open-cell lithiation experiments are carried out using a Nanofactory (now FEI) holder designed for simultaneous scanning tunneling microscopy (STM) and TEM (i.e., an STM-TEM holder), as described in [32]. This holder is loaded with two wires, one on each end so that they face one another. One end of the holder is immobile; in the experiments described below the working electrode (i.e., the material being lithiated) is mounted on this side, generally by affixing a copper half-grid to a 0.03175 cm diameter Al wire using a conductive Ag epoxy. The opposite side of the holder is a two-piece ball-and-socket joint. The ball is attached to a ceramic rod that runs down the shaft of the holder, and features mechanical motors for coarse movement as well as piezoelectric actuators that allow nanometer-precision motion in three dimensions. The socket

is formed by three pieces of wire bent in a U-shape to form six prongs on a metal carrier shaped like a top-hat.

The top-hat is loaded with 0.0254 cm diameter W wire, cut so that its tip is 1 mm or less from the material to be lithiated. The wire is secured to the top-hat by tightening a pair of screws on opposite sides of the top-hat. Li metal, which acts as both the counter- and reference electrode, is scraped onto the W wire and the top-hat is loaded into the holder in a glove box with a He atmosphere. The holder is sealed in a plastic bag within the glove box for transfer to the TEM. During its brief exposure to the air while the holder is inserted into the microscope and the airlock pumps down, an oxide layer forms on the surface of the Li metal, and the Li_2O acts as a solid electrolyte. After using the controller software to make contact between the two electrodes, an electric potential can be applied across the two ends of the holder to drive Li into and out of the working electrode. The potential can be applied using the Nanofactory controller, or, for greater precision, versatility and access to a more reliable femtoammeter, the holder can be hooked up to a Solaratron Modulab potentiostat.

There are many challenges associated with the open-cell lithiation experiment. First is the limited choice of electrolyte materials. In the case of a solid-state half-cell, the oxide (and nitride, and hydroxide) layer that forms on the surface of the Li metal is the only option, and this processes that result in the formation of this layer cannot be reliably controlled.

Although it is possible to use an ILE, and in fact this has the advantage of being compatible with commercial electrode materials like $LiCoO_2$ and $LiFePO_4$, specimen geometry dictates whether or not this approach is usable. Specimens with large aspect ratios are required (i.e., nanowires); otherwise, the liquid will wick onto the specimen, rendering it opaque and possibly leaving the counter electrode dry, eliminating the contact between the electrodes. Furthermore, even in

situations where the specimen geometry allows the use of an ILE, it is important not to over-expose the liquid to the electron beam as this can cause it to solidify.

Because the rate at which an electrode is charged or discharged has a significant effect on how the structural changes within the electrode take place, it must be noted that building a "nano-battery" within the TEM in this way results in very high current densities when lithiating and delithiating the specimen. It may be that such high current densities produce results in the TEM that are not analogous to processes that occur in commercial-scale batteries at time scales characteristic of real-world battery use.

Furthermore, the effects of the electron beam must also be considered. Lithium atoms tend to be extremely mobile, and evidence has been recorded of lithium that had been drawn out of a tin needle then going back into the tin under the influence of the beam.

2.4.2 Liquid cell holders

The liquid cell experiments will be carried out using the CINT Discovery platform, which makes use of the Nanofactory 16-lead electrical holder (shown in Figure 2.3). The Discovery platform itself is a specially designed chip with 10 electrodes (5 arranged in a line on each end of the chip) that run to the electron-transparent window. The actual arrangement of the electrodes on the window is completely customizable by the user, and is patterned using electron beam lithography in the SEM. On either side of the window are two large wells that hold ceramic alignment beads; another, smaller chip with an electron-transparent window in the center fits onto these alignment beads (so-called because their purpose is to align the windows on the top and bottom chips). This top chip is secured to the base chip with epoxy, and features two small holes on either side of the window that go all the way through the chip. This allows the cell to be filled with a liquid, such as a commercial organic electrolyte used in LIBs, at which point the cell

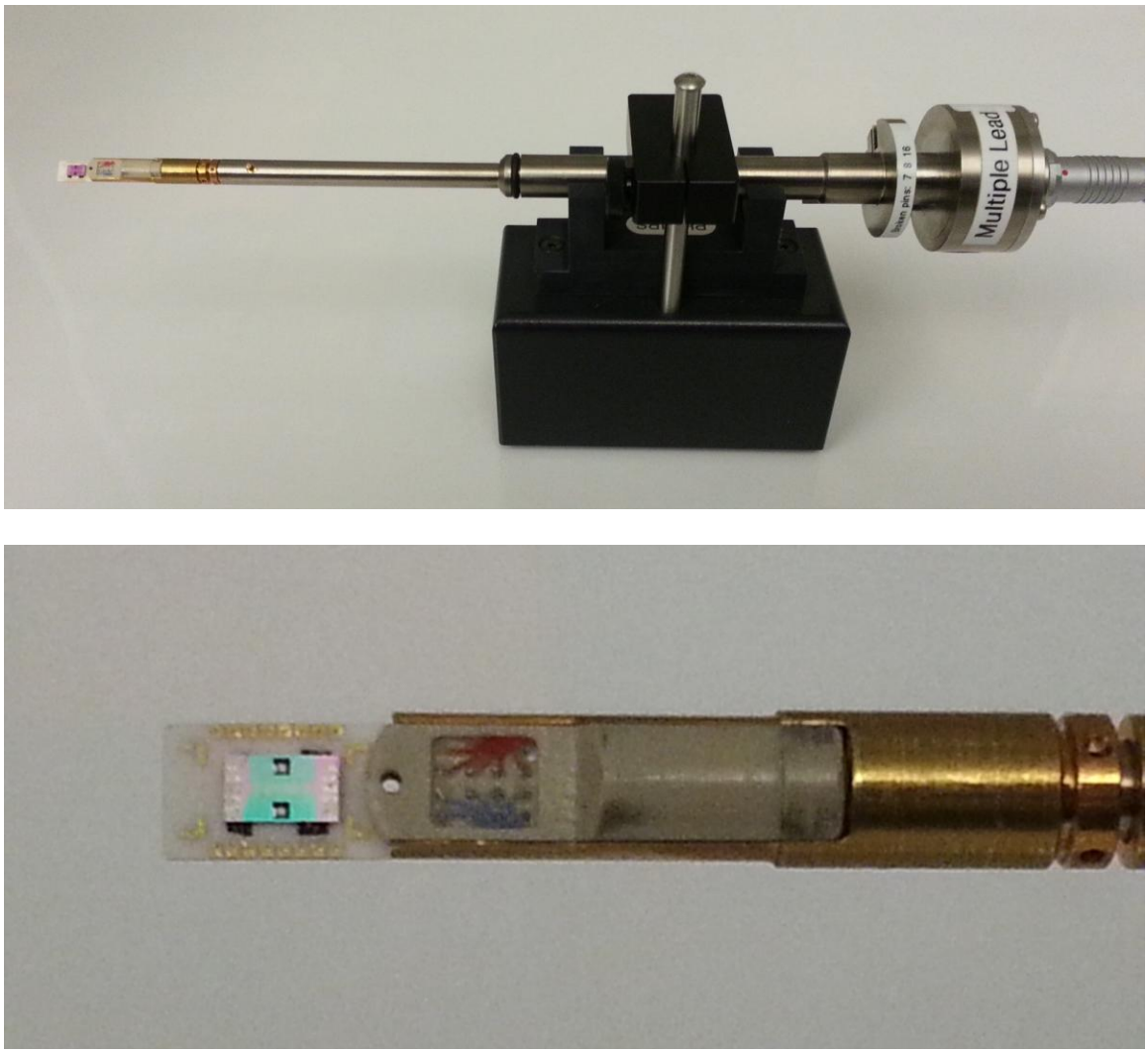

Figure 2.3. The Nanofactory 16-lead electrical holder, with a close-up view of the chip carrier mounted with an un-sealed Discovery platform chip.

is sealed, mounted onto the chip carrier, and the appropriate electrodes are wire bonded to the corresponding leads on the holder; a sealed, wire-bonded chip on the chip carrier is shown in Figure 2.4. This allows electrochemical experiments to be performed in a liquid in the TEM.

In cases where electrochemical capabilities are not needed but a fresh supply of liquid and/or different liquids are required, the Hummingbird Scientific liquid flow cell can be used. For the Hummingbird holder, the liquid cell is made in much the same way: by sandwiching the liquid between two silicon nitride windows. More flexibility is available in terms of window thickness; windows as thin as 5 nm or as thick as 100 nm may be used. However, there is no alignment mechanism as with the Discovery platform, so the alignment of the windows must be performed by eye under a visible light microscope by the user. Separation of the windows is achieved by placing four drops of a gold nanoparticle suspension around the perimeter of the bottom grid; the space between the windows is then determined by the size of the Au particles. Typically, a suspension of 250 nm particles is used. The cell is sealed by rubber O-rings, but within the seal are two orifices that connect to the liquid lines that run to the base of the holder. This allows the flow of fluids into and out of the cell. The line in is connected to a syringe in a pump that allows selection of the flow rate, and the line out disposes of the used fluid in an appropriate waste container.

In general, it is important to consider that the overall thickness of a liquid cell is greater than the sum of the window thickness and the nominal separation between the windows. The pressure differential between the liquid cell and the vacuum of the microscope column will always cause the windows to bow out, and this can be exacerbated by flowing liquid through the cell as this increases the pressure. Because of this, it is common practice in liquid cell TEM to attempt to place the region of interest of the specimen as near to the corner of the window as possible, or in

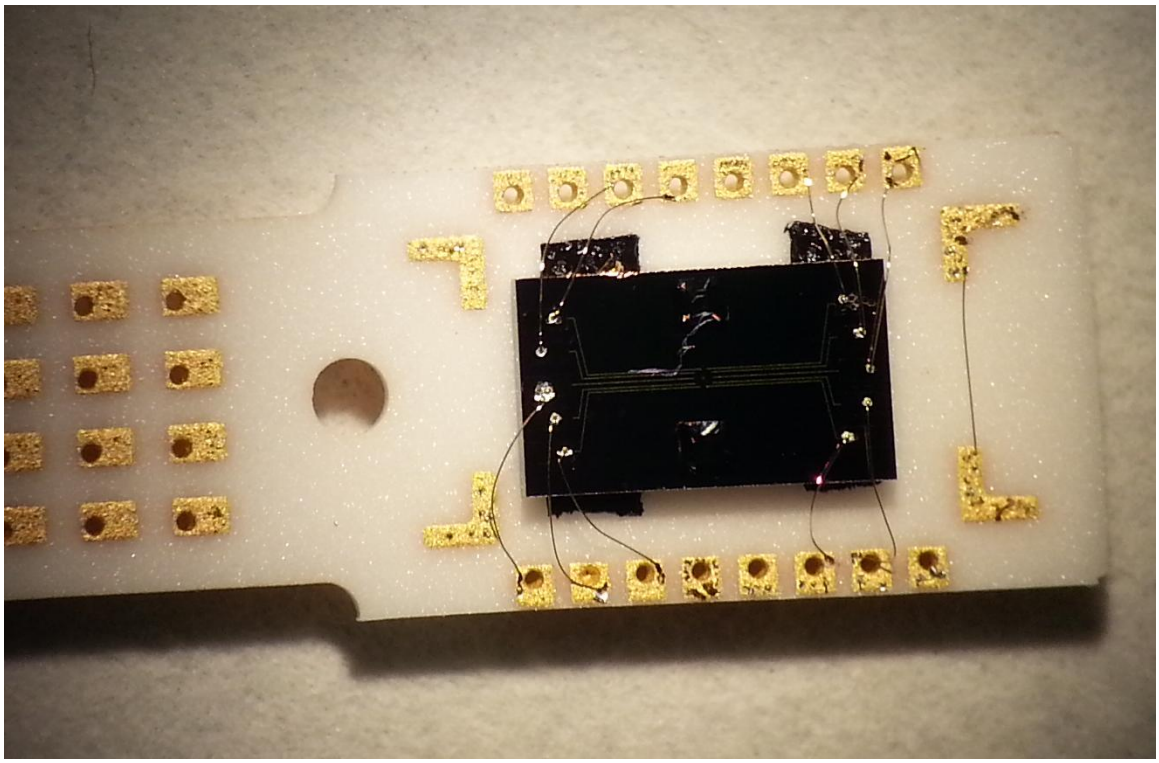

Figure 2.4. A chip carrier for the Nanofactory 16-lead electrical holder, mounted with an un-sealed Discovery platform chip. The electrical leads on the chip are wire-bonded to gold leads on the chip carrier. The two large wells above and below the window hold the alignment beads, which ensure that the window on the lid sits directly above the window on the chip.

cases where there is no specific area of interest to simply choose to operate near the corners of the window, since the corners will be least affected by the bowing of the windows and the liquid thickness will be the smallest.

There are many other important considerations when performing liquid cell TEM. Interactions between the liquid(s) to be used and the membrane should be kept to a minimum; it has not been unknown for the liquid to etch away portions of the window, exposing the microscope column to severe out-gassing from the specimen. Furthermore, interactions between the electron beam itself and the liquid can be problematic; the formation of bubbles can interfere with imaging processes of interest or even force the liquid out of the viewable area.

2.4.3 Heating holders

Two different holders are used for the in-situ heating experiments. The first is a Gatan model 628 single-tilt heating holder, shown in Figure 2.5. It features a crucible-style heater, which is loaded with standard 3 mm TEM grids, and the temperature is determined by a calibration curve relating the input current to the temperature of the heater. Typical heating rates for experiments using this holder are 5-10 °C/minute. Maximum temperature can vary by holder design; the holder at CINT is rated for 1200 °C maximum, and liquid cooling is required for temperatures exceeding 500 °C, which exacerbates the significant thermal drift.

The crucible is made from the refractory metal tantalum, and so it is important to consider the phase diagram of Ta and the material(s) of interest at the desired temperature range. In particular, great care should be taken none of the components of the crucible or the specimen is part of a eutectic system. This could cause the specimen to melt unexpectedly and fuse to the holder, or even melt the entire crucible itself, which could cause serious damage to the microscope. Care

Figure 2.5. The Gatan model 628 heating holder, along with its controller hardware.

must also be taken not to overtighten the hex ring that secures the specimen in the holder, as solid-state welding can occur at high temperatures over extended periods of time.

The second heating holder is the Protochips Aduro 300 double-tilt holder. Specimens are mounted on silicon chips designed specifically for this holder; Figure 2.6 a and b show the holder and a chip, respectively. Current is applied to a small array of heaters that cross the main window, which has 49 7 μm diameter holes in a square 7x7 arrangement with a 20 nm holey carbon or silicon nitride membrane for viewing the specimen. Thus, while heating is much more localized than for the Gatan holder, the viewable area is much smaller. The Protochips holder also has a maximum operating temperature of 1200 °C, but no liquid cooling is required and the maximum heating rate is 10^6 °C/s. This rapid heating and cooling rate can be used to create sharp steps in the temperature profile for an experiment, and the controller software records temperature data every millisecond for the duration of an experiment (although the number of data points exported can be any fraction of these). The temperature is determined using a calibration file specific to each chip, which is created at the factory using an optical pyrometer. The β-tilt axis is handled by the Protochips controller software and has a range of ±8°.

The major challenge for in-situ heating in the TEM is to know, reliably, what the temperature of the specimen is. In the case of the crucible-style heaters, the temperature read out by the controller is the crucible temperature, not the temperature at the specimen, much less the particular area of interest on the specimen. While it is possible to calculate the temperature profile within the crucible, it is non-trivial to map this profile onto the specimen because, even if the grid is perfectly aligned within the crucible by the user during loading, tightening the hex ring on the holder often shifts the grid an unknown distance. Although this could be overcome by, for example, recording visible light micrographs of the specimen in the holder after loading,

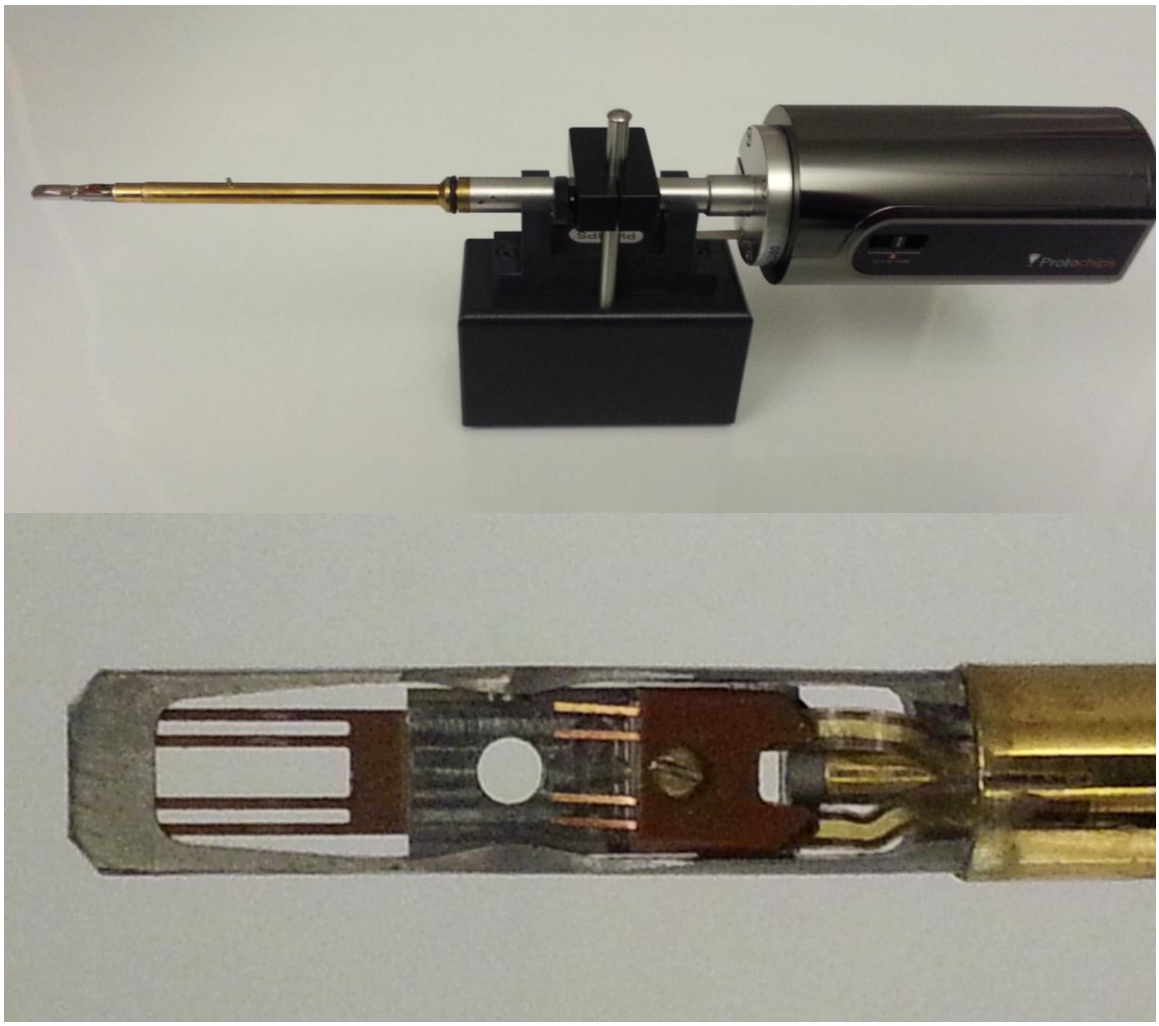

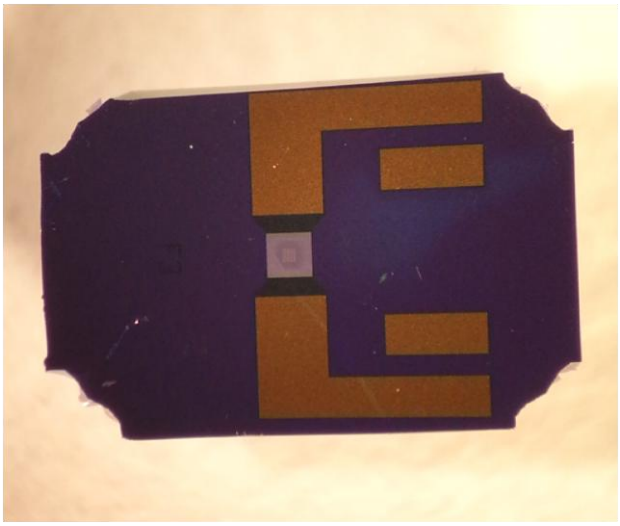

Figure 2.6. (a) The Protochips Aduro 300 double-tilt heating holder, with a close-up view of the end of the holder. (b) A heater chip for the Aduro 300 holder.

extra care would be required to correctly relate the electron micrographs to such a reference micrograph (possibly using a grid specially designed for this purpose, provided such a grid is available in the proper material), and ultimately the user is still at the mercy of the accuracy of the crucible temperature measurement.

In the case of chips with localized heaters, the user is essentially in the dark as to what the real temperature at the region of interest is, aside from what the controller software reads out. The calibration curve generated at the factory for such chips is likely based on the average temperature of the entire heated area ("likely" because the exact details of chip calibration are not publicly available), but significant variations in temperature can occur even between adjacent viewing windows. Low-magnification images of several such windows from the same chip, having experienced the same nominal temperature profile, are shown in Figure 2.7 a-c. A qualitative heat map based on the amount of material remaining in each window is presented in Figure 2.7 d. A well-known idea for calibrating temperature is to deposit low melting point metals or alloys and then actually melt them in the microscope. However, many microscope owners or managers are not comfortable with deliberately melting metals in their machines, and furthermore, since each chip is slightly different, the very act of calibrating one this way would ruin it for future use. It may be that as TEM holders push towards the "lab-in-the-gap" ideal, a method for directly measuring the temperature of localized regions of the specimen can be implemented within the column. At the present time, however, accurate temperature measurements within the TEM remain a significant challenge.

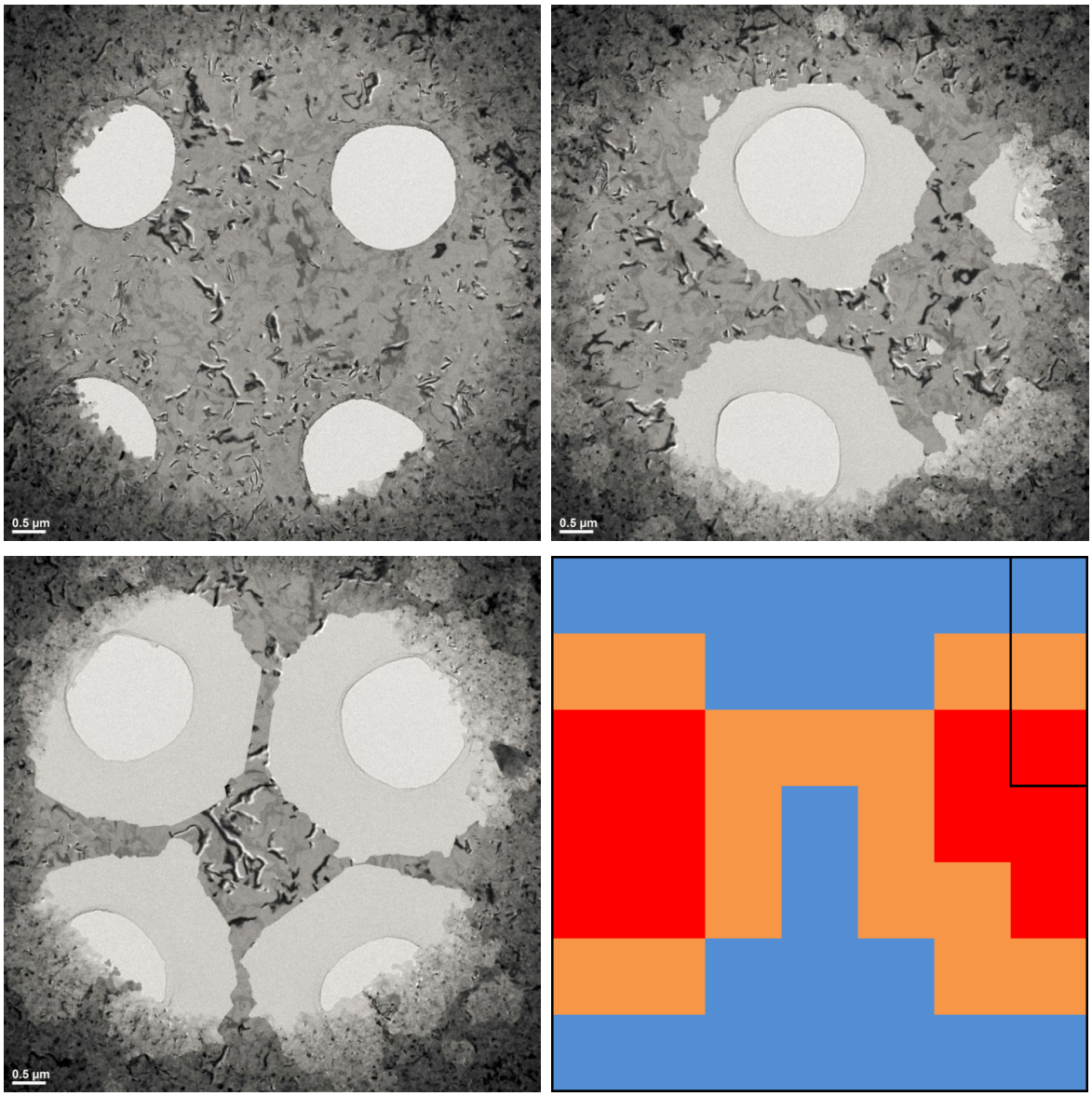

Figure 2.7. (a-c) Low-magnification, bright-field TEM images of three different windows in a Protochips heater chip after a heating experiment on a thin GST film. The heat map in (d) was constructed from similar images of all 49 windows, based on the amount of material remaining in each window. The three windows in the boxed area correspond to the images in (a-c).

2.5 Other software

This section describes some of the other software that was important to this work. In particular, the video recording software used to acquire data during in-situ experiments and image simulation software are discussed.

2.5.1 VirtualDub and Camtasia

Just as careful consideration must be given to the computer hardware that supports in-situ TEM experiments, the software used to acquire the data is critical to ensuring the preservation of information in the results. In this work, two different programs were used to record video during the in-situ experiments.

First is VirtualDub, which is a free video capture and compression program licensed under the GNU General Public License. The dimensions of the video that can be recorded are dependent on the resolutions supported by the graphics card, which is problematic since the "search" window in Digital Micrograph on the Tecnai F30 at CINT is 1024x1024 pixels and in this case, the maximum resolution that VirtualDub could capture was 640x480 (effectively 480x480 since the input is square). On the other hand, by tying directly into the video card, VirtualDub is capable of recording video at whatever frame rate the video card can render frames at, which may be faster than the monitor's refresh rate.

Camtasia is a screen capture and video editing program by TechSmith. The area of the screen to be captured is totally customizable by the user, which gives it an advantage over VirtualDub. However, the maximum frame rate attainable by a *screen capture* software is dependent on the refresh rate of the screen. Since most LCD monitors attached to TEMs (i.e., not new ones) refresh at 59 or 60 Hz, if the camera on the microscope is capable of higher frame rates they will

be lost on such a program. On the other hand, most high-speed cameras are capable of generating such a massive amount of data at a very high rate that they come with specialized acquisition software from the camera manufacturer.

2.5.2 Image simulation

As discussed in Chapter 1, the contribution that any particular set of lattice planes makes to the contrast in a high-resolution (i.e., phase contrast) image is determined by the contrast transfer function. The variables contributing to the form of the contrast transfer function that are always directly within the control of the operator are the defocus Δf and the specimen thickness t; if the microscope is equipped with a spherical aberration corrector then C_s is also a freely tunable parameter that may be used to manipulate the contrast transfer function. When planes whose corresponding reciprocal lattice vectors are beyond the first zero of the transfer function are contributing to the image contrast, then the image contrast is not directly interpretable and any analysis must rely on comparisons to simulated images.

Traditionally, this was achieved by loading the relevant crystal structure into the simulation software along with all of the (fixed) parameters of the microscope necessary to calculate the contrast transfer function, then systematically varying both the defocus and specimen thickness and comparing the experimental image to the resulting array of simulated ones to try and find a match. Clearly, this is a brute-force method, albeit a sophisticated one; great care must be taken even when using simulations to aid image interpretation because different structures can result in identical images with the appropriate combinations of microscope parameters. An example of such an array of simulated images for MoS_2 is shown in Figures 2.8, with the specimen thickness varying along the row of images.

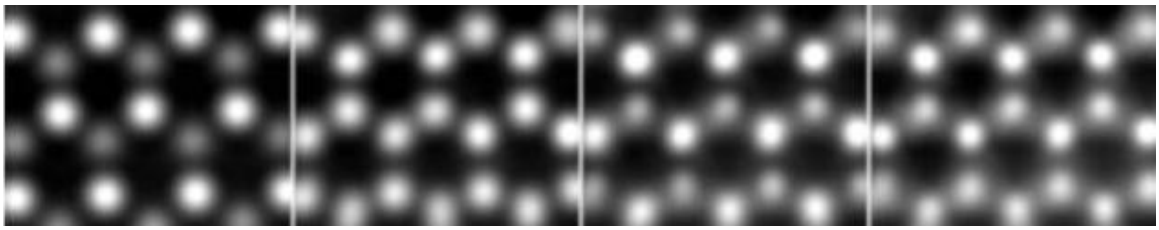

Figure 2.8. Simulated HRTEM images of MoS_2 for specimen thicknesses of one, two, three and four layers. Adapted with permission from Enyashin, A. N., Bar-Sadan, M., Houben, L., & Seifert, G. (2013). Line defects in molybdenum disulfide layers. *J Phys Chem C*, 117(20), 10842-10848 [77]. Copyright 2013 American Chemical Society.

Image simulation software packages make use of different variations of the multislice method, which was developed to take into account the propagation of the electron wave through the empty spaces between atoms. The core of the multislice method, common to many simulation approaches, is the division of the specimen into slices (corresponding to crystallographic planes within the specimen where possible) that are thin enough to obey the weak phase-object approximation discussed in Chapter 1. Each slice is represented by its projected potential at the exit-plane of the slice. The electron wave interacts with the first projection plane, propagates through empty space, and then interacts with the next projection plane, and so on until it has interacted with every slice (projection plane).

Where the image simulation approaches diverge is in their representation of the electron wave; this can be done by considering the amplitude and phase of the wave at different points in reciprocal space (the diffracted beam approach), or by representing the electron as a series of Bloch waves and only considering the ones that dominate the image contrast.

One of the most popular image simulation programs is JEMS, written by Pierre Stadelmann of the École Polytechnique Fédérale de Lausanne (EPFL, Switzerland). JEMS uses the traditional FFT-multislice approach, but can also perform Bloch wave calculations.

MacTempas by Total Resolution is based on the work of Roar Kilaas, and, as the name indicates, is available exclusively to Mac users. It uses the FFT-multislice approach.

xHREM by HREM Research Inc. is an image simulation suite for both Windows and Mac; Windows users can also make use of their Digital Micrograph plugins. This software uses the FFT-multislice approach and is based on the work of Kazuo Ishizuka.

2.6 Facilities

This research was carried out at the Center for Integrated Nanotechnologies (CINT) at Sandia National Laboratories (Albuquerque, NM) and Los Alamos National Laboratory (Los Alamos, NM), as well as the Institute of Materials Science (IMS) at UConn. CINT is a DOE BES national user facility; use of the facility is free of charge as long as a user proposal has been accepted that is expected to generate publications with CINT acknowledgements. Active user proposals relevant to the projects outlined above were maintained at CINT starting from spring 2013.

3 Characterization of MoS_2

Transition metal dichalcogenides (TMDCs, TMCs or TMDs; although all of these acronyms are used in the literature, this work will use the first as both the "di-" prefix and "-chalcogenide" root are important enough for understanding the chemical makeup of the material from the name as to warrant a place in the acronym) have the general formula MX_2, where M is a metal from the transition series and X is a chalcogen, usually S, Se, or Te [78]. Many of them have a layered structure although some do not; pyrite (FeS_2) is a well-known example of the latter, but usually in the literature the TMDC acronym is used when describing and comparing the layered compounds and so the word "layered" has become implied.

A general (but brief) discussion of the chemistry of TMDCs is included to provide context for the specific case of MoS_2, followed by a detailed discussion on the structure and properties of the latter and how these apply to batteries.

3.1 The Chemistry of Layered TMDCs

3.1.1 Background: Ligand-field theory

By necessity this chapter involves a brief discussion of some aspects of quantum chemistry, particularly ligand-field theory (LFT; or its progenitors, crystal-field theory and molecular orbital theory), which was developed specifically to accurately treat transition metal complexes (see [79], the original paper by Griffith and Orgel). Although this complex subject is well beyond the scope of this work, a short background section on some relevant concepts from LFT will enable a significantly clearer and deeper discussion of TMDCs and their properties. The following discussion was informed largely by [80].

First, from the point of view of LFT, the basic building block of a TMDC is not the unit cell of the crystal but rather the MX_6 cluster itself. In this case the X atoms are the ligands, although the term originates from the coordination of transition metals by complex molecules. The coordination of the M atom can be trigonal prismatic or octahedral in TMDCs. In the former case, the MX_6 cluster belongs to the D_{3h} point group while the octahedral coordination corresponds to the O_h point group.

Point groups consist of specific combinations of symmetry operations that can be applied to (in this case) the MX_6 "molecule" and leave it indistinguishable. A point group can also be further divided into irreducible representations, which are subsets of the symmetry operations that are applicable to certain mathematical functions. This is important because electron orbitals are described by mathematical functions. The orbitals are denoted with subscripts corresponding to these functions; for d orbitals these are: z^2, x^2-y^2, *xy*, *xz*, and *yz*. A schematic drawing of the d-orbitals is shown in Figure 3.1.

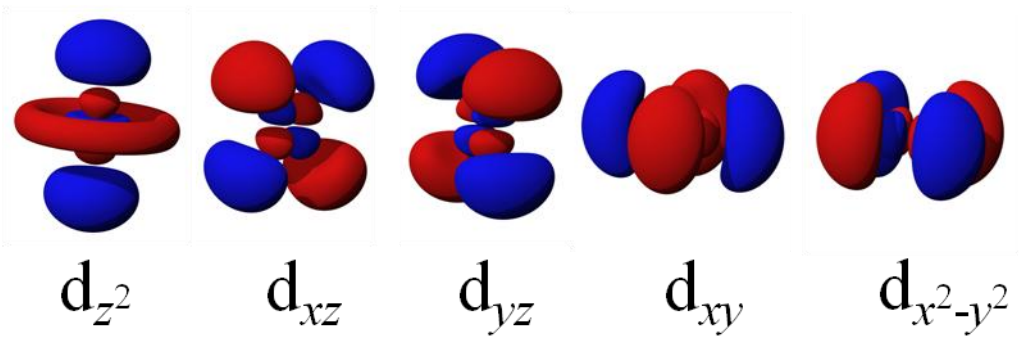

Figure 3.1. Illustrations of the shapes of the five d-orbitals.

Representations are denoted by a capital letter, which may be accompanied by any of these: a prime or double prime, a subscript number 1 or 2, and/or a subscript letter g or u.

- The letter designates whether the representation is symmetric (A) or anti-symmetric (B) with respect to rotation about the principle axis, or whether it is degenerate (E for doubly degenerate and T for triply degenerate representations). If a representation is degenerate then the two (or three) functions it applies to cannot be treated separately and the corresponding orbitals are said to belong to an orbital group; this is important to understanding how the energies of the d orbitals split.
- Prime (double prime) indicates that the representation is symmetric (anti-symmetric) with respect to the σ_h operation (i.e., the horizontal mirror plane normal to the principal rotation axis).
- Subscript 1 (2) indicates that the representation is ultimately symmetric (anti-symmetric).
- Subscript g (u) indicates that the representation is symmetric (anti-symmetric) with respect to the inversion center operation.
- Note that a given point group may not contain all of the symmetry operations that pertain to these annotations. D_{3h} does not have an inversion center, for example.

The (anti-) symmetry tracked by the annotations takes account of the fact that the orbital(s) in question will never be isolated in LFT, and so there is no exchange degeneracy.

With regard to TMDCs, the relevant representations describing the D_{3h} point group are quite different from those describing the O_h point group. In the former, d_{z^2} belongs to the A'_1 representation, $d_{x^2-y^2}$ and d_{xy} to E', and d_{xz} and d_{yz} to E". In the latter, d_{z^2} and $d_{x^2-y^2}$ belong to the E_g representation while d_{xy}, d_{xz}, and d_{yz} belong to the T_{2g} representation. As discussed in the

following section, this particular point is critical to understanding how the chemistry of TMDCs dictates their structures.

In the context of a transition metal coordinated by ligands, the energy levels of these orbital groups then depends on the proximity of the metal's d orbitals to the ligands. This illustrates the intimate relationship between the physical and electronic structures of the TMDCs.

3.1.2 Patterns in TMDC chemistry

Unlike graphite, which is formed by single-atom layers of tightly-bound carbon rings, the layers in a TMDC material are actually slabs of three atomic planes, and the atoms in each of these planes form a hexagonal net. Chalcogen atoms make up the top and bottom planes while the transition metal atoms occupy the interstices. The geometry of these interstices is determined by the stacking of the chalcogen planes, which can have the sequence AA or AB. In the former case the interstitial sites have a trigonal prismatic geometry and half of these are occupied by transition metal atoms; the latter stacking sequence gives rise to octahedral interstices, all of which are occupied, and tetrahedral sites that are not occupied. Table 3.1 lists the layered TMDCs with their c/a ratios, organized by the coordination geometry of the metal atom and by increasing occupancy of the outermost d shell, after [78] and [81].

As a cautionary note, it is important to pay close attention to the meaning of c, especially when making or reading about comparisons between TMDCs. The various polymorphs are denoted by a two-character abbreviation: a number and a capital letter. The number designates how many X-M-X slabs are in the unit cell, while the letter indicates the crystal system the structure belongs to. So, because the unit cells of the various TMDC structures are built up by stacking the slabs in different ways, it is not useful to directly compare the c lattice parameter (or any related figure such as c/a) between structures because it is dominated by the periodicity of the stacking

Table 3.1.1. The layered TMDCs, organized by the group of the transition metal, and by coordination geometry. Adapted from Kertesz and Hoffmann, and Wilson and Yoffe. Phases in parentheses are metastable.

Trigonal Prismatic			**Octahedral**	
Formula	*c/a*	TM group	Formula	*c/a*
		4B	TiS_2	1.67
			$TiSe_2$	1.70
			$TiTe_2$	1.72
			ZrS_2	1.59
			$ZrSe_2$	1.63
			$ZrTe_2$	1.68
			HfS_2	1.61
			$HfSe_2$	1.64
		5B	VSe_2	1.82
			VTe_2	1.80
NbS_2	1.80			
$NbSe_2$	1.82			
			$NbTe_2$	1.78
(TaS_2)	1.83		TaS_2	1.75
$TaSe_2$	1.85		$(TaSe_2)$	1.80
			$TaTe_2$	1.80
MoS_2	1.94	6B	(MoS_2)	
$MoSe_2$	1.96			
$MoTe_2$	1.98		$(MoTe_2)$	1.89
WS_2	1.96			
WSe_2	1.98			
			WTe_2	1.93

sequence. For example, 2H-MoS_2 and 3R-MoS_2 have c = 1.2295 nm and 1.837 nm, respectively, but this conveys little information beyond the twofold stacking sequence of the former compared to the threefold stacking sequence of the latter (cf. §3.2). Instead, useful comparisons are made by taking c as the combined width of one slab plus that of the van der Waals gap (or the distance between the metal planes in adjacent slabs). Returning to the MoS_2 example, after normalizing for the stacking sequence it is much more straightforward to compare $c/2 \approx 0.615$ nm for the 2H polytype with $c/3 \approx 0.612$ nm for 3R, and then to discuss the subtle physical reasons for the difference between the two. It is common for any explicit statement of this normalization factor to be neglected since it quickly becomes cumbersome and, for the experienced reader, is implied anyway by the name of the structure.

Examining some of the trends in Table 3.1, it can be observed that (a) the preference for octahedral vs. prismatic coordination of the transition metal is correlated to the group of the metal, and (b) the c/a ratio in materials where M is trigonal-prismatically coordinated tends to be larger than when M is octahedrally coordinated (illustrated best with metals like Ta whose sulfide exhibits octahedral coordination while the selenide takes on trigonal prismatic coordination).

The first trend is related to the progressive filling of the d shell with each step to the right along the transition series, and how the d band splits differently depending on the coordination geometry. The energy of a d shell in a crystalline solid will split into five energy bands due to the five-fold degeneracy associated with the space quantum number m_l being removed; the exact details of this splitting depend on the symmetry of the crystal [71].

In the case of octahedral coordination, this manifests itself as three bands with much lower energy than the other two. The three low-energy d bands are associated with the $\mathbf{t_{2g}}$ orbital group,

although it must be stressed that each individual band does not correspond directly to a particular orbital (i.e., d_{xy}, d_{xz}, and d_{yz} all contribute to all three bands) [82]. Furthermore, the energy spread of the $\mathbf{t_{2g}}$ bands is generally small, and it contains the Fermi level.

However, for trigonal prismatic coordination, the five d orbitals are split 1-2-2 rather than 3-2, which is intuitive in the context of the different representations of the D_{3h} and O_h point groups discussed in the previous section. The lowest-energy band corresponds to d_{z^2} and never crosses above the Fermi level. The next two bands occur after a significant energy gap and correspond to the **e'** orbital group (d_{xy} and $d_{x^2-y^2}$), and the final two bands correspond to the **e"** orbital group (d_{xz} and d_{yz}).

This explains why structures with the trigonal prismatic coordination tend to be increasingly favored moving from group 4B (no electrons in the outer d shell assuming the two chalcogen atoms attain their theoretical formal charge of -2 each) to group 6B (two electrons in the d shell, fully populating the d_{z^2} band), while the step to group 7B sees an abrupt return to the preference for octahedral coordination as the $\mathbf{t_{2g}}$ bands can accommodate six electrons and are at a much lower energy than the **e'** bands associated with trigonal prismatic coordination.

The second trend is reflective of the fact that a smaller value of *c* will, in general, increase the relative energetic favorability of octahedral coordination. If the decrease in *c* is due to a decrease in the thickness of the slab, the distance between the M and X planes is decreased. This exacerbates the energy "penalty" that is suffered by structures with trigonal prismatic coordination due to an extra possible interaction between the d orbitals of the M atoms with the p orbitals of the X atoms (specifically, only one of the two possible arrangements of the chalcogens' $p_{x,y}$ orbitals can interact with the metal's d orbitals in the octahedral case because the O_h point group has a center of symmetry) [81]. It should be noted that this discussion is

influenced heavily by the work of Kertesz and Hoffmann, who used a rigid band model to obtain their results. That is, they used their calculated band structure for $ReSe_2$ to make generalizations about all of the TMDCs. While this approximation is far from perfect, and indeed semiconductors tend to give density functional theory a hard time in general (or did in the 1980s), it is illustrative enough for the scope of this work.

This is all to emphasize, scientifically but without wandering too far afield, three important facts. First, the overall occupancy of the d bands in a TMDC has a significant impact on the preferred coordination geometry of the metal because, second, the relative energies of the d orbitals depend strongly on the symmetry of the crystal. Third, the proximity of the planes of transition metal atoms to the planes of chalcogen atoms has implications for the relative stability of the two possible structures of a slab. These facts will be important to the discussion in Chapter 4, which is primarily concerned with putting a strongly electropositive foreign species, Li, into the van der Waals gap.

3.2 The Structure and Properties of MoS_2

The most common, naturally-occurring polytype of MoS_2 is the hexagonal 2H phase. The stacking sequence in the [0001] direction is often denoted as AbABaB, with capital letters representing S planes and lower-case letters representing Mo planes. This is not to be confused with the 2H-NbS_2 structure, which has the same coordination geometry within slabs, but the stacking sequence is AbACbC. The coordination of Mo by S is trigonal prismatic. A detailed model of the 2H structure is shown in Figure 3.2a, and some of its basic physical properties are listed in Table 3.2 (after [78]).

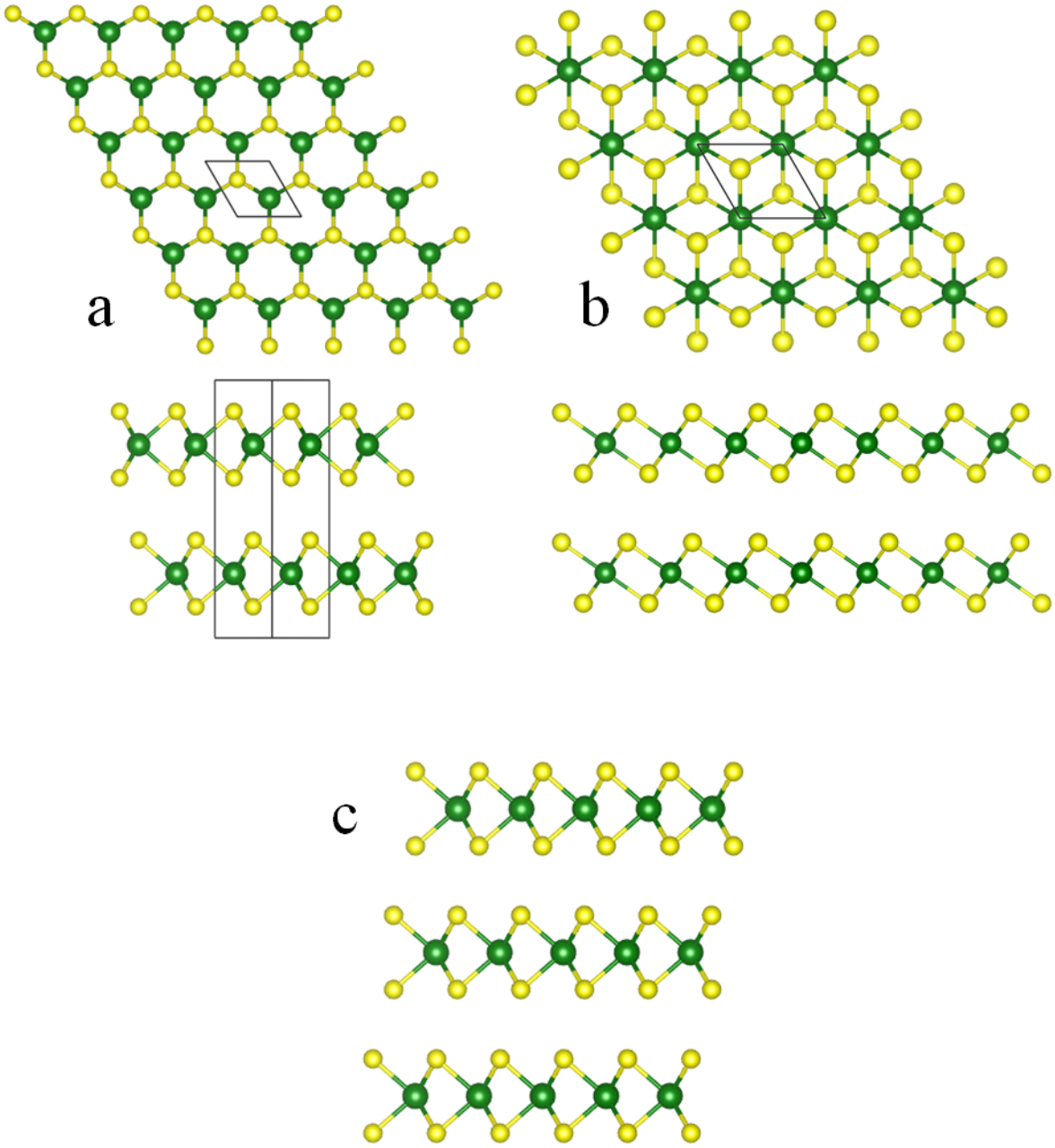

Figure 3.2. (a) The structure of 2H-MoS_2, showing a single layer in the [0001] projection and two layers in the $[11\bar{2}0]$ projection. (b) The structure of 1T-MoS_2. (c) The structure of 3R-MoS_2 in the $[11\bar{2}0]$ projection. A single layer in the [0001] projection is identical to the 2H structure.

Table 3.2. Basic structural properties of 2H-MoS_2

a	3.16 Å
c	2 x 6.15 Å
c/a	1.95
Mo-S bond length	2.41 Å
S-Mo-S Slab height	3.19 Å
v.d.W. gap height	2.96 Å

Table 3.3. Elastic constants (in GPa) and Debye temperature of MoS_2

c_{11}	c_{33}	c_{44}	c_{12}	c_{13}	θ
235	52	19	-54	23	335 K

2H-MoS_2 is a semiconductor with an indirect bandgap (i.e., the minimum energy of the conduction band occurs at a different point in the first Brillouin zone than the maximum energy of the valence band) of ~1.2 eV [83].

Naturally, because of the strong covalent bonding within slabs (i.e., in the basal plane) compared to the weak van der Waals bonding between slabs, many of the physical properties of MoS_2 are strongly anisotropic. The average atomic displacements due to thermal vibrations, for example, are larger in the [0001] direction by a factor of about 1.6 for Mo atoms and 1.3 for S atoms compared to their respective displacements within the basal plane.

Unsurprisingly, then, the linear thermal expansion coefficient for the *c*-direction (α_c = 8.65 x 10^{-6}/°C [84]) is over 4.5 times larger than that of the basal plane (α_a = 1.9 x^{-6}/°C [84]). However, because of the van der Waals gap, interactions between slabs are limited and so the thermal conductivity of MoS_2 is much greater within the basal plane (~99 $Wm^{-1}K^{-1}$ at room temperature [85]) than in the perpendicular direction (~2.3 $Wm^{-1}K^{-1}$ at room temperature [85]).

The mechanical properties of MoS_2 are similarly anisotropic, illustrated qualitatively by the fact that it cleaves readily on the basal plane. This is the basis for its widespread use as a solid lubricant [86]. Quantitatively, the elastic constants of 2H-MoS_2, as reported by Feldman, are given in Table 3.3.

In general, the binding energy of sulfur to any transition metal is lower than that of oxygen. For example, based on the survey of first-row transition metal monoxides and monosulfides by Bauschlicher and Maitre, the V-O bond has an energy of 6.44 eV compared to the binding energy of V-S which is 4.62 eV [87]. The difference between the binding energies of the oxide and sulfide is a maximum at Ti, after which it generally decreases across the row; the percent difference between the binding energy in CuO and CuS is less than 2% [87].

While the anisotropy of many properties of MoS_2 and the other layered TMDCs was a significant motivator for the original burst of research on this class of materials, today there is a strong emphasis on how the properties of MoS_2 change as the number of slabs in the crystal approaches (and reaches) one. This is the reason MoS_2 has attracted such significant interest as a 2D nanomaterial.

For example, modern DFT calculations with advanced algorithms capable of handling bandgaps in semiconductors have predicted that both the magnitude and nature of the bandgap in MoS_2 depend on the thickness of the crystal: in the limiting case of a single S-Mo-S slab the bandgap is direct (at K; see the labeling of the Brillouin zone in Figure 3.3) with magnitude 1.8eV [88].

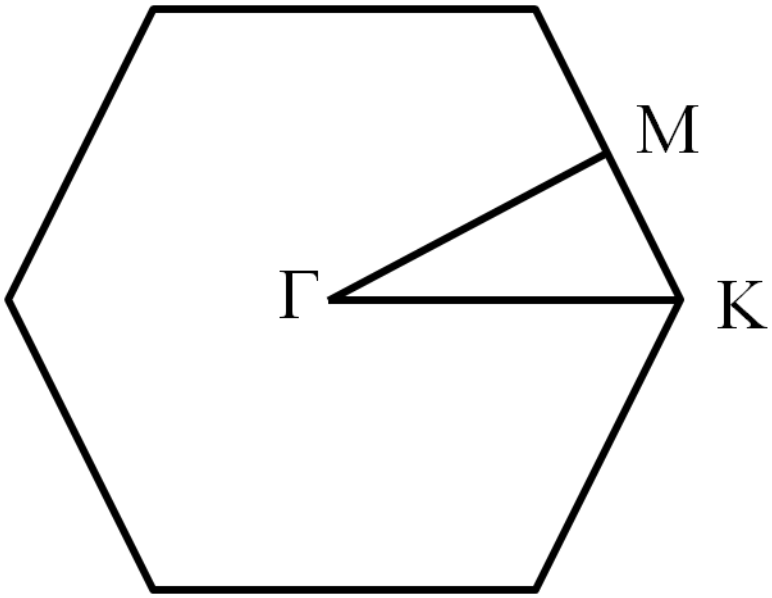

Figure 3.3. The first Brillouin zone of 2H-MoS_2 with the points bounding the irreducible wedge labeled.

The bandgap increases because the valence band maximum at Γ becomes progressively more negative with decreasing thickness while the conduction band minimum at (Γ+K)/2 becomes more positive. Meanwhile, the *local* extrema of both bands at K remain relatively unchanged so that they eventually become *global* extrema when the number of layers in the crystal reaches one. This prediction was confirmed by the experimental observation of strong photoluminescence in monolayer MoS_2, which is not a phenomenon associated with the bulk material [89]. Similar manipulation of the bandgap of semiconducting TMDCs thicker than one layer has also been achieved by straining thin films (e.g., [90] for MoS_2 and [91] for WSe_2) and by heating them [92]. In each case the indirect-direct bandgap transition is due to the mitigation of M-M d_{z^2} orbital interactions between layers [91]: the monolayer case eliminates such interactions entirely, while heating or bending a multilayer film increases the separation of the metal atoms, so that the multilayer effectively becomes a group of monolayers "in series." Single layers of MoS_2 and other TMDCs are therefore of interest in electronics, as flexible transistors with tunable bandgaps [93].

A metastable, trigonal phase of MoS_2 also exists in which the coordination geometry of the MoS_6 clusters is octahedral. This structure is known as 1T-MoS_2 and is illustrated in Figure 3.2b. The 2H-1T transformation in MoS_2 is usually associated with its intercalation by Li; indeed, assuming the electron associated with the Li+ ion is donated to Mo the analysis of [81] applies nicely to the change in coordination geometry of the 1T phase.

Like the other TMDCs for which the metal atom is octahedrally coordinated, 1T-MoS_2 is metallic rather than semiconducting because the Fermi level is contained within what would otherwise be the top of the valence band (see, e.g., Figure 13 in [94] comparing the density of

states for the different coordination geometries, or Figure 2 in [82] comparing the band structures).

Another rarely but naturally occurring polymorph of MoS_2 is the 3R structure, which belongs to the rhombohedral crystal system and has the stacking sequence AbABcBCaC. The S atoms coordinate the Mo atoms in a trigonal prismatic arrangement in this structure as well, so that the chief difference between the 2H and 3R polytypes is the stacking sequence of the slabs. The 3R structure is shown in Figure 3.2c.

Comparison to graphite: apt or not?

The quintessential layered material is graphite, and much of what had been learned about the intercalation behavior of graphite (research on which began, it appears, in 1926 with potassium as the guest species [95]) was used to inform the study of insertion reactions in other materials. However, there are important distinctions that separate graphite from the layered TMDCs, and so the question of whether or not comparisons between the two are valid must be addressed.

Graphite is the most stable form of carbon at standard temperature and pressure (although the diamond structure is stable enough that even a small gemstone would take many thousands of years to spontaneously transform into graphite); it belongs to the hexagonal crystal system (space group $P6_3/mmc$) with a = 2.41 Å and c = 6.71 Å. The basal planes are separated by a van der Waals gap of $c/2$ = 3.35 Å. Within the basal plane, the carbon atoms are arranged in hexagonal rings so that each C atom is covalently bonded to three other C atoms. The structure of graphite is shown in Figure 3.5. Comparing Figure 3.2 and Figure 3.5, there is actually only one similarity between the structures: the gap that is between 3-3.35 Å wide separating every slab, across which the only attractive forces are weak van der Waals interactions.

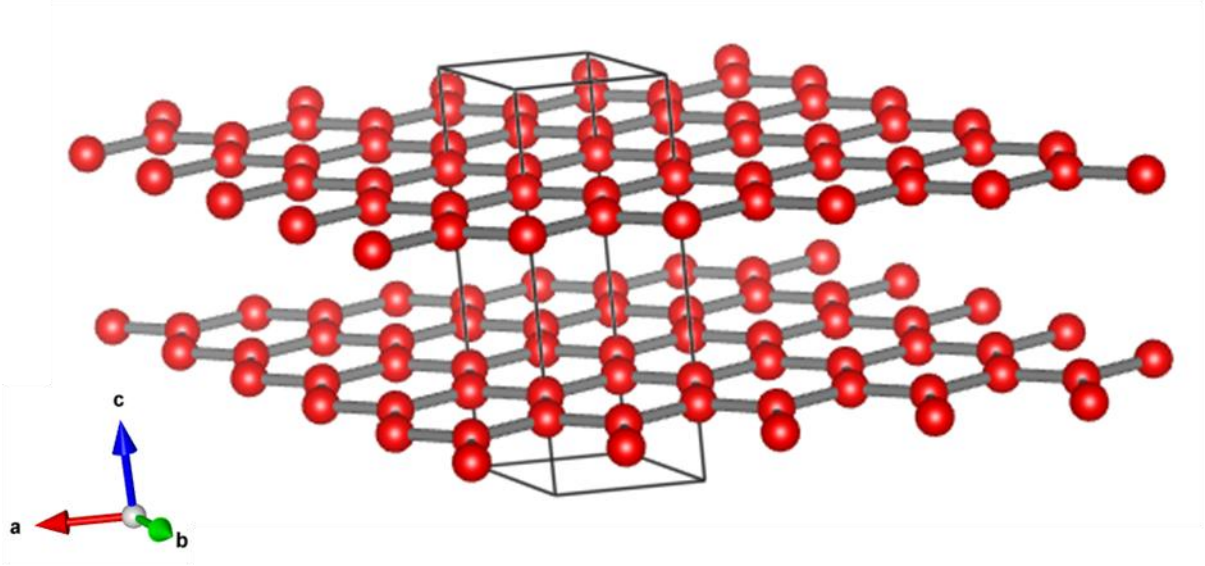

Figure 3.5. Structural model of graphite.

Everything else is different. Graphite contains only carbon atoms and so each slab is only one atom thick; TMDCs contain two different kinds of atoms and each slab is on the order of the thickness of the van der Waals gap. Bonds in graphite lie strictly within the basal plane; the bond directions in TMDCs always contain a *c*-component because the bonding is between the metal atoms and the chalcogen atoms situated above and below. Furthermore, the bonding in graphite involves only s and p orbitals; the bonding in TMDCs involves the d orbitals of the metal atom, which behave in such a complex way that an entire branch of physical chemistry was developed to treat them. The carbon atoms in graphite are arranged in a honeycomb-type net; each plane of atoms in a TMDC is arranged in a simple hexagonal net. A single slab of graphite (i.e., a sheet of graphene) is an excellent electrical conductor; a single slab of a TMDC may be either conducting (metallic) or semiconducting.

In general, then, it must be admitted that graphite is not, in fact, a suitable model for the much more complex layered TMDCs.

3.3 Exfoliation

The precise mechanism by which the 2H to 1T transformation occurs has not, as yet, been satisfactorily explained in the literature. The chemical exfoliation of MoS_2 is typically achieved by intercalating the structure with lithium, then exposing the lithiated MoS_2 to water. The lithium ions react violently with the oxygen in the water and, in theory, the layers are "blown apart" in the process. However, explanations of the process tend to leave off there, with no explanation for how the arrangement of the S atoms is actually changed. When a mechanism is cited, it is generally assumed that a shear of the S planes takes place, as described by van Landuyt, van Tendeloo and Amelinckx for TaS_2 [96, 97]; this concept will be thoroughly discussed in Chapter 4.

3.4 Diffraction patterns from MoS_2

Figure 3.6 a-f shows simulated and experimental diffraction patterns from MoS_2. The zone axes are [0001], [$10\bar{1}0$], and [$11\bar{2}0$].

Figure 3.7a shows another diffraction pattern at the [0001] zone axis, but in this case the layers were separated during the specimen preparation process and rotated slightly with respect to one another. The splitting of each spot into a small hexagonal pattern is characteristic of double diffraction through a low-angle twist boundary (cf. §18.9 in [62]). The corresponding bright-field image is presented in Figure 3.7b. Because of the very small distance between the spots, widely-spaced fringes are visible in the image even though the smallest objective aperture (10 μm actual diameter, or 2.65 nm^{-1} in the back-focal plane) is centered on the direct beam.

3.5 HRTEM imaging of MoS_2

The structure of MoS_2 (and TMDCs in general) depends not only on the arrangement of the sulfur atoms about the Mo atoms in each layer, but also on how the layers are stacked. This implies that some of the TMDC structures become indistinguishable when the material is thinned to a single layer since in this limiting case only the coordination of the metal atom can vary; for example, a single layer of 3R-MoS_2 is identical to a single layer of 2H-MoS_2. This section is concerned with how high-resolution TEM images have been used in the past to distinguish the phases of single- and few-layer TMDCs, as well as some interesting side-effects of using lithium to chemically exfoliate these materials.

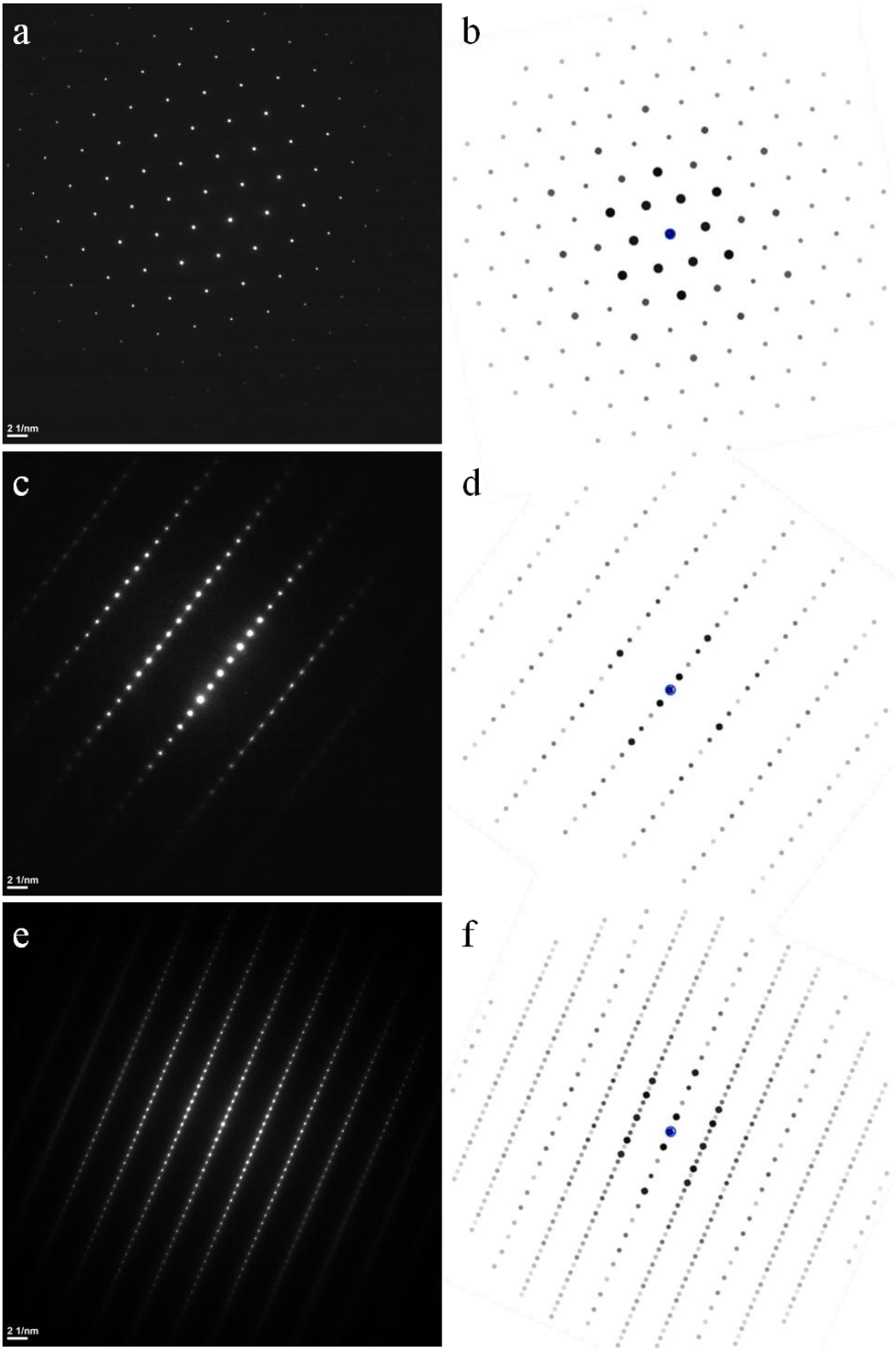

Figure 3.6. Experimental and simulated diffraction patterns of 2H MoS_2 at three different zone axes: (a, b) [0001], (c, d) [$1\bar{1}00$], (e, f) [$11\bar{2}0$].

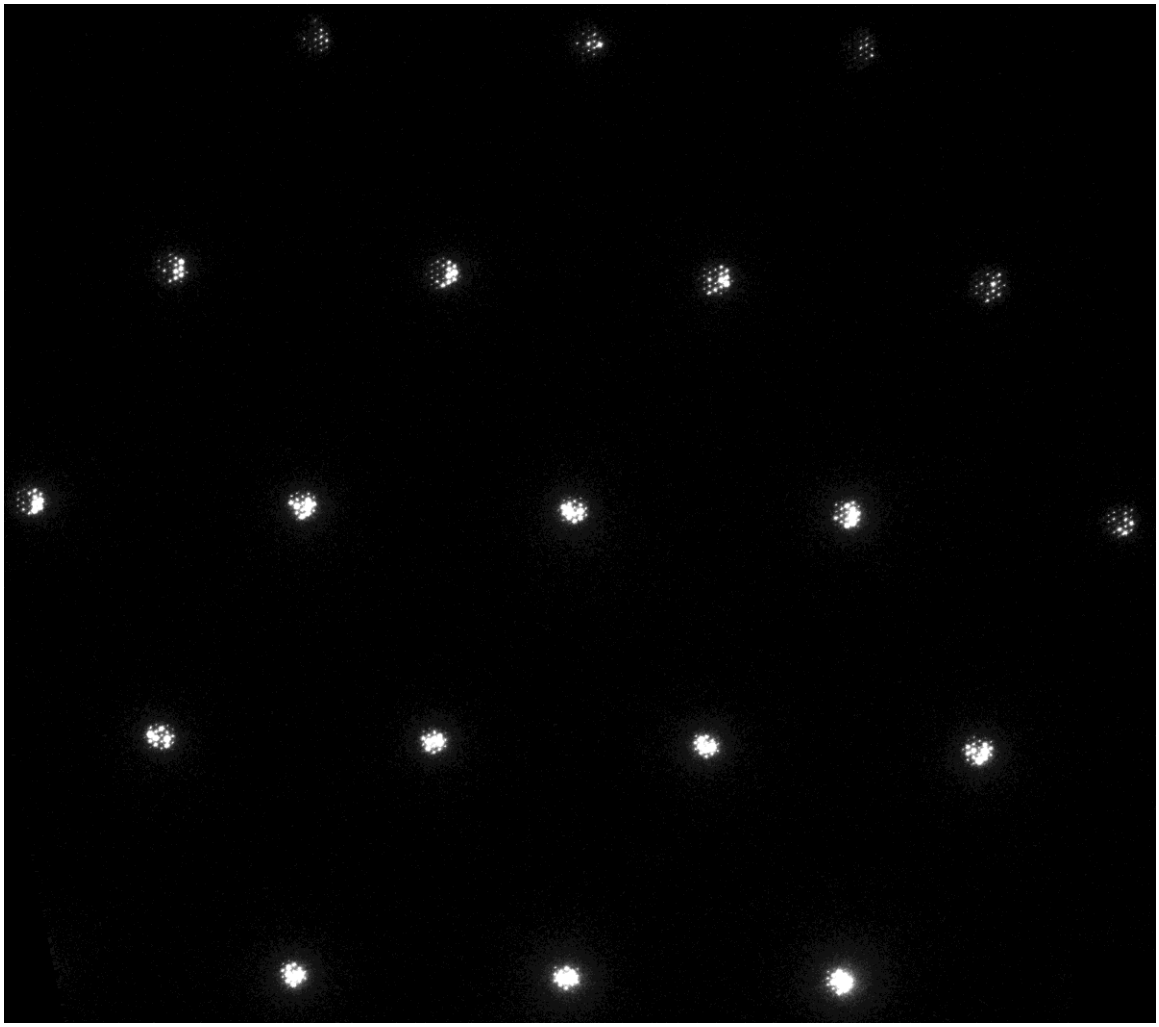

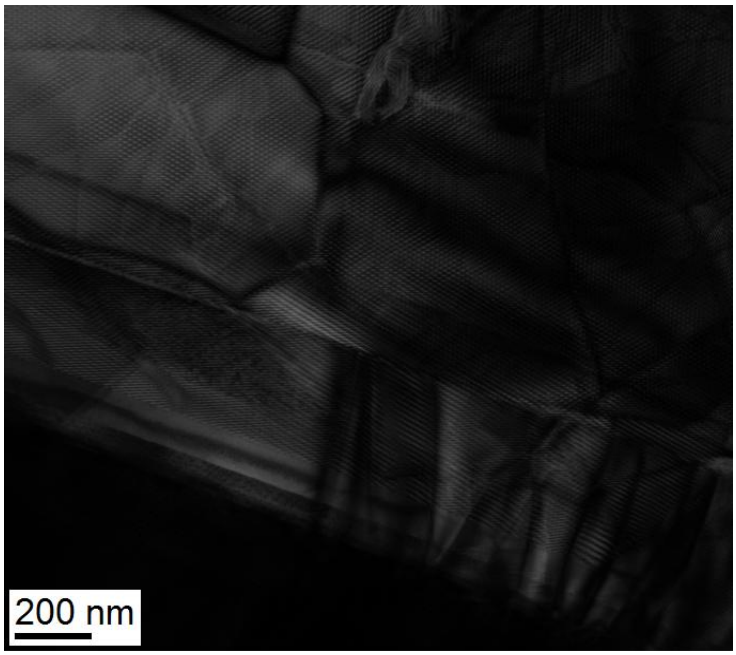

Figure 3.7. (a) Diffraction pattern from MoS_2 on the [0001] zone. Each spot is split into a small array of spots because of the overlap of two flakes of material. (b) The corresponding bright-field image.

3.5.1 Plan view

Comparing the 2H and 1T structures looking along [0001], the major difference for single-layer MoS_2 is the quantity and occupancy of the sulfur columns. In the 2H case, there are three columns of sulfur atoms arranged about the Mo atoms, each with two S atoms in it. A simulated image of a single layer of the 2H structure is shown in Figure 3.8. On the other hand, in the 1T case there are six sulfur columns surrounding each Mo atom, each containing only one S atom; a simulated image of a single layer of the 1T structure is shown in Figure 3.9.

Interestingly, many images of 1T MoS_2 show clustering of Mo atoms, in varying superstructures. The most common of these are known as the 1T' and 1T" structures, and examples of these superstructures in MoS_2 are shown in Figures 3.10. The common explanation for the formation of these superstructures is a Jahn-Teller distortion of the MX_6 clusters.

An experimental image of 2H-MoS_2 in the plan-view orientation is shown in Figure 3.11.

3.5.2 Parallel to (0001)

As discussed in §2.5, it is straightforward to prepare MoS_2 lamellae in the FIB with foil planes of $\{10\bar{1}0\}$ and $\{1\bar{2}10\}$. The latter orientation is particularly useful as the stacking sequence of the layers can be directly observed, which is demonstrated schematically in the structural model shown in Figure 3.12a. The $[10\bar{1}0]$ projection is shown in Figure 3.12b. Corresponding high-resolution micrographs are shown in Figures 3.13 and 3.14.

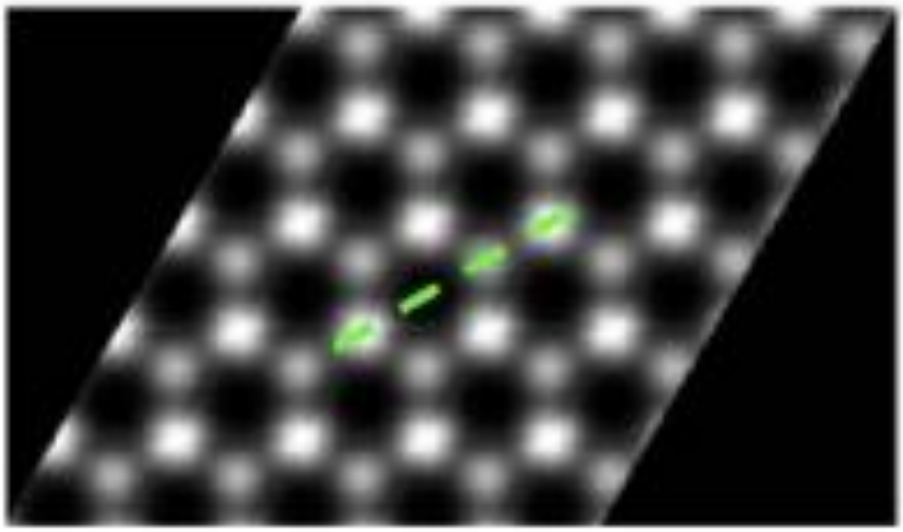

Figure 3.8. Simulated image of a single layer of 2H MoS_2 viewed along the [0001] direction. Adapted with permission from Eda, G., Fujita, T., Yamaguchi, H., Voiry, D., Chen, M., & Chhowalla, M. (2012). Coherent atomic and electronic heterostructures of single-layer MoS2. *ACS Nano*, 6(8), 7311-7317 [98]. Copyright 2012 American Chemical Society.

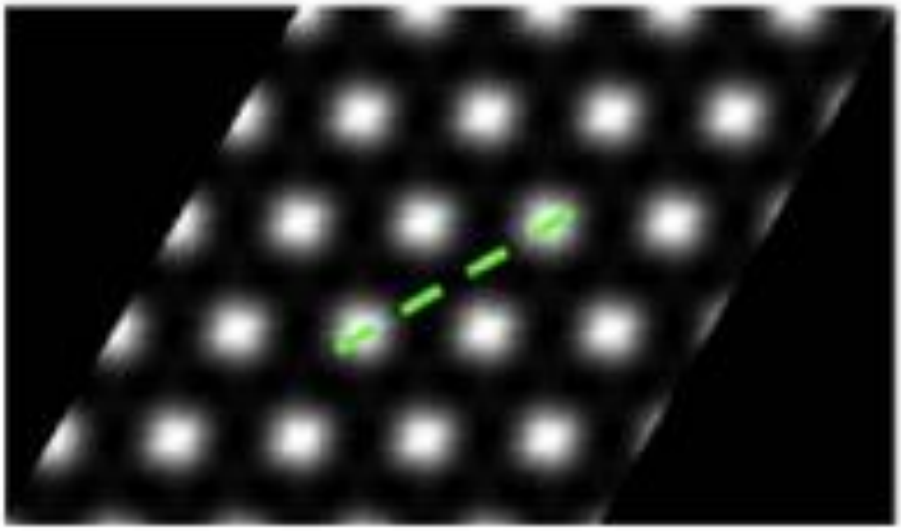

Figure 3.9. Simulated image of a single layer of 1T MoS_2 viewed along the [0001] direction. Adapted with permission from Eda, G., Fujita, T., Yamaguchi, H., Voiry, D., Chen, M., & Chhowalla, M. (2012). Coherent atomic and electronic heterostructures of single-layer MoS2. *ACS Nano*, 6(8), 7311-7317 [98]. Copyright 2012 American Chemical Society.

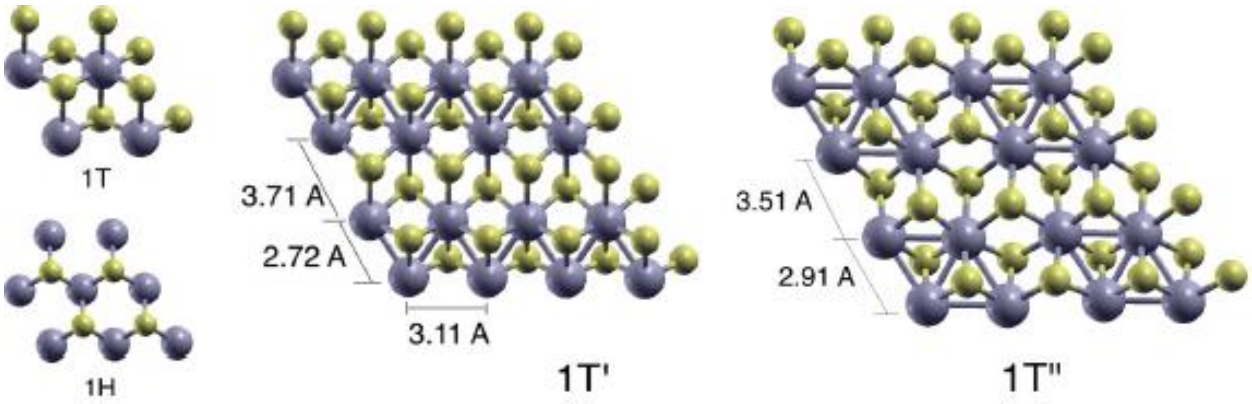

Figure 3.10. Schematics of the 1T’ and 1T” superstructures in layered TMDCs. Reprinted figure with permission from Calandra, M., *Phys Rev B*, 88(24), 245428, 2013 [99]. Copyright 2013 by the American Physical Society.

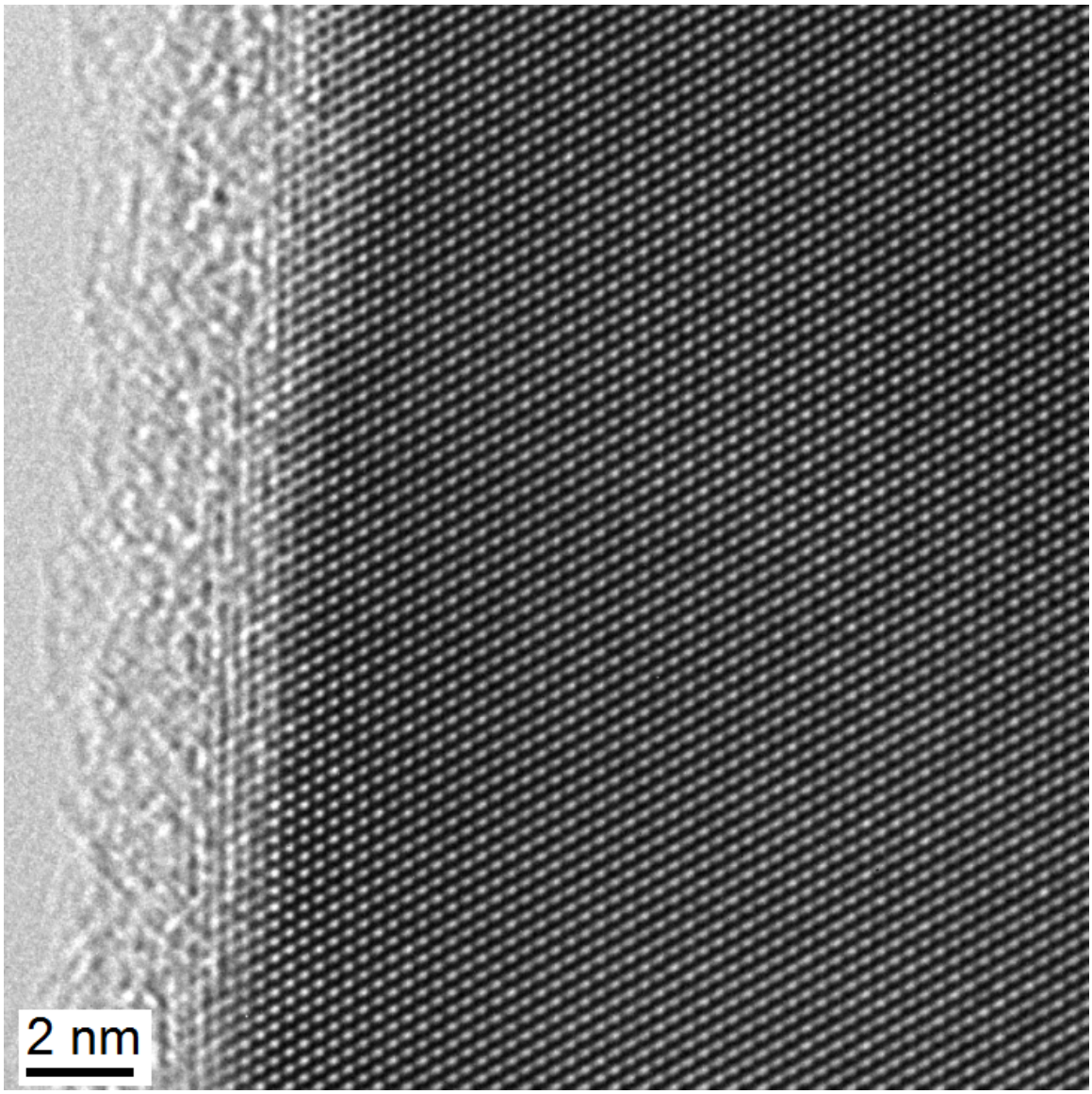

Figure 3.11. Experimental high-resolution TEM image of MoS_2 on the [0001] zone.

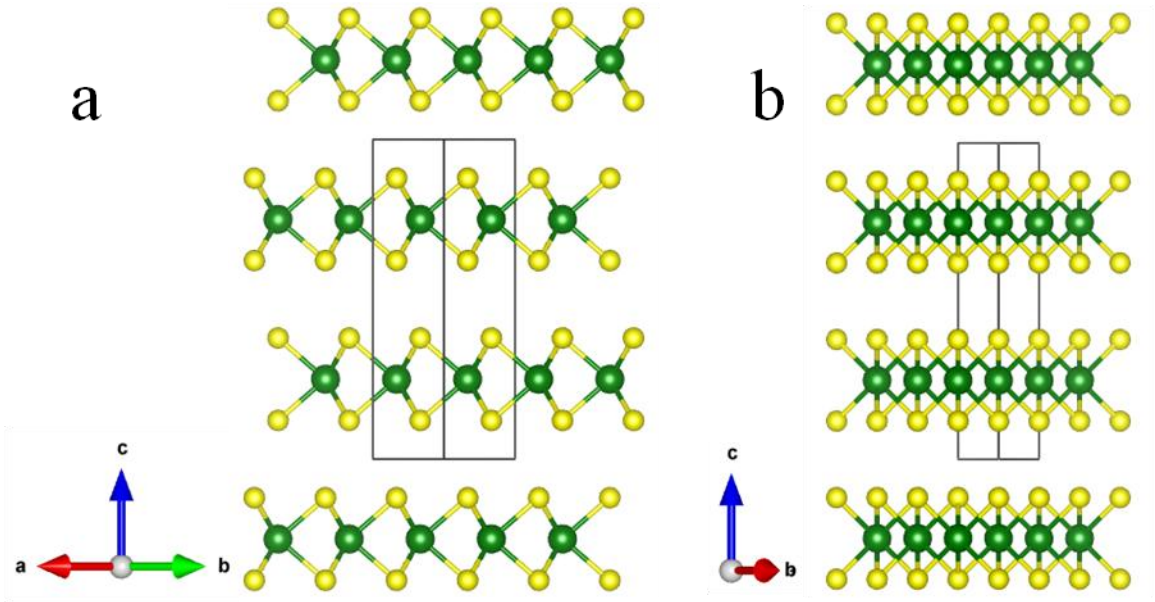

Figure 3.12. Structural models of MoS2 as viewed along the (a) $[1\bar{2}10]$ and (b) $[10\bar{1}0]$ directions.

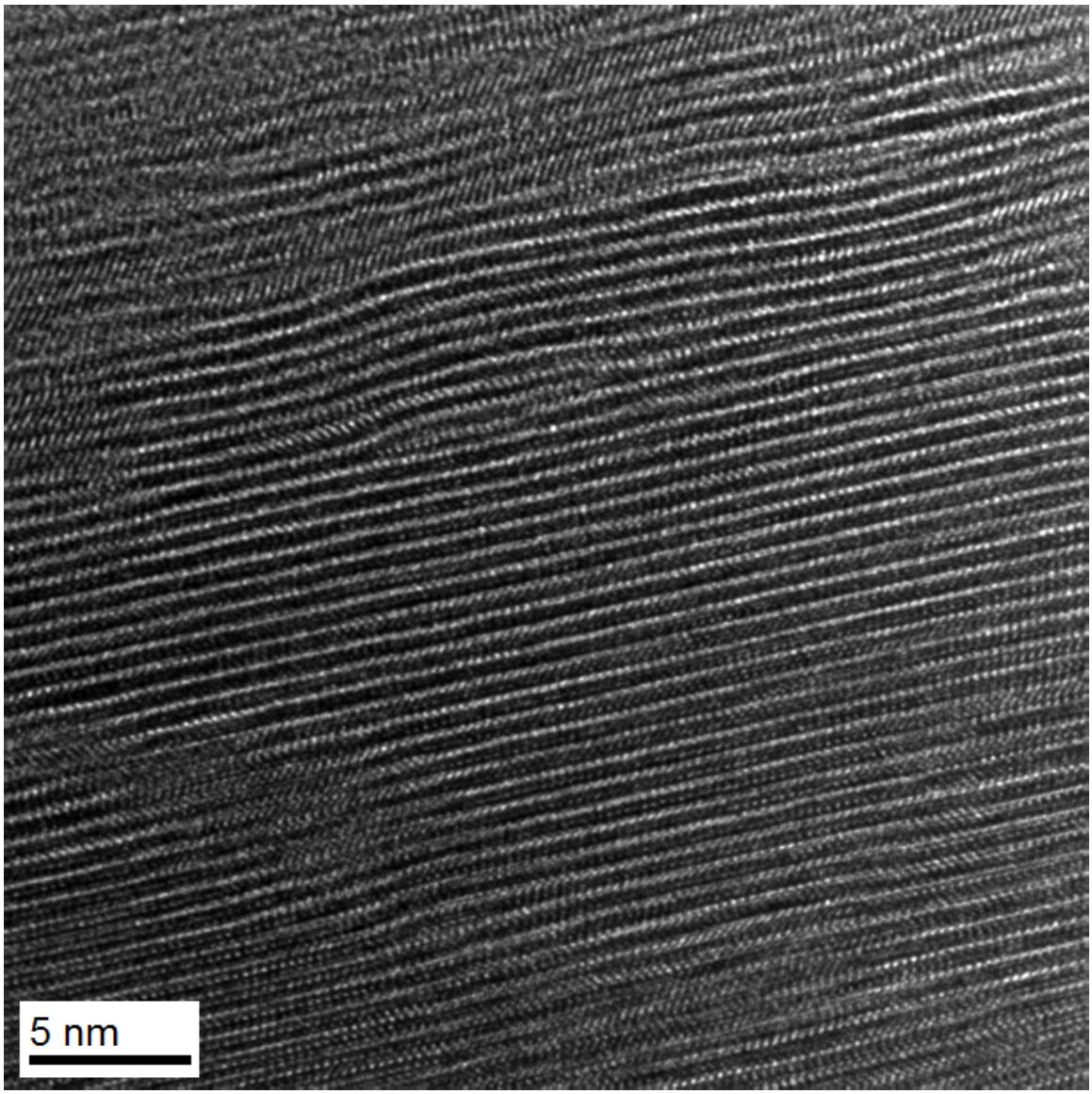

Figure 3.13. HRTEM image of a MoS2 FIB lamella with foil plane $(1\bar{2}10)$.

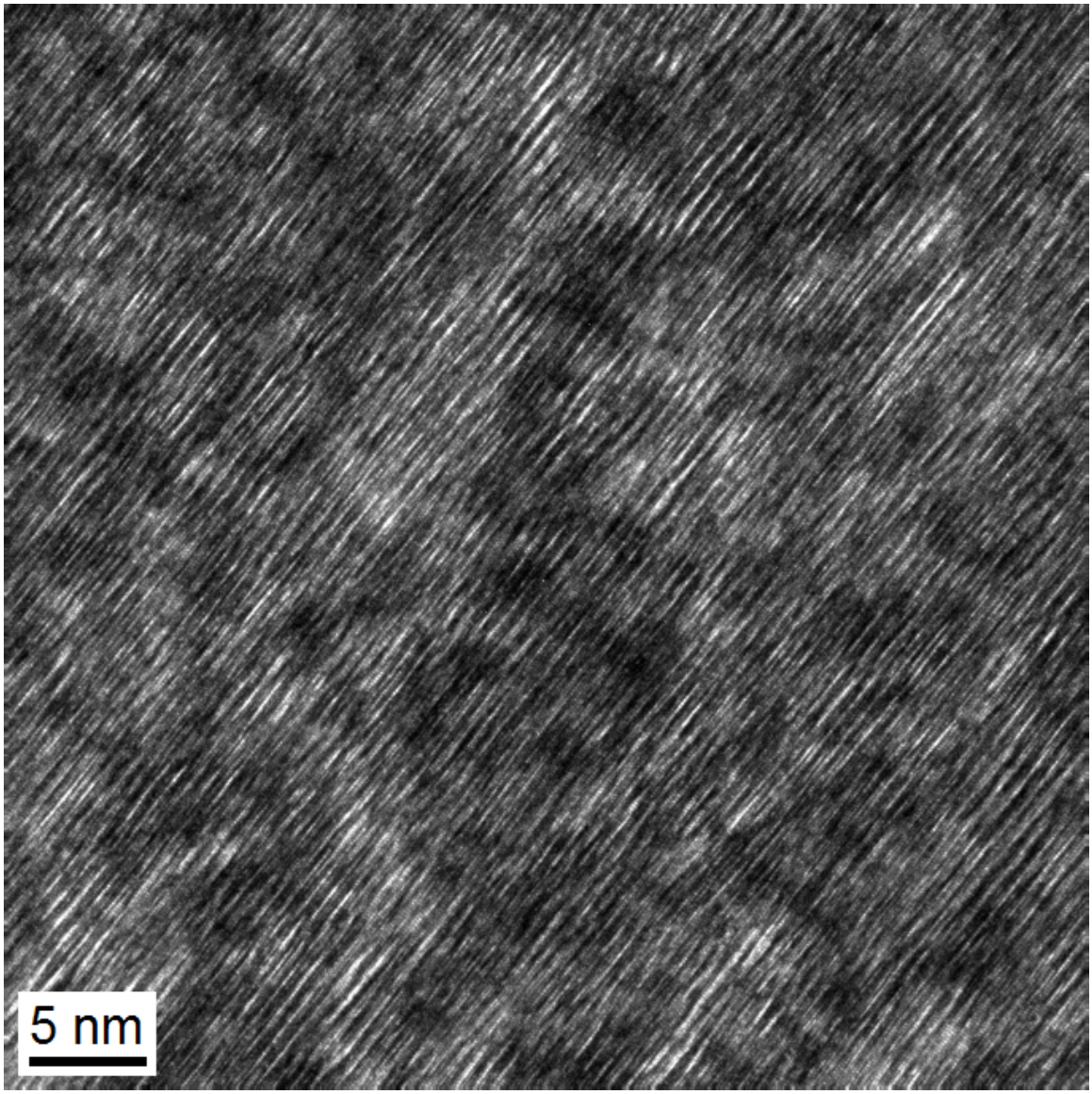

Figure 3.14. HRTEM image of a MoS2 FIB lamella with foil plane $(10\bar{1}0)$.

3.5.3 STEM vs. TEM

The MoS_2 sample used for this work was formed naturally, and as such the specimens prepared from it reflect the fact that it is a "real material." However, examining the same specimen in both a probe-corrected microscope and an image-corrected machine revealed an interesting discrepancy. Although the resolving power of these TEMs was approximately equal, the "quality" of the images obtained was certainly not. This is illustrated in Figure 3.15. The image in (a) was recorded in HAADF-STEM mode on the probe-corrected (200kV) Titan at Sandia, while the image in (b) was recorded in conventional TEM mode on the image-corrected (300kV) Titan at Los Alamos. The images were recorded from the same area of the same specimen, but the material appears to be of much higher quality in the STEM image. That is, the basal planes appear to be much straighter not only in the horizontal direction in the image, but also through the specimen thickness as well. On the other hand, in the phase-contrast image the planes are obviously buckled along the length and depth of the foil.

This raises the question of why the two images look so different, and also which is better. It is hypothesized that condensing the beam into such a small probe, as is possible only with AC-STEM, gives rise to a strong channeling effect as the electrons in the probe traverse the specimen, which tends to artificially straighten out planes that are actually bent (cf. §10.4 of [100]). So, although the STEM image is certainly more interpretable at the atomic scale, the phase-contrast image contains more realistic information about what the specimen really looks like at the nanoscale.

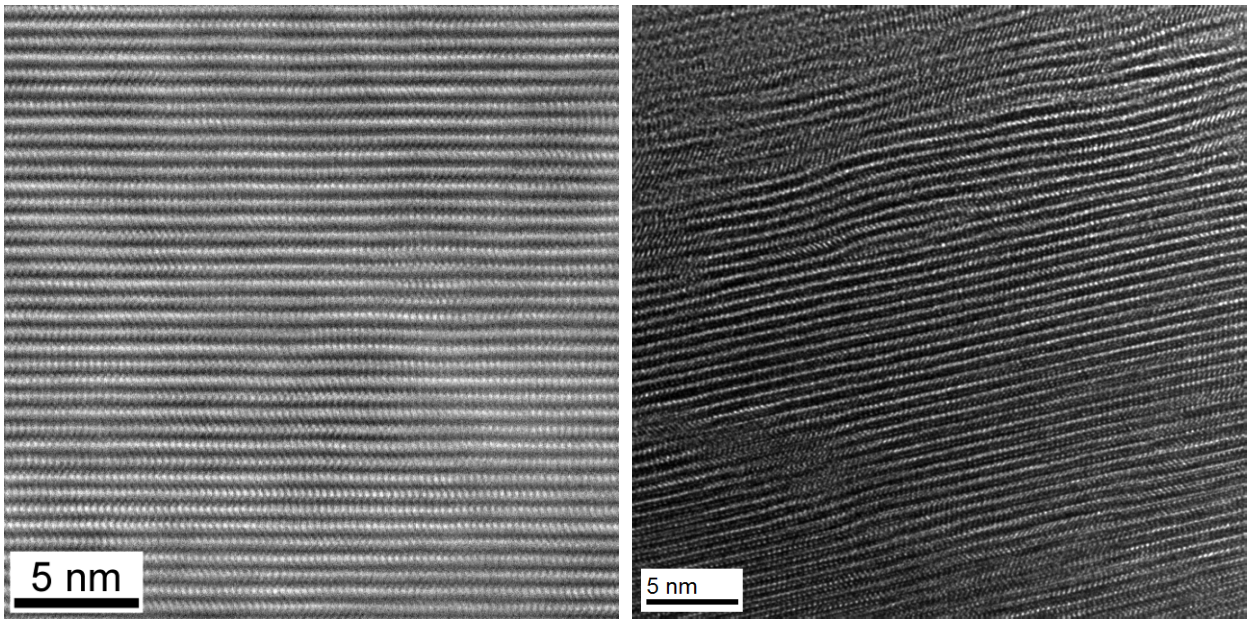

Figure 3.15. Comparison of experimental images of MoS_2 viewed along $[1\bar{2}10]$. (a) HAADF-STEM image, courtesy of Paul Kotula; (b) HRTEM image.

3.6 Dislocations in MoS_2

When dealing with dislocations in hexagonal metals, it is common practice to use the fcc structure as a stepping-off point so that the expected glide plane will be the close-packed one (i.e., the basal plane) and the Burgers vector will be of the type $^1/_3\langle 11\bar{2}0\rangle$ [101]. This is in spite of the fact that complicating factors such as the *c*/*a* ratio, which is neither 1 (as for fcc materials) nor constant for hcp materials and can cause the predominant glide plane to change to $\{1\bar{1}00\}$. In fact, although the presence of a trigonal-prismatic arrangement of sulfur atoms about each metal atom should make things even more convoluted, some reports have even attempted to discuss dislocations in MoS_2 with reference to the fcc structure (e.g., [76]).

The shortest lattice vector in the basal plane is just *a*, or $^1/_3\langle 11\bar{2}0\rangle$, which is the distance between adjacent Mo or S atoms. The next-shortest vector is $\langle 1\bar{1}00\rangle$, although it should be noted that taking these two displacements as Burgers vectors of dislocations, $|\mathbf{b}|^2$ (which is, in theory, proportional to the dislocation energy) is three times greater for the latter (19.97) as compared to the former (6.66).

The growth of twisted or spiral structures about a screw dislocation located at their center was proposed in 1951 by Burton, Cabrera, and Frank [102], and Zhang et al. have applied this thinking to the growth of spiral, pyramidal nanostructure of MoS_2 [103]. This raises the possibility of non-basal dislocations in MoS_2, which is not a common consideration in layered materials. The shortest lattice vector between layers is $^1/_6\langle\bar{2}203\rangle$, although it is more intuitive to think of this vector as the orthogonal components $^1/_3\langle\bar{1}100\rangle + {}^1/_2\langle 0001\rangle$. Although Zhang and coworkers do not explicitly hypothesize a Burgers vector for the screw dislocation that facilitates the growth of the spiral structures they describe, it may be inferred that they probably meant only the $^1/_2\langle 0001\rangle$ component, although for only a few layers it would be difficult to distinguish

$\frac{1}{2}\langle 0001\rangle$ from $\frac{1}{6}\langle \bar{2}203\rangle$. Comparing values of $|\mathbf{b}|^2$ as an approximation for the dislocation energy, $\frac{1}{2}\langle 0001\rangle$ is associated with nearly six times the strain energy of a perfect, $\frac{1}{3}[11\bar{2}0]$-type dislocation; however, the authors do claim to nucleate such dislocations by pushing the CVD system far from equilibrium.

Figure 3.16 introduces a slightly different consideration: a dislocation in WS_2 (which is isostructural with MoS_2) with its Burgers vector in the basal plane, but with a dislocation line with a component out of the basal plane. At the arrow in the image, an extra half-plane of W atoms is clearly visible. In this limiting case, where the number of slabs in the material is one, this is a pure edge dislocation; it is the first of its kind to be experimentally reported.

3.7 Stacking faults in MoS_2

Because MoS_2 is a layered material, and because there exist naturally-occurring phases with both AB- and ABC-type stacking sequences, conventional wisdom dictates that the stacking fault energy in MoS_2 should be quite low. However, in spite of the high interest in MoS_2 at various times over the last four decades, experimental evidence for stacking faults in MoS_2 has not been reported except in the very early days of TEM work on dislocations by Amelinckx and Delavignette [104] and Pashley and Presland [105], or in cases where it had been mechanically worn as a solid lubricant [76, 106]. This is partly because, as discussed in §3.2, so much of the recent interest in MoS_2 has been focused on single layers, which obviously cannot contain stacking faults (of the basal plane).

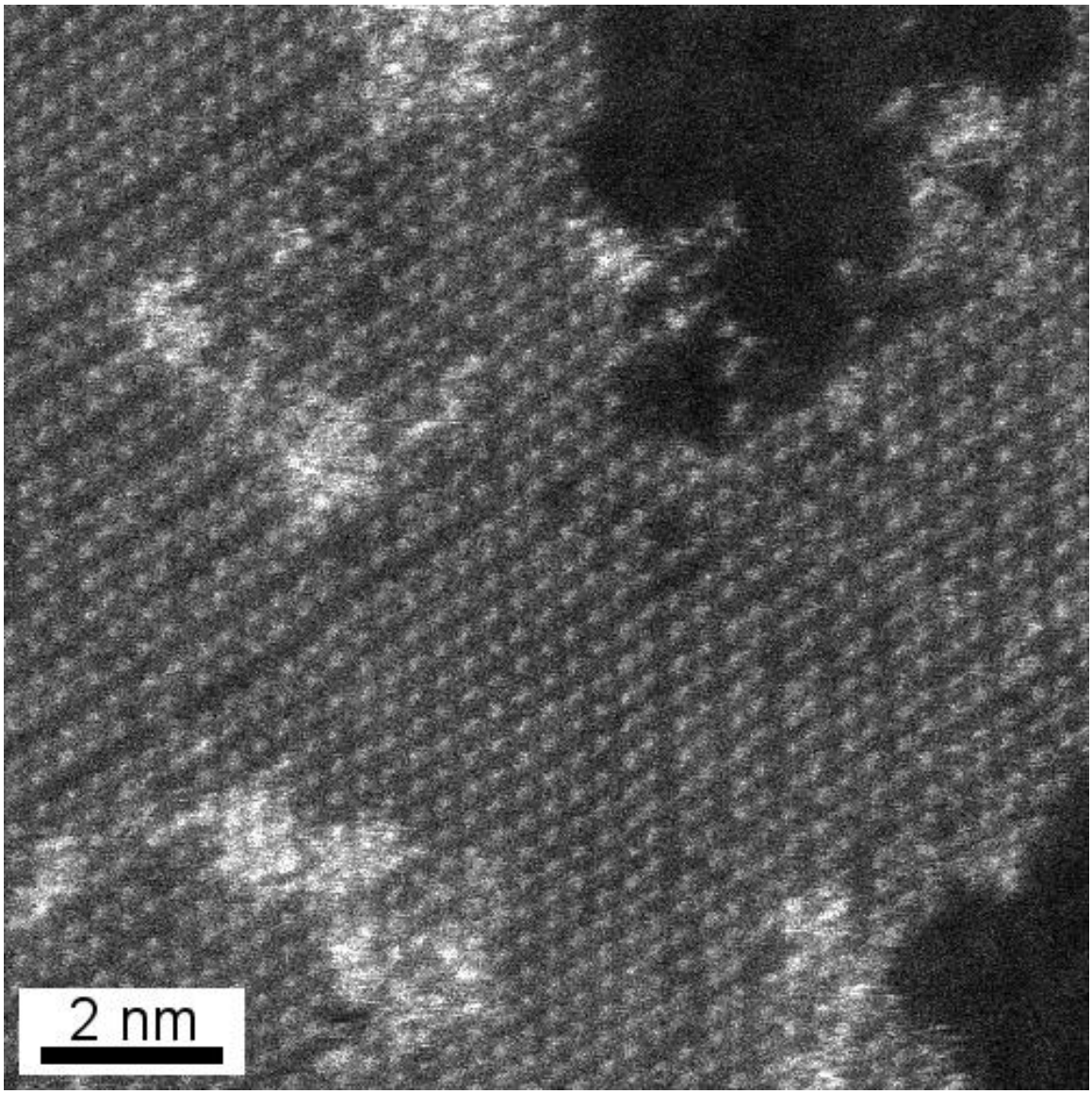

Figure 3.16. HAADF-STEM image of an edge dislocation in WS_2 with its line perpendicular to the basal plane. Image courtesy of Paul Kotula.

3.8 Dislocation dissociation in MoS_2

3.8.1 Background

The classic examples come from hexagonal networks of perfect dislocations that dissociate into a triangular network of partial dislocations. Consider the reaction of three perfect dislocations (see Figure 3.17a):

$$^1/_3[2\bar{1}\bar{1}0] + {}^1/_3[\bar{1}2\bar{1}0] \rightarrow {}^1/_3[11\bar{2}0] \quad (3.1)$$

The perfect dislocations would be expected to dissociate according to the reactions:

$$^1/_3[2\bar{1}\bar{1}0] \rightarrow {}^1/_3[10\bar{1}0] + {}^1/_3[1\bar{1}00] \quad (3.2a)$$

$$^1/_3[\bar{1}2\bar{1}0] \rightarrow {}^1/_3[01\bar{1}0] + {}^1/_3[\bar{1}100] \quad (3.2b)$$

$$^1/_3[11\bar{2}0] \rightarrow {}^1/_3[10\bar{1}0] + {}^1/_3[01\bar{1}0] \quad (3.2c)$$

Which is analogous (but not identical) to the splitting of perfect dislocations into Shockley partials in the fcc structure. This leads to a network of alternating open and closed nodes as the partial dislocations repel one another as shown in Figure 3.17b, with the separation of the partials dictated by the stacking fault energy of the material. In the limiting case of negligible stacking fault energy, the partial dislocations will become perfectly straight and form a triangular network, where the triangles centered on open nodes contain stacking faults (see Figure 3.17c).

Applied to MoS_2, the partials in eq. 3.2a represent positive and negative permutations of the stacking symbol starting from an A site, the partials in eq. 3.2b are analogous starting from a B site, while the partials in eq. 3.2c represent positive and negative permutations *ending* at a C site (so that multiplying both sides by -1 would make it analogous to the first two equations).

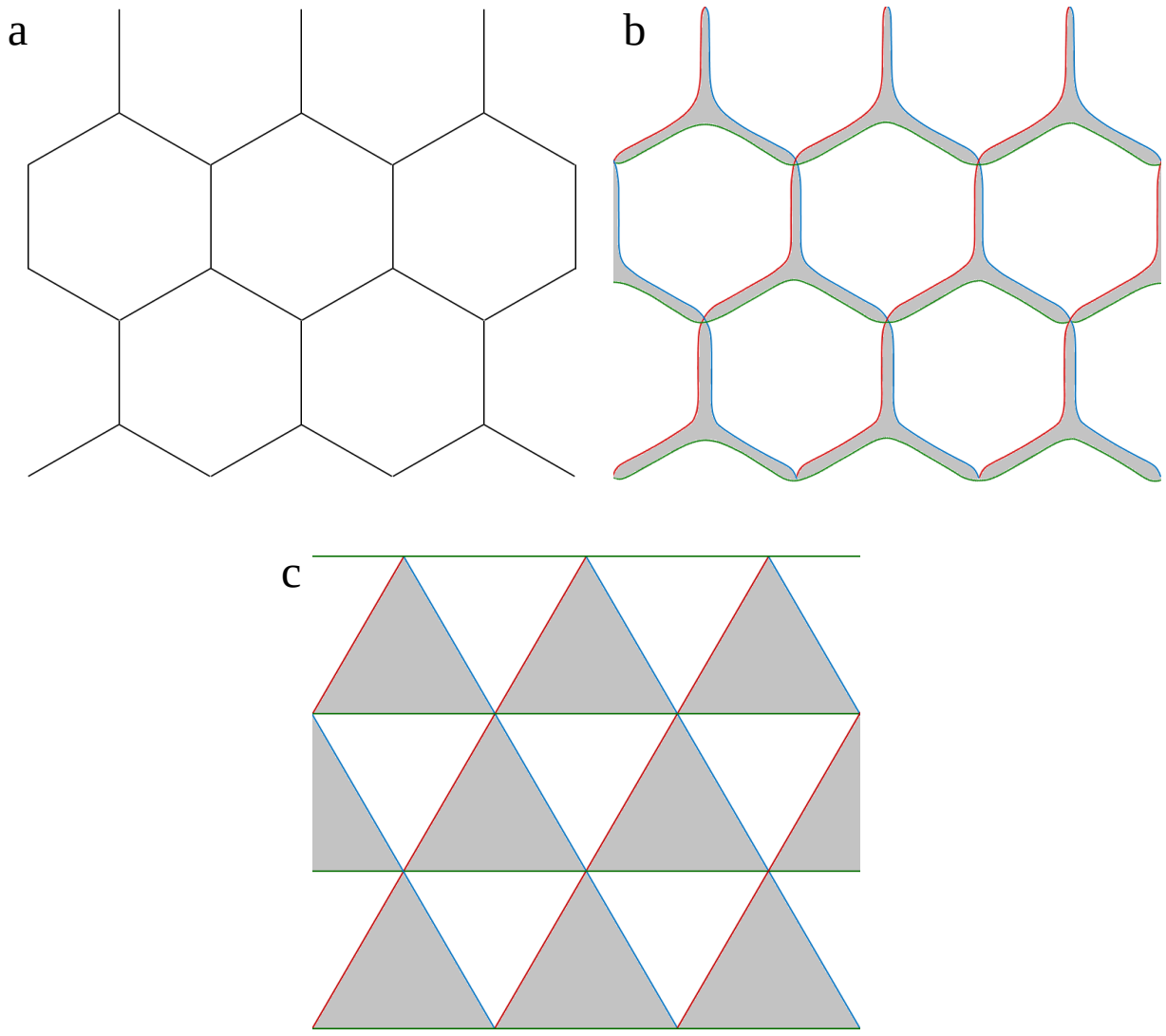

Figure 3.17. Schematic showing the interaction of dislocations in MoS_2. (a) The reaction of three perfect dislocations; (b) the dissociation of the perfect dislocations and subsequent repulsion between the partials; (c) the limiting case of maximum partial dislocation repulsion when the stacking fault energy is negligible. In (b) and (c), the grayed areas indicate stacking faults.

Regarding the contrast in images of these dislocations and stacking faults, a perfect dislocation will be in contrast in any image taken when a $\{11\bar{2}0\}$ reflection is strong, because **g.b** will be either 1 or 2. However, for two of the six $\{10\bar{1}0\}$ reflections **g.b** is zero and, if only these reflections are strong, a perfect dislocation can be put out of contrast.

The opposite is true for the partial dislocations described above; if a $\{10\bar{1}0\}$ reflection is strong then **g.b** is either $^2/_3$ or $\pm^1/_3$ and the partial will be in contrast in the image, and **g.b** is zero for two of the $\{11\bar{2}0\}$ reflections.

An extra consideration in the case of MoS_2 is whether the dislocation occurs on an S-plane or a Mo-plane; since the atomic arrangements within these planes are identical, dislocations with the same Burgers vectors may be expected. However, although the Burgers vectors would be identical, the stacking fault energy associated with the dissociation of such dislocations would be vastly different. This is because Mo-Mo interactions may be expected to be stronger than S-S interactions, and also because each S plane is bounded on one side by the van der Waals gap. Therefore, the strain energy associated with moving an S atom should be considerably less than that of moving a Mo atom.

3.8.2 Dissociated nodes in MoS_2: dark-field imaging using high-index reflections

Traditionally, imaging of dislocations is accomplished by the weak-beam dark-field technique [107-109]. This approach involves setting a particular excitation error ($\mathbf{s_g}$) for a reflection **g**, chosen such that **g·b** is between 0 and 1, so that the strain field of the dislocation bends the planes associated with **g** into the Bragg condition in the immediate vicinity of the core. In the dark-field image, this causes a very small region near the dislocation core to appear bright, while the rest of the image is dark.

The excitation error $\mathbf{s_g}$ represents the separation of the surface of the Ewald sphere, which has a radius of λ^{-1}, from the reciprocal lattice point at **g**. In general, it is desirable to set $|\mathbf{s_g}| \approx 0.2\ \text{nm}^{-1}$, as calculations have shown that this excitation error leads to the narrowest dislocation image [110]. Setting $\mathbf{s_g}$ is achieved by aligning the spot at **g** with one of the Kikuchi lines associated with the **g** systematic row; which line should be used depends on the material, the reflection, and the energy of the electron beam.

To correctly apply the weak-beam dark-field technique, there is another requirement on the diffraction conditions that must be met: **g** must be the only strongly excited reflection, so that other diffracted beams cannot confuse the image contrast via double diffraction. This is commonly known as the two-beam condition; the second beam is the direct beam.

However, it is not possible to set up a two-beam condition using a microscope operating at 300 kV. The curvature of the Ewald sphere is too small (i.e., its surface is quite flat), so that there are always many reciprocal lattice points with a low excitation error. An example of a diffraction pattern from MoS_2 in an orientation that would otherwise be suitable for weak-beam imaging is shown in Figure 3.18. There are at least 30 strongly excited reflections in this pattern. The coupling of two diffracted beams **g** and **h** is related to the difference in their respective excitation errors, $\mathbf{s_g}$-$\mathbf{s_h}$. The closer this quantity is to zero, the more strongly the beams are coupled (see Ch. 27 of [62]).

Weak-beam dark-field imaging is further complicated in intermediate-voltage microscopes because low-index reflections are preferable for the technique so that $\mathbf{g}\cdot\mathbf{b}$ will not exceed 1; this is preferable because the image contrast gets more complicated for $\mathbf{g}\cdot\mathbf{b} > 1$. However, this requires very large tilts in order to reach an appropriate excitation error, again due to the large radius of the Ewald sphere for 300 keV electrons.

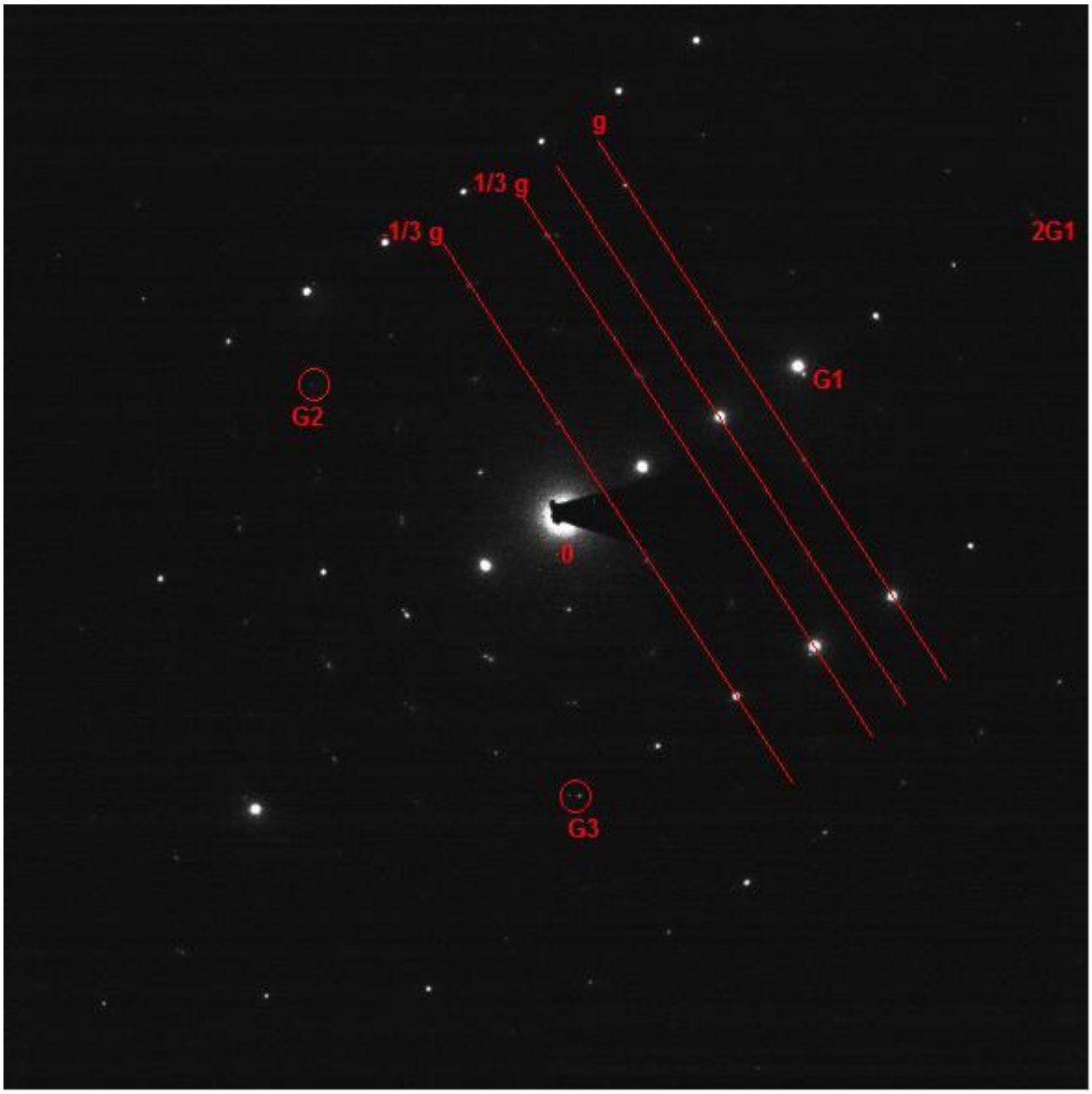

Figure 3.18. Diffraction pattern near the MoS_2 [0001] zone axis demonstrating the large number of excited reflections at an orientation that would otherwise be suitable for weak-beam dark-field imaging. The Kikuchi line labeled ‘g’ was deliberately placed between (2/3)G1 and G1.

In light of these considerations, Figure 3.19 presents three dark-field images of MoS_2 formed in the Tecnai F30 by weakly-excited $\{3\bar{3}00\}$-type reflections. The image in Figure 3.19a was recorded at the diffraction conditions demonstrated in Figure 3.18 after the $(03\bar{3}0)$ reflection, labeled G1, was tilted onto the optic axis using the dark-field beam tilt coils. Figures 3.19 b and c were recorded for similar conditions with the reflections labeled G2 and G3 excited, respectively. G2 is the $(3\bar{3}00)$ reflection, while G3 is the $(\bar{3}030)$. The direction of the reciprocal lattice vector used to form each image is indicated, and corresponding bright-field images are shown in Figures 3.20a-c. Note that the contrast near the dislocations is not uniform across the dark-field images; this is likely due to slight bending of the specimen changing the diffraction conditions locally. A change in orientation of only a fraction of a degree has a significant effect on the position of the Kikuchi lines relative to the diffraction spots, so if s changes across the image then the contrast of the dislocations will as well.

This region of the specimen clearly contains a dislocation network with open and closed nodes. An open node is indicated by the arrow in Figure 3.19a, and Figure 3.19d shows a schematic of the dislocation network with an open node similarly indicated. It is interesting that only one set of partial dislocations is in contrast in each of the three images, when in theory all three sets should be in contrast in all three images because $\mathbf{g}\cdot\mathbf{b}$ cannot equal zero for $\mathbf{g} = \{3\bar{3}00\}$ and $\mathbf{b} = {}^{1}/_{3}\langle 1\bar{1}00\rangle$; the only possible values of this dot product are ±1 and 2. Incidentally, this is why there is no stacking fault contrast between the partials: $\mathbf{g}\cdot\mathbf{b}$ must be non-integral to produce such contrast [105], which is not possible for the reflections chosen to form the images.

Because the Burgers vectors of the dissociated partials is already known, as discussed above, the image contrast in this case can be used to evaluate the viability of using high-index reflections for weak-beam-*like* imaging of dislocations in intermediate-voltage TEMs. In addition to the

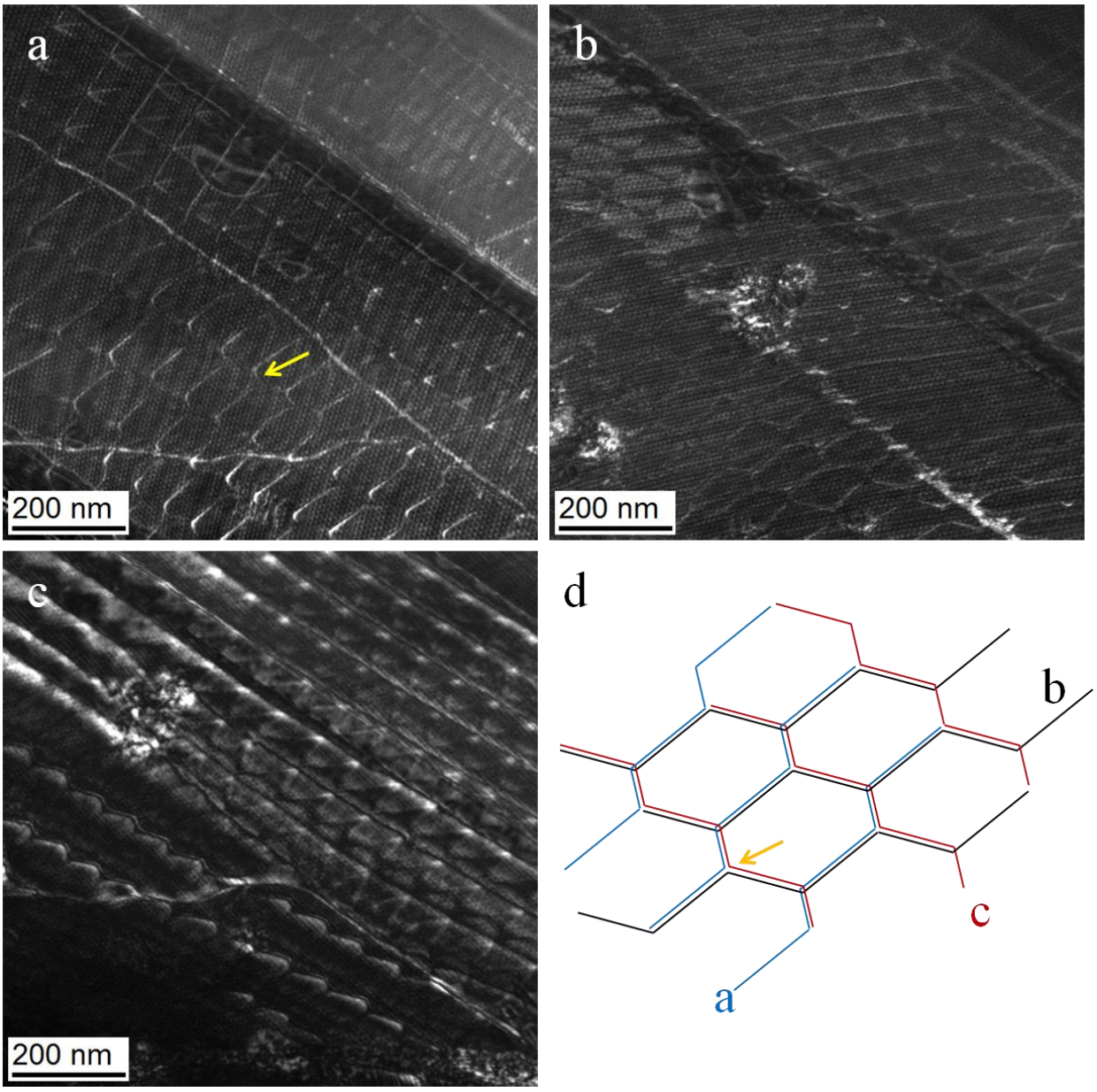

Figure 3.19. Dark-field images formed with three different $\{3\bar{3}00\}$-type reflections. A schematic of the combined dislocation contrast is shown in (d), with an open node indicated as in (a).

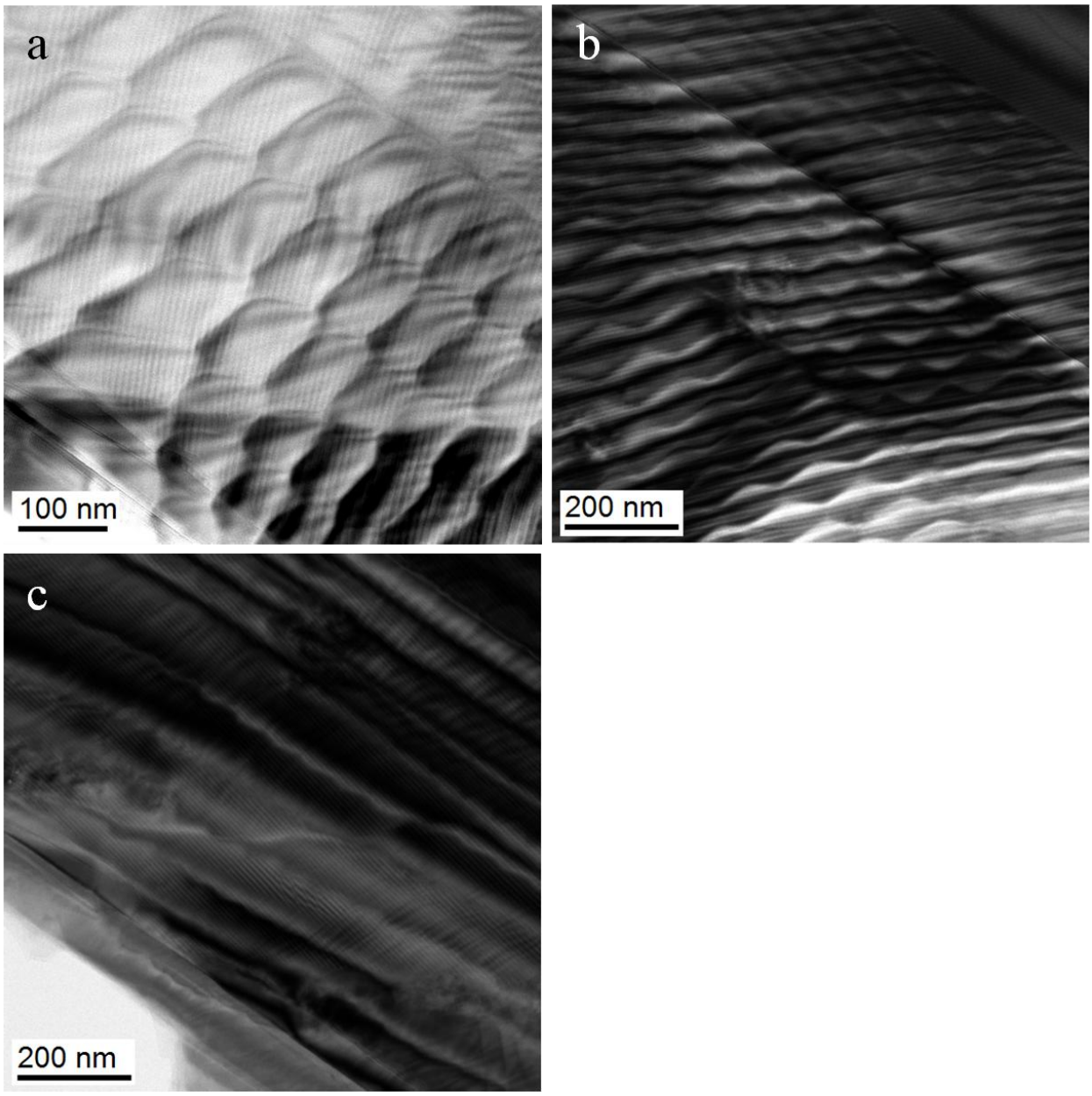

Figure 3.20. Bright-field images corresponding to the dark-field images in Figure 3.19 a-c.

extra complications in image contrast that arise when $\mathbf{g}\cdot\mathbf{b} > 1$ as discussed above, a dark-field technique using high-index reflections was never considered before because the further a beam lies from the optic axis, the more it is affected by spherical aberration. Even though the reflection of interest is tilted onto the optic axis, the associated diffracted beam still interacts with the direct beam, which must be tilted off-axis and is therefore more strongly affected by aberrations. However, objective lenses in modern microscopes have significantly lower spherical aberration coefficients compared to the TEMs of the late 1950s when the weak-beam dark-field technique was developed at Cambridge. Furthermore, in a C_s-corrected microscope any ill effects of using a beam further from the optic axis can be eliminated almost entirely. Finally, intermediate-voltage TEMs were not commonly available when much of the weak-beam work on dislocations was being done. Today, however, 200 kV and 300 kV machines are far more common and so a discussion of how to image dislocations in such TEMs is appropriate. Indeed, there has been some work recently by Phillips, Brandes, Mills and de Graef on how to obtain diffraction contrast dislocation images using STEM [111]; high-resolution phase-contrast images along the dislocation line are a common alternative, though only the edge component of a dislocation may be visualized in this way. It has been proposed that high-resolution images of screw dislocations viewed end-on can provide indirect information about the dislocation core by a lattice rotation [112] induced by an Eshelby twist [113]. However, this requires exceedingly thin specimens and the relaxed structure of a dislocation core in such a specimen will not represent its structure in the bulk material. The topic of imaging dislocations in intermediate-voltage TEMs will be discussed further in Chapter 7.

3.9 MoS_2 in batteries

3.9.1 The history of intercalation of TMDCs

The intercalation of graphite predates the intercalation of TMDCs by nearly 50 years; research on the latter began in the early 1970s (e.g., [11, 114-116]), first with the insertion of organic molecules [117] and then metals- often alkali metals attached to organic molecules as in [11]. By then it was known that the large variation in electrical properties of the TMDCs was related to the subtle variations in their layered structures, and that by manipulating the layers with intercalant species, the electronic properties could thus be precisely tailored [11]. Indeed, the ability of guest species within the van der Waals gap to modify the d-band structure of TMDCs was noted by Wilson and coworkers [116]. At that time there was a particular interest in inducing and enhancing superconducting properties in some of the layered TMDCs, including MoS_2 [114]. In fact, MoS_2 crystals intercalated to an alkali:Mo molar ratio of 0.3-0.4:1 by Li, Na, K, Rb, and Cs are all superconducting, with critical temperatures ranging from 3.7 K to 6.3 K [114]. $NbSe_2$ was investigated with particular vigor [11, 115], because it has the highest superconducting transition temperature in its pure form of the naturally-superconducting TMDCs [115].

Then, in 1976, Whittingham published an article in *Science* [118] proposing TiS_2 as "one of a new generation of solid cathode materials." This was on the basis of its intercalation reaction with lithium. Shortly afterward, in the early 80s, a commercial rechargeable MoS_2-Li metal battery was produced for a short time by the company Moli Energy [9]. Predictably for a cell with a Li-metal electrode, these batteries were prone to Li dendrite formation, which limited their useful lifetime and posed a serious safety risk [9]. With complex oxides like YBCO coming to dominate superconductivity research and the commercialization of the dominant graphite-

$LiCoO_2$ lithium battery by Sony in the 90s, research on the intercalation of TMDCs waned for many years. However, the recent explosion of interest in 2-dimensional materials, along with an increasing ability to develop complex nanocomposite materials, has brought the layered TMDCs and their intercalation complexes back to the forefront of materials research.

3.9.2 Electrochemical characteristics of MoS_2

MoS_2 has a voltage of 2.0 V vs. Li/Li^+, assuming it is not lithiated to the point that Li_2S begins to form [9]. For an anodic potential this is rather high; in a full cell vs. $LiCoO_2$, for example, the cell voltage would be only ~1.5 V (since $LiCoO_2$ has a voltage of ~3.5 V vs. Li/Li^+ [4]). This would put such a cell on the borderline between low and medium energy quality; an electrochemical cell provides high energy quality if the cell voltage exceeds 3.5 V [1]. As a nanocomposite with graphene, MoS_2 anodes have demonstrated capacities as high as 1290 mAh/g [119]. In some circumstances, MoS2 anodes have been demonstrated to retain a capacity of 554 mAh/g after 20 cycles at a rate of 50C (i.e., full discharge in only 72 seconds) [120].

In comparison, the capacity for graphite anodes is traditionally cited as 372 mAh/g [121], although the capacity of carbonaceous anodes has been pushed beyond this by modifying the microstructure [122]. The voltage of graphite vs. Li/Li^+ is 0.2 V and so cells using graphitic anodes can more easily provide high energy quality; this is part of graphite's desirability as a commercial electrode in addition to its low cost and structural stability during cycling.

4 Intercalation of MoS_2

This chapter summarizes work on the in-situ TEM lithiation of MoS_2. Three main publications exist so far: two from other researchers with the MoS_2 in the plan-view orientation, and one resulting from this work with the material edge-on.

4.1 Modern literature on the lithiation of MoS_2

There have already been some results published on the lithiation of MoS_2 in the plan-view orientation (i.e., with the beam normal to the basal planes) [59, 123].

From a scientific point of view, the overall quality of the papers that have been published so far on the lithiation of MoS_2 in the plan-view orientation derives from the novelty of the experiment rather than the insight of the conclusions drawn. In fact, many important questions still remain unanswered. For example, during the in-situ experiment bands of dark contrast can be observed forming in the bright-field image, as shown in Figure 4.1. This is our data, and it is consistent with that of, e.g., [123]. However, no explanation for what might give rise to this contrast is presented in [123] because no mention is made of them at all. This is in spite of the fact that MoS_2 is known to take up lithium by two different mechanisms, one of which implies the precipitation of Mo which could, in theory, explain the dark bands in the images of lithiated MoS_2.

Both of these papers attribute the "wavy" surface of the reaction front to "[…] a sliding motion of slabs with respect to one another, changing of sites of the Mo atoms associated with Fermi surface nesting, and the John-Teller [sic] effect" [59, 123].

Regarding this analysis, the first suggestion explaining the wavy appearance of the reaction front is the S-Mo-S slabs sliding with respect to one another. However, no analysis on a possible

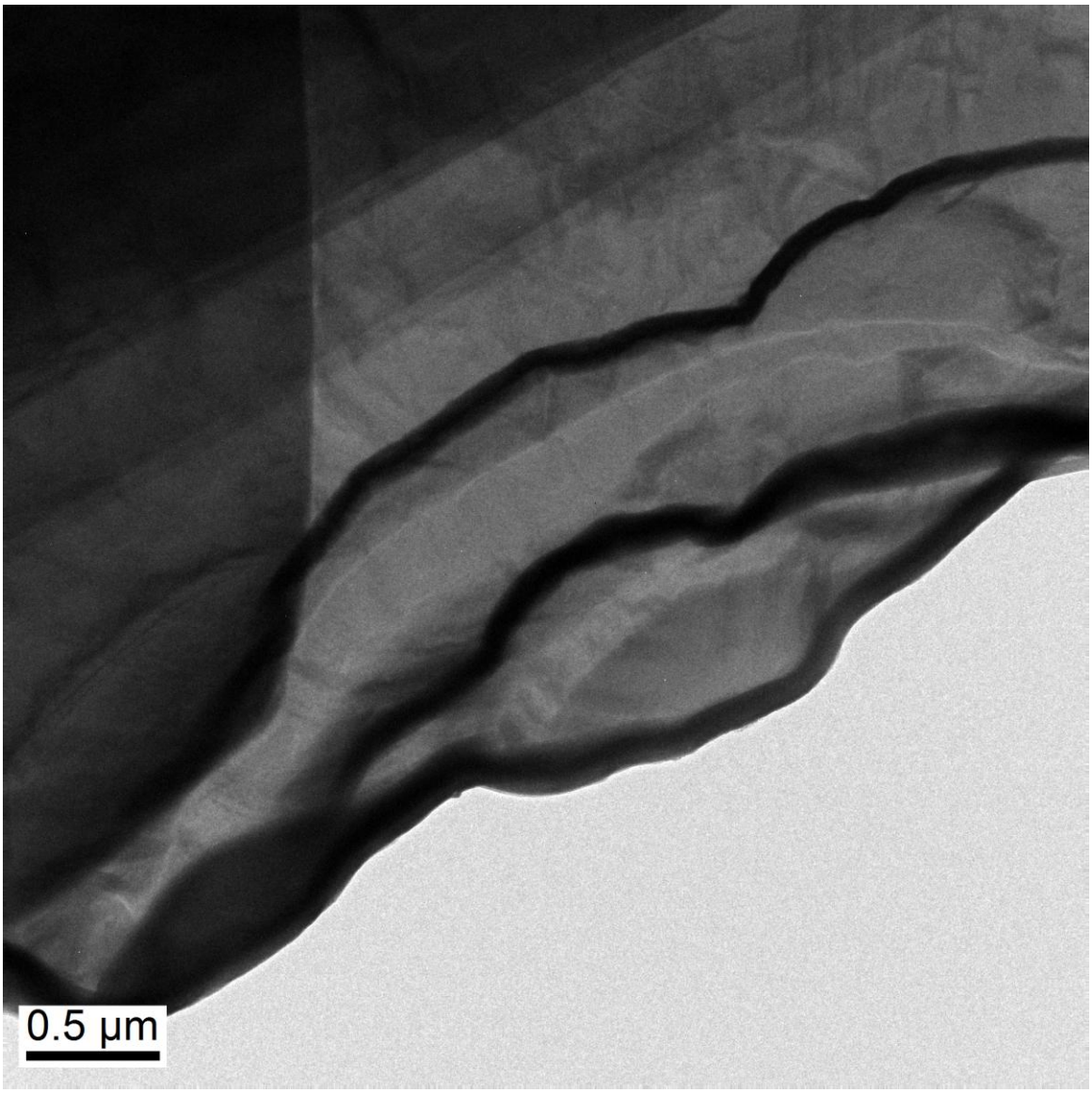

Figure 4.1. Bands of dark contrast appear during the lithiation of MoS_2 in the plan-view orientation.

origin of a shear force, its magnitude, or how the resulting shear might affect the image contrast is presented. Second is the suggestion that the Mo atoms are changing sites, which is in fact a very interesting proposition that is discussed in great detail in §4.7; however once again there is no thought given to how the motion of Mo atoms might affect the image contrast. This is made abundantly clear by the proposed mechanism for the motion of the Mo atoms, i.e., Fermi surface nesting *and* the Jahn-Teller effect. Not only are the results of a Jahn-Teller distortion likely to be undetectable in a low-magnification bright-field image (although HRTEM and electron diffraction are certainly sensitive to such a distortion), but the structural distortions associated with Fermi surface nesting (usually called the Peierls distortion for 1D crystals or discussed in relation to charge density waves in 2D) are not the same as those associated with the Jahn-Teller effect.

While both kinds of distortion describe a reduction in symmetry that removes a degeneracy of the ground state of a system in such a way that the total energy is lowered, in the case of a Jahn-Teller distortion the splitting of energy levels does not necessarily occur at the Fermi level and so the splitting, if large enough, will move the Fermi level. In other words, the exact position of the Fermi level does not determine whether or how the distortion will occur [81].

In the case of a Peierls distortion, the energy levels are split by the strong scattering (splitting of energy) of electrons with momentum $\pm\mathbf{k_F}$, which implies that the energy splitting does occur at the fermi level, and is caused by large regions of the Fermi surface that are parallel and separated by the wave vector $2\mathbf{k_F}$ (this is what is referred to as Fermi surface nesting) [81]. A serious foray into energy band theory is far beyond the scope of this thesis and so the monumentally simplified and heuristic explanation that, because the "F" subscript denotes a particular relationship to the

Fermi energy the form of this latter distortion does depend strongly on the Fermi level (or by extension, the Fermi surface) will have to suffice.

Neither [123] nor [59] present or reference any calculations of the Fermi surface of MoS_2, from which it follows that there is no discussion of how the introduction of Li might change the Fermi surface and introduce nested regions to it, let alone comparisons to the Fermi surfaces of TMDCs with different d shell occupancies and whether these might naturally have nested regions.

4.2 The challenge of MoS_2

Transition metal dichalcogenides (TMDCs), such as MoS_2, are layered materials that can store Li by the intercalation mechanism [94, 124]. While the original work on this subject dates back to the 1970s [11, 125-128], TMDCs and their composites (especially using carbon) are once again being examined for battery applications because of their high capacities and, especially, their excellent rate capabilities [9].

The 2H (hexagonal) phase of MoS_2 is the equilibrium structure at standard conditions [129]. After chemical exfoliation the orthorhombic 1T phase is commonly observed [130-132], which has several supercell variations due to Mo clustering [99], as discussed in Chapter 3.

Traditionally, experiments involving the intercalation of layer materials (*in situ* or *ex situ*) are conducted such that the electron beam is perpendicular to the layers because this orientation makes specimen preparation simpler (see, e.g., [11]). In this case, however, a novel experimental geometry was achieved by using the FIB, so that the electron beam was parallel to the basal planes. A large piece of natural MoS_2 was placed on an SEM stub with the (0001) planes parallel to the stub surface, so that the lamella cut with the FIB had the (0001) planes parallel to the

surface normal. The lamella was affixed to a copper Omniprobe half-grid and loaded into the immobile end of the STM-TEM holder as described in §2.4.

The key results from this work were:

i) The successful in-situ lithiation of a layered material in a geometry that had never been reported before.

ii) During the lithiation process, planar defects ("platelets") appeared in the lamella that can step from basal plane to basal plane. The angle that the step makes with the basal planes is consistent with the angle of the relrods visible in the diffraction pattern; see §4.5 below.

During the lithiation of MoS_2 in the plan-view geometry, dark bands (in bright-field TEM images) were observed to form in the material as the reaction proceeded, as shown in Figure 4.1. These bands have not been satisfactorily explained in the literature; it is hypothesized that this may be mass contrast from the precipitation of Mo, if the MoS_2 is being reduced by the Li to form Li_2S, and furthermore that the platelets observed in the edge-on geometry may be related to this expulsion of Mo.

4.3 Detailed study of Li intercalation in MoS_2

Using a solid-state cell in the Nanofactory holder, the lithiation of MoS_2 in both the plan-view and edge-on geometries described above will be repeated using high-angle annular dark-field (HAADF, or Z-contrast) STEM imaging. This is to test the hypothesis that Mo is being reduced by the Li and forms precipitates.

Immediately following the lithiation of the specimens in the edge-on geometry, the specimens will be transferred to a double-tilt holder and analyzed in TEM mode. This will allow a full crystallographic analysis of the steps in the planar defects described above.

4.4 Lithiation of MoS_2 in the edge-on orientation

Although data on the in-situ lithiation of MoS_2 with the layers perpendicular to the electron beam was collected before any papers on this subject were published, the first paper [123] came out while the data was being analyzed and so a different approach was necessary. The research presented in the next section was conceived from the idea of watching the basal planes of a layered material expand and contract, at atomic resolution, as lithium was inserted and removed. Unfortunately, this was impossible to achieve as even the recording of high-resolution images before the experiment began resulted in obvious damage to the specimen, as shown in the indicated areas of Figure 4.2.

However, even though it was necessary to carry out the experiment at low magnification, surprising results were obtained and, as a paper should do, as many new questions were raised as old questions were answered. These results and new questions are presented in the following section.

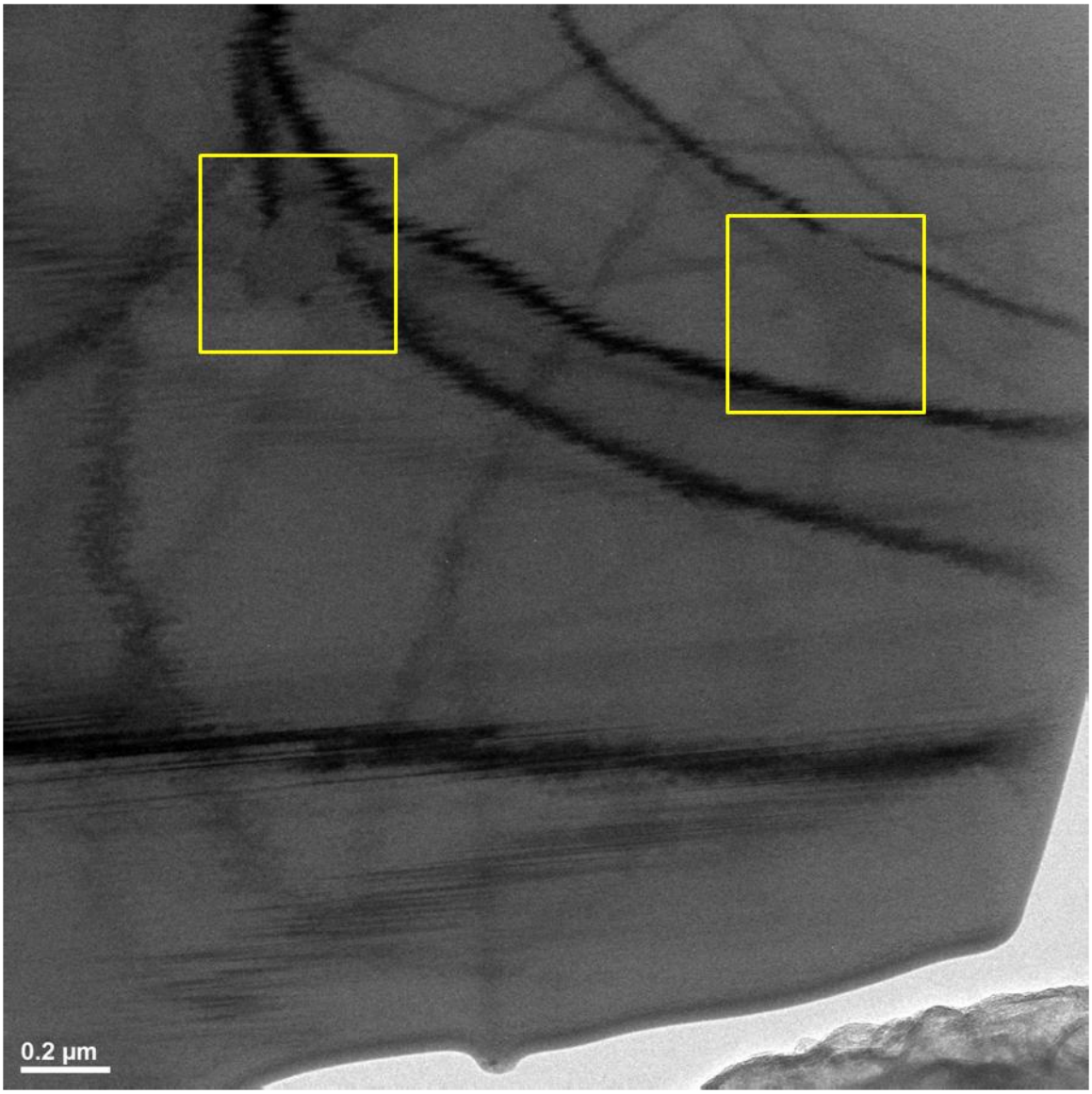

Figure 4.2. Bright-field TEM image of the MoS_2 lamella before the lithiation experiment. The indicated regions were damaged by the beam while recording high-resolution images.

4.5 In-Situ TEM Observations of the Lithiation of Molybdenum Disulfide

Janish MT, Carter CB, Scripta Mater 107 (2015) 22-25 [133]

Research into new materials for energy storage is at an exciting stage with both new materials and well-known materials showing new physical phenomena [134-138]. Layered materials such as the transition metal dichalcogenides (TMDCs) are attracting renewed interest for battery applications [139] as a special example of insertion electrode materials that can take advantage of the intercalation mechanism [94, 124]. Work on the intercalation of alkali metals in TMDCs began in the 1970s [11, 125-128], during which time many fundamental observations were made. For example, it was shown that the sodiated phase of $NbSe_2$ is orthorhombic with Na atoms occupying the octahedral sites in the van der Waals gap [11], and that the general stoichiometry of a fully-lithiated MX_2 compound (where M is a transition metal, usually in group 4B or 5B, and X is S, Se, or Te) is $LiMX_2$ except in the case of VSe_2, which formed Li_2VSe_2 [126].

Although bulk molybdenum disulfide (MoS_2) can exist with different structures the 2H (hexagonal) phase is the most stable and is the predominant phase that occurs in nature [129]. The orthorhombic 1T structure is commonly observed after exfoliation, which is achieved by lithiating the MoS_2 and reacting the lithiated material with water [130-132]. Transition metal clustering in this phase can lead to 2x1 (1T'), 2x2 (1T'') and other supercell variations [99]. However, if these materials are to be used commercially in batteries it is likely that they will be in the form of sheets that are rather thicker than those formed by the exfoliation process. The present study addresses the lithiation of such practical materials

While considerable understanding of these materials can be achieved by examining specimens after lithiation or after delithiation (i.e., ex-situ), observing the same specimens before, during and after lithiation has obvious advantages. In-situ TEM is the only technique that allows

specific sites on the specimen to be monitored in this way with atomic resolution. The usual geometry used for such studies is to examine the layer materials with the beam normal to the layers since this orientation greatly simplifies specimen preparation (see, e.g., [11]). In the present report, a novel experimental geometry was used such that the electron beam was parallel to the (0001) planes. This geometry allowed direct observation of the Li intercalation process, in-situ in the TEM. Lamellae of single crystal MoS_2 have been examined in this way; this approach can easily be extended to other layer materials, and to special orientations or materials that do not cleave readily along a particular plane.

The MoS_2 lamella described here was prepared using an FEI Strata 400S dual-beam focused ion beam (FIB) instrument. Bulk, natural MoS_2 was oriented with the basal planes parallel to the sample holder surface, so that the lamella had the basal planes parallel to its surface normal. The lamella was lifted out in-situ and placed on a Cu Omniprobe TEM half-grid. TEM analysis was carried out using an FEI Tecnai F30 instrument operating at 300 kV.

The holder used for the TEM experiment was a Nanofactory Instruments scanning-tunneling-microscopy (STM) model, which was originally intended to correlate TEM images with local density of states measurements. To this end, the TEM-STM holder accepts two inputs. The end nearest to the tip of the holder is fixed, and fits a piece of 0.013 inch-diameter wire (w), which was Al for this experiment; the Cu FIB grid with the MoS_2 lamella was affixed to the Al wire with a conductive Ag epoxy. The end closest to the base of the holder is ball-shaped, and fits into the socket of a so-called “top-hat” that holds the second electrode, typically mounted on a 0.01 inch-diameter tungsten wire. This end is equipped with both mechanically- and piezo-driven motors for coarse and fine motion control in three dimensions (to nanometer precision) within the TEM. Li metal, which acted as the counter-electrode, was scraped onto the tip of the W wire

and loaded into the holder in a He-filled glove box. During transfer from the glove box to the microscope, the Li metal was partially oxidized, and the Li_2O layer subsequently acts as the solid electrolyte.

Contact was made between the Li source and the MoS_2 lamella and a potential of -2.5 V was applied across the holder for 350 s; video was recorded throughout. The electrodes were then disconnected to allow for the acquisition of images and diffraction patterns, then reconnected and the -2.5 V potential reapplied while video was recorded. More images and diffraction data were collected after the electrodes were disconnected again.

Figure 4.3 shows frames of the video of the lamella at different stages of the experiment. In Figure 4.3a the MoS_2 is shown just before contact is made with the Li source, which is visible at the lower-right corner of the image; Figure 4.3 b-d shows the progression of lithiation 26 s, 78 s, and 171 s after the -2.5 V potential was applied, respectively. The most striking feature of the lithiated material is the group of straight lines of lighter contrast running horizontally across the specimen. The first such line to appear is arrowed in Figure 1b. The extension of the lines increased from right to left during observation; Additional lines then appeared with the appearance of the lines proceeding sequentially from the bottom of the lamella, nearest to the Li source, to the top. Although the lines appear to be perfectly straight, they were actually observed to step abruptly from one basal plane to a parallel one. The stepping direction could be either up or down.

The low-magnification images shown in Figure 4.4 are bright-field images of the MoS_2 recorded before and after lithiation and clearly show the increase in size that this block of MoS_2 experiences.

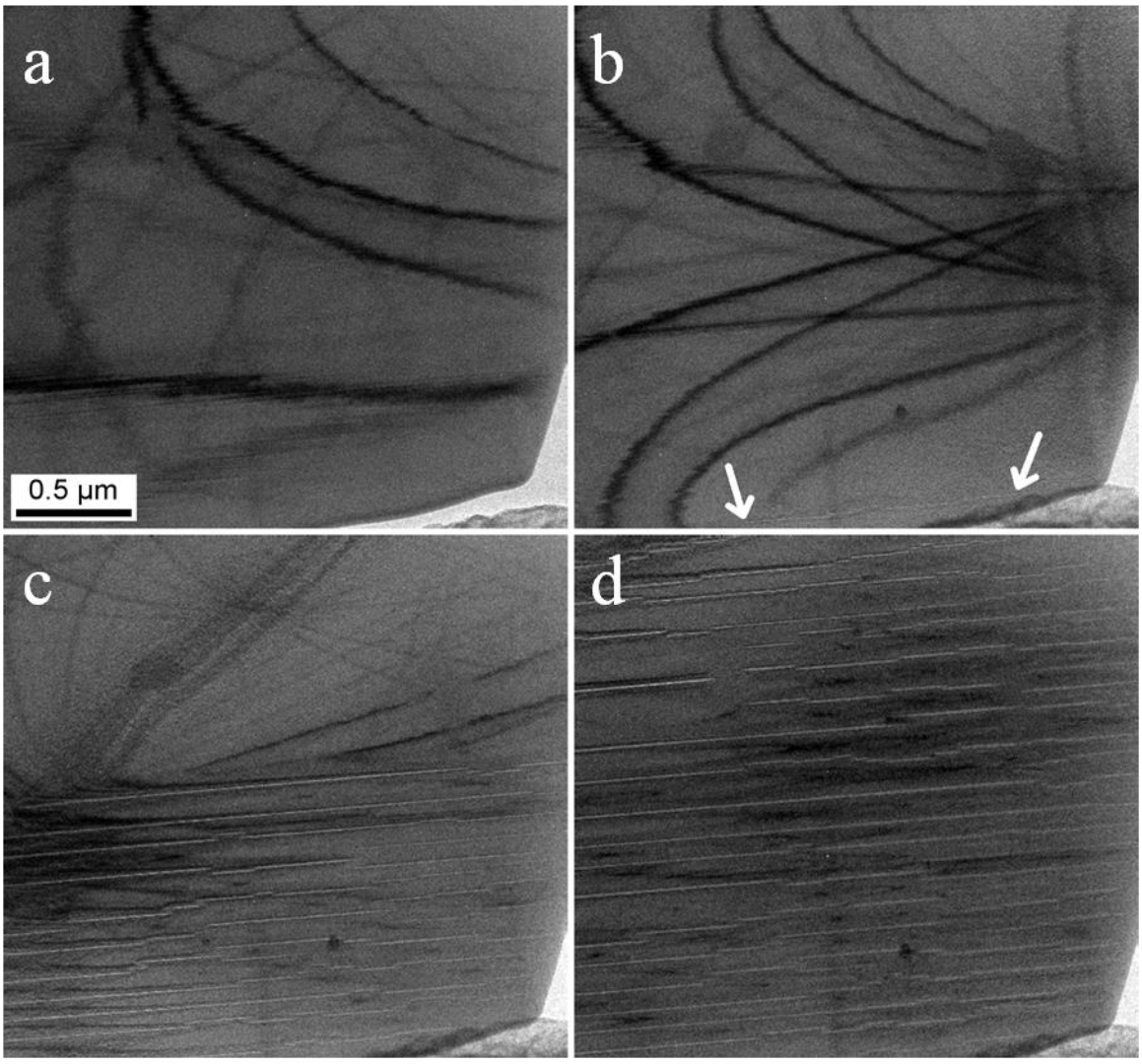

Figure 4.3. Frames from the video recorded during the lithiation experiment; the Li source is visible in the lower right corner. (a) before contact is made between the Li source and the MoS_2 lamella; (b) 26s after the potential of -2.5 V was applied; (c) 78 s after the potential was applied; and (d) 171 s after the potential was applied.

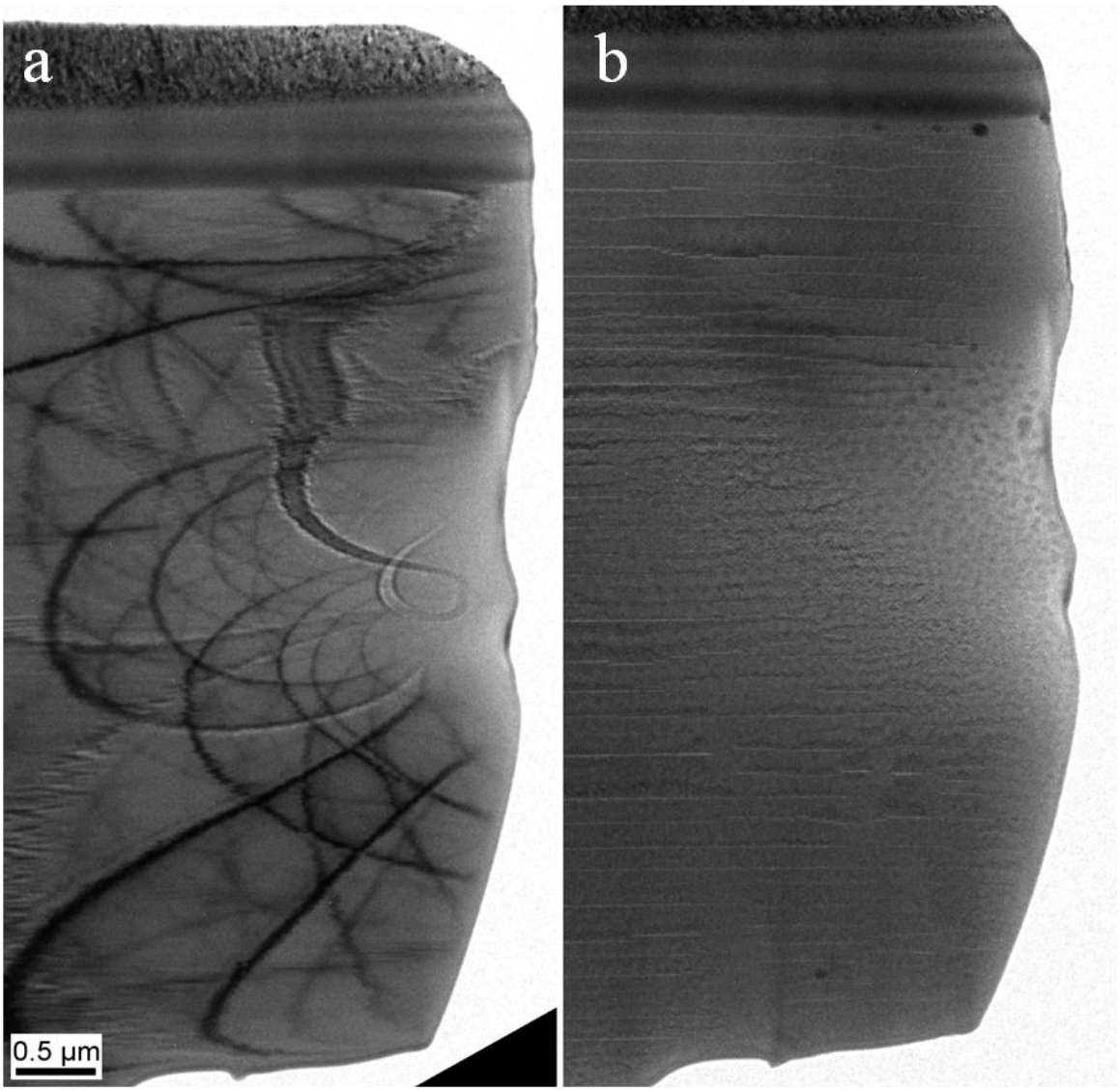

Figure 4.4. Low-magnification bright-field TEM images of the MoS_2 FIB lamella (a) before and (b) after lithiation, showing the location of the light bands (the platelets) and the expansion of this specimen of MoS_2 normal to the *c* planes.

Figure 4.5 shows high-magnification images of the MoS_2 before and after lithiation, each with the corresponding diffraction pattern. The average spacing of the (0002) planes in Figure 3a is 0.61 nm, which gives c = 1.22 nm; this value is in good agreement with the literature value of 1.2295 nm [78]. The FIB processing has clearly damaged this thin area of the specimen but it has not changed the spacing of the basal planes. The lighter lines in Figures 1-3 are actually typically 3-4 fringes thick.

Although the intuitive assumption when examining Figure 4.5b is that the lighter lines correspond to lithiated material (because they are lighter) and so should have a wider spacing, in fact the average spacing of the fringes inside these bands of lighter lines corresponds to c = 1.14 nm while the average spacing of the fringes in the rest of the image corresponds to c = 1.28 nm. The latter represents a 4.9% expansion in the [0001] direction relative to the initial spacing of the MoS_2 planes. These bands are thus proposed to be platelets of Mo-poor material (referring to them as platelets to distinguish them from the MoS_2 lamella that is the TEM specimen; not 'sheets' because the thickness is important).

Figure 4.5b also features one of the previously mentioned steps in the platelets. The planes are visibly distorted between the tips of the two lines in the center of the image, and the tips appear to be complementary in shape, i.e., they are related by a 180° rotation normal to the image. All of these features terminate (i.e., change planes) in the same way. After stepping across 12 or more planes, the platelet continues with the same width suggesting that it is, indeed, a continuous defect, as expected from the in-situ observation.

The streak along the (0002) systematic row in the diffraction pattern in Figure 4.5d is due to these platelets. It appears as a streak rather than a series of very closely spaced spots because of the relatively large distance between the platelets, and because they are not quite evenly spaced.

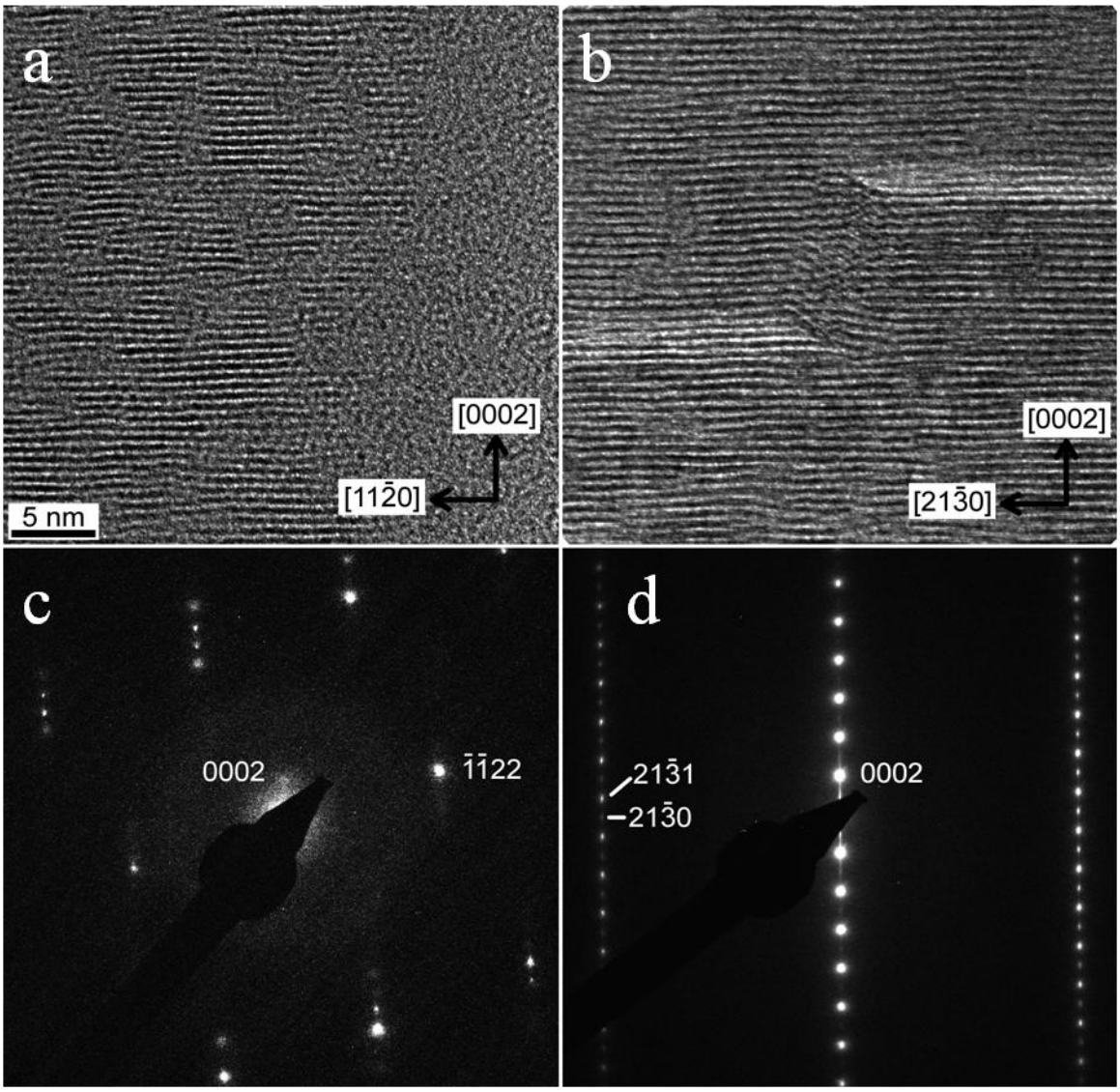

Figure 4.5. High-magnification TEM images of the MoS_2 lamella (a) before and (b) after lithiation, with the corresponding selected-area diffraction patterns in (c) and (d). Damage caused by the FIB can be seen in 'a' but the basal plane spacing is not altered.

Because the in-situ holder is only equipped with single-tilt capabilities, and in fact the nature of the in-situ experiment precludes tilting without significant risk to the specimen, extensive analysis using dark-field imaging could not be performed. However, initial dark-field imaging did confirm that there is no localized strain field associated with the platelet.

The initial lithiation of MoS_2 is proposed to involve a transformation from trigonal prismatic coordination of Mo by S to octahedral coordination [140]. The geometry used in the present study is not able to detect this transformation directly since the electron beam is parallel to the basal planes; the $LiMoS_2$ is proposed to have the 1T structure (rather than the 2H structure of the original MoS_2) [140]. However, the spacing of the basal-plane fringes in Figure 4.5b is particularly interesting. It is well-known that upon sufficient lithium insertion (after the initial structural changes within the basal planes), the Li begins to react with MoS_2 to form Li_2S according to

$$4Li + MoS_2 \rightarrow Mo + 2Li_2S$$

There does not appear to be any documentation of how this reaction proceeds or what happens to the Mo after the reaction occurs. The observations from the present study suggest that the observed contraction in the basal planes within the platelets is related to planar defects caused by the expulsion of Mo at the beginning of this reaction. The important observation is that the material remains crystalline even as the Mo is expelled. It is possible that the contraction is simply related to the occupancy of the Li atoms and the degree of lithiation in the platelets; DFT calculations have predicted *c* values ranging from 1.1999 nm to 1.42262 nm for partially lithiated material [82]. Ultimately the Mo does apparently form a separate phase in the in-situ experiment as will be reported elsewhere. A recent study found that the *c* lattice parameter increased by ~0.8 Å, ~6.5%, after chemical lithiation [141] which is larger than the result obtained from the

analysis of Figure 4.5b but actually quite close to the total expansion of the lamella in the vertical direction in Figure 4.4.

In discussing the expansion of TMDCs it is noted that an error in reporting the magnitude of the expansion in the *c* direction has developed over the years. For example, Li et al. [141] mention an expansion of 0.025 nm in their introduction, citing a 1994 paper on the diffusion of Li in MoS_2 [142]. However, Santa-Ana et al. obtained this value from a 1987 review paper by Friend and Yoffe [143]; in this and many other older papers on the subject of intercalation of TMDCs, the style was to report *c* as a multiple of the individual layer thickness. For example, *c* for MoS_2 is reported as 2 x 0.615 nm rather than 1.23 nm [143]. Therefore the cited 0.025 nm expansion is actually from 0.615 nm to 0.640 nm (~4.1%), while the two more recent papers might give the misleading impression that the expansion is only ~2%, from 1.2295 nm to 1.2545 nm.

Figure 4.6 superimposes a drawing on the image of the defect stepping to clarify this special feature of Figure 4.5b. The basal-oriented platelets have been outlined by blue lines that are 4 basal planes wide; these two boxes are themselves connected by a set of green lines to suggest how the blue boxes are connected. The inset schematic then summarizes how the platelet steps between two basal segments. The platelet changes orientation from one basal plane onto an inclined plane and then back onto a parallel basal plane so that it is inclined to the electron beam where the step occurs. The inclined segment of the platelet could not be imaged directly (and hence the distortion, although visible, cannot be directly interpreted) since the Nanofactory holder used for the experiment is single-tilt, but it is interesting to note that the green box is not perpendicular to the basal plane. In fact it is never so aligned between any of the basal-oriented platelets, but always appears similar to the orientation outlined schematically in Figure 4.6, even if this involves stepping in the opposite direction of the Li motion as the defect propagates. The

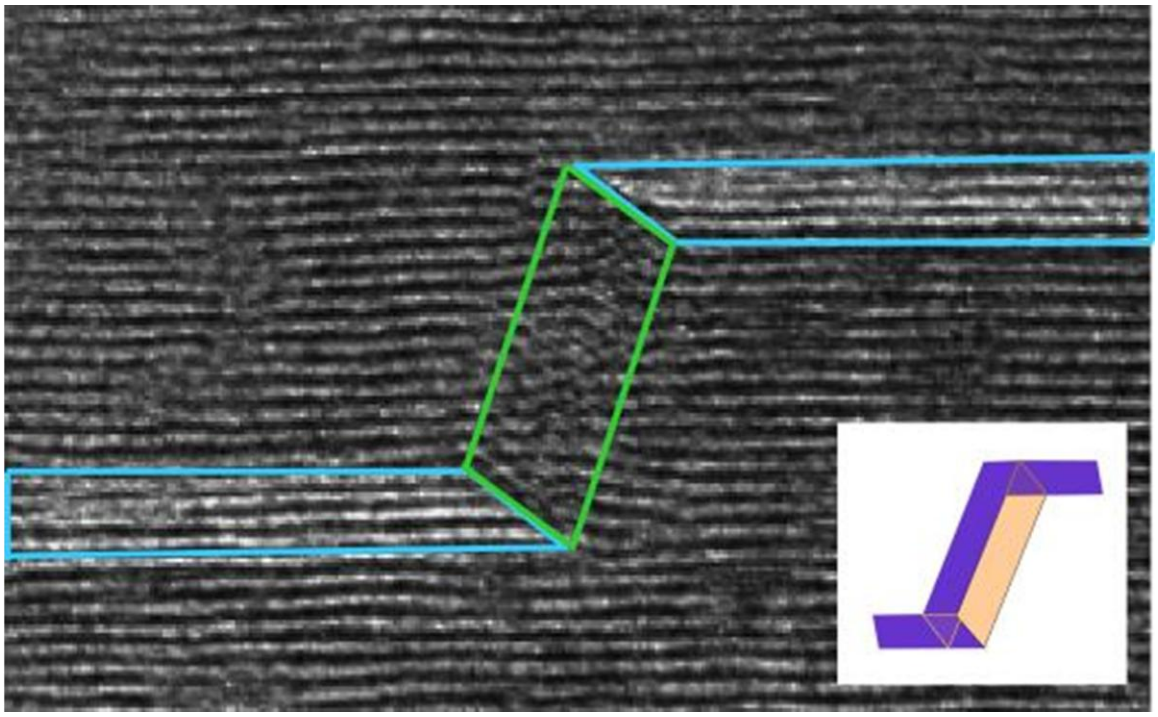

Figure 4.6. Schematic illustration of the features in Fig. 4.5.3b. The blue boxes outline two edge-on blocks of ~4 basal planes that are connected by another block in green that is inclined to the electron beam and to the c-axis of the MoS_2.

inclined platelet must therefore be faceting onto a pyramidal plane rather than a prismatic plane. Indeed, close examination of the (0002) and (000$\bar{2}$) spots in Figure 3d reveals “relrods” (which refers to the distortion of the points in the reciprocal lattice due to the non-infinite dimensions of specimen features) protruding very slightly from the spots. While these features are small enough as to make measurements on them difficult, they suggest a characteristic angle for the steps between platelets in the range of 36° - 48°, which is consistent with the 38° angle between the bottom basal segment of the platelet and the step between the basal segments in Figures 4.5b and 4.6.

The lithiation of MoS_2 involves an expansion of the MoS_2 layers as the Li intercalates along the basal plane. In the early stages, the lithiation process involves an expansion of the basal planes as has been observed in this study and a subsequent macroscopic expansion normal to these planes. This process is facilitated by the formation of blocks of material (referred to as platelets in this report) that lie primarily on the basal plane but can step from one plane to a parallel one and have a smaller plane spacing. These platelets are interpreted as being the first stages of the expulsion of Mo metal from the structure. This expulsion is expected to be relatively easy, and does occur quite rapidly during in-situ observation, because the material remains crystalline during the process.

4.6 Strategies for answering new questions

To address these new questions, follow-up experiments have been devised and a second paper is in preparation. As described in Chapter 2, the FIB instrument has been used to prepare new specimens using the surface steps to control the orientation so that the crystallography is much easier to analyze in the new specimens than it was in the specimen described in the experiment

above. Additionally, this paper will address some of the questions that the previous reports of the lithiation of MoS_2 in the plan-view orientation have failed to ask in the first place.

4.7 Exploration of an alternative mechanism for the lithiation of MoS_2

Janish MT, Carter CB, in preparation

There is a well-known (e.g., [144]) structural transformation that occurs in MoS_2 during lithium insertion, which involves a change in coordination geometry of the Mo atoms from trigonal prismatic to octahedral. The motivation for this work stems from a general feature of the modern literature on the lithiation behavior of molybdenum disulfide. While all of the work seems to agree that the structure undergoes a transformation from the equilibrium 2H phase, in which the Mo atoms are coordinated by six S atoms in a trigonal prismatic arrangement, to the metastable 1T phase, in which Mo atoms are coordinated by six S atoms in an octahedral arrangement, there is not a convincing argument for the mechanism by which this transformation occurs.

This is not to suggest that no mechanism has been proposed. According to conventional wisdom, Li^+ ions are inserted into the van der Waals gap of any layer material, and if this is the case then the rearrangement of the S atoms about the Mo atoms is necessarily a result of a shear within the S-Mo-S sheets that make up the crystal.

However, it is important to critically examine how this conventional wisdom came to be, and whether all of the assumptions that it implies are actually valid for the reaction of Li with MoS_2. The advantage of the mechanism proposed in this work is that it takes full account of the preferred structures as determined by computation, such as the preferred site of the Mo and Li and is consistent with both Pauling's rules and the analysis of Kertesz and Hoffman [81].

To begin, consider the model intercalation system: Li insertion into graphite. In what ways does the MoS_2-Li system actually resemble the C-Li system? The van der Waals gap is actually the only similarity, as discussed in Chapter 3. In fact, as early as 1975 questions were raised as to whether a simple intercalation mechanism could account for the features of lithiated MoS_2 [125]. And yet, it is assumed that both systems interact with Li in the same way because of the van der Waals gap.

Certainly, just because C-Li is the model system does not mean that there is not a rich body of literature on the subject of intercalated TMDCs. Systematic studies of alkali metal intercalation in TMDCs were published in the 1970s and 1980s, e.g., [116, 128, 143, 145, 146], although it is interesting to note that the target application in these early studies was often superconductivity, while today's research is largely focused on batteries. A key feature of these original experiments is the method by which the alkali metal atoms were introduced to the host TMDC: it was a chemical process in which the metal was dissolved in liquid ammonia, and the TMDC was then infiltrated with the ammonia solution (e.g., [11]). Naturally, the only space in the TMDC structure that is large enough to accommodate the ammonia molecules is the van der Waals gap.

In contrast, the lithiation (or sodiation, magnesiation, potassiation…) of TMDCs for battery applications is an electrochemical process in which the only species going into the host structure is a Li^+ ion, which is considerably smaller than an ammonia formula unit.

Now consider some of the early work on TaS_2, involving the 1T to 2H phase transformation upon heating [96, 97]. These papers both propose and give direct evidence for the shear mechanism, as the partial dislocations implied by this mechanism are actually imaged. But upon critical examination, how analogous is the process of heating a pure material to that of inducing a chemical reaction with an applied voltage? Clearly in the former case a shear mechanism

associated with the glide of partial dislocations is the only option, while in the latter case this is not necessarily so. Furthermore, the 2H-TaS_2 structure is distinct from the 2H-MoS_2 structure in its stacking sequence. The former is isostructural with NbS_2, which has a stacking sequence of AbACbC. That is, the Ta atoms all occupy B sites so that partial dislocations on just half of the S planes can change the sequence to AbCAbC. This is not so for MoS_2, since the Mo atoms alternate between A and B sites in successive layers.

In terms of point defects, DFT calculations have shown that in bulk MoS_2, the energy of formation of a Mo vacancy is 3 eV while the energy of formation of a Mo interstitial in an octahedral site in the van der Waals gap is 3.91 eV [147]. In theory, then, the energy barrier associated with moving a Mo atom into an octahedral site is nearly 7 eV per atom. However, this does not account for the presence of Li ions, their associated electrons, or the applied voltage driving the electrochemical lithiation of MoS_2.

Due to the shear mechanism proposed by van Landuyt, van Tendeloo and Amelinckx [96, 97], it seems convenient to frame the mechanism proposed here in terms of dislocations for the sake of direct comparison. The vector that connects a trigonal prismatic Mo site to the nearest octahedral site in the van der Waals gap is of the type $\frac{1}{12}\langle\bar{4}04\bar{3}\rangle$. This is reminiscent of the sessile partial with Burgers vector $\frac{1}{6}\langle 20\bar{2}3\rangle$ in the hcp system (analogous to the Frank partial in the fcc system) (see Ch. 11 of [101]) with the key difference being the magnitude in the *c*-direction. The lowest-index (closest-packed) plane in this zone is $(1\bar{2}10)$ and would ordinarily represent the most likely glide plane for a dislocation with this Burgers vector. Although it is customary to compare the value of $|\mathbf{b}|^2$ to get a rough estimate of relative dislocation energies (see Table 4.1), this method assumes an isotropic medium, which, as discussed in Chapter 3, does not apply to MoS_2 at all. Due to the relative weakness of the interlayer bonding compared to intralayer bonding, a

Table 4.1. Burgers vectors of selected dislocations in MoS_2 and the square of their magnitudes.

Type	**b**	$\|\mathbf{b}\|^2$
Perfect	$\frac{1}{3}\langle 2\bar{1}\bar{1}0\rangle$	6.66
Shockley partial	$\frac{1}{3}\langle 10\bar{1}0\rangle$	2.22
Trig. Prism. site – octahedral site	$\frac{1}{12}\langle \bar{4}04\bar{3}\rangle$	11.67

displacement in the *c*-direction may be expected to contribute significantly less strain energy than a similar displacement within the basal plane. In fact, rewriting the Burgers vector of the first 'Shockley partial' from Equation 3.2a as $\frac{1}{12}[40\bar{4}0]$ (although, as described in §3.8, a dislocation with this Burgers vector is not actually a Shockley partial, only analogous to one), it is easy to see that a translation between trigonal prismatic and octahedral sites for a Mo atom simply involves the action of a Shockley partial combined with an additional displacement of $[000\frac{1}{4}]$. Because of this, it is clear that $(1\bar{2}10)$ cannot be the glide plane: Mo atoms alternate between A and B sites, while the octahedral interstices are C sites. A single Shockley-type Burgers vector can only permute the stacking index in one direction; i.e., the dislocation that would move a B-Mo to a C site would also move an A-Mo to a B site. Therefore, the glide plane must be the lowest-index plane that contains only A or B sites so that dislocations that permute the stacking sequence in opposite directions can operate independently. Such a plane does not exist. Figure 4.7 shows the 2H-MoS_2 structure as viewed along the $[\bar{4}04\bar{3}]$ zone with the unit cell and trace of $(1\bar{2}10)$ shown for clarity. It is obvious that in this projection, every Mo column contains Mo atoms in both A and B sites and so the motion of a single $\frac{1}{12}[\bar{4}04\bar{3}]$ dislocation on any plane could not produce the necessary result. Any description of this mechanism involving dislocations, then, would revolve around the action of (a) a $[000\frac{1}{4}]$- type dislocation on every Mo plane followed by (b) Shockley partials of alternating sense (A→C and C→B) gliding on the new Mo planes. In fact this is more intuitive: if a Mo atom were to move from its trigonal prismatic site, it would do so in the *c* direction first due to the lower energy barrier (cf. the relative magnitudes of the thermal vibrations in- and out-of-plane discussed in §3.2). However, in the fcc system, the Frank partial is sessile- that is, it doesn't glide, but it can climb, and the

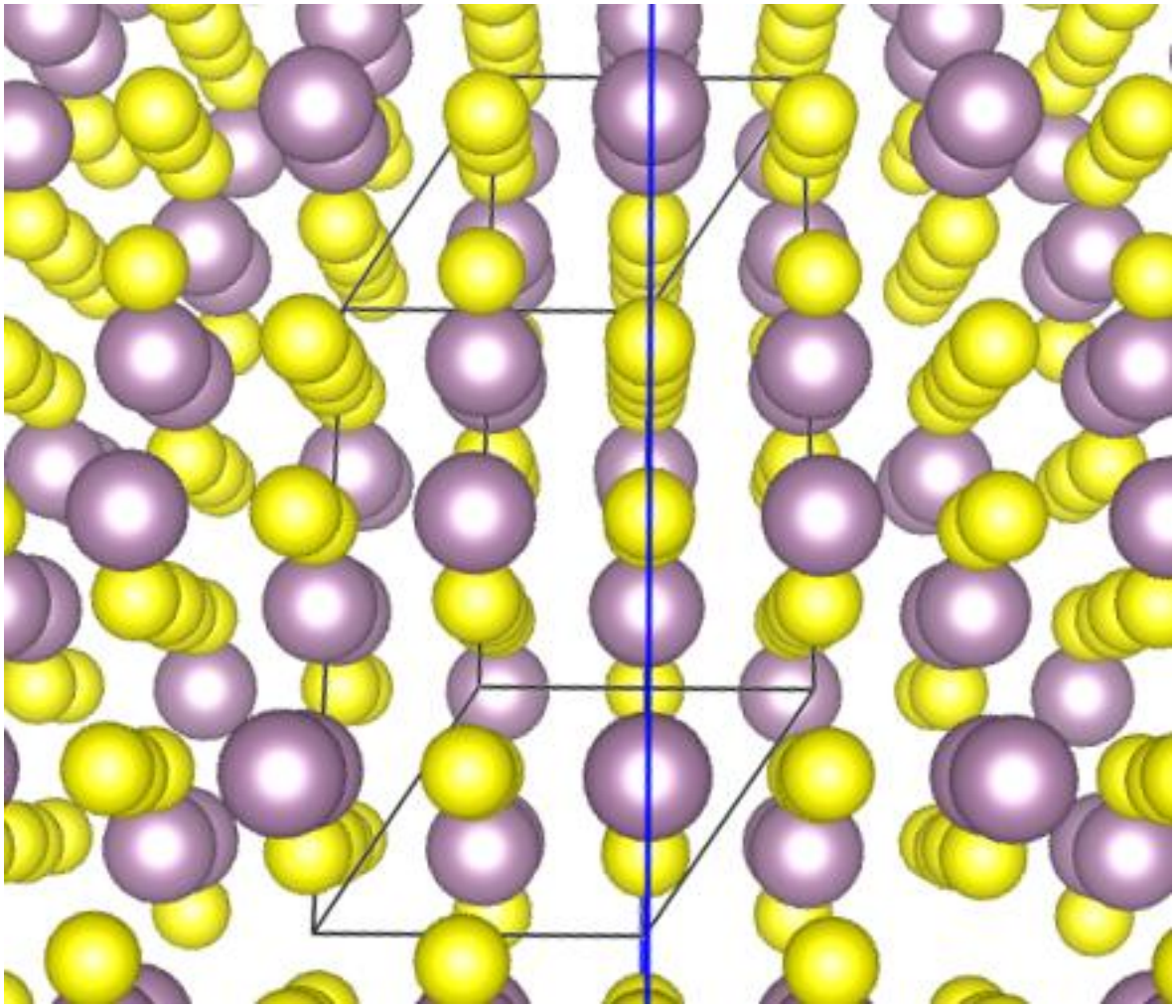

Figure 4.7. MoS2 viewed along $[\bar{4}04\bar{3}]$. Mo atoms are purple and S atoms are yellow; the trace of $(1\bar{2}10)$ is shown in blue. It is impossible to draw a plane in this zone that contains Mo atoms on only A or B sites.

experimental results are consistent with climb if they are viewed with a dislocation mechanism in mind.

Taking all of this into account, it is proposed that rather than sitting in the van der Waals gap, each Li ion that is added to the host MoS_2 structure instead displaces and reduces a Mo atom. The oxidation state of the Mo atom changes from 4^+ to 3^+, so that its electronic structure is that of a group 7 transition metal rather than group 6. The group 7 transition metals naturally adopt an octahedral coordination in their dichalcogenide compounds, and there are octahedral sites available in the van der Waals gap for the now-interstitial Mo^{3+} to sit in.

One obviously different feature associated with this mechanism is the coordination of the Li atoms. If Li replaces Mo in the original structure, then its coordination by S must be the 6-fold trigonal prismatic arrangement. Although most papers in the current literature tend to agree on octahedral coordination of Li, some argue for tetrahedral coordination instead; while some first-principles studies have been published on this subject (e.g., [82]) only tetrahedral and octahedral sites were considered for Li atoms due to the assumption of their location in the van der Waals gap. In general, one would expect the spherically symmetric s orbitals of the Li atom to favor coordination geometries with higher symmetry (so octahedral or tetrahedral rather than trigonal prismatic), but it is once again worth noting that during an electrochemical reaction, the system is not in equilibrium.

Whittingham and Gamble [125] also considered the lithiation of TMDCs with excess transition metal atoms sitting in the van der Waals gap, so the idea of, e.g., Mo atoms "intercalating" MoS_2 is not actually completely new.

5 Characterization of Sn Wires

The rationale for choosing tin in this work, as well as the methods by which Sn specimens were prepared, were introduced in chapter 2. This chapter describes what is currently known about Sn, from its structure, to the defects therein, to its present and potential applications. On the subject of dislocations in Sn, some new results are presented since the study of defects in Sn at the atomic scale is not well-represented in literature. Additionally, TEM is one of the most important methods of studying dislocations in materials, requiring an intimate understanding of both the crystal structure of the material in question as well as the physics of the microscope itself. By including the detailed study of dislocations in any material in a student's thesis research, the mastery of some of the most advanced microscopy techniques is then required. Moreover, the lithiation process in Sn is reversible and, as demonstrated in Chapter 6, it is possible for the delithiated material to return to a single-crystal state. In this case, it may be expected that dislocations would be left behind and may play some role in subsequent discharge cycles. In the case of a polycrystalline delithiated phase, the same may be said regarding grain boundaries.

5.1 The structure and properties of Sn

Below 13.2 °C, Sn has the diamond cubic structure. The α-phase, also known as gray tin, has a lattice constant of a = 0.649 nm. The α-phase is sometimes called semi-conductor Sn, since the diamond structure is characteristic of covalent bonding. The α-Sn structure is shown in Figure 5.1a.

At standard pressure, Sn crystallizes in the β-phase as shown in Figure 5.1b (also known as white tin; body-centered tetragonal, a = 0.583 nm, c = 0.318 nm) above 13.2 °C up to its melting point of 232 °C. At very high pressures there are two other high-temperature phases, γ and σ; however,

these phases will not be considered in this work as the exceedingly high pressures involved are not relevant to the normal operating conditions of batteries.

The spontaneous conversion of white tin to gray tin at low temperatures is known as tin pest, and poses a significant concern to applications where tin is used because while the commonly-used β-phase is quite soft and malleable, the α-phase is brittle. Because of this, impurities are often added to depress the β to α transformation temperature.

The structural relationship between the α and β phases of Sn is rather curious. The β structure can be derived by compressing the diamond cubic structure along one axis so that *c* is reduced from 0.649 nm to 0.318 nm; this is accompanied by an expansion of *a* and *b* to 0.824 nm [148]. This is an extreme example of the Poisson effect; α-Sn has a Poisson ratio of 0.33 whereas the phase transformation corresponds to $\nu = 0.53$. However, the Poisson ratio is defined for small strains, which is not a valid approximation in this case. Since this new cell has tetragonal symmetry, we reduce the number of atoms in the unit cell by redefining *a* as half of the (001) plane face diagonal while *c* remains the same, resulting in the body-centered tetragonal cell with lattice parameters as noted above. The relationship between the two structures is shown schematically in Figure 5.1c. The β-phase is significantly denser than the α-phase (7.37 g/cm^2 compared to 5.77 g/cm^2, respectively). The increase in density can be rationalized by a change in the character of the bonding. β-Sn is the metallic phase of Sn while the α-phase is semiconducting (as Si and Ge, with which it shares its structure, are), and metallic bond "lengths" are generally much shorter than covalent ones.

The electrical conductivity of β-Sn is 8.7×10^6 S/m [149], which is ~15% of the conductivity of the international annealed copper standard (IACS).

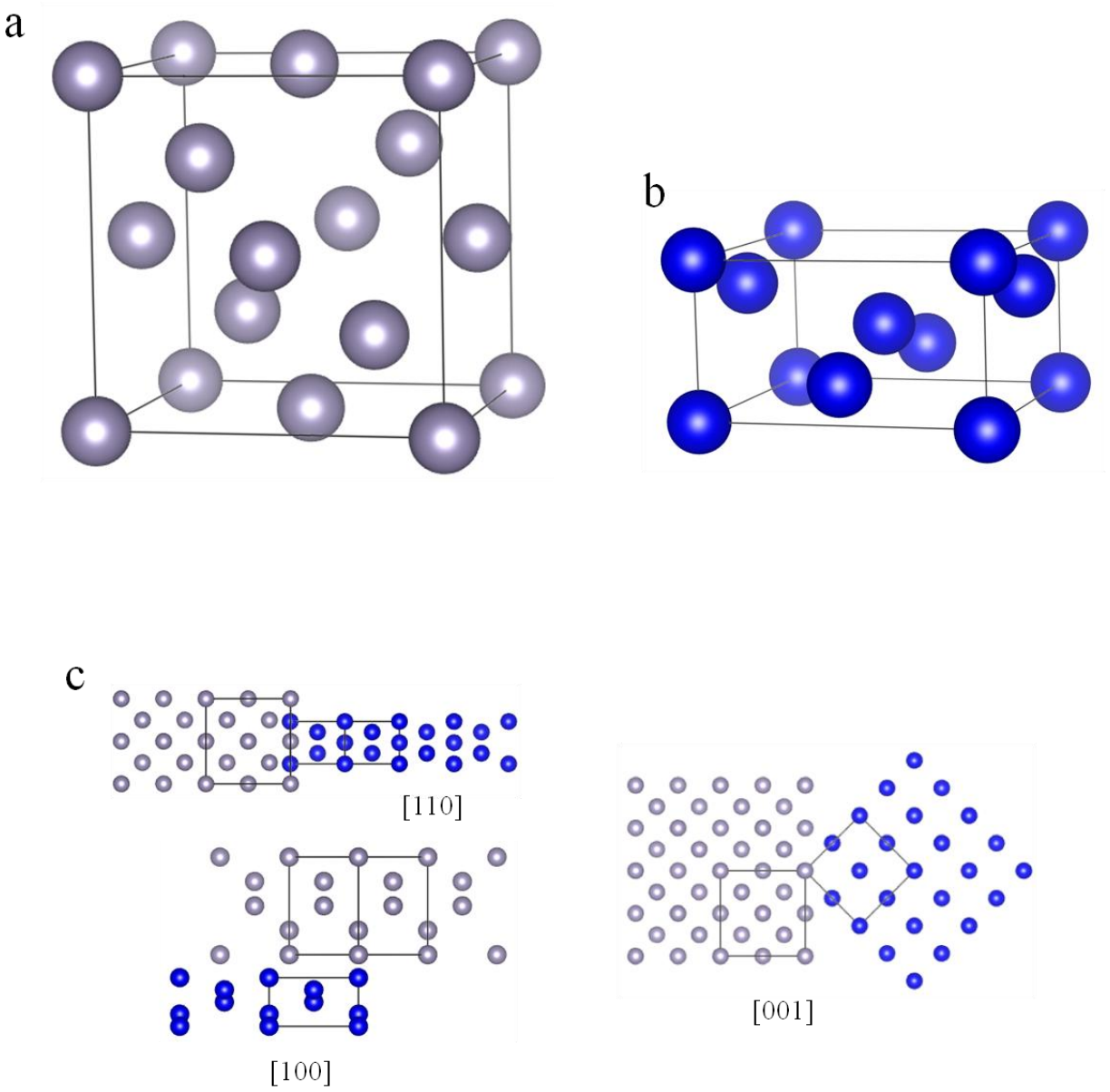

Figure 5.1. Schematic diagrams of the structures of (a) α-Sn and (b) β-Sn; (c) the relationship between the two structures along the indicated directions in the β-phase.

At atomic number 50, Sn is a post-transition metal and is in group 4A, below C, Si, and Ge which all have well-known stable (or metastable) diamond cubic structures.

The four shortest lattice vectors in the β-Sn structure are ⟨001⟩, ½⟨111⟩, ⟨100⟩, and ⟨101⟩. Of these, dislocations with Burgers vectors corresponding only to the first two have been experimentally observed in bulk Sn [150]. Dislocations with the Burgers vector ⟨101⟩ have been reported, based on observations of epitaxy-grown, thin films of Sn by Vook [151], but this was later attributed by Fiedler to the thin-film geometry of the specimens used in that study [150]. Vook himself hypothesized that the specimen geometry was responsible for the (001)[*hkl*] slip system reported in his work [151], which had not been reported before, but he did not extend this analysis to the Burgers vectors of the dislocations.

A brief summary of the introduction and experimental sections, along with key results and conclusions of each paper will be included.

5.2 Sn Wires

> *Mackay DT, Janish MT, Sahaym U, Kotula PG, Jungjohann KL, Carter CB, Norton MG, J Mater Sci 49 (2014) 1476-1483 [70]*

Like other nanomaterials, the properties of one-dimensional (1D) nanostructures have proven to be quite different from those of their corresponding bulk materials, which has led to many new applications [152-156]. Unfortunately, processes for fabricating these 1D structures are difficult to commercialize; in general they are either too complex or do not generate a high enough yield (or both) to be industrially viable (see, for example, a recent paper on Sn nanopillars [157]).

Perhaps the best-known method for growing arrays of 1D nanostructures, especially Si nanowires [158], is the vapor-liquid-solid (VLS) mechanism [159]. The growth of many 1D

nanostructures has been attributed to this mechanism [160-162], which attests to its versatility; however, any process that takes advantage of the VLS mechanism requires high temperatures since the catalyst is in the liquid phase and the reactants are gaseous [163, 164]. Furthermore, the VLS growth mechanism commonly requires an inert atmosphere, and growth rates of the nanostructures is slow.

Another route to producing arrays of 1D nanostructures is by electroplating with a template. Anodic aluminum oxide (AAO) is commonly used as a template material, and Sn nanowires have been produced this way (e.g., [165, 166]). However, this fabrication technique requires many steps, some of which are ultimately wasteful (and costly); in particular, the template requires time and material to produce, only to be destroyed at the end of the process.

In the present work, Sn nanoneedles (so-called because of their tapered shape, as shown in Figure 5.2) were electrodeposited from an alkaline Sn solution onto Cu foils (10 mm x 7 mm x 0.75 mm coupons, 99.99% pure, Alfa Aesar; 10 mm x 10 mm x 10 μm TLB-DS and TLB-PLSP coupons, Oak Mitsui). 3 g of sodium hydroxide and 28 g of sodium stannate trihydrate were dissolved in deionized water to make 200 ml of solution. The Cu substrates from Alfa Aesar were polished and cleaned in a 9.4 M NaOH solution, then soaked in sulfuric acid for 15 s to remove the oxide layer from the surface. The Oak-Mitsui foils were used as-received. The Cu coupons were soaked in the electroplating solution for 30 min before the deposition. Sn was deposited on the Cu substrates using a voltage of 2.4 V, a current density of 35 mA/cm^2, and a temperature of 55 °C for 11 min. The solution was agitated with a 2.5 cm magnetic stir bar at 320 rpm. Needles were scraped from the deposited films onto standard Cu TEM grids with lacey carbon support films.

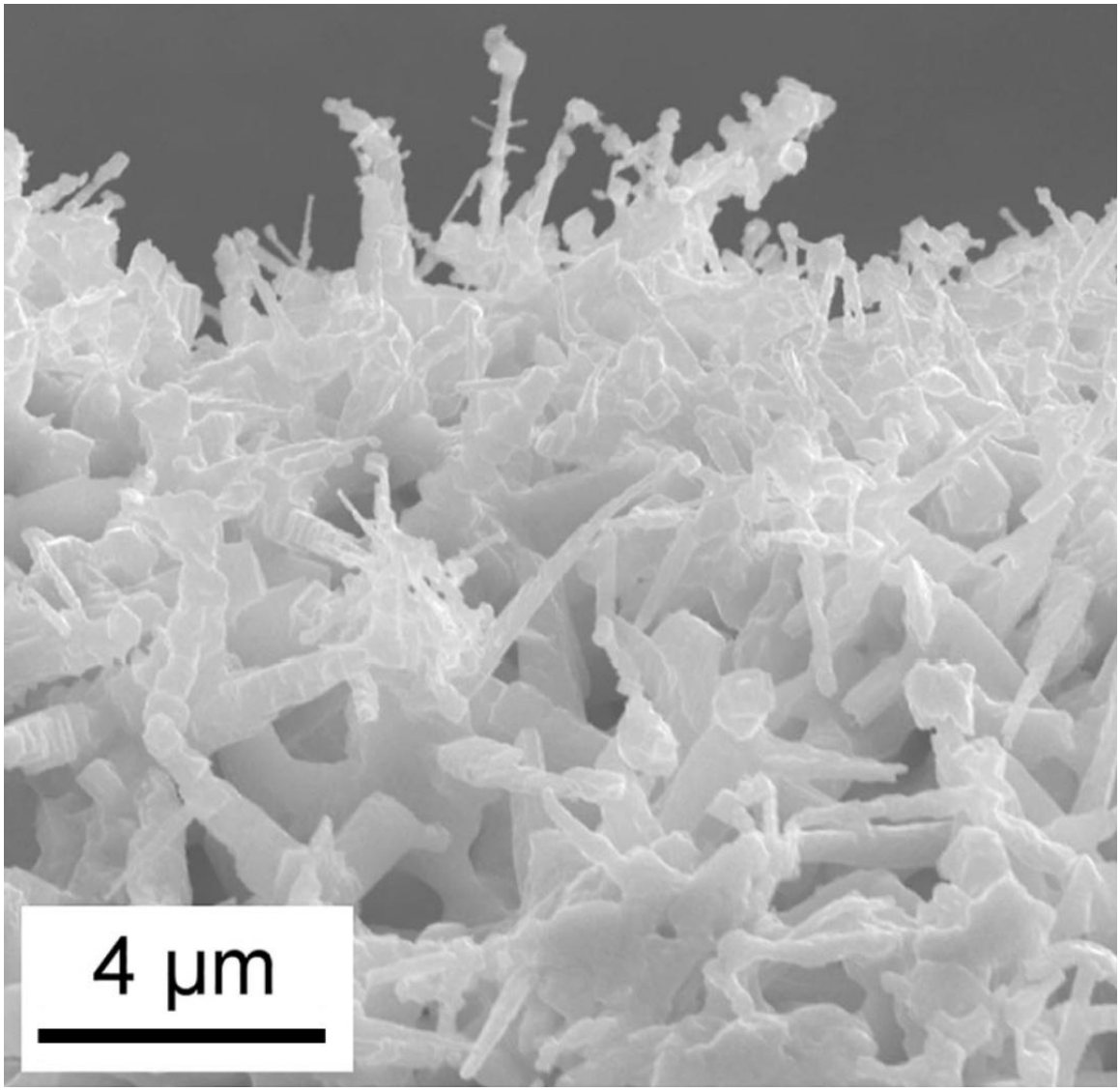

Figure 5.2. Scanning electron micrograph showing the tapered shape of the Sn needles. Image courtesy of David Mackay.

The key results from this work were:

i) Large arrays of Sn nanoneedles can be produced by this process. Cu films of standard sizes for commercial LIBs were coated in this way.

ii) The needles are generally single-crystal, distinguishing them from Sn dendrites (see Figs. 3a and 4a), with a distinct cap on the end.

iii) The process has few steps and does not require high temperature. It is industry scalable, but does not require industrial-level or high-tech resources to produce in large quantities; electrodeposition is carried out in small facilities around the world. Thus the Sn nanoneedles are not a model system, but "real" materials.

This is not to say that model systems are not valuable, and Sn whiskers could provide a path for a systematic study of the interaction of Sn with Li. A scanning electron micrograph showing several large whiskers, grown on a Sn film deposited on a Cu substrate, is shown in Figure 5.3. With the careful use of a micromanipulator and a FIB, individual whiskers can be removed from the Sn film and prepared for use in in-situ experiments; clearly, for experiments in the TEM this requires the thinning of one or more sections of the whisker using the FIB. The orientation of the whisker could be controlled in this way, whereas with the electroplated needles it is necessary to simply work with whatever is available.

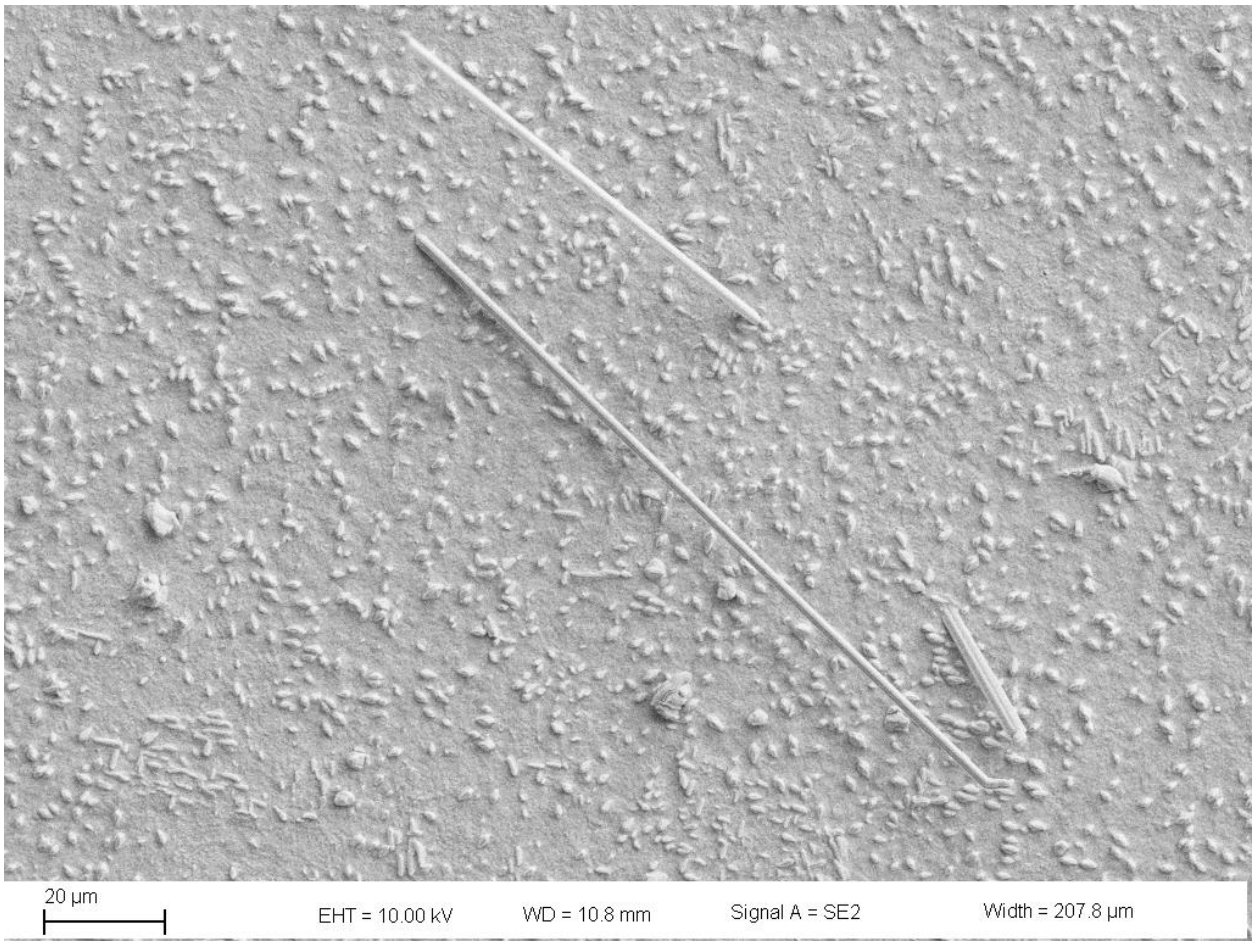

Figure 5.3. Scanning electron micrograph showing three whiskers on a Sn film that was deposited on a Cu substrate. Image courtesy of Joe Michael.

5.3 Grain boundaries in Sn

5.3.1 In literature

Grain boundaries are characterized by the degree of misorientation between two grains, as well as how this misorientation is achieved. Low-angle grain boundaries are those for which the misorientation angle is ~10° or less, and larger misorientations are associated with high-angle grain boundaries. If one visualizes a section of perfect crystal that is cut in half, the two halves can be tilted with respect to one another about an axis parallel to their plane of contact and rejoined (if the faces at which contact is made are polished to be parallel once again). This is known as a tilt boundary; tilt boundaries are usually described as an array of edge dislocations. Alternatively, if the two halves of the perfect crystal are rotated with respect to one another about an axis perpendicular to the plane of contact and rejoined, a twist boundary is formed. Twist boundaries are generally described as an array of intersecting screw dislocations. Schematic representations of tilt and twist boundaries are shown in Figures 5.4 a and b, respectively [101]. Although it is possible to describe any such boundary as either tilt or twist, one interpretation generally makes discussing the orientation relationship between the two grains much easier. For example, a low-angle tilt boundary might be just as accurately described by a 180° rotation about a high-index plane, but this would muddle the analysis unnecessarily.

Rowenhorst and Voorhees conducted measurements of the energy of many different grain boundaries in Sn [167]. They concluded that most misorientation angles had a similarly high energy, in the range of 230-260 mJ/m^2, but that some specific misorientation angles (namely 6°, 25°, 27°, 57°, and 65°) were associated with significantly lower grain boundary energies [167]. The latter two misorientation angles match very closely with the twinning angles of the two known twinning systems in Sn (discussed in more detail below).

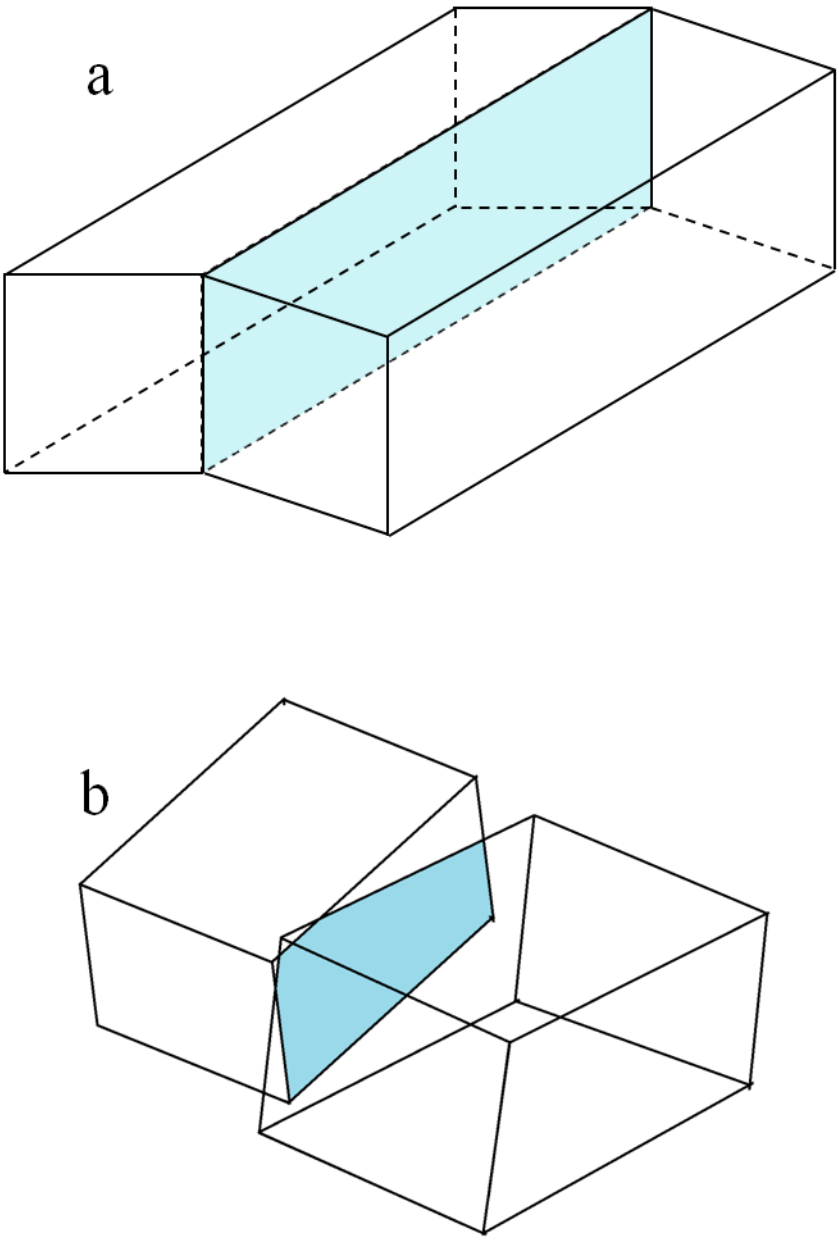

Figure 5.4. Schematic representation of (a) a tilt boundary; and (b) a twist boundary. After Hirth and Lothe.

If two Sn grains are tilted about [001] with a misorientation of 28.08°, one in every 17 lattice sites will be coincident and this is the special $\sum$=17 boundary [168].

In fact, the migration of [001] tilt boundaries in Sn is somewhat problematic [169], although whether this is related to an actual engineering problem or simply an accumulation of basic scientific data is not made clear in refs. [168] or [169].

The change in misorientation of subgrains in Sn during creep was measured by Suh, Cohen, and Weertman with the aim of determining whether diffusion or cross-slip controls creep in this material [170]. Creep is particularly relevant here since room temperature is a high fraction of the melting point of Sn ($0.59T_{melt}$). The accumulation of edge dislocations in subgrain boundaries was suggested by J. Friedel as the model for cross-slip-controlled creep, and it is easy to visualize how this would necessarily change the misorientation angle of the boundary by considering the addition of extra dislocations as shown in Figure 5.5. In this sense the misorientation angle should increase proportionally to the creep strain in a predictable manner [170]. However, the measurements of Suh et. al. determined that the actual change in misorientation angle of the subgrains was much less than would be expected for a cross-slip mechanism, and thus they concluded that in Sn creep is controlled by diffusion [170].

As a brief aside, the subject of self-diffusion in Sn is rather interesting. For the sake of this discussion, it is noted that diffusion can be described by the Arrhenius equation:

$$D = D_0 \exp\left(\frac{-Q}{RT}\right)$$

where D is the diffusion coefficient at the absolute temperature T, R is the gas constant, Q is the activation energy, and D_0 is the temperature-independent frequency factor. In a plot of ln(D) vs. T^{-1}, the activation energy is the slope and the frequency factor is the y-intercept.

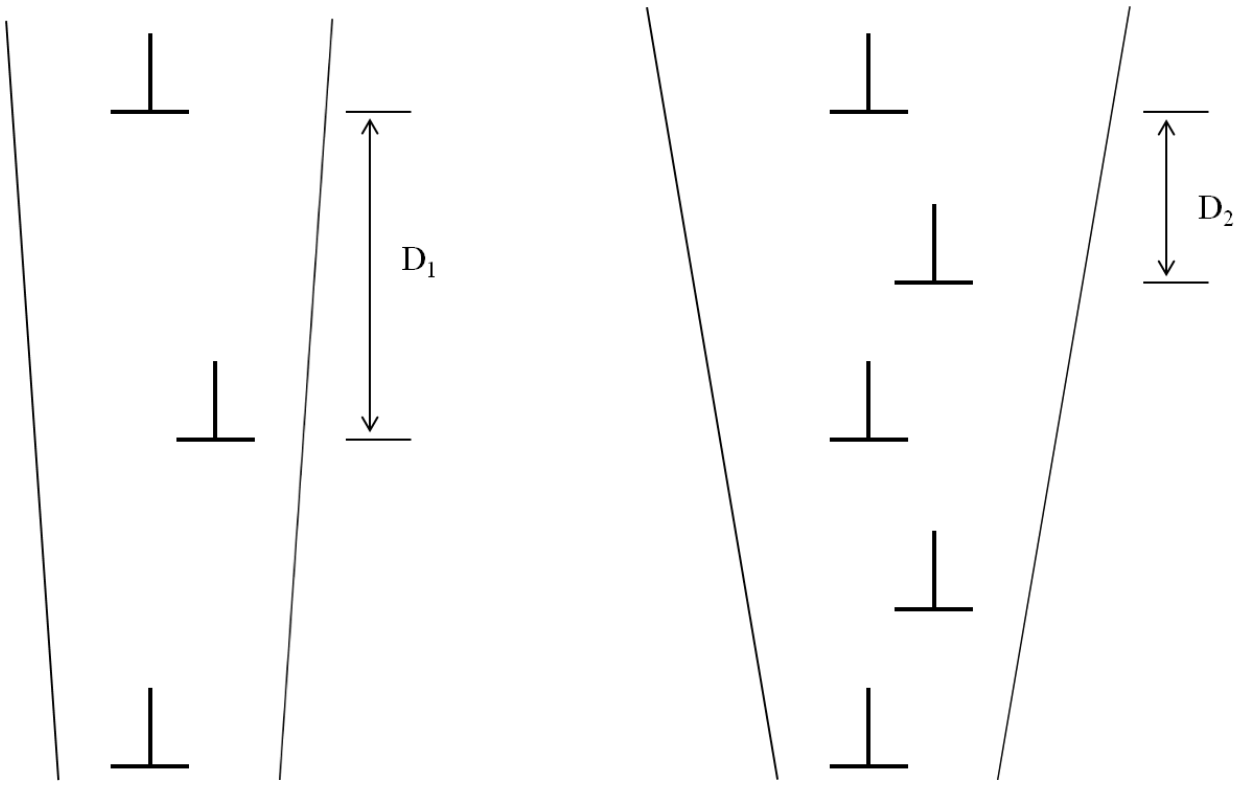

$$D = b/\theta \quad \longrightarrow \quad \theta = b/D$$

Figure 5.5. Illustration of how the accumulation of edge dislocations at a subgrain boundary changes the misorientation angle of the grains.

As may be expected, Sn has different diffusion rates in the *a*- and *c*- directions: at 180 °C, D_a is 5.5×10^{-11} cm^2/s compared to $D_c = 9.9 \times 10^{-11}$ cm^2/s [171]. However, because the activation energy is higher for diffusion in the *c*-direction, diffusion rates along *a* and *c* are equal at around 125 °C, and below this temperature diffusion is faster along *a* [171].

Compared to Cu, Sn has a frequency factor that is 8 orders of magnitude lower in the *a*-direction and 5 orders of magnitude lower in the *c*-direction; however, the activation energy for self-diffusion in Sn is lower than for Cu [171-173] (see Table 5.1). A deep discussion of these phenomena is, unfortunately, beyond the scope of this work.

5.3.2 In the Sn nanoneedles described in this work

A high-resolution TEM image of a grain boundary in an as-grown β-Sn nanowire is shown in Figure 5.6a. The labeled boxes indicate the grains to which the fast-Fourier transforms (FFTs) in Figures 5.6 b & c correspond; based on the FFTs it is apparent that the small grain towards the top of the image is oriented with the [001] direction parallel to the beam while the large grain is oriented with [010] in the beam direction. Perhaps surprisingly, upon close examination there is a set of planes that appears to be exactly common to the two grains, and this is confirmed by the presence of identical pairs of spots in the two FFTs which are indexed as (200). This means that the two grains are oriented at exactly 90° to one another. This is reminiscent of the Σ=99 boundary in spinel [174], and is illustrated schematically by the simple model in Figure 5.6d. Note that the dumbbells in the lower grain cannot be resolved by the microscope that was used to acquire these images and so they appear as slightly oblong points. This actually gives the false impression of registry between the [001] planes of the lower grain and the [020] planes of the upper grain when in fact there is theoretically a ~0.27 Å mismatch between them. Once again, the resolution of the microscope used to acquire these images is not sufficiently high to

Table 5.1. Relevant parameters describing self-diffusion in Cu and Sn. Based on data from [171-173].

	D_0 (cm^2/s)	Q (kcal/mol)
Cu	0.78	50.5
Sn (*a*)	3.7×10^{-8}	5.9
Sn (*c*)	1.2×10^{-5}	10.5

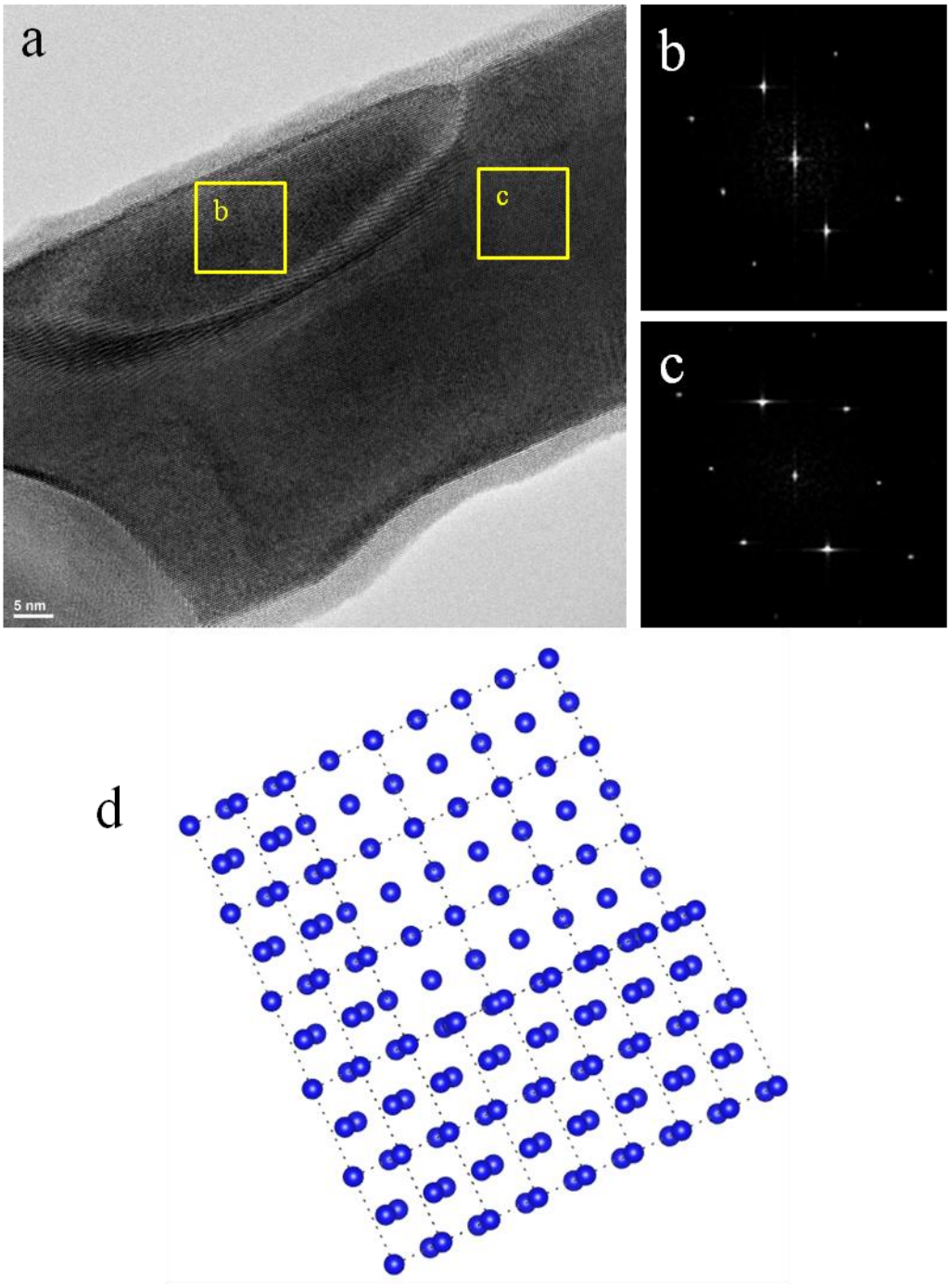

Figure 5.6. Experimentally observed grain boundary in a β-Sn nanowire. (a) HRTEM image of the grain boundary; (b, c) FFTs of the grains corresponding to the boxes labeled in (a); (d) schematic model of the two grains in (a).

determine whether there is some compression in the [001] direction in the bottom grain (or the expansion along [100] that would accompany such a compression); regardless the noise in the image in the boundary region would preclude such precise measurements. Judging by what appears to be a complex moiré pattern at the boundary (shown at higher magnification in Figure 5.7a and lower magnification in Figure 5.7b), the interface is far from flat and is not particularly close to being viewed edge-on anywhere along its length except possibly at the top-right region of Figure 5.6a; two high-magnification images from this area are shown in Figure 5.8. The images are identical but the annotations indicate the ambiguity of the location of the boundary.

5.4 Twin boundaries in Sn

Twinning modes cannot be generalized for all tetragonal materials like they can be for bcc and fcc metals. This is because the ratio of the lattice parameters *c*/*a* is not fixed for tetragonal materials, which introduces another degree of complication. This is similar to the case of hcp materials; for example, a Kikuchi map of Au applies just as easily to Cu, but the same cannot be said of Ti (*c/a* = 1.59) and Zn (*c/a* = 1.86). Two twinning systems have been reported for β-Sn. The primary system occurs on {301} planes in $<\bar{1}03>$ directions, while a much-less-commonly observed twinning system occurs on $\{\bar{1}01\}$ planes in <101> directions. The latter system is in fact the reciprocal to the former; two twinning systems are said to be reciprocal if the elements K_1 and η_2 of one twin have the same indices as K_2 and η_1 of the other twin [175].

When a bar of tin is bent, it makes a crackling noise known as the “tin cry” or “tin scream” that is associated with the formation of deformation twins.

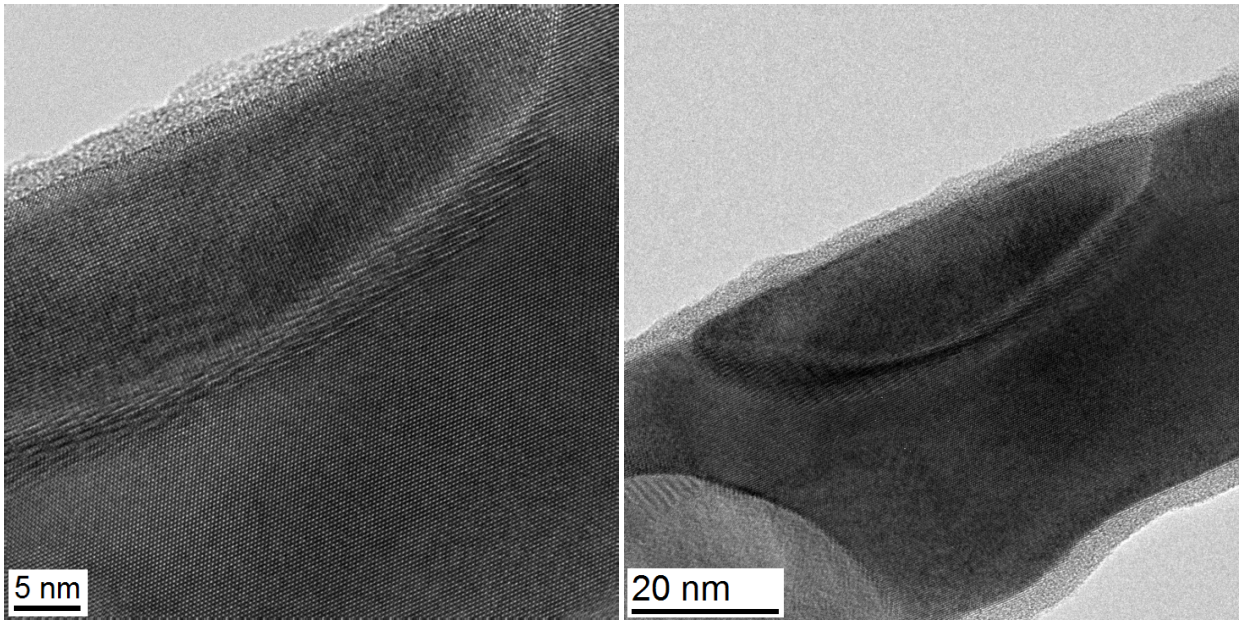

(a) (b)

Figure 5.7. (a) High- and (b) intermediate-magnification images of the grain boundary in the Sn needle shown in Figure 5.6a.

Maruyama and Kiho were able to promote the growth of $(\bar{1}01)$ twins in Sn by suppressing the broadening of the (301) twins [175]. This was achieved by an external constraint—a glass tube was used to confine the crystal. (In fact, the crystals were grown inside the glass tubes). When a normal impact stress was applied to the crystal, twin bands of both the primary and reciprocal types were observed to form with thicknesses around 100 μm. The two types of twin bands intersected one another frequently, and additional twins were observed at the intersections.

There are two conditions required for secondary twin formation, according to Cahn [176]. First, the traces of the crossing and secondary twins must be parallel in the plane of the crossed twin; second, the direction, sense, and magnitude of shear have to be identical in the crossing and secondary twins [176]. Interestingly, Maruyama and Kiho observed that the secondary twins in β-Sn did not obey the second criterion. Furthermore, another study by Pratt reported secondary twins at twin intersections in single crystal Zn that did not meet Cahn's first criterion.

The twins generated at the intersections of the reciprocal twins in β-Sn were of three varieties. First is the secondary twin, which "succeeds the crossing" twin in the crossed twin band; second is the bouncing twin, which is reflected at the intersection in the matrix; the third variety manifests itself as the narrowing or broadening of the crossed twin on either side of the intersection.

Six-fold cyclic twinning occurs during the solidification of SnAgCu and related lead-free solders, but is not common in pure Sn [177]. As the solder solidifies, it crystallizes very rapidly by dendritic growth, and yet the cyclic twin structures bear some resemblance to those found in some minerals that grow by precipitation from solution over long periods of time [177]. The microstructure of the solidified solder joint depends strongly on the temperature at which it solidifies, which can vary significantly because Sn and Sn-based melts (like solders) can be

supercooled by as much as 100 °C before crystallization begins. It is also significant that the growth velocities of Sn crystals from the liquid phase are highly orientation-dependent, with [110] and $[1\bar{1}0]$ directions being strongly preferred over, for example, [001]. The average rotation about [001] between the grains in these twins is observed to be about 60°, and both {301} and {101} twinning systems are thought to be active [177]. Their respective twinning angles are 62.8° and 57.2° so the equal representation of the primary twinning system and its reciprocal would yield an average rotation of exactly 60° and preclude the need for a relaxation at the twin boundaries to accommodate the excess or deficit 16.8° rotation that would occur if only one of the twinning systems were to be expressed.

This is in contrast to the five-fold cyclic twinning observed in, for example, Ge; in this case the ~353° total rotation of five successive {111} twins is "stretched" to 360° by such a lattice strain [178].

5.5 Dislocations in Sn

Working on dislocations in β-Sn is challenging for two main reasons. This first is that the tetragonal symmetry of its crystal structure makes all of the relevant analysis pertaining to dislocations complicated and unintuitive. Any plane whose indices are non-zero for both *l* and either *h* or *k* does not have its normal parallel to the crystallographic direction of the same indices. For example, [111] is not parallel to $\mathbf{g}_{111}$, but rather nearly parallel to $\mathbf{g}_{11\,11\,6}$. This makes selecting diffraction conditions for weak-beam imaging of dislocations in β-Sn in the TEM difficult. The second reason is that there is very little literature on the subject of dislocations in β-Sn, which is almost certainly a direct result of the complications just discussed. Furthermore, most of the literature that does exist on this topic focuses on the analysis of surface slip lines in bulk samples (e.g., [179]). Only a few other TEM studies on dislocations in Sn have been

published [151, 180-182]. All of the Sn films in [151] were prepared by evaporation onto cleaved NaCl and were in the [001] orientation as a result. Having access to only one orientation when studying dislocations in a material is a significant disadvantage; for example, it proved impossible to study (110)[001] and (100)[001] slip due to the orientation limitation. This study reported the first observation of (001)[*hkl*] slip, which it attributed to the thin film geometry of the specimen. As always, it will be important to consider the implications of the specimen geometry on the applicability of the results as this work is extended to other foil orientations.

Partial dislocations with the Burgers vector ½[010] were reported to be observed by Ojima and Taneda [181]. They also recorded images of tilt boundary dislocations [182]; in both of these papers the foil plane of the Sn film was also (001).

In [180] the nucleation and growth of twins in Sn films was studied in six specimens, four of which had a foil plane of (001), while the other two were in the (110) orientation.

By using modern specimen-preparation techniques it is now possible to examine sections of single-crystal Sn whiskers in arbitrary orientations. Foil planes of (100), (001), (110), and (211) were chosen for a more in-depth study of how dislocations behave in Sn. The four shortest lattice vectors in the β-Sn lattice are <001>, ½<111>, <100>, and <101>. Therefore these are the most likely Burgers vectors for dislocations in Sn [150]. Table 5.2 below is reproduced from Fiedler and Vagera [150], and details the experimentally observed glide systems in β-Sn.

Table 5.2. Summary of the experimentally observed glide systems in β-Sn. Adapted and expanded from Fiedler and Vagera (1975).

Author	Polanyi	Obinata	Lorenz	Brümmer	Vook
Year	1925	1933	1968	1970	1964
Glide systems reported	[001](100) [001](110) [101](010)	[001](100) [001](110) [101](101) [101](121)	[001](100) [001](110) [111](110) [101](101)	[111](110) [100](011)	[111](110) [101](101) [101](121) [011](100) [*hkl*](001)

6 Lithiation of Sn Wires

The earliest report of a successful in-situ TEM lithiation experiment was that of Huang et al. [32], who observed the lithiation of SnO_2 nanowires. Their work is relevant to the lithiation of pure Sn in the sense that it was this paper that set the bar for such experiments in the TEM, and also because even a convertible oxide electrode ultimately derives its reversible capacity from Li alloying with the metal that is reduced during the first cycle.

Some researchers from the same group (i.e., the collaboration between Huang's group at CINT-SNL and Mao's group at Pittsburgh) also published work on the lithiation and sodiation of Sn nanoparticles, focusing on the pulverization of the particles after repeated cycling in the case of lithiation and competing pulverization and agglomeration processes in the case of sodiation [183]. As discussed in Chapter 1, the lithiation of these Sn particles was reported to be a two-step process, with amorphous Li_xSn as an intermediate phase while the fully-lithiated phase was reported to be crystalline $Li_{22}Sn_5$.

The lithiation of Sn nanowires coated in a carbon shell has also been reported [184]. In this case the wires were originally SnO_2, and during the reduction process to create Sn wires the carbon shell was deposited. Although in many cases creating composite electrodes with a carbon component has been shown to improve the electrode's performance (e.g., [119, 185-188]), the main problem facing the production of these composite materials is scalability. This issue is discussed in more detail in the paper below, which deals with the lithiation of Sn nanoneedles that are produced by an industry-scalable process.

Traditionally, materials that alloy with Li have been limited by the mechanical instability caused by the large volume changes during cycling. However, it has been discovered that nano-structured electrodes, which by nature include a significant amount of empty space, can be used to overcome

this issue. As a result, Li-alloy electrode materials such as Sn are being revisited by the scientific community.

Sn nanoneedles (described in detail in the following section) were electrodeposited on two different TEM grids: first on Cu Omniprobe FIB half grids, then on 300-mesh parallel-bar Cu grids that were cut in half after the deposition. The Cu half-grids were mounted in the fixed end of the Nanofactory STM-TEM holder as described in §2.4. Individual needles were successfully cycled and the microstructural evolution of the needles was observed. In one case, when the reaction proceeded more slowly, the needle transformed from single-crystal Sn to a polycrystalline Sn-rich intermetallic, then back to single-crystal Sn.

The key results from this work were:

i) The demonstration of the lithiation and delithiation of single-crystal Sn nanoneedles one at a time within the TEM.

ii) In a majority of cases, the lithiated needles were polycrystalline Li-Sn intermetallics, as shown in Fig. 1.

iii) The needles were amorphized when the reaction proceeded very quickly (see Fig. 2).

iv) It was not possible to delithiate the needles in most cases. This could be due to inconsistent performance of the Nanofactory holder, or due to some property of the lithiated material. For example, if the needle becomes disconnected from the source it cannot delithiate. Another common failure mechanism for this kind of experiment is the shorting of the half-cell that occurs if the working electrode material breaks through the oxide layer on the Li metal as the former expands; direct electrical contact between the electrodes compromises the cell entirely.

v) In the case of successful delithiation, the needle transformed back to single-crystal β-Sn as shown in Figs. 3 and 4. It is possible that this is due to a certain orientation relationship between

the pristine Sn and the lithiated phase being maintained for low lithium content and only partial lithiation of the needle. Alternatively (or perhaps additionally), the proximity of room temperature to the melting point of Sn, along with the energy input from the electron beam and the electric field across the cell may increase the kinetics for the elimination of defects such as grain boundaries during delithiation.

6.1 TEM in-situ lithiation of tin nanoneedles for battery applications

Janish MT, Mackay DT, Liu Y, Jungjohann KL, Carter CB, Norton MG, J Mater Sci 51 (2016) 589-602. DOI 10.1007/s10853-015-9318-0 [189]

Energy-storage technology has been identified as an area of national need in the United States [6]; research in this field takes similar priority all across the world. Energy storage devices, i.e., batteries, are naturally at the heart of the modern, mobile world, but they are also crucial in the push to reduce dependence on fossil fuels [190-196]. Fully electric vehicles will require significantly more energy-dense, power-dense batteries if they are to rival the performance consumers have come to expect from gasoline vehicles. Power grids will need improved batteries if they are to load level the generation of wind and solar farms on a large scale [6, 197].

Before these materials engineering problems can be overcome, two basic materials science questions must be answered: what are the basic mechanisms by which batteries work, and what are the mechanisms by which critical inefficiencies are introduced? Progress in the field of in-situ microscopy over the last 5 years has brought materials characterization techniques to the point where these two questions can begin to be fully explored. In-situ TEM has become particularly powerful in this regard, especially in relation to Li batteries since model materials can be observed lithiating and delithiating (e.g., [32, 198]). This paper considers the advantages

that Sn offers as a possible anode material, either as the metal itself, as an alloy or as a component of a composite material.

6.1.1 Background Review

Lithium alloys had been studied as possible anode materials for lithium-ion batteries (LIBs) even before SONY commercialized the market-dominating carbon-based chemistry in the 1990s, and have continued to generate significant research since [10, 199, 200] because their theoretical specific capacities exceed those of carbonaceous anodes. Compared to Li metal, which was the original anode material of choice for LIBs, lithium alloys exhibit superior cycling performance due to the decreased activity of Li. Pure Li anodes are susceptible to dendrite formation, which ultimately causes a short circuit and (sometimes catastrophic) failure of the battery. Mitigating the activity of Li by alloying it with other elements comes at the cost of both a reduction in cell potential and the extra weight and volume of the alloying metal, which significantly reduces the specific capacity of the cell.

Among the materials that form alloys with Li, elemental Sn has generated considerable interest due to its high theoretical specific capacity of 994 mAh/g [201] relative to many other LIB candidate materials as summarized previously in Table 1.1. The structure of Sn is relatively open—it contains a large amount of space. At room temperature β-Sn is body-centered tetragonal with a structure that is closely related to the low-temperature, diamond-cubic-structured α-phase; actually alloys or 2-phase Si/Sn particles are also being explored [202]. Si nanowires (NWs) [203] and nanoparticles (NPs) have been extensively explored as candidate anode materials but are not economical. The β-Sn structure is related to the diamond cubic structure by an extreme compression of the latter along the *c*-direction (with attendant expansion along *a* and *b*), with a redefinition of the unit cell such that there are four atoms per cell rather than eight ($[100]_{\beta}$ ||

$[110]_{\alpha}$). However, neither bulk material nor continuous films of Sn are useful in practice because the large volume change that occurs during lithiation and delithiation causes mechanical failure of the electrode [204, 205]. This phenomenon is not unique to Sn; all Li-alloys suffer from this characteristic [191].

The effect of mechanical stresses caused by the increase in volume can be alleviated by decreasing the dimensions of the material being lithiated. Both nanoparticles [206] and arrays of one-dimensional Sn nanostructures [207] have been used to achieve this stress reduction; the same is true for Si [208] and Ge [209]. The total stresses that build up during the expansion and the subsequent contraction that occurs during cycling are not so large when the dimensions of the material are small. This reduces the associated stresses and prevents mechanical failure (i.e. delamination from the current collector) [210]. However, the nanoparticle approach is at a disadvantage since it relies on the use of a binder material to maintain electrical contact between the current collector and all of the particles; the extra weight of the binder significantly reduces the gravimetric energy density of such electrodes.

The lithiation of Si has been studied extensively. Liu et al. described in-situ TEM experiments on Si nanowires, with an emphasis on improving the conductivity and charging rate by carbon coating and phosphorous doping [211]. They found that each individual modification to the Si NWs increased the charging rate by an order of magnitude, and that the effects of both modifications were cumulative. They also identified two distinct steps in the lithiation process; initially the Si NWs underwent solid-state amorphization but eventually re-crystallized in the $Si_{15}Li_4$ phase. The anisotropic lithiation behavior of Si was also highlighted in this study, as the cross-section of the NWs changed from circular to dumbbell-shaped; the largest expansion occurs in <110> directions while the smallest expansion occurs along <111>. More recent work

has also related the presence of a carbon “skin” or shell on Si NWs to a reduction in the total volume expansion experienced by the wires during lithiation [212].

The same group also reported on the size dependence of the fracture of crystalline Si nanoparticles, finding that particles with diameters less than 150 nm did not crack or fracture upon lithiation while larger particles experienced catastrophic mechanical failure [208]. McDowell et al. performed similar experiments on amorphous Si nanoparticles, and reported that particles up to 870 nm in diameter resisted mechanical failure upon lithiation [33]. They also discovered that the rate of the reaction is more constant for amorphous Si than for crystalline Si (in the latter case, the reaction slows down as it proceeds). Similar to the case of Si NWs, Si NP-carbon composites have also attracted considerable interest. For NPs, however, the carbon acts as a support and the sole conduction mechanism (rather than simply facilitating conduction). Reports on Si NPs decorating and contained in C nanofibers [186] and Si NPs enveloped in rumpled graphene sheets [187] have been published recently. In the latter study, the lithiation process was shown to change from isotropic to anisotropic during the reaction, which was attributed to more uniform electrical contact with the NPs provided by the graphene sheets. Good electrical contact with the current collector is one of the main barriers for implementing nanostructured anodes into real batteries.

Because it is so closely related to Si, the lithiation behavior of Ge has also been examined in-situ in the TEM. A study on Ge NPs found that crystalline Ge is much tougher than Si, with crystalline Ge NPs as large as 620 nm in diameter undergoing several full cycles of lithiation and delithiation without cracking [209]. Similar to the case of amorphous Si NPs, this resistance to failure is attributed to a more isotropic stress distribution at the reaction front. After delithiation the Ge NPs were observed to adopt an amorphous phase rather than reverting to crystalline Ge.

During subsequent lithiation cycles the particles progressed from amorphous Ge to amorphous Li_xGe to crystalline $Li_{15}Ge_4$ (the same Li content as the fully lithiated phase of Si). In this case the Ge NPs were attached to the end of Pt rods; more recent work has been done on Ge NP clusters in porous, nitrogen-doped carbon nanofibers [188], although in this case the lithiation and delithiation behavior of the material was not observed in-situ in the TEM. These composite nanofibers were prepared by electrospinning a mixture of polymers with GeO_2 dissolved in water followed by heat treatment at 600 °C. The Ge NPs formed by this process were very small, with diameters around 20 nm. Interestingly, some of the delithiated Ge NPs were observed to be crystalline even after several cycles. Because this was an ex-situ experiment, the crystallinity of the cycled Ge NPs could be an artifact of the TEM specimen preparation process. Studying the lithiation behavior of Ge NWs, Liu et al. reported that the amorphous, delithiated phase was highly porous, and that in fact the pores tended to remain in the same positions after every delithiation cycle [34]. In a later paper Liu et al. demonstrated that the lithiation behavior of Ge NWs can be drastically altered by coating the NWs with a thin (1-5 nm thick) layer of Si [213]. They showed that in this material, the lithiation reaction proceeded only axially along the NW (Ge <111>), rather than axially and radially at the same time. Furthermore, the volume expansion was also shown to be almost entirely limited to the axial direction. This phenomenon was explained by the higher chemical potential barrier for Li ion diffusion at the Si surface. Because there is no such directional preference for Li insertion in Ge, the path of least resistance for a Li ion in this geometry is simply axially down the Ge NW, with surface diffusion followed by radial lithiation through the Si layer being far less favorable. These findings indicate that control over the composition, doping, size, shape, orientation, and surface functionality of

nanostructured anodes will impact their performance in real battery applications. Therefore, attention must be given to each aspect of their incorporation on a current collector.

Stepping once more down Group 4 brings the discussion to Sn. Although the stable structure of Sn at room temperature deviates from the diamond cubic of Si and Ge, the β-Sn structure is still very closely related. Indeed, Sn forms intermetallic compounds with Li with many of the same ratios and structures as Si does, however, most processes used to create nanostructures are slow and resource-intensive. This is particularly so for nanoparticles of Sn [214] or hollow Sn spheres [215]. The difficulty in using nanoparticles is that they must be supported [216], even during preparation when using template synthesis [217], which may negate the advantage of their small size unless they are effectively unconstrained. One approach to achieve this is to support the Sn particles on fibers [185, 206, 218, 219] or even inside fibers [220], inside carbon shells [221] or nanotubes [214] or inside carbon 'onions' [222] or as C/Sn composite [223]. An alternative is to coat the Sn on a fiber [224].

A facile, template-free, low-temperature, industry-scalable method for preparing nanostructured tin anodes has been patented [207] and described in the literature [70]; this represents Sn's greatest advantage over Si or Ge, which have higher specific capacities [225]. The approach is to grow Sn nanowires using electrochemical deposition thus follows the method used for Si and Ge but with a commercially viable technology. This process has the potential for significantly increasing the energy storage and is not substrate-exclusive. A related materials structure has recently been produced by first growing SnO_2 nanowires using CVD and then reducing these to produce the Sn wires [184]; the drawbacks of using this indirect and much more expensive process will be discussed below. The present study reports on the microstructural changes that these materials undergo during lithiation and delithiation as observed through in-situ experiments

in the transmission electron microscope (TEM); preliminary reports of the lithiation of the materials produced by this novel approach have been given elsewhere [70, 226, 227].

6.1.2 Experimental

Although the technology has been demonstrated by manufacturing batteries using Sn nanoneedles as will be shown in this report, the detailed mechanisms are still being elucidated. For this purpose, in-situ TEM is the instrument of choice since it allows the chemistry and structure to be monitored down to the atomic scale, in principle, under operating conditions; i.e., in an *operando* mode. A Nanofactory TEM-STM holder was used for the in-situ experiment, which was carried out in an FEI Tecnai F30 TEM operated at 300 kV. The holder accepts one wire at each end for specimen mounting [32]; one end is fixed while the other is equipped with both mechanical motors and piezoelectric actuators so that contact can be made with 3D nanometer accuracy within the microscope. The Sn nanoneedles have been prepared by several routes that are based on the method described in [70]. In general this involves electroplating the Sn needles onto Cu TEM grids. FIB grids were used originally because the half-grid geometry makes them ready for mounting in the in-situ holder as-is, but in terms of specimen economy 400-mesh parallel-bar grids, cut in half after the deposition, are far superior. Bars can be removed from these grids with tweezers, so that one grid actually contains tens of independently testable beams coated in the material.

The Sn-plated Cu half-grid, which acts as the working electrode, is then attached to a piece of Al wire, 0.033 cm in diameter, using conductive epoxy; this wire is then used to mount the tin needles into the fixed end of the holder. Next, the holder is brought into a glove box with a dry He atmosphere where freshly-cut Li metal is scraped onto a piece of W wire, 0.025 cm in diameter, and mounted into the mobile end of the holder for use as the counter- and reference

electrode. A layer of Li_2O forms on the surface of the Li metal during the seconds of transfer from an air-tight bag into the microscope, and this oxide layer acts as the solid electrolyte.

Once the holder is in the microscope, the motor drive is used for coarse movements to bring the Li/Li_2O close to the Sn needle that is to be tested. Preliminary images and diffraction patterns are recorded and then the video recording is started; the piezo-drive is then used to make contact between the Li_2O layer and the Sn needle. The potential applied across the holder is initially set to be 0 V, and is gradually increased to -3 V in -0.5 V decrements. When delithiation is successful, the potential is held at +3 V. Video is recorded continuously throughout this process.

When performing in-situ microscopy, the choice of video recording software can have a significant impact on the information contained in the results. Specifically, the available recording frame rates and resolutions depend on the recording software, and if either of these is too low, then information may be lost.

6.1.3 Results

Characterization of the needles before lithiation is summarized in Figure 6.1. Figure 6.1a is a low-magnification SEM image showing the Sn coating on the Cu FIB grid. Figure 6.1b is a higher-magnification view of the same sample and demonstrates how the needles cover the surface; Figure 6.1c shows how this translates into the TEM. Figure 6.2 is a high-magnification, bright-field (BF) TEM image of a single needle with a corresponding diffraction pattern inset. The diffraction pattern is consistent with the tetragonal β-phase of Sn. There was no evidence of significant oxidation of the Sn needles. Small areas of moiré fringes on some of the needles suggested the possible onset of oxidation, but small regions of SnO or SnO_2 on the surface of a needle are not expected to have a significant influence on the results of the experiment.

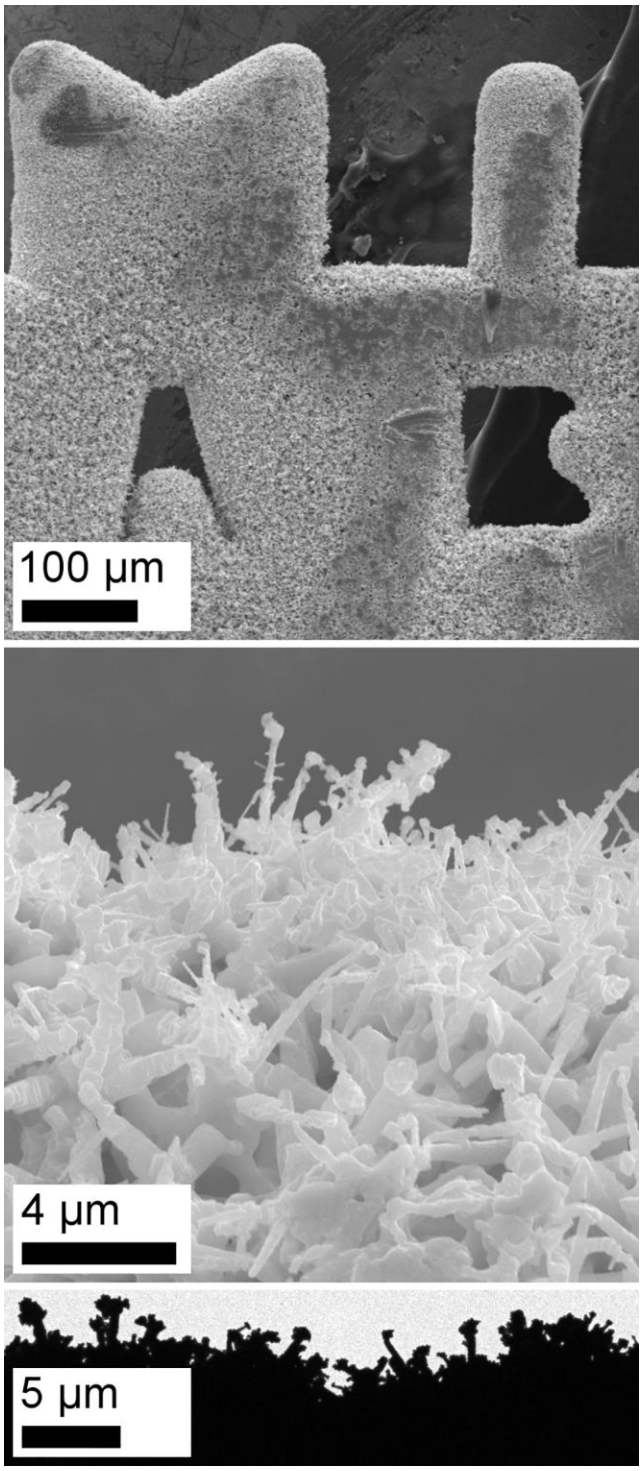

Figure 6.1. (a) Low-magnification secondary-electron SEM image of the Sn needles coating a copper Omniprobe FIB grid; (b) High-magnification SEM image of the same grid; (c) Low-magnification bright-field TEM image showing needles sticking out from the edge of the grid.

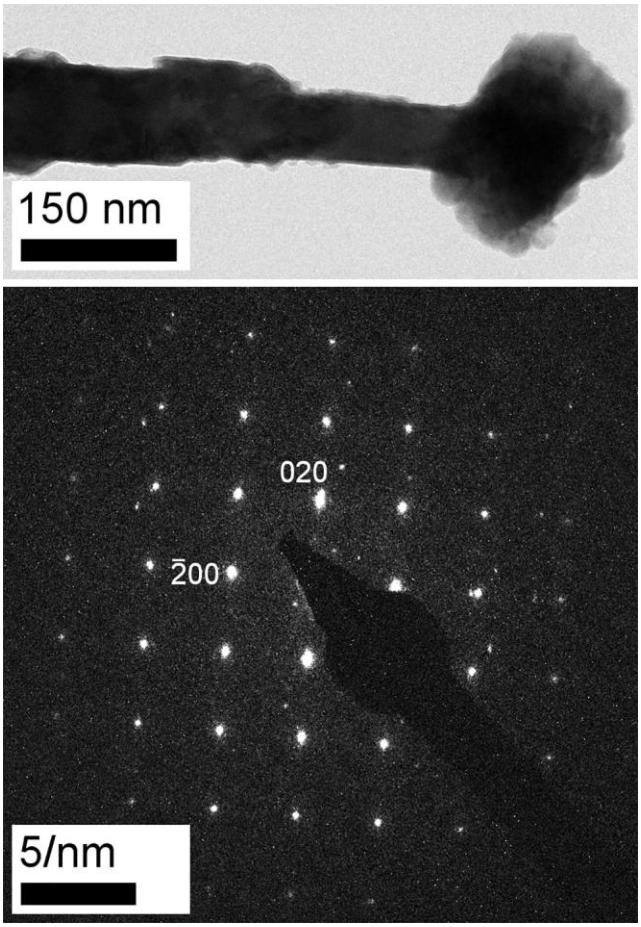

Figure 6.2. (a) High-magnification bright-field TEM image of a single Sn needle with (b) its corresponding diffraction pattern.

Figures 6.3 and 6.4 illustrate the progression of the lithiation process. Figure 6.3a shows a large needle with other, smaller needles branching off it. The Li source is visible at the bottom of the image. In general, the Li sources in these experiments did not show any rapid change due only to the electron beam. Figure 6.4 shows higher-magnification images of the small needle that branches off near the base of the large one, near the top of Figure 6.3a. In Figure 6.4a, the potential is still at 0 V; Figure 6.4b shows the needle just after the voltage of -3 V was applied and although it has moved, this is mainly due to the expansion of the large needle as it begins to lithiate. The length and radius of the needle both continue to increase noticeably in each subsequent image until it reaches its final state in Figure 6.4d, in which the contrast is lighter and more uniform.

Figures 6.3 c & d compare the entire large needle and its diffraction pattern after the experiment to its state before, as shown in Figures 6.3 a & b. The large needle and both of the smaller needles branching off of it increase substantially in length and radius between Figures 6.3a and 6.3b; however the other Sn structures visible in the top corners of the images, which were not in contact with the Li source and in fact are quite far removed from the needle of interest in the z-direction, did not change throughout the experiment. The spots in the pattern in Figure 6.3b are consistent with β-Sn, as expected. The first three rings in the pattern in Figure 6.3d correspond to d-spacings of 0.388 nm, 0.238 nm, and 0.204 nm. These plane spacings are close to the expected values for several of the Li-Sn intermetallics, although the fully-lithiated $Li_{17}Sn_4$ phase is the best match due to the lack of any rings between the first and second.

Figure 6.5 shows four bright-field TEM images of a different needle during a lithiation experiment along with the corresponding diffraction patterns taken at key timepoints shown in Figure 6.6. The pattern corresponding to Figure 6.5a (Figure 6.6a) was taken before contact was

made with the Li source (while the image shows contact being made); the spots match with single-crystal β-Sn and this needle in particular was nearly aligned on the [001] zone axis. The pattern in Figure 6.6b was recorded after lithiation, and it differs from the pattern in Figure 6.3d in three important ways. First, the rings are not as complete in Figure 6.6b suggesting significant texturing of the lithiated material. Second, upon careful examination rows of spots matching almost exactly with those in Figure 6.6a (i.e., corresponding to Sn metal) can be identified. Finally, although the rings corresponding to 0.201 nm and 0.238 nm d-spacings could correspond to nearly any phase, the ring corresponding to 0.261 nm is likely attributable to Li_2Sn_5, and other spots and rings are also present that do not match either Sn or the fully lithiated phase. This indicates that the original Sn structure has been partially preserved during lithiation, and that in this case the needle was not driven to the fully lithiated $Li_{17}Sn_4$ phase. Figure 6.6c represents the biggest surprise of this study. After delithiating the needle at +3 V the diffraction pattern returns to that of single-crystal β-Sn, this time oriented almost perfectly on the [001] zone axis (a rotation of just 7.8° about [010] compared to the pattern in Figure 6.6a). The image in Figure 6.5d was recorded at a higher magnification to show the Li source material built up on the outside of the needle after it was delithiated and the two electrodes were detached from one another. The built-up Li went back into the needle under the effects of the beam when the bias was returned to 0 V and the electrodes were separated, resulting in the final diffraction pattern in Figure 6.6d. Once again, in Figure 6.6d, systematic rows of spots matching (corresponding to Sn metal) those of Figures 6.6a and 6.6c can be identified, along with spots indicating the presence of lithiated material.

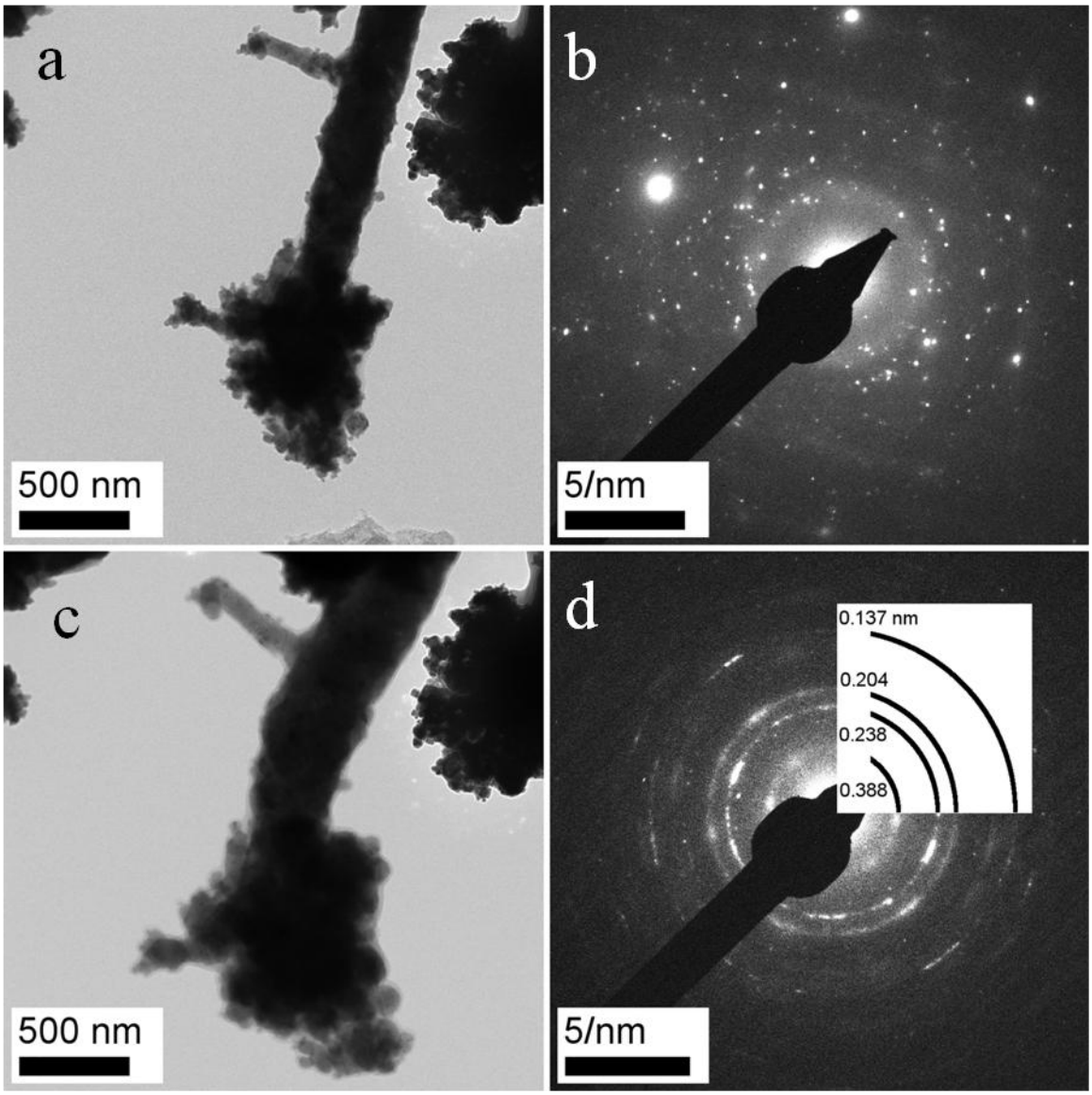

Figure 6.3. (a) A large, branched needle before contact with the Li source, which is visible at the bottom of the image, and (b) its diffraction pattern; (c) The same needle and (d) its diffraction pattern after the Li source was detached. The rings in (d) are labeled with their corresponding d-spacings for comparison with Table 6.2.

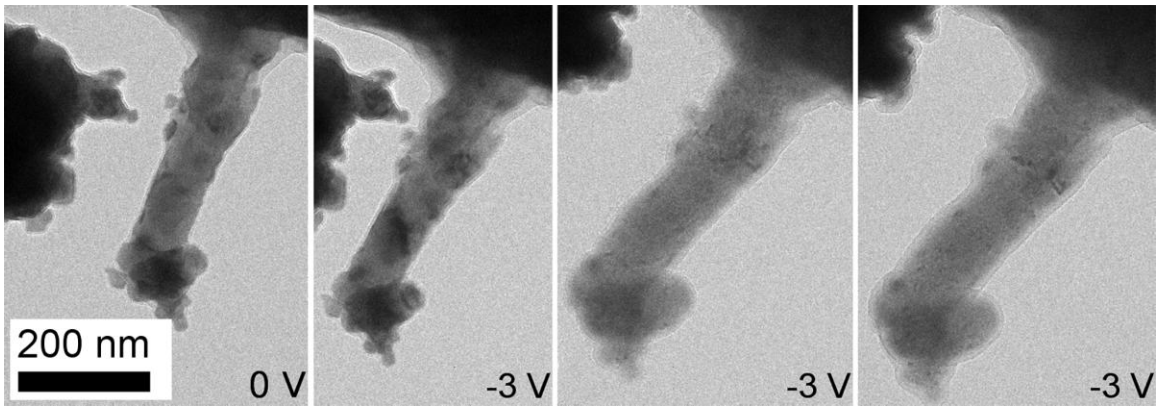

Figure 6.4. High-magnification bright-field images of the small needle close to the base of the larger needle shown in Figure 6.3; (a) immediately after the potential of -3 V was applied; (b) at the onset of lithiation of the small needle; (c) after extensive lithiation; and (d) after complete lithiation.

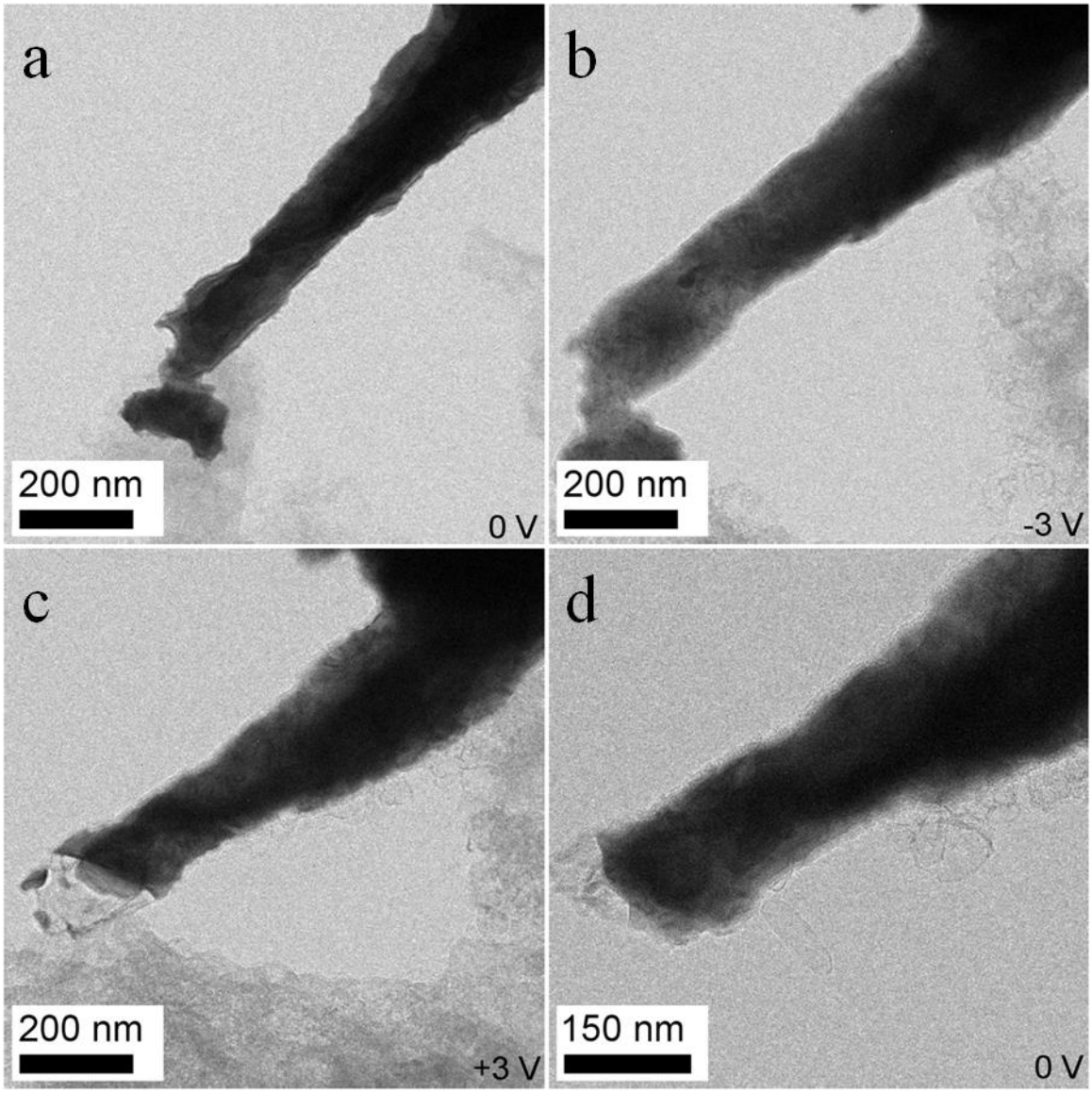

Figure 6.5. BF TEM images from key timepoints during the experiment: (a) before lithiation, consistent with β-Sn but off-axis; (b) after lithiation, consistent with a polycrystalline Li-Sn alloy; (c) after delithiation, again consistent with β-Sn and nearly on the [001] zone axis; and (d) partial re-lithiation after separating the two electrodes, caused by the beam.

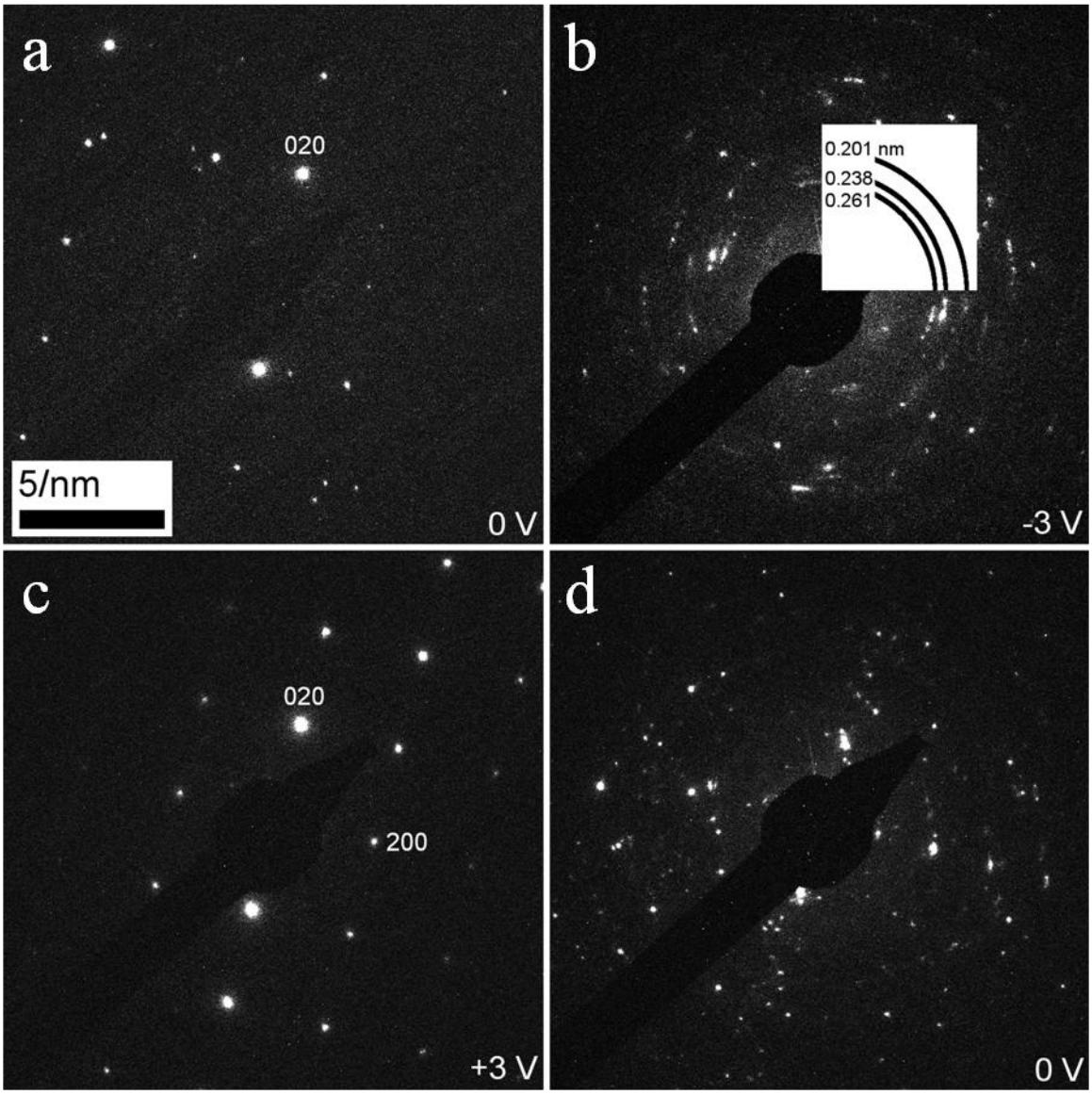

Figure 6.6. Diffraction patterns corresponding to the images in Fig 6.1.5 for key timepoints during the experiment: (a) before lithiation, consistent with β-Sn but off-axis; (b) after lithiation, consistent with a polycrystalline Li-Sn alloy; (c) after delithiation, again consistent with β-Sn and nearly on the [001] zone axis; and (d) partial re-lithiation after separating the two electrodes, caused by the beam.

Figure 6.7a shows another needle, which broke when the Li source contacted it, before lithiation. Figure 6.7b shows the same needle after lithiation. In this case, there is a significant loss of diffraction contrast in the lithiated needle along with the large volume expansion; the reaction proceeded much more quickly on this run compared to the one discussed with Figures 6.5 and 6.6.

6.1.4 Discussion

Inspecting Figures 6.3 and 6.4, it is obvious that the needles undergo a significant change in volume and crystal structure during lithiation. The large needle, which was in direct contact with the Li_2O during the experiment, appears to have experienced a larger volume change than the small needle branching off of its base. This observation is consistent with the experimental observation of the branching needle taking more time and a higher voltage to participate in the reaction. It is difficult to quantify the increase in volume because a single TEM image always shows a projection of the specimen. However as a first approximation, if the linear increase seen in this wire is taken to be representative, then the approximate 19% increase in the length of the large needle along with a 53% increase in diameter results in a final volume increase of 178%. The small needle, which was not in contact with the Li source, experienced only partial lithiation with a 16% increase in length and a 35% increase in diameter, or a 111% increase in volume. For full lithiation, the total volume increase is expected to be 300% [228]. The difference may be attributable to the very low area of the Sn film that is actually reacting with the Li source. If some of the Li is being driven further into the thick areas of the specimen, then the volume change in the needle(s) of interest will not be as great.

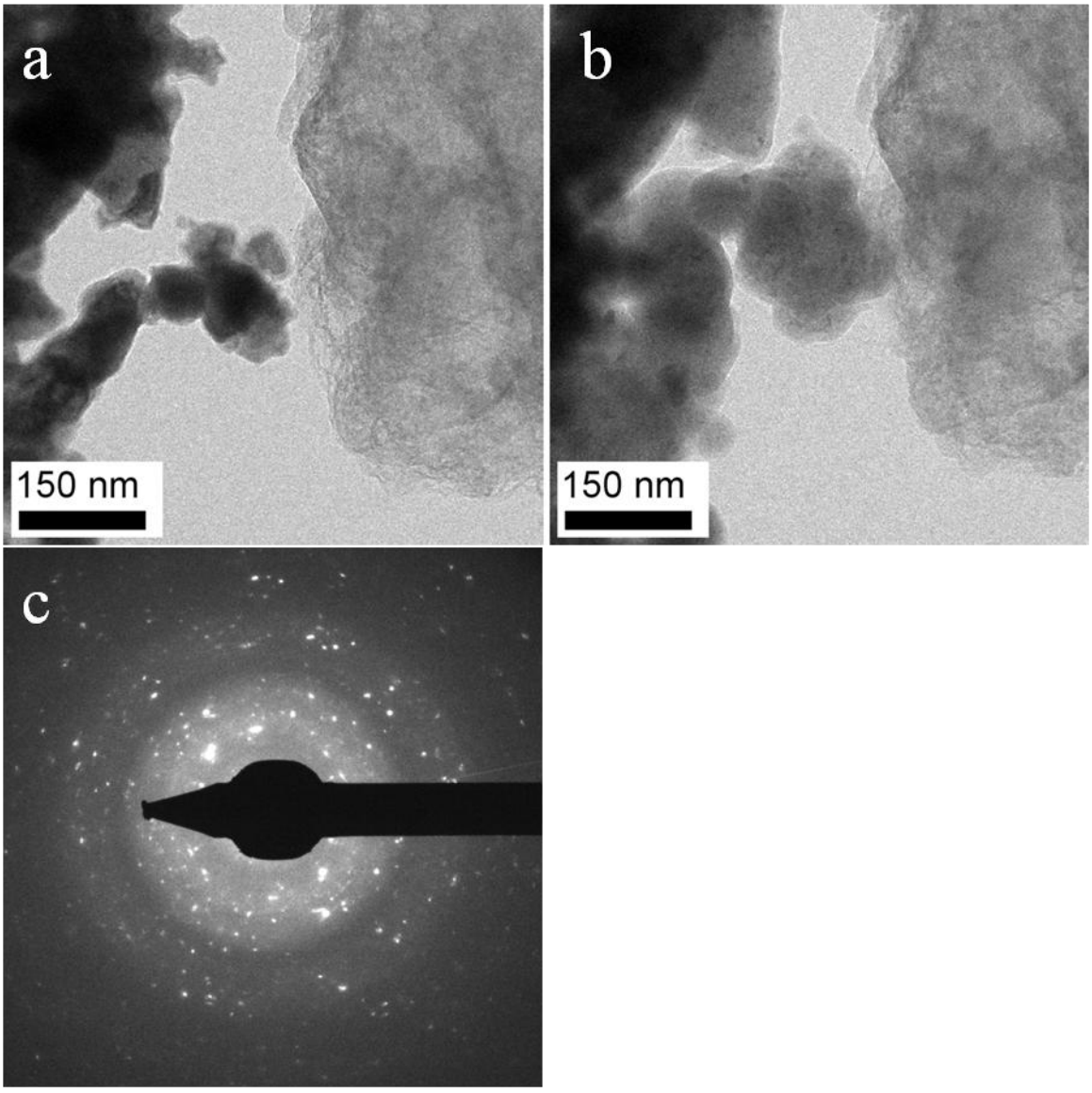

Figure 6.7. Two BF images (a) before and (b) after lithiation showing loss of contrast and larger increase in volume; (c) the diffraction pattern corresponding to the lithiated area in (b), which contained the needle that was in contact with the Li source and shows a pronounced amorphous halo in addition to spots.

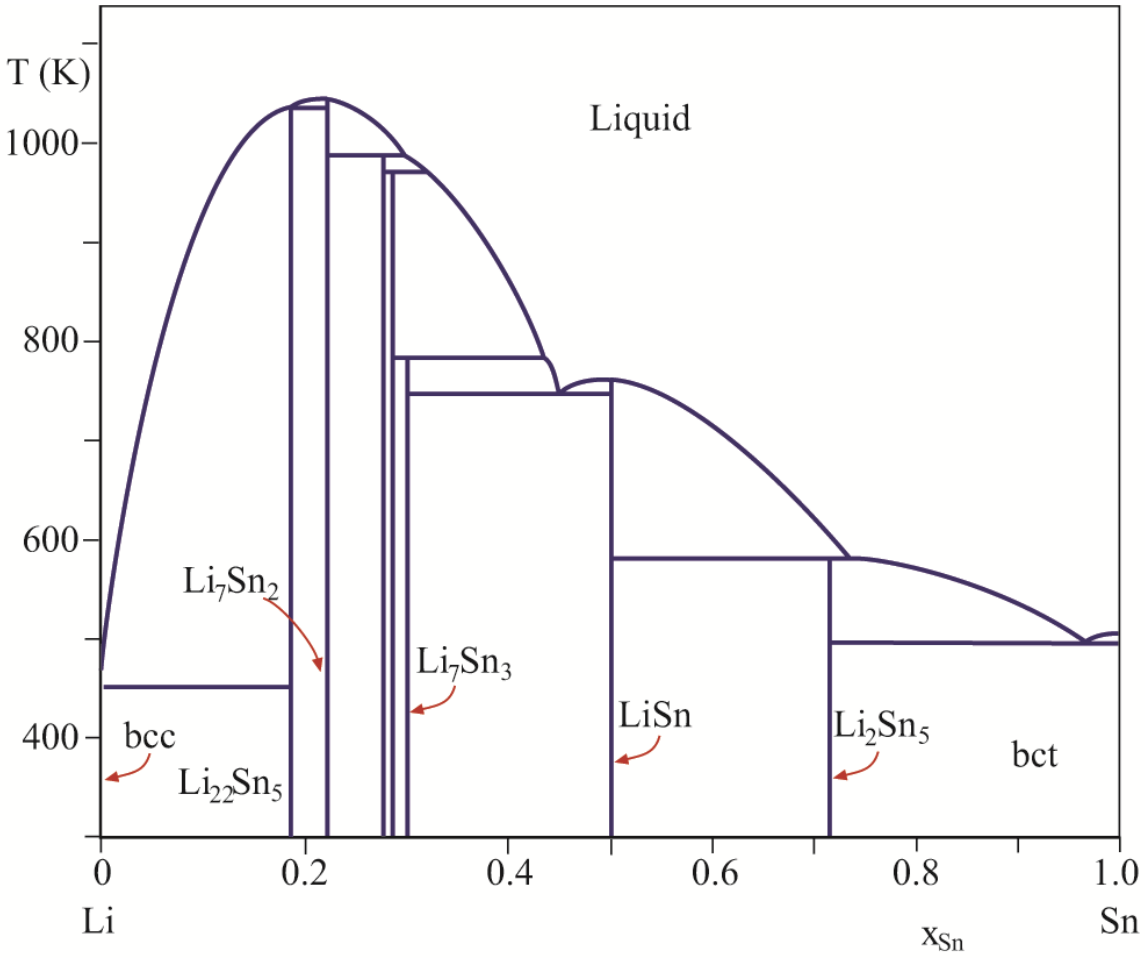

Figure 6.8. The equilibrium phase diagram for the Li-Sn system.

The equilibrium phase diagram for the Li-Sn system is shown in Figure 6.8. Li forms many intermetallic compounds with Sn. The fully-lithiated compound is generally cited as $Li_{22}Sn_5$ in most of the literature today (e.g. [183]); however, this does not take into account a series of structural refinements that have been made beginning in 1987 [229] and culminating in a combined X-ray and neutron diffraction study at Argonne in 2003, which ultimately revised the composition to $Li_{17}Sn_4$ [40]. $Li_{17}Sn_4$ has an fcc structure (space group F-43m) with a = 1.96907 nm [40]. Its structure is very closely related to $Li_{22}Sn_5$ (fcc, space group F23, a = 1.978 nm); the actual compositions are $Li_{340}Sn_{80}$ vs. $Li_{352}Sn_{80}$ and the difference between the two lies in the exact occupancy and distribution of the Li sites. Since electrons interact much more strongly with the heavier Sn atoms, and since the lattice constants of the two structures are within 0.01 nm of one another, it is not possible to differentiate between the $Li_{17}Sn_4$ and $Li_{22}Sn_5$ structures in the TEM.

The large, complex structure of the fully-lithiated phase (cited in this work as $Li_{17}Sn_4$) means its diffraction pattern features a great number of reflections, and many of these overlap with reflections associated with the other compounds formed by Li and Sn. This can make the analysis of Li-Sn diffraction patterns quite difficult; Table 6.1 lists the important d-spacings for each Li-Sn intermetallic to aid the discussion of the various diffraction patterns presented in this work. Of course, the materials studied here are not in equilibrium.

Other materials such as Si have been shown to expand anisotropically upon lithiation [211]. The anisotropic expansion of Si upon lithiation is attributed to the anisotropic diffusion rate of Li in Si, which is related to the cross-sectional area of the "channels" between columns of atoms. These channels are very small in <111> directions in the diamond cubic structure, and largest along the <110> directions. Preliminary results do not suggest this to be the case for Sn, even

though a similar disparity in channel width exists. If the Sn does indeed expand isotropically, then the kinetics of the reactions in these experiments are likely too fast for the thermodynamically favorable diffusion pathways to dominate. This hypothesis is supported by the recent work of Luo et al. [187] who demonstrated that the lithiation of graphene-encapsulated Si nanoparticles proceeds isotropically at first, but after several minutes the interface between the lithiated and pristine material develops facets, suggesting anisotropic lithiation. However, it is important to note that so far, it has not been possible to identify such an interface between lithiated and pristine Sn in the materials used is this study.

Comparing the results of Figures 6.3-6.7, it is likely that the needle in Figure 6.5 was not lithiated to as great an extent as the ones in Figures 6.3 and 6.7; the rings in Figure 6.6b match best with the lowest Li-content Li-Sn phases. In this case, an option in the controller software (i.e., the current range) that limits the nominal current through the holder to 10 nA was used. While the accuracy of such small current measurements is uncertain and the current through the needle is certainly considerably smaller than this value, the rate of the reaction was indeed greatly reduced in this experiment. The needle shown in Figure 6.7 represents the opposite extreme; in this experiment, lithiation proceeded very quickly (i.e., in seconds), possibly due to a short circuit or overvoltage caused by a particularly thin or broken layer of Li_2O. Clearly, improved methods for measuring the actual current will be required for quantitative analysis. The loss of diffraction contrast in the image, along with the diffuse rings in the diffraction pattern in Figure 6.7c, suggests that this needle was partially amorphized during lithiation. The presence of spots within the diffuse rings indicates that some crystallinity remains. It is proposed that the very high reaction rate was responsible for partly amorphizing the needle.

Table 6.1. List of d-spacings in Li-Sn intermetallics for planes whose reflections have relative intensities above 20% in X-ray diffraction spectra. Data is based on ICDD tables.

Phase	d (Å)	Relative Intensity (%)	h	k	l	Comments
Li_2Sn_5	4.59	40.1	2	1	0	Bright ring/pair of rings at r = 3.07-3.2 nm^{-1}.
	3.25	87.5	3	1	0	
	3.13	100.0	0	0	1	Tetragonal crystal system, space group P4/mbm (127).
	2.49	60.4	4	1	0	
	2.25	59.7	3	1	1	
	2.11	37.4	3	2	1	
	1.95	45.1	4	1	1	
LiSn	5.00	48.1	1	0	0	Ring at r = 2 nm^{-1}, then two broad rings in the ranges of 2.67-3.14 nm^{-1} and 4.00-4.27 nm^{-1}.
	3.75	100.0	0	0	2	
			1	0	1	
	3.44	87.9	-1	0	2	Monoclinic crystal system, space group P2/m (10).
	3.18	85.8	0	1	0	
	2.50	54.8	0	0	3	
			-1	0	3	
	2.43	66.3	0	1	2	
			1	1	1	
	2.34	65.1	-1	1	2	
	1.96	42.3	0	1	3	
			-1	1	3	
Li_7Sn_3	4.09	100.0	0	1	1	Broad ring in the range of r = 2.4-3.1 nm^{-1} (or three distinct rings); one ring at r = 4.24 nm^{-1} and nothing significant further out than this.
	3.58	60.9	2	1	0	
			-2	2	0	
	3.27	30.4	2	0	1	Monoclinic crystal system, space group P21/m (11).
			-2	1	1	
	2.36	61.1	0	0	2	
			-4	1	0	
	2.35	28.3	2	2	1	
			-2	3	1	
	2.04	24.9	4	0	1	
			-4	2	1	
Li_5Sn_2	4.02	100.0	1	0	1	Bright ring at r = 2.5 nm^{-1}, possibly "smudged out" to 2.63 nm^{-1}. Another, dimmer ring at r = 4.22-4.3 nm^{-1}.
	3.79	39.0	0	1	2	
	3.31	20.0	0	0	6	
	2.85	20.0	0	1	5	Rhombohedral crystal system, space group R-3m (166).
	2.37	36.0	1	1	0	
	2.33	33.0	1	0	7	
	1.92	21.0	1	1	6	

Phase	d (Å)	Relative Intensity (%)	h	k	l	Comments
$Li_{13}Sn_5$	3.96	100.0	0	1	1	Bright ring at r = 2.5 nm^{-1}, may be "smudged out" to 2.92 nm^{-1}. Another ring at r = 4.26 nm^{-1} should be sharper than the Li_5Sn_2 ring at nearly the same spacing, with fewer spots in between these rings. Hexagonal crystal system, space group P-3m1 (164).
	3.68	34.4	0	1	2	
	3.42	20.9	0	0	5	
	2.35	37.6	1	1	0	
	2.34	37.4	1	0	6	
	1.94	21.6	1	1	5	
Li_7Sn_2	4.16	93.2	1	3	0	Bright ring centered around 2.45 nm-1 (2.4 nm^{-1}-2.5 nm^{-1} range). Another ring (or 2 rings) between this and a bright ring at r = 4.31 nm^{-1}; the next ring is at r = 4.85 nm^{-1}. Orthorhombic crystal system, space group Cmmm (65).
	4.08	71.2	1	1	1	
	4.00	41.0	2	2	0	
	3.91	100.0	0	2	1	
	3.41	41.6	2	0	1	
	3.18	36.4	3	1	0	
	2.32	87.2	1	5	1	
			3	3	1	
	2.06	24.0	1	3	2	
$Li_{17}Sn_4$	4.52	41.9	3	3	1	Nothing significant between bright rings at r = 2.63 nm^{-1} and 4.31 nm^{-1}; next ring after 4.31 nm^{-1} is further out than the one for Li_7Sn_2, at r = 5.05 nm^{-1}. Cubic crystal system, space group F-43m (216).
	4.02	81.4	4	2	2	
	3.79	100.0	5	1	1	
	2.32	93.7	6	6	0	
	1.98	21.3	9	3	3	

(Table 6.1, continued)

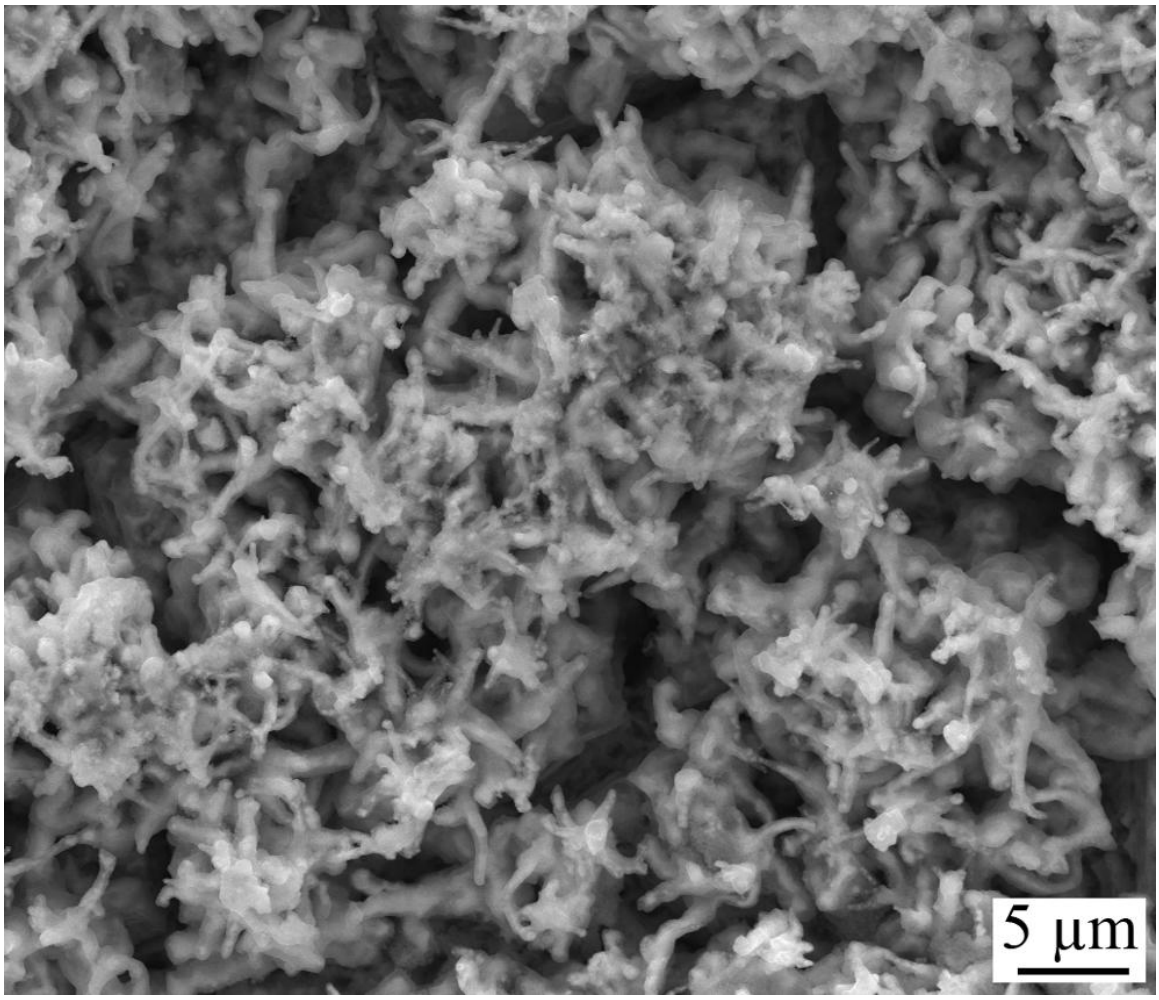

Figure 6.9. Scanning electron micrograph of the tin nano-needle anode after a single lithiation cycle in a coin battery.

There are some significant drawbacks of the technique currently being used that may contribute to such inconsistency. First, it is very difficult to control the size and shape of the Li counter electrode, on a scale meaningful for in-situ TEM, when the electrode is made by scratching Li onto a piece of wire in a glove box. The Li source used in the experiment that generated Figure 6.5 featured a very small protrusion; while this was convenient for making contact with very small needles it also made it difficult to maintain contact as material was drained from the protrusion. In comparison, the edge of the Li source in Figure 6.3a protrudes much less, and has a much larger area of contact with the bulk of the electrode to draw lithium from. The same is true for the Li source in Figure 6.7.

Second, when performing electrochemical experiments in a high-energy electron beam, the nominal potential difference between the two electrodes is inherently suspect. Related to this is the variable thickness of the Li_2O layer formed on the Li electrode during transfer from the glove box to the TEM. Driving Li ions through a thicker electrolyte layer would be more difficult, and it is reasonable to expect that the reaction would proceed differently at the same (nominal) applied potential for different oxide layer thicknesses.

The lack of control over the size and shape of the lithium counter-electrode is a major drawback to this technique, as is the inability to reliably delithiate the needles. It is also, of course, not possible simultaneously to directly record in-situ diffraction data while recording the images.

However, while the experiment summarized in Figures 6.5 and 6.6 was different from the others, it may also have been the most representative of how this material really behaves in a full-scale battery. Figure 6.9 shows an image of the tin nano-needle anode after a single lithiation cycle in a coin battery. The needles are clearly still present as was found in the in-situ TEM work and there is a clear SEI layer. Other coin cells were opened after various numbers of higher cycles

which will allow a full, (separate) ex-situ study of the development of the SEI layer, which is critical to the long-term operation of any lithium-ion battery.

The approach described in this work differs significantly from that of Li et al. [184]. The latter reports on Sn-C composite wires prepared by the reduction of SnO_2 wires, in comparison to the pure Sn needles reported here that have the advantage of being prepared by an industry-scalable process. While the C coating appears to be advantageous in these in-situ TEM experiments, both for improved conductivity and in limiting the volume expansion of the material, it is essential to remember that the ultimate application of these materials will be in real batteries with organic liquid electrolytes. It seems unlikely that a few-atomic-layer carbon coating will have a significant effect on the chemistry of the solid-electrolyte interphase (and by extension the performance of the electrode), and as such studies on pure Sn may provide information that is more relevant to the performance of the ultimate product of these studies.

One of the main disadvantages of nanomaterials is their dependence on processes like the vapor-liquid-solid (VLS) growth mechanism [230], which is used to grow Si (and other) NWs [231-234]. This approach relies on the passage of the material of interest, in vapor (V) form, through a liquid (L) catalyst droplet, which mediates its deposition as a solid (S) on the substrate. The vapor-phase reactant(s) and liquid catalyst naturally require that the process take place at high temperature, and the catalyst itself is generally an expensive metal. For example, Si NWs are grown with an Au catalyst at ~500 C [235], while C nanotubes have been grown with a Ni catalyst at ~800 C [236]. The expense of high-temperature processing is exacerbated by low growth rates, and the cost may be further increased for reactions that require an inert atmosphere. While this is certainly sustainable for creating model systems for exploratory studies, production of nanomaterials using the VLS mechanism is ill-suited to industrial-scale applications.

An alternative preparation route is to electroplate nanomaterials with the aid of a template; for Sn this has been achieved by, e.g., using anodic aluminum oxide as a template material [237, 238]. However, template-reliant processes are composed of many steps, which also limits scaling them up to commercial levels due to increased expense. Additionally, the template material is ultimately discarded, which would drive up the cost of anything produced by this type of approach.

The results described in this paper are unique in that they represent a material produced by an electroplating process that is both template-free (i.e., quite simple) and low temperature; the arrays Sn nanoneedles can be formed on Cu substrates that are large enough to be relevant to the battery industry. This processing route can also be extended to other substrates, however, it is interesting to note that the intermetallic, Cu_6Sn_5, that can form when Sn needles grow on a Cu substrate has also been considered as a candidate for LIBs [239].

6.1.5 Conclusions

It has been demonstrated that individual, single-crystal Sn nanoneedles can be studied during electrochemical lithiation inside the TEM. In most cases, the needles transformed into a polycrystalline Li-Sn intermetallic compound, though sometimes they appeared to amorphize if the reaction proceeded quickly enough. In many cases the reaction could not be reversed, and it is unclear if this is a result of the properties of the lithiated needles or simply inconsistent performance of the special holder required to carry out these experiments. When the reaction was reversed successfully, it was discovered that the Sn needle reverted to its original single-crystal, β-Sn structure.

These preliminary lithiation experiments on Sn nanoneedles raise many questions. It is possible that the lithiation rate is orientation-dependent, and that a high rate of lithiation causes

amorphization of the Sn needles. It is clear that the reaction is reversible in some cases and not in others. This can be related to variations in the quality of electrical contact between the electrodes between experiments; poor contact may be due to physical (volume changes of the electrodes) or chemical (impedance of the solid electrolyte layer or possible build-up of a high-impedance layer between the electrodes) phenomena that are difficult to control. It is particularly interesting that crystalline Sn can definitely be reformed upon delithiation of an Sn-Li compound. However, the fundamental lack of control over the exact experimental conditions from run to run makes the isolation of variables difficult. This control is being improved with the development of new on-chip devices [32, 240], including devices allowing the use of other liquid electrolytes [241, 242]. It is stressed that it has been demonstrated that the electrochemical plating process used to produce the materials examined in this study means that they are indeed suitable for use in commercial coin-cell batteries.

6.2 Remaining questions

Several questions arise from these preliminary results. For example, it is not yet clear whether the lithiation rate of the needles depends on their orientation; if this is indeed the case then some needles may be preferentially amorphized by a faster reaction rate. Why the reaction is irreversible in some cases, but not in others, also remains a problem. Perhaps the most intriguing question is: how can single-crystal Sn re-form from a polycrystalline Li-Sn intermetallic when delithiation is successful?

However, variables are difficult to isolate without precise control over experimental conditions between runs. This issue can be addressed in part by the use of a new, more advanced potentiostat that has been installed at CINT since these experiments were performed, as well as the recent development of new on-chip devices [12, 15].

6.3 Reversibility of Li insertion in Sn nanoneedles in the Sn-rich regime

Using the new potentiostat at CINT, much greater control over the potential applied across the Nanofactory STM-TEM holder, as well as the current flowing through it, is possible. This will be used to perform a detailed study of the early stages of the lithiation of Sn nanoneedles, in which it has been demonstrated that a reversible transformation from single crystal Sn to polycrystalline Li-Sn to single crystal Sn can occur.

Cyclic voltammetry data may also be collected; experiments combining this technique with electron diffraction will be designed to isolate and analyze individually the transitions between the various Li-Sn intermetallics during the lithiation process.

Using CINT's unique Discovery Platform, which consists of a small electrical chip that can be sealed, the lithiation and delithiation of Sn nanoneedles will be studied in a commercial liquid electrolyte, as discussed in Chapter 7.

7 Future Research

7.1 Chemical lithiation and exfoliation of MoS_2

As discussed in Chapter 3, the specifics of the 2H-1T phase transformation have not yet been satisfactorily described in the literature. Using the Hummingbird liquid flow cell, it should be possible to observe this phase transformation directly. The 1T phase is generally observed after chemical lithiation of MoS_2, and this can be achieved by soaking MoS_2 in, e.g., a 1.6M solution of n-butyl lithium in hexane [243].

To reproduce this reaction in the TEM, MoS_2 lamella will be placed at the corners of silicon nitride TEM windows (membrane thickness 5 nm, Norcada) in both the plan-view and edge-on orientations. The liquid cell will be loaded with plain hexane, with additional hexane flowed through the tubes leading into and out of the holder to minimize the introduction of oxygen to the n-butyl lithium solution.

When the holder is situated in the microscope with pure hexane flowing through it and preliminary images have been recorded, the syringe supplying the hexane will be switched to one containing the n-butyl lithium in hexane. It will be important to take all measures possible to minimize the exposure of this solution to air while it is transferred from the glove box and hooked up to the holder.

With the n-butyl lithium solution flowing through the cell, the MoS_2 will begin to lithiate chemically, and the structural changes will be monitored with periodic imaging. Because the 1T phase is metastable and has been known to revert to the 2H phase upon modest heating [96, 97] or even under the effects of high-energy electron radiation (as observed during this work), it is

likely that low-dose techniques will be required to properly capture the structural evolution of the MoS_2 as it lithiates.

Upon full lithiation of the MoS_2, it will also be possible to observe, *in situ*, the exfoliation process. Exposure of lithiated MoS_2 to water, methanol, ethanol, and isopropanol has been reported to result in exfoliation [243]. To avoid a potentially vigorous reaction with the n-butyl lithium solution, the latter will be cleared from the liquid lines with hexane, and then the exfoliating solvent will be introduced to the holder.

There are several potential challenges facing this experiment. In the first place, the chemical intercalation of MoS_2 is a rather slow process. For example, Joensen et al. describe soaking the MoS_2 in the n-butyl lithium solution for two days before full lithiation is achieved [243]. Furthermore, although this process is commonly used to produce the 1T phase of MoS_2, it is possible that this will be impossible to detect in this experiment because the thickness of the cell will preclude high-resolution imaging. Since liquid-cell microscopy is commonly performed using STEM rather than conventional TEM, conventional diffraction will also be unavailable for the verification of the phase of the MoS_2. It may be possible to work around these limitations using nanodiffraction in STEM mode, or, cell thickness permitting, EELS to check for signs of the 1T phase. Additionally, some exposure to air of the n-butyl lithium solution will be unavoidable, which may have a negative impact on the results. Finally, the exfoliation reaction results in significant hydrogen evolution. Although the literature on this subject describes the process for bulk quantities of MoS_2 and hence the majority of this gas certainly comes from the reaction of the lithium solution with the exfoliating solvent, it is possible that hydrogen bubbles created during exfoliation could confuse the image contrast, block further reaction of the lithiated MoS_2 with the solvent, or, at worst, rupture the cell windows.

To assess the risk of the latter, the first run of this experiment will be performed with thicker, more robust silicon nitride windows (50 nm). Although this will have a significant, adverse effect on the quality of images that can be obtained, it will serve as a safe proof-of-concept, and catastrophic failure of a liquid cell inside the microscope must be avoided at all costs.

7.2 Electrochemical and chemical sodiation of MoS_2

Although it is important to improve the performance of the currently-dominant LIB technology as much as possible, the future of battery technology must also be considered. Sodium is a strong candidate eventually to replace lithium as the energy-storing ion of choice, chiefly due to its natural abundance on earth and the fact that it is not geographically isolated as lithium is. This being the case, sodium is also significantly cheaper than lithium; in fact, last year the per-ton cost of Na was $1/20^{th}$ that of Li [9]. However, since the Li-ion technology is already decades old, Na-ion batteries currently lag behind their LIB counterparts significantly on every figure of merit [9]. Growing usefulness in battery applications is also likely to eventually drive the price of Na up, although it may be guessed that its abundance will ensure that it remains cheaper than Li.

To this end, the electrochemical and chemical lithiation experiments performed on MoS_2 will be repeated, with the lithium replaced by sodium. The initial electrochemical experiments will be conducted using the solid-state half-cell setup in the Nanofactory STM holder, with MoS_2 specimens prepared in both plan-view and edge-on orientations as described in **§2.5**. Liquid-cell experiments using the Discovery platform will also be carried out, although the preparation and transfer of appropriately-sized MoS_2 specimens will represent a particular challenge. The chemical sodiation experiment will be carried out in the Hummingbird holder, with the electrolyte in the fluid lines to prevent evaporation but not flowing through the cell.

7.3 Comparison with synthetic MoS_2 specimens

As mentioned briefly in Chapter 1, synthetic MoS_2 is more pure and tends to be more crystallographically perfect than natural samples. The resources and manpower were not available to undertake the preparation of synthetic specimens during this project; a detailed chemical analysis of the impurities contained in the natural sample along with analogous in-situ TEM experiments conducted on synthetic MoS_2 could elucidate what role, if any, is played by impurities in the lithiation and delithiation processes in MoS_2. Additionally, the 3R polytype is commonly observed in synthetic MoS_2 specimens prepared by the acidification of ammonium tetrathiomolybdate followed by heat treatment [244]. A comparison of the lithiation of 3R-MoS_2 to the 2H variety, especially in the "edge-on" orientation with the basal planes parallel to the beam, may be very enlightening with respect to the discussion of the lithiation mechanism of MoS_2 presented in Chapter 4.

7.4 Electrochemical sodiation of Sn nanoneedles

The electrochemical lithiation experiments performed on Sn nanoneedles will also be repeated, with the lithium replaced by sodium. The fully-sodiated phase is $Na_{15}Sn_4$, which is crystalline, but several intermediate, amorphous phases have been reported to occur before this final phase is formed [245]. The theoretical specific capacity of a Sn anode in a Na-ion battery is 847 mAh/g, which is slightly lower than the 994 mAh/g capacity of Sn in a LIB [9]. As for the case of Li insertion, loading the Sn structure with such a large quantity of Na results in a dramatic volume expansion. Fully-sodiated Sn nanoparticles have been reported as swelling up to 4.59 times their original volume [245].

7.5 Lithiation and sodiation of Sn nanoneedles supported on graphene

Because some materials have been shown to take up lithium in different ways when supported on "sheets of graphene" compared to making direct contact with the current collector [55], this phenomenon would be intriguing to examine with the Sn material described in Chapter 6. The graphene sheets will be prepared by mechanical exfoliation, and loaded onto an etched W probe. The Sn needles will then be gently scraped from a Cu substrate onto the graphene. Because Cu_6Sn_5 has also been investigated as a LIB electrode material [31], and because it forms readily at the Cu-Sn boundary, it may be possible to investigate Cu_6Sn_5 in this way as well.

7.6 Sn Whiskers

One of the most puzzling characteristics of Sn is its tendency to spontaneously develop long, single-crystal whiskers on its surface over time; this is especially characteristic of Sn films electroplated onto Cu [246, 247]. This is a significant problem in the microelectronics industry, which widely uses Sn-based solders and protective coatings. Although this phenomenon has been known for many years, its mechanism is still not understood. In the case of Sn films on Cu substrates, the continuous formation of the Cu-Sn intermetallic phase at the interface is widely accepted as the source of the stress that drives whisker formation. However, no correlation between the features of the Cu-Sn layer and the locations where whiskers are formed has been found. Furthermore, as Lee and Lee point out, the formation of Cu_6Sn_5 actually causes a reduction in total volume (which may account for the voids that are commonly seen along the Cu-Sn interface), although a compressive stress in the Sn film can still be induced if the intermetallic phase forms in the Sn grain boundaries [247]. This is because the intermetallic is primarily formed by the Cu diffusing into the Sn [247].

The structure of the grain boundaries in the Sn films has also been implicated in whisker formation, especially because whiskers frequently border more than one grain and thus intersect the grain boundary at their base. It is argued that the grain boundary provides a diffusion pathway for Sn atoms to be extruded so as to relieve the stress induced by the growing Cu-Sn phase beneath. Some have argued that new grains that were not originally present in the Sn films nucleate after deposition and grow into whiskers. Chason et. al. recently proposed an interesting variation on this idea, in which two grains pinch in on a third grain between them [246]. This sort of grain boundary motion might occur if the strain-energy density of the center grain is higher than that of the two on either side of it, because then such grain boundary migration would result in a reduction of the total strain-energy density in the film. The points at the top and bottom are envisioned as being held in place by the surface grooves at the top and by Cu-Sn intermetallic grains at the bottom. This mechanism explains how an oblique grain boundary could be formed underneath a surface grain without the need for actually nucleating and growing the surface grain [246]. A qualitative argument against such a mechanism might be that it seems unreasonable to expect such a grain, whose energy is high enough so as to spontaneously shrink while its neighboring grains grow into it, to be a favorable destination for migrating Sn atoms. An alternative mechanism involves the formation of sub-grain boundaries by arrays of dislocations, which "may have a lower barrier for forming surface grains than stress-assisted grain boundary migration" [246].

Lee and Lee proposed that the growth of whiskers could be related to the expansion of dislocation loops by climb on (100) planes until it meets the grain boundary, at which point it glides in the [100] direction [247].

Other materials have also been shown to produce such single-crystal whiskers; for example, some work has been done on Bismuth whiskers [248]. Bi is very near to Sn in the periodic table, being one period down and one group to the right. In this case as well, the role of grain boundaries, specifically their mobility (or lack thereof) and orientation with respect to the whisker is thought to be quite significant, although the driving stress is provided by elevated temperature rather than the formation of an intermetallic within the grain boundaries. The grain boundary mobility is related to the formation of hillocks vs. whiskers. If the grain boundaries of the growing feature are immobile, then a whisker can form; if the grain boundaries allow grain broadening, then a hillock will form instead [248]. Such hillocks are also observed in Sn, but in Sn the entire process seems to be somewhat more complex and so it is not safe to draw analogous conclusions.

7.7 Imaging dislocations in intermediate-voltage microscopes

In 1961, Howie and Whelan developed a dynamical theory of diffraction as applied to images of dislocations and stacking faults [249, 250]; their work included equations to take into account many diffracted beams, which must be the basis for contrast analysis in intermediate-voltage microscopes in which many beams will always contribute to the image. In order to extend this analysis to defects imaged in intermediate-voltage TEMs, experimental images of well-understood defects (e.g., dislocations in FCC metals) will be recorded using 300 keV electrons. Advanced image simulation techniques will be employed if relevant software exists, or developed if it does not.

References

[1] R.A. Huggins, Advanced batteries: materials science aspects, Springer, 2009.
[2] K. He, H.L. Xin, K. Zhao, X. Yu, D. Nordlund, T.C. Weng, J. Li, Y. Jiang, C.A. Cadigan, R.M. Richards, M.M. Doeff, X.Q. Yang, E.A. Stach, J. Li, F. Lin, D. Su, Transitions from near-surface to interior redox upon lithiation in conversion electrode materials, Nano Lett 15 (2015) 1437-1444.
[3] S. Liu, J. Xie, Q. Su, G. Du, S. Zhang, G. Cao, T. Zhu, X. Zhao, Understanding Li-storage mechanism and performance of MnFe2O4 by in situ TEM observation on its electrochemical process in nano lithium battery, Nano Energy 8 (2014) 84-94.
[4] E. Strelcov, J. Cothren, D. Leonard, A.Y. Borisevich, A. Kolmakov, In situ SEM study of lithium intercalation in individual V2O5 nanowires, Nanoscale 7 (2015) 3022-3027.
[5] Lead acid battery market analysis by product (SLI, stationary, motive), by construction method (flooded, VRLA), by application (automotive, UPS, telecommunication, electric bikes, transport vehicles) and segment forecasts to 2022, 2016 (2016)
[6] U.S. Department of Energy, Grid energy storage, (2013) 1-66.
[7] M. Obrovac, L. Christensen, D. Le, J. Dahn, Alloy design for lithium-ion battery anodes, J Electrochem Soc 154 (2007) A849-A855.
[8] X.H. Liu, L. Zhong, S. Huang, S.X. Mao, T. Zhu, J.Y. Huang, Size-dependent fracture of silicon nanoparticles during lithiation, ACS Nano 6 (2012) 1522-1531.
[9] T. Stephenson, Z. Li, B. Olsen, D. Mitlin, Lithium ion battery applications of molybdenum disulfide (MoS2) nanocomposites, Energy & Environmental Science 7 (2014) 209.
[10] R.A. Huggins, Lithium alloy negative electrodes formed from convertible oxides, Solid State Ionics () 113–115 (1998) 57–67.
[11] C.B. Carter, P.M. Williams, An electron microscopy study of intercalation in transition metal dichalcogenides, Philos Mag 26 (1972) 393-398.
[12] L. Marton, Electron microscopy of biological objects, Nature 133 (1934) 911.
[13] M. Knoll, E. Ruska, Das Elektronenmikroskop, Zeitschrift für Physik 78 (1932) 318-339.
[14] L. Marton, La microscopie electronique des objets biologiques, Bull. Acad. Roy. Med. Belg 21 (1935) 600-617.
[15] F. Krause, Das magnetische Elektronenmikroskop und seine Anwendung in der Biologie, Naturwissenschaften 25 (1937) 817-825.
[16] U. Valdrè, Electron microscope stage design and applications, Journal of Microscopy 117 (1979) 55-75.
[17] M.J. Whelan, Proc 4th Int Congr on Electron Microsc 1 (1958) 96.
[18] D. Pashley, A. Presland, The observation of anti-phase boundaries during the transition from CuAu I to CuAu II, J Inst Met 87 (1958) 419-428.
[19] H.G.F. Wilsdorf, Apparatus for the deformation of foils in an electron microscope, Review of Scientific Instruments 29 (1958) 323-324.
[20] P. Forsyth, R. Wilson, Device for straining and fracturing thin foil specimens inside an electron microscope, Journal of Scientific Instruments 37 (1960) 37-38.
[21] P. Price, On dislocation loops formed in zinc crystals during low temperature pyramidal glide, Philosophical Magazine 6 (1961) 449-451.
[22] G.R. Piercy, R.W. Gilbert, L.M. Howe, A liquid helium cooled finger for the Siemens electron microscope, J Sci Instrum 40 (1963) 487.
[23] J.A. Venables, Liquid helium cooled tilting stage for an electron microscope, Review of Scientific Instruments 34 (1963) 582-583.

[24] H.G. Heide, K. Urban, A novel specimen stage permitting high-resolution electron microscopy at low temperatures, Journal of Physics E 5 (1972) 803-808.
[25] E.P. Butler, In situ experiments in the transmission electron microscope, Rep Prog Phys 42 (1979) 833-895.
[26] G. Dupouy, F. Perrier, P. Verdier, Amelioration du contraste des images d'objets amorphes minces en microscopie electronique, J Microsc 5 (1966) 655.
[27] H. Hashimoto, T. Naiki, M. Mannami, K. Fujita, Structure and Properties of Thin Films, (1959)
[28] K.A. Taylor, R.M. Glaeser, Hydrophilic Support Films of Controlled Thickness and Composition, Review of Scientific Instruments 44 (1973) 1546.
[29] D.F. Parsons, V.R. Matricardi, R.C. Moretz, J.N. Turner, Electron microscopy and diffraction of wet unstained and unfixed biological objects, Advances in Biological and Medical Physics 15 (1974) 161-270.
[30] A.D. Maynard, Don't define nanomaterials, Nature 475 (2011) 31.
[31] W. Choi, J.Y. Lee, H.S. Lim, Electrochemical lithiation reactions of Cu6Sn5 and their reaction products, Electrochemistry Communications 6 (2004) 816-820.
[32] J.Y. Huang, L. Zhong, C.M. Wang, J.P. Sullivan, W. Xu, L.O. Zhang, S.X. Mao, N.S. Hudak, X.H. Liu, A. Subramanian, H. Fan, L. Qi, A. Kushima, J. Li, In Situ Observation of the Electrochemical Lithiation of a Single SnO_2 Nanowire Electrode, Science 330 (2010) 1515-1520.
[33] M.T. McDowell, S.W. Lee, J.T. Harris, B.A. Korgel, C. Wang, W.D. Nix, Y. Cui, In situ TEM of two-phase lithiation of amorphous silicon nanospheres, Nano Lett 13 (2013) 758-764.
[34] X.H. Liu, S. Huang, S.T. Picraux, J. Li, T. Zhu, J.Y. Huang, Reversible nanopore formation in Ge nanowires during lithiation-delithiation cycling: an in situ transmission electron microscopy study, Nano Lett 11 (2011) 3991-3997.
[35] T.D. Hatchard, J.R. Dahn, In situ XRD and electrochemical study of the reaction of lithium with amorphous silicon, Journal of The Electrochemical Society 151 (2004) A838.
[36] W. Liang, H. Yang, F. Fan, Y. Liu, X.H. Liu, J.Y. Huang, T. Zhu, S. Zhang, Tough germanium nanoparticles under electrochemical cycling, ACS Nano 7 (2013) 3427-3433.
[37] J. Wang, F. Fan, Y. Liu, K.L. Jungjohann, S.W. Lee, S.X. Mao, X. Liu, T. Zhu, Structural Evolution and Pulverization of Tin Nanoparticles during Lithiation-Delithiation Cycling, Journal of the Electrochemical Society 161 (2014) F3019-F3024.
[38] L. Xu, C. Kim, A.K. Shukla, A. Dong, T.M. Mattox, D.J. Milliron, J. Cabana, Monodisperse Sn nanocrystals as a platform for the study of mechanical damage during electrochemical reactions with Li, Nano Lett 13 (2013) 1800-1805.
[39] C. Kim, M. Noh, M. Choi, J. Cho, B. Park, Critical size of a nano SnO2 electrode for Li-secondary battery, Chemistry of Materials 17 (2005) 3297-3301.
[40] C. Lupu, J.-G. Mao, J.W. Rabalais, A.M. Guloy, J.W. Richardson, X-ray and neutron diffraction studies on "$Li_{4.4}Sn$", Inorg Chem 42 (2003) 3765-3771.
[41] A.J. Leenheer, K.L. Jungjohann, K.R. Zavadil, C.T. Harris, Phase Boundary Propagation in Li-Alloying Battery Electrodes Revealed by Liquid-Cell Transmission Electron Microscopy, ACS Nano 10 (2016) 5670-5678.
[42] J.T. Harris, J.L. Hueso, B.A. Korgel, Hydrogenated amorphous silicon (a-Si:H) colloids, Chemistry of Materials 22 (2010) 6378-6383.
[43] Y. Liu, N.S. Hudak, D.L. Huber, S.J. Limmer, J.P. Sullivan, J.Y. Huang, In situ transmission electron microscopy observation of pulverization of aluminum nanowires and

evolution of the thin surface Al2O3 layers during lithiation-delithiation cycles, Nano Lett 11 (2011) 4188-4194.
[44] W. Liang, L. Hong, H. Yang, F. Fan, Y. Liu, H. Li, J. Li, J.Y. Huang, L.Q. Chen, T. Zhu, S. Zhang, Nanovoid formation and annihilation in gallium nanodroplets under lithiation-delithiation cycling, Nano Lett 13 (2013) 5212-5217.
[45] C.J. Wen, R.A. Huggins, Electrochemical investigation of the lithium-gallium system, Journal of the Electrochemical Society 128 (1981) 1636-1641.
[46] W. Xia, Q. Zhang, F. Xu, H. Ma, J. Chen, K. Qasim, B. Ge, C. Zhu, L. Sun, Visualizing the Electrochemical Lithiation/Delithiation Behaviors of Black Phosphorus byin SituTransmission Electron Microscopy, The Journal of Physical Chemistry C 120 (2016) 5861-5868.
[47] L.-Q. Sun, M.-J. Li, K. Sun, S.-H. Yu, R.-S. Wang, H.-M. Xie, Electrochemical Activity of Black Phosphorus as an Anode Material for Lithium-Ion Batteries, The Journal of Physical Chemistry C 116 (2012) 14772-14779.
[48] A. Kushima, X.H. Liu, G. Zhu, Z.L. Wang, J.Y. Huang, J. Li, Leapfrog cracking and nanoamorphization of ZnO nanowires during in situ electrochemical lithiation, Nano Lett 11 (2011) 4535-4541.
[49] D.A. Cogswell, M.Z. Bazant, Coherency strain and the kinetics of phase separation in LiFePO4 nanoparticles, ACS Nano 6 (2012) 2215-2225.
[50] Y.J. Zhu, J.W. Wang, Y. Liu, X.H. Liu, A. Kushima, Y.H. Liu, Y.H. Xu, S.X. Mao, J. Li, C.S. Wang, J.Y. Huang, In Situ Atomic-Scale Imaging of Phase Boundary Migration in FePO4 Microparticles During Electrochemical Lithiation, Adv. Mater. 25 (2013) 5461-5466.
[51] P. Pradere, J.F. Revol, L. Nguyen, R. St. John Manley, Lattice imaging of poly-4-methyl-pentene-1 single crystals; use and misuse of Fourier averaging techniques, Ultramicroscopy 25 (1988) 69-80.
[52] S.J. Kim, S.Y. Noh, A. Kargar, D.L. Wang, G.W. Graham, X.Q. Pan, In situ TEM observation of the structural transformation of rutile TiO2 nanowire during electrochemical, lithiation, Chem. Commun. 50 (2014) 9932-9935.
[53] Q. Su, J. Zhang, Y. Wu, G. Du, Revealing the electrochemical conversion mechanism of porous Co3O4 nanoplates in lithium ion battery by in situ transmission electron microscopy, Nano Energy 9 (2014) 264-272.
[54] P. Poizot, S. Laurelle, S. Grugeon, L. Dupont, J.-M. Tarascon, Nano-sized transition-metal oxides as negative-electrode materials for lithium-ion batteries, Nature 407 (2000) 496-.
[55] Q. Su, J. Xie, J. Zhang, Y. Zhong, G. Du, B. Xu, In situ transmission electron microscopy observation of electrochemical behavior of CoS(2) in lithium-ion battery, ACS Appl Mater Interfaces 6 (2014) 3016-3022.
[56] X. Li, D. Xiao, H. Zheng, X. Wei, X. Wang, L. Gu, Y.-S. Hu, T. Yang, Q. Chen, Ultrafast and reversible electrochemical lithiation of InAs nanowires observed by in-situ transmission electron microscopy, Nano Energy 20 (2016) 194-201.
[57] L.Q. Zhang, X.H. Liu, Y. Liu, S. Huang, T. Zhu, L. Gui, S.X. Mao, Z.Z. Ye, C.M. Wang, J.P. Sullivan, J.Y. Huang, Controlling the lithiation-induced strain and charging rate in nanowire electrodes by coating, ACS Nano 5 (2011) 4800-4809.
[58] I. Cuttress, Intel's 'tick-tock' seemingly dead, becomes 'process-architecture-optimization', 2016 (2016)
[59] Z. Zeng, X. Zhang, K. Bustillo, K. Niu, C. Gammer, J. Xu, H. Zheng, In situ study of lithiation and delithiation of MoS2 nanosheets using electrochemical liquid cell transmission electron microscopy, Nano letters 15 (2015) 5214-5220.

[60] R. Nesper, H.G. von Schnering, Li21Si5, a Zintl phase as well as a Hume-Rothery phase, J Solid State Chem 70 (1987) 48-57.
[61] G.R. Goward, N.J. Taylor, D.C.S. Souza, L.F. Nazar, The true crystal structure of Li17M4 revised from Li22M5, J Alloys Compd 329 (2001) 82-91.
[62] D.B. Williams, C.B. Carter, Transmission Electron Microscopy, 2nd ed, Springer, USA, 2009.
[63] M. Haider, P. Hartel, H. Muller, S. Uhlemann, J. Zach, Information transfer in a TEM corrected for spherical and chromatic aberration, Microsc Microanal 16 (2010) 393-408.
[64] J.C.H. Spence, High resolution transmission electron microscopy, 3rd ed., Oxford University Press, Oxford, 2003.
[65] C.-L. Jia, M. Lentzen, K. Urban, High-resolution transmission electron microscopy using negative spherical aberration, Microscopy and Microanalysis 10 (2004) 174-184.
[66] K.W. Urban, The new paradigm of transmission electron microscopy, MRS Bulletin 32 (2007) 946-952.
[67] C.L. Jia, L. Houben, A. Thust, J. Barthel, On the benefit of the negative-spherical-aberration imaging technique for quantitative HRTEM, Ultramicroscopy 110 (2010) 500-505.
[68] G. Mobus, G. Necker, M. Ruhle, Adaptive Fourier-filtering technique for quantitative evaluation of high-resolution electron micrographs of interfaces, Ultramicroscopy 49 (1993) 46-65.
[69] S. Jewell, S.M. Kimball, Mineral commodity summaries 2015, (2015) 1-196.
[70] D.T. Mackay, M.T. Janish, U. Sahaym, P.G. Kotula, K.L. Jungjohann, C.B. Carter, M.G. Norton, Template-free electrochemical synthesis of tin nanostructures, J. Mater. Sci. 49 (2014) 1476-1483.
[71] R. Eisberg, R. Resnick, Quantum physics of atoms, molecules, solids, nuclei, and particles, 2, Wiley, New York, 1985.
[72] F.W. Horton, Molybdenum: its ores and their concentration, with a discussion of markets, prices, and uses, Govt. print. off., 1916.
[73] M. Schlesinger, M. Paunovic, Modern Electroplating, Wiley, Hoboken, NJ, 2010.
[74] M. Galiński, A. Lewandowski, I. Stępniak, Ionic liquids as electrolytes, Electrochimica Acta 51 (2006) 5567-5580.
[75] N.J. Dudney, Addition of a thin-film inorganic solid electrolyte (Lipon) as a protective film in lithium batteries with a liquid electrolyte, Journal of Power Sources 89 (2000) 176-179.
[76] N. Takahashi, M. Shiojiri, S. Enomoto, High resolution transmission electron microscope observation of stacking faults of molybdenum disulphide in relation to lubrication, Wear 146 (1991) 107-123.
[77] A.N. Enyashin, M. Bar-Sadan, L. Houben, G. Seifert, Line defects in molybdenum disulfide layers, J Phys Chem C 117 (2013) 10842-10848.
[78] J.A. Wilson, A.D. Yoffe, The transition metal dichalcogenides discussion and interpretation of the observed optical, electrical and structural properties, Adv Phys 18 (1969) 193-335.
[79] J.S. Griffith, L.E. Orgel, Ligand-field theory, Quarterly Reviews, Chemical Society 11 (1957) 381-393.
[80] C.L.B. Macdonald, Character tables for point groups, (2002)
[81] M. Kertesz, R. Hoffmann, Octahedral vs trigonal-prismatic coordination and clustering in transition metal dichalcogenides, J Am Chem Soc 106 (1984) 3453-3460.
[82] A.N. Enyashin, G. Seifert, Density-functional study of Li_xMoS_2 intercalates ($0 \leq x \leq 1$), Comp Theor Chem 999 (2012)

[83] K.K. Kam, B.A. Parkinson, Detailed photocurrent spectroscopy of the semiconducting group VI transition metal dichalcogenides, J Phys Chem 86 (1982) 463-467.
[84] S.H. El-Mahalawy, B.L. Evans, The thermal expansion of 2H-MoS2, 2H-MoSe2 and 2H-WSe2 between 20 and 800°C, J Appl Cryst 9 (1976) 403-.
[85] A.N. Gandi, U. Schwingenschlögl, Thermal conductivity of bulk and monolayer MoS2, EPL (Europhysics Letters) 113 (2016) 36002.
[86] V. Buck, Morphological properties of sputtered MoS2 films, Wear 91 (1983) 281-288.
[87] C.W. Bauschlicher, P. Maitre, Theoretical study of the first transition row oxides and sulfides, Theor Chim Acta 90 (1995) 189-203.
[88] Q.H. Wang, K. Kalantar-Zadeh, A. Kis, J.N. Coleman, M.S. Strano, Electronics and optoelectronics of two-dimensional transition metal dichalcogenides, Nat Nanotechnol 7 (2012) 699-712.
[89] A. Splendiani, L. Sun, Y. Zhang, T. Li, J. Kim, C.Y. Chim, G. Galli, F. Wang, Emerging photoluminescence in monolayer MoS2, Nano Lett 10 (2010) 1271-1275.
[90] H.J. Conley, B. Wang, J.I. Ziegler, R.F. Haglund, Jr., S.T. Pantelides, K.I. Bolotin, Bandgap engineering of strained monolayer and bilayer MoS2, Nano Lett 13 (2013) 3626-3630.
[91] S.B. Desai, G. Seol, J.S. Kang, H. Fang, C. Battaglia, R. Kapadia, J.W. Ager, J. Guo, A. Javey, Strain-induced indirect to direct bandgap transition in multilayer WSe2, Nano Lett 14 (2014) 4592-4597.
[92] S. Tongay, J. Zhou, C. Ataca, K. Lo, T.S. Matthews, J. Li, J.C. Grossman, J. Wu, Thermally driven crossover from indirect toward direct bandgap in 2D semiconductors: MoSe2 versus MoS2, Nano Lett 12 (2012) 5576-5580.
[93] B. Radisavljevic, A. Radenovic, J. Brivio, i.V. Giacometti, A. Kis, Single-layer MoS2 transistors, Nature nanotechnology 6 (2011) 147-150.
[94] E. Benavente, M.A. Santa Ana, F. Mendizabal, G. Gonzalez, Intercalation chemistry of molybdenum disulfide, Coordination Chemistry Reviews 224 (2002) 87-109.
[95] K. Fredenhagen, G. Cadenbach, Die bindung von kalium durch kohlenstoff, Zeitschrift für anorganische und allegmeine chemie 158 (1926) 249-263.
[96] J. van Landuyt, G. van Tendeloo, S. Amelinckx, Electron diffraction study of inter- and intrapolytypic phase transitions in transition metal dichalcogenides I, Phys Stat Solidi A 26 (1974) 359-376.
[97] J. van Landuyt, G. van Tendeloo, S. Amelinckx, Electron diffraction study of inter- and intrapolytypic phase transitions in transition metal dichalcogenides II, Phys Stat Solidi A 26 (1974) 585-592.
[98] G. Eda, T. Fujita, H. Yamaguchi, D. Voiry, M.W. Chen, M. Chhowalla, Coherent atomic and electronic heterostructures of single-layer MoS2, ACS Nano 6 (2012) 7311-7317.
[99] M. Calandra, Chemically exfoliated single-layer MoS2: Stability, lattice dynamics, and catalytic adsorption from first principles, Phys Rev B 88 (2013) 245428-245421-245426.
[100] C.B. Carter, D.B. Williams, Transmission Electron Microscopy, (2016)
[101] J.P. Hirth, J. Lothe, Theory of Dislocations, 2nd ed., Wiley, New York, 1982.
[102] W.-K. Burton, N. Cabrera, F. Frank, The growth of crystals and the equilibrium structure of their surfaces, Philosophical Transactions of the Royal Society of London A: Mathematical, Physical and Engineering Sciences 243 (1951) 299-358.
[103] L. Zhang, K. Liu, A.B. Wong, J. Kim, X. Hong, C. Liu, T. Cao, S.G. Louie, F. Wang, P. Yang, Three-dimensional spirals of atomic layered MoS2, Nano Lett 14 (2014) 6418-6423.

[104] P. Delavignette, S. Amelinckx, Observation des dislocations dans des cristaux a structure lamellaire, Proc. Eur. Reg. Conf. Electron Microscopy 1 (1960) 404-408.
[105] D.W. Pashley, A.E.B. Presland, Observations on dislocations in molybdenite, Proc. Eur. Reg. Conf. Electron Microscopy 1 (1960) 417-422.
[106] N. Takahashi, M. Shiojiri, Stacking faults in hexagonal and rhombohedral crystals produced by mechanical operation in relation to lubrication, Wear 167 (1993) 163-171.
[107] D.J. Cockayne, I.L.F. Ray, M.J. Whelan, Investigations of dislocation strain fields using weak beams, Philosophical Magazine 20 (1969) 1265-1270.
[108] D.J. Cockayne, Principles and practice of the weak-beam method of electron microscopy, J. Microsc.-Oxf. 98 (1973) 116-134.
[109] R.C. Crawford, I.L.F. Ray, D.J.H. Cockayne, The weak-beam technique applied to superlattice dislocations in iron-aluminium alloys, Philosophical Magazine 27 (1973) 1-7.
[110] P.B. Hirsch, A. Howie, M.J. Whelan, A kinematical theory of diffraction contrast of electron transmission microscope images of dislocations and other defects, Philos Trans Roy Soc A 252 (1960) 499-529.
[111] P.J. Phillips, M.C. Brandes, M.J. Mills, M. De Graef, Diffraction contrast STEM of dislocations: Imaging and simulations, Ultramicroscopy 111 (2011) 1483-1487.
[112] R. Gröger, K.J. Dudeck, P.D. Nellist, V. Vitek, P.B. Hirsch, D.J.H. Cockayne, Effect of Eshelby twist on core structure of screw dislocations in molybdenum: atomic structure and electron microscope image simulations, Philosophical Magazine 91 (2011) 2364-2381.
[113] J.D. Eshelby, The twist in a crystal whisker containing a dislocation, Philosophical Magazine 3 (1958) 440-447.
[114] R.B. Somoano, V. Hadek, A. Rembaum, Alkali metal intercalates of molybdenum disulfide, J Chem Phys 58 (1973) 697-701.
[115] P.M. Williams, B.A. Robinson, Electron microscopy study of organic intercalation complexes in NbSe2, Nat Phys Sci 245 (1973) 79-80.
[116] J.A. Wilson, F.J. Di Salvo, S. Mahajan, Charge density waves and superlattices in the metallic layered transition metal dichalcogenides, Adv Phys 24 (1975) 117-201.
[117] F.R. Gamble, F.J. DiSalvo, R.A. Klemm, T.H. Geballe, Superconductivity in layered structure organometallic crystals, Science 168 (1970) 568-570.
[118] M.S. Whittingham, Electrical energy storage and intercalation chemistry, Science 192 (1976) 1126-1127.
[119] K. Chang, W. Chen, In situ synthesis of MoS2/graphene nanosheet composites with extraordinarily high electrochemical performance for lithium ion batteries, Chem Commun 47 (2011) 4252-4254.
[120] H. Hwang, H. Kim, J. Cho, MoS2 nanoplates consisting of disordered graphene-like layers for high rate lithium battery anode materials, Nano letters 11 (2011) 4826-4830.
[121] J.R. Dahn, T. Zheng, Y. Liu, J.S. Xue, Mechanisms for lithium insertion in carbonaceous materials, Science 270 (1995) 590.
[122] L. Ji, Z. Lin, M. Alcoutlabi, X. Zhang, Recent developments in nanostructured anode materials for rechargeable lithium-ion batteries, Energy & Environmental Science 4 (2011) 2682-2699.
[123] L. Wang, Z. Xu, W. Wang, X. Bai, Atomic mechanism of dynamic electrochemical lithiation processes of MoS2 nanosheets, J Am Chem Soc 136 (2014) 6693-6697.
[124] M. Winter, J.O. Besenhard, M.E. Spahr, P. Novak, Insertion electrode materials for rechargeable lithium batteries, Adv. Mater. 10 (1998) 725-763.

[125] M.S. Whittingham, F.R. Gamble Jr, The lithium intercalates of the transition metal dichalcogenides, Mater Res Bull 10 (1975) 363-371.
[126] D.W. Murphy, F.J. Di Salvo, H. G.W., J.V. Waszczak, Convenient preparation and physical properties of lithium intercalation compounds of group 4B and 5B layered transition metal dichalcogenides, Inorg Chem 15 (1976) 17-21.
[127] M.S. Whittingham, Role of ternary phases in cathode reactions, J Electrochem Soc 123 (1976) 315-320.
[128] M.S. Whittingham, Chemistry of intercalation compounds: metal guests in chalcogenide hosts, Prog Solid State Chem 12 (1978) 41-99.
[129] C.B. Carter, M.G. Norton, Ceramic Materials: Science and Engineering, 2nd, Springer, New York, 2013.
[130] M. Chhowalla, H.S. Shin, G. Eda, L.J. Li, K.P. Loh, H. Zhang, The chemistry of two-dimensional layered transition metal dichalcogenide nanosheets, Nat. Chem. 5 (2013) 263-275.
[131] V. Nicolosi, M. Chhowalla, M.G. Kanatzidis, M.S. Strano, J.N. Coleman, Liquid exfoliation of layered materials, Science 340 (2013) 1420-+.
[132] Q.M. Su, Z.M. Dong, J. Zhang, G.H. Du, B.S. Xu, Visualizing the electrochemical reaction of ZnO nanoparticles with lithium by in situ TEM: two reaction modes are revealed, Nanotechnology 24 (2013) 6.
[133] M. Janish, C. Carter, In-situ TEM observations of the lithiation of molybdenum disulfide, Scripta Materialia 107 (2015) 22-25.
[134] S. Bhattacharya, A.R. Riahi, A.T. Alpas, In-situ observations of lithiation/de-lithiation induced graphite damage during electrochemical cycling, Scripta Materialia 64 (2011) 165-168.
[135] S.Q. Wang, J.Y. Zhang, N. Ding, C.H. Chen, Synthesis of nanobelt-tangled spheroids of copper (II) oxide at room temperature and their application for lithium-ion batteries, Scripta Materialia 60 (2009) 1117-1120.
[136] L. Wang, Y. Yu, P.-C. Chen, C.-H. Chen, Electrospun carbon–cobalt composite nanofiber as an anode material for lithium ion batteries, Scripta Materialia 58 (2008) 405-408.
[137] D. Chakravarty, D.J. Late, Exfoliation of bulk inorganic layered materials into nanosheets by the rapid quenching method and their electrochemical performance, European Journal of Inorganic Chemistry 2015 (2015) 1973-1980.
[138] M. Tan, Z. Wang, J. Peng, X. Jin, Facile Synthesis of Large and Thin TiS2Sheets via a Gas/Molten Salt Interface Reaction, Journal of the American Ceramic Society 98 (2015) 1423-1428.
[139] H. Wang, H. Feng, J. Li, Graphene and graphene-like layered transition metal dichalcogenides in energy conversion and storage, Small 10 (2014) 2165-2181.
[140] C.M. Julien, Lithium intercalated compounds - Charge transfer and related properties, Mater. Sci. Eng. R-Rep. 40 (2003) 47-102.
[141] D. Li, C. Zhang, G. Du, R. Zeng, S. Wang, Z. Guo, Z. Chen, H. Liu, Enhanced electrochemical performance of MoS_2 for lithium ion batteries by simple chemical lithiation, J Chinese Chem Soc 59 (2012) 1196-1200.
[142] M.A. Santa Ana, V. Sanchez, G. Gonzalez, Temperature effects on the diffusion of Lithium in MoS2, Electrochim Acta 40 (1994) 1773-1775.
[143] R.H. Friend, A.D. Yoffe, Electronic properties of intercalation complexes of the transition metal dichalcogenides, Adv Phys 36 (1987) 1-94.

[144] A.N. Enyashin, L. Yadgarov, L. Houben, I. Popov, M. Weidenbach, R. Tenne, B.-S. M., G. Seifert, New route for stabilization of 1T-WS_2 and MoS_2 phases, J Phys Chem C 115 (2011) 24586–24591.
[145] B.G. Silbernagel, Lithium intercalation complexes of layered transition metal dichalcogenides: an NMR survey of physical properties, Solid State Comm 17 (1975) 361-365.
[146] M.A. Py, R.R. Haering, Structural destabilization induced by lithium intercalation in MoS_2 and related compounds, Can. J. Phys. 61 (1983) 76-84.
[147] H.P. Komsa, A.V. Krasheninnikov, Native defects in bulk and monolayer MoS2 from first principles, Physical Review B 91 (2015)
[148] U. Müller, Symmetry relationships between crystal structures: applications of crystallographic group theory in crystal chemistry, OUP Oxford, 2013.
[149] E.C. Technology, Conductivity of metals sorted by resistivity, 2016 (2013)
[150] R. Fiedler, I. Vagera, On the Burgers Vectors in β-Sn Single Crystals, physica status solidi (a) 32 (1975) 419-424.
[151] R.W. Vook, Dislocations in evaporated single crystal tin films, Acta Metallurgica 12 (1964) 197-207.
[152] M. Guo, M. Fung, F. Fang, X. Chen, A. Ng, D. AB, W. Chan, ZnO and TiO2 1D nanostructures for photocatalytic applications, J Alloys Compd 509 (2011) 1328-1332.
[153] C. Koenigsmann, S. Wong, One-dimensional noble metal electrocatalysis: a promising structural paradigm for direct methanol fuel cells, Energy Environ Sci 4 (2011) 1045-1528.
[154] M. Spencer, Gas sensing applications of 1D-nanostructured zinc oxide: Insights from density functional theory calculations, Prog Mater Sci 57 (2012) 437-486.
[155] J. Tian, Z. Xu, C. Shen, F. Liu, N. Xu, H.-J. Gao, One-dimensional boron nanostructures: prediction, synthesis, characterizations, and applications, Nanoscale 2 (2010) 1375-1389.
[156] T. Zhai, X. Fang, Y. Bando, D. Goldberg, One-dimensional CdS nanostructures: synthesis, properties, and applications, Nanoscale 2 (2010) 168-187.
[157] M. Burek, A. Budiman, Z. Jahed, N. Tamura, M. Kunz, S. Jin, S. Han, G. Lee, C. Zamecnik, T. Tsui, Fabrication, microstructure, and mechanical properties of tin nanostructures, Mater Sci Eng A 528 (2011) 5822-5832.
[158] V. Schmidt, J. Wittemann, S. Senz, U. Gosele, Silicon nanowires: a review on aspects of their growth and their electrical properties, Adv Mater 21 (2009) 2681-2702.
[159] R. Wagner, W. Ellis, Vapor-liquid-solid mechanism of single crystal growth, Appl Phys Lett 4 (1964) 89-90.
[160] D. McIlroy, D. Zhang, Y. Kranov, M. Norton, Nanosprings, Appl Phys Lett 79 (2001) 1540-1542.
[161] D. Panda, T. Tseng, One-dimensional ZnO nanostructures: fabircation, optoelectronic properties, and device applications, J. Mater. Sci. 48 (2013) 6849-6877.
[162] B. Thabethe, G. Malgas, D. Motaung, T. Malwela, C. Arendse, Self-catalytic growth of tin oxide nanowires by chemical vapor deposition process, Nanomater (2013)
[163] C. Chan, H. Peng, G. Liu, K. McIlwrath, X. Zhang, R. Huggins, Y. Cui, High-performance lithium battery anodes using silicon nanowires, Nat Nanotechnol 3 (2008) 31-35.
[164] E. Kukovitsky, S. L'vov, N. Sainov, VLS-growth of carbon nanotubes from the vapor, Chem Phys Lett 317 (2000) 65-70.
[165] C. Chen, Y. Bisrat, Z. Luo, R. Schaak, C. Chao, D. Lagoudas, Fabricaiton of single-crystal tin nanowires by hydraulic pressure injection, J Nanotechnol 17 (2006) 367-374.

[166] T. Djenizian, I. Hanzu, M. Eyraud, L. Santinacci, Electrochemical fabrication of tin nanowires: a short review, C R Chim 11 (2008) 995-1003.
[167] D.J. Rowenhorst, P.W. Voorhees, Measurements of the grain boundary energy and anisotropy in tin, Metall. Mater. Trans. A-Phys. Metall. Mater. Sci. 36A (2005) 2127-2135.
[168] E.L. Maksimova, L.S. Shvindlerman, B.B. Straumal, Transformation of ∑17 special tilt boundaries to general boundaries in tin, Acta Metallurgica 36 (1988) 1573-1583.
[169] D.A. Molodov, B.B. Straumal, L.S. Shvindlerman, The effect of pressure on migration of (001) tilt grain-boundaries in tin bicrystals, Scripta Metallurgica 18 (1984) 207-211.
[170] S.H. Suh, J.B. Cohen, J. Weertman, X-ray diffraction studies on the misorientation of subgrains during creep of tin single crystals, Scripta Metallurgica 15 (1981) 517-522.
[171] W. Boas, P.J. Fensham, Rate of self-diffusion in tin crystals, Nature 164 (1949) 1127-1128.
[172] P.J. Fensham, Self-diffusion in tin crystals, Australian Journal of Scientific Research A 3 (1950) 91-104.
[173] S.J. Rothman, N.L. Peterson, Isotope effect and divacancies for self-diffusion in copper, physica status solidi (b) 35 (1969) 305-312.
[174] C.B. Carter, ∑=99 and ∑=41 grain boundaries, Acta Metallurgica 36 (1988) 2753-2760.
[175] S. Maruyama, H. Kiho, Intersections of {301}, {101} Twin Bands in Tin, Journal of the Physical Society of Japan 11 (1956) 516-521.
[176] R. Cahn, Twinned crystals, Advances in Physics 3 (1954) 363-445.
[177] L.P. Lehman, Y. Xing, T.R. Bieler, E.J. Cotts, Cyclic twin nucleation in tin-based solder alloys, Acta Materialia 58 (2010) 3546-3556.
[178] J.W. Faust, H.F. John, The growth of semiconductor crystals from solution using the twin-plane reentrant-edge mechanism, Journal of Physics and Chemistry of Solids 25 (1964) 1407-1415.
[179] R. Fiedler, A.R. Lang, Dislocation generation at surfaces of tin single-crystals, J. Mater. Sci. 7 (1972) 531-&.
[180] J.T. Fourie, F. Weinberg, F.W.C. Boswell, The growth of twins in tin single crystals as observed by transmission electron microscopy, Acta Metallurgica 8 (1960) 851-863.
[181] K. Ojima, Y. Taneda, Observations of dislocations in white tin using high-resolution electron microscopy, Japanese Journal of Applied Physics 27 (1988) L496-L498.
[182] K. Ojima, Y. Taneda, An arrangement of boundary dislocations in white tin observed by high-resolution electron microscopy, Japanese Journal of Applied Physics 28 (1989) L500-L502.
[183] J.W. Wang, F.F. Fan, Y. Liu, K.L. Jungjohann, S.W. Lee, S.X. Mao, X.H. Liu, T. Zhu, Structural evolution and pulverization of tin nanoparticles during lithiation-delithiation cycling, J Electrochem Soc 161 (2014) F3019-F3024.
[184] Q. Li, P. Wang, Q. Feng, M. Mao, J. Liu, S.X. Mao, H. Wang, In Situ TEM on the reversibility of nanosized Sn anodes during the electrochemical reaction, Chem Mater 26 (2014) 4102-4108.
[185] X.J. Bai, B. Wang, H.P. Wang, J.M. Jiang, Preparation and electrochemical properties of profiled carbon fiber-supported Sn anodes for lithium-ion batteries, J. Alloy. Compd. 628 (2015) 407-412.
[186] M. Gu, Y. Li, X. Li, S. Hu, X. Zhang, W. Xu, S. Thevuthasan, D.R. Baer, J.G. Zhang, J. Liu, C. Wang, In situ TEM study of lithiation behavior of silicon nanoparticles attached to and embedded in a carbon matrix, ACS Nano 6 (2012) 8439-8447.

[187] L. Luo, J. Wu, J. Luo, J. Huang, V.P. Dravid, Dynamics of electrochemical lithiation/delithiation of graphene- encapsulated silicon nanoparticles studied by in-situ TEM, Sci Rep 4 (2014) 1-6.
[188] W. Wang, Y. Xiao, X. Wang, B. Liu, M. Cao, In situ encapsulation of germanium clusters in carbon nanofibers: high-performance anodes for lithium-ion batteries, ChemSusChem 7 (2014) 2914-2922.
[189] M.T. Janish, D.T. Mackay, Y. Liu, K.L. Jungjohann, C.B. Carter, M.G. Norton, TEM in situ lithiation of tin nanoneedles for battery applications, Journal of Materials Science 51 (2016) 589-602.
[190] M. Armand, J.M. Tarascon, Building better batteries, Nature 451 (2008) 652–657.
[191] J.B. Goodenough, Y. Kim, C. Mater, Challenges for rechargeable Li batteries, 22 (2009) 587–603.
[192] H. Wu, G. Chan, J.W. Choi, I. Ryu, Y. Yao, M.T. McDowell, S.W. Lee, A. Jackson, Y. Yang, L. Hu, Y. Cui, Stable cycling of double-walled silicon nanotube battery anodes through solid- electrolyte interphase control, Nature Nanotechn 7 (2012) 310–315.
[193] J.M. Tarascon, M. Armand, Issues and challenges facing rechargeable lithium batteries, Nature 414 (2001) 359–367.
[194] B. Kang, G. Ceder, Battery materials for ultrafast charging and discharging, Nature 458 (2009) 190–193.
[195] M.S. Whittingham, Lithium batteries and cathode materials, Chem Rev 104 (2004) 4271–4301.
[196] P. Poizot, S. Laruelle, S. Grugeon, L. Dupont, J.M. Tarascon, Nano-sized transition-metal oxides as negative-electrode materials for lithium-ion batteries, Nature 407 (2000) 496-499.
[197] P. Denholm, J. Jorgenson, M. Hummon, T. Jenkin, D. Palchak, B. Kirby, O. Ma, M. O'Malley, The value of energy storage for grid applications, (2013)
[198] M.H. Shao, In situ microscopic studies on the structural and chemical behaviors of lithium-ion battery materials, J Power Sources 270 (2014) 475-498.
[199] R.A. Huggins, Lithium alloy negative electrodes, J Power Sources 81–82 (1999) 13-19.
[200] J. Wang, I.D. Raistrick, R.A. Huggins, Behavior of some binary lithium alloys as negative electrodes in organic solvent-based electrolytes, J Electrochem Soc 133 (1986) 457-460.
[201] A.R. Kamili, D.J. Fray, Tin-based materials as advanced anode materials for lithium ion batteries, Rev Adv Mater Sci 27 (2011) 14-24.
[202] H. Wang, H. Huang, L. Chen, C. Wang, B. Yan, Y. Yu, Y. Yang, G. Yang, Preparation of Si/Sn-based nanoparticles composited with carbon fibers and improved electrochemical performance as anode materials, ACS Sustainable Chem & Eng 2 (2014) 2310-2317.
[203] C.M. Wang, In situ transmission electron microscopy and spectroscopy studies of rechargeable batteries under dynamic operating conditions: A retrospective and perspective view, J. Mater. Res. 30 (2015) 326-339.
[204] C.-M. Park, J.-H. Kim, H. Kim, H.-J. Sohn, Li-alloy based anode materials for Li secondary batteries, Chem Soc Rev 39 (2010) 3115-3141.
[205] M. Park, H. Sun, H. Lee, J. Lee, J. Cho, Lithium-air batteries: survey on the current status and perspectives towards automotive applications from a battery industry standpoint, Adv Energy Mater 2 (2012) 780-800.
[206] M. Egashira, H. Takatsuji, S. Okada, J. Yamaki, Properties of containing Sn nanoparticles activated carbon fiber for a negative electrode in lithium batteries, J Power Sources 107 (2002) 56-60.

[207] M.G. Norton, U. Sahaym, Lithium-ion natteries with nanostructured electodes and associated methods of making, (2012) 1-5.
[208] X.H. Liu, L. Zhong, S.X. Mao, T. Zhu, J.Y. Huang, Size-dependent fracture of silicon nanoparticles during lithiation, ACS Nano 6 (2012) 1522-1531.
[209] W. Liang, H. Yang, F. Fan, Y. Liu, X.H. Liu, J.Y. Huang, T. Zhu, S. Zhang, Tough germanium nanoparticles under electrochemical cycling, ACS Nano 7 (2013) 3427-3433.
[210] Z. Wei, H. Mao, T. Huang, A.i. Yu, Facile synthesis of Sn/TiO2 nanowire array composites as superior lithium-ion battery anodes, J Power Sources 223 (2013) 50-55.
[211] X.H. Liu, L.Q. Zhang, L. Zhong, Y. Liu, H. Zheng, J.W. Wang, J.H. Cho, S.A. Dayeh, S.T. Picraux, J.P. Sullivan, S.X. Mao, Z.Z. Ye, J.Y. Huang, Ultrafast electrochemical lithiation of individual Si nanowire anodes, Nano Lett 11 (2011) 2251-2258.
[212] T.D. Bogart, D. Oka, X. Lu, M. Gu, C. Wang, B.A. Korgel, Lithium ion battery performance of silicon nanowires with carbon skin, ACS Nano 8 (2014) 915-922.
[213] Y. Liu, X.H. Liu, B.M. Nguyen, J. Yoo, J.P. Sullivan, S.T. Picraux, J.Y. Huang, S.A. Dayeh, Tailoring lithiation behavior by interface and bandgap engineering at the nanoscale, Nano Lett 13 (2013) 4876-4883.
[214] Y. Zhong, X. Li, Y. Zhang, R. Li, M. Cai, X. Sun, Nanostructued core–shell Sn nanowires @ CNTs with controllable thickness of CNT shells for lithium ion battery, Appl Surf Sci 332 (2015) 192-197.
[215] H. Hou, X. Tang, M. Guo, Y. Shi, P. Dou, X. Xu, Facile preparation of Sn hollow nanospheres anodes for lithium-ion batteries by galvanic replacement, Mater Lett 128 (2014) 408-411.
[216] B. Wang, B. Luo, X. Li, L. Zhi, The dimensionality of Sn anodes in Li-ion batteries, Mater Today 15 (2012) 544-552.
[217] C.R. Sides, N. Li, C.J. Patrissi, B. Scrosati, C.R. Martin, Nanoscale materials for lithium-ion batteries, MRS Bull 27 (2002) 604-607.
[218] Z. Shen, Y. Hu, Y. Chen, X.W. Zhang, K. Wang, R. Chen, Tin nanoparticle-loaded porous carbon nanofiber composite anodes for high current lithium-ion batteries, J Power Sources 278 (2015) 660-667.
[219] J. Xie, Y. Zheng, S. Liu, G. Cao, X. Zhao, One-pot in-situ synthesis of Sn/carbon-fibers nanocomposite by chemical vapor deposition and its Li-storage properties, J Mater Sci Technol 28 (2012) 275-279.
[220] Y. Yu, L. Gu, C.B. Zhu, P.A. van Aken, J. Maier, Tin nanoparticles encapsulated in porous multichannel carbon microtubes: preparation by single-nozzle electrospinning and application as anode material for high-performance Li-based batteries, J. Am. Chem. Soc. 131 (2009) 15984-15985.
[221] N. Liu, Z. Lu, J. Zhao, M.T. McDowell, H.W. Lee, W. Zhao, Y. Cui, A pomegranate-inspired nanoscale design for large-volume-change lithium battery anodes, Nat Nanotechnol 9 (2014) 187-192.
[222] C. Cui, X.H. Liu, N. Wu, Y. Sun, Facile synthesis of core/shell-structured Sn/onion-like carbon nanocapsules as high-performance anode material for lithium-ion batteries, Mater Lett 143 (2015) 35-37.
[223] W. Li, R. Yang, J. Zheng, X. Li, Tandem plasma reactions for Sn/C composites with tunable structure and high reversible lithium storage capacity, Nano Energy 2 (2013) 1314-1321.

[224] X. Xia, X. Wang, H.M. Zhou, X. Niu, L.G. Xue, X.W. Zhang, Q.F. Wei, The effects of electrospinning parameters on coaxial Sn/C nanofibers: Morphology and lithium storage performance, Electrochim. Acta 121 (2014) 345-351.
[225] C.D. Owen, D.T. Mackay, M.G. Norton, Growth mechanism for one-dimensional tin nanoneedles, J Mater Sci 51 (2015)
[226] M.T. Janish, D.T. Mackay, Y. Liu, K.L. Jungjohann, C.B. Carter, M.G. Norton, Lithiation of tin nanoneedles investigated by in-situ TEM, Microsc. Microanal.. 19 (suppl. 2) (2014) 1878-1879.
[227] M.T. Janish, D.T. Mackay, K.L. Jungjohann, Y. Liu, C.B. Carter, M.G. Norton, Initial observations of the lithiation of tin nanoneedles, IMC-18 (2014) MS-14-P-3454-3451-3452.
[228] M. Winter, J.O. Besenhard, Electrochemical lithiation of tin and tin-based intermetallics and composites, Electrochim. Acta 45 (1999) 31-50.
[229] R. Nesper, H. Schnering, Li21Sn5, a Zintl phase as well as a Hume-Rothery phase, J Solid State Chem 70 (1987) 48-57.
[230] R.S. Wagner, W.C. Ellis, Vapor-liquid-solid mechanism of single crystal growth, Appl Phys Lett 4 (1964) 89-90.
[231] V. Schmidt, J.V. Wittemann, S. Senz, U. Gosele, Silicon nanowires: a review on aspects of their growth and their electrical properties, Adv Mater 21 (2009) 2681-2702.
[232] D.N. McIlroy, D. Zhang, Y. Kranov, M.G. Norton, Nanosprings, Appl Phys Lett 79 (2001) 1540-1542.
[233] D. Panda, T.Y. Tseng, One-dimensional ZnO nanostructures: fabrication, optoelectronic properties, and device applications, J Mater Sci 48 (2013) 6849–6877.
[234] B.S. Thabethe, G.F. Malgas, D.E. Motaung, T. Malwela, C.J. Arendse, Self-catalytic growth of tin oxide nanowires by chemical vapor deposition process, Nanomater (2013)
[235] C.K. Chan, H. Peng, G. Liu, K. McIlwrath, X.F. Zhang, R.A. Huggins, Y. Cui, High-performance lithium battery anodes using silicon nanowires, Nature nanotechnology 3 (2008) 31-35.
[236] E.F. Kukovitsky, S.G. L'vov, N.A. Sainov, VLS-growth of carbon nanotubes from the vapor, Chem Phys Lett 317 (2000) 65-70.
[237] C.C. Chen, Y. Bisrat, Z.P. Luo, R.E. Schaak, C.G. Chao, D.C. lagoudas, Fabrication of single-crystal tin nanowires by hydraulic pressure injection, J Nanotechn 17 (2006) 367-374.
[238] T. Djenizian, I. Hanzu, M. Eyraud, L. Santinacci, Electrochemical fabrication of tin nanowires: A short review, C R Chimie X (2008) 995-1003.
[239] H. Zhao, C. Jiang, X. He, J. Ren, C. Wan, Advanced structures in electrodeposited tin base anodes for lithium ion batteries, Electrochimica Acta 52 (2007) 7820-7826.
[240] A. Subramanian, N.S. Hudak, J.Y. Huang, Y. Zhan, J. Lou, J.P. Sullivan, On-chip lithium cells for electrical and structural characterization of single nanowire electrodes, Nanotechnology 25 (2014) 265402.
[241] A.J. Leenheer, J.P. Sullivan, M.J. Shaw, C.T. Harris, A sealed liquid cell for in situ transmission electron microscopy of controlled electrochemical processes, J Microelectromech S 24 (2015)
[242] A. Leenheer, K. Jungjohann, K. Zavadil, J. Sullivan, C. Harris, Lithium electrodeposition dynamics in aprotic electrolyte observed in situ via transmission electron microscopy, ACS Nano 9 (2015) 4379-4389.
[243] P. Joensen, R.F. Frindt, S.R. Morrison, Single-layer MoS2, Materials Research Bulletin 21 (1986) 457-461.

[244] H. Wang, P. Skeldon, G. Thompson, G. Wood, Synthesis and characterization of molybdenum disulphide formed from ammonium tetrathiomolybdate, Journal of materials science 32 (1997) 497-502.
[245] J.W. Wang, X.H. Liu, S.X. Mao, J.Y. Huang, Microstructural evolution of tin nanoparticles during in situ sodium insertion and extraction, Nano Lett 12 (2012) 5897-5902.
[246] E. Chason, F. Pei, C.L. Briant, H. Kesari, A.F. Bower, Significance of Nucleation Kinetics in Sn Whisker Formation, Journal of Electronic Materials 43 (2014) 4435-4441.
[247] B.Z. Lee, D.N. Lee, Spontaneous growth mechanism of tin whiskers, Acta Materialia 46 (1998) 3701-3714.
[248] J. Ham, W. Shim, D.H. Kim, K.H. Oh, P.W. Voorhees, W. Lee, Watching bismuth nanowires grow, Appl. Phys. Lett. 98 (2011) -.
[249] A. Howie, M.J. Whelan, Diffraction contrast of electron microscope images of crystal lattice defects II: the development of a dynamical theory, Proc Roy Soc A263 (1961) 217-237.
[250] A. Howie, M.J. Whelan, Diffraction contrast of electron microscope images of crystal lattice defects III: results and experimental confirmation of the dynamical theory of dislocation image contrast, Proc Roy Soc (1962) 206-230.